ABSTRACT

Title of Dissertation: EXCURSION IN THE QUANTUM LOSS LANDSCAPE: LEARNING, GENERATING AND SIMULATING IN THE QUANTUM WORLD
Ali Rad
Doctor of Philosophy, 2024

Dissertation Directed by: Ali Rad
Department of Physics

Statistical learning is emerging as a new paradigm in science. This has ignited interest within our inherently quantum world in exploring quantum machines for their advantages in learning, generating, and predicting various aspects of our universe by processing both quantum and classical data. In parallel, the pursuit of scalable science through physical simulations using both digital and analog quantum computers is rising on the horizon.

In the first part, we investigate how physics can help classical Artificial Intelligence (AI) by studying hybrid classical-quantum algorithms. We focus on quantum generative models and address challenges like barren plateaus during the training of quantum machines. We further examine the generalization capabilities of quantum machine learning models, phase transitions in the over-parameterized regime using random matrix theory, and their effective behavior approximated by Gaussian processes.

In the second part, we explore how AI can benefit physics. We demonstrate how classical

Machine Learning (ML) models can assist in state recognition in qubit systems within solid-state devices. Additionally, we show how ML-inspired optimization methods can enhance the efficiency of digital quantum simulations with ion-trap setups

Finally, in the third part, we focus on how physics can help physics by using quantum systems to simulate other quantum systems. We propose native fermionic analog quantum systems with fermion-spin systems in silicon to explore non-perturbative phenomena in quantum field theory, offering early applications for lattice gauge theory models.

EXCURSION IN THE QUANTUM LOSS LANDSCAPE: LEARNING, GENERATING, AND SIMULATING IN THE QUANTUM WORLD

by

Ali Rad

Dissertation submitted to the Faculty of the Graduate School of the
University of Maryland, College Park in partial fulfillment
of the requirements for the degree of
Doctor of Philosophy
2024

Advisory Committee:
Professor Mohammad Hafezi, Chair/Advisor
Professor Michael Gullans, Co-Advisor
Professor Zohreh Davoudi
Professor Victor Albert
Professor Christopher Jarzynski

Preface

"We have to remember that what we observe is not nature itself, but nature exposed to our method of questioning."

— Werner Heisenberg, Gifford Lectures at 1955

Dedication

To Mr. M. Hadaadi,

Who has devoted his life to guiding and nurturing children at Kanoon. He altered the course of my world-line within the future light cone when I was 8 years old by showing me the wonders of the universe in the smallest Stellarium on Earth (and likely in the solar system) Beneath the starry skies, near the Lut Desert.

Acknowledgments

I owe my deepest gratitude to all the great people and beautiful minds who have made this thesis possible and who have enriched my graduate experience in ways I will cherish forever.

First and foremost, I would like to thank my advisor, Prof. Mohammad Hafezi for giving me the invaluable opportunity to work with him. His multidisciplinary research was inspiring to me. I am also deeply grateful to my co-advisor, Prof. Michael Gullans for all his patience and support. I would like to thank Zohreh Davoudi, Prof. Norbert Linke, and Prof. Soheil Feyzi for allowing me to conduct research with them. I sincerely thank Prof. Victor Albert, and Prof. Christopher Jarzynski for agreeing to serve on my thesis committee and for their invaluable time reviewing my manuscript.

I would like to express my gratitude to my colleagues and friends at JQI and QuICS, who have enriched my graduate life in countless ways. Special thanks to Andrea, Alireza (Seif), Gautam, Alex, and Ella for their support and camaraderie.

I extend my thanks to the ghosts of the Atlantic building (especially, the second floor), who kept me company during countless overnight stays in the dungeon of the office and tried to be nice.

A special thanks to all the baristas at my sanctuary for focus and productivity, the Starbucks in College Park Shopping Center, for serving me countless grande Caffè Misto with refills.

I was extremely fortunate to have the support of two great companies, Mahmood and Amin

Joon, during the final phase of my PhD. My heartfelt thanks go to Mahmood for his unwavering support and late-night deep conversations, accompanied by the taste of pomegranate and almond croissant, that words cannot fully appreciate. I am also grateful to Amin Joon for his extragalactic support and for brightening others' days with his presence, like a Type Ia supernova on steroids.

I would like to thank my ex-roommates, Seyed Ali L., Fath, Amir, Parham, and Mohammad, for their companionship and for letting me steal their tasty food. Thanks to my community friends, Reza, Majid, Batoul, Alireza P., Masoud, Ali F., and Seyed Ali H.M. for their friendship. I would like to thank my many friends from the IGSF community with whom I grew together. Thanks to my music instructors, Maestro S. Ahmadi and S. Araghi, who accepted my endless excuses due to deadlines and added color to my life during my PhD journey.

I owe my deepest thanks to my family. My mother, who has protected me through life's hardships and prioritized our education and growth. Words cannot express my gratitude to my brother, who supported me through the ups and downs of being a poor grad student and helped me stay grounded and not evaporate!

I want to extend my thanks to all those I may have inadvertently missed but who hold a special place in my heart. Finally, I would like to remember the beloved Behrad, who left us too soon, for his deep brotherhood, solid mentorship at the recreation center, and all our late afternoon tea chats and diet cheating with Chicken Panini at Busboys and Poets. To all the innocent passengers of flight PS752, to all the people in the November 2019 movement, and the Women-Life-Freedom 2022 movement, who devoted their lives to a brighter future and whose tragedies have transformed me multiple times during this journey.

Manuscripts, Contributions, and Funding

The chapters of this thesis are based on the following works:

- Chapter. 2: **Ali Rad**, Alireza Seif, and Norbert M. Linke. "Surviving the barren plateau in variational quantum circuits with Bayesian learning initialization." preprint arXiv:2203.02464 (2022) [1]. Presented at APS March Meeting (2022), T37. 005.

  This project was defined by Norbert. As the main author, I developed the methodology, conducted the simulations, and generated the results. All authors contributed to writing the draft.

- Chapter. 3: **Ali Rad**. "Deep Quantum Neural Networks are Gaussian Process". preprint arXiv:2305.12664 (2023) [2]. Under review, NeurIPS 2024 Conference (2024), Submission Number: 13408.

  This research was partially motivated by my other research at the Department of Computer Science: **Ali Rad**, Amir Nili, Soheil Feyzi, "N^2TK: Node Neural Tangent Kernel". The manuscript was prepared for ICLR (2020).

  As a solo author, I defined the problem, developed the methodology, conducted the simulations, generated the results, and wrote the draft.

- Chapter. 4: **Ali Rad**. "Double Descent in Learning with Quantum Machines", under review, NeurIPS 2024 Conference (2024), Submission Number: 13421.

- Chapter. 5: **Ali Rad**, Ayush Varshney, Mohammad Hafezi, and Alireza Seif. "Hamiltonian Calibration Through Pruning Control Parameters." (2023) –Unpublished Manuscript–I developed the simulations and the method, which were initially developed by Alireza and Ayush. I rewrote the draft and generated the final results.

- Chapter. 6: **Ali Rad**, Alexander Schuckert, Eleanor Crane, Gautam Nambiar, Fan Fei, Jonathan Wyrick, Richard M. Silver, Mohammad Hafezi, Zohreh Davoudi, and Michael J. Gullans. "Analog Quantum Simulator of a Quantum Field Theory with Fermion-Spin Systems in Silicon." preprint arXiv:2407.03419 (2024) [3]. Presented at APS March Meeting Abstracts (2023), D74. 010 and RQS workshop (2022)

  This project was defined by Michael and Mohammad. As the main author, I developed the methodology, conducted the simulations, and generated the results. I wrote the early version of the draft, and the theory part was developed by Gautam and Zohreh.

I would like to acknowledge the research support from the Joint Quantum Institute (JQI), the Quantum Information and Computer Science (QuICS), and the Robust Quantum Simulation Institute (RQS) at the University of Maryland. Additionally, I am grateful for the following research funding that made these works possible:

U.S. Department of Energy (DOE), Office of Science, National Quantum Information Science Research Centers, Quantum Systems Accelerator. AFOSR MURI FA9550-19-1-0399, NSF QLCI OMA-2120757, ARL W911NF1920181, Minta Martin, and Simons Foundations. Office of Nuclear Physics, via the program on Quantum Horizons: QIS Research and Innovation for Nuclear Science (award no. DE-SC0023710), the National Science Foundation's Quantum Leap Challenge Institute in Robust Quantum Sim- ulation (award no. OMA-2120757) and DOE's

Quantum Systems Accelerator program (award no. DE-AC02-05CH11231).

Table of Contents

List of Tables

List of Figures

List of Abbreviations

BAS	Bars-and-Stripes
BO	Bayesian Optimization
BP	Barren Plateau
CNN	Convolutional Neural Network
CPU	Classical Processing Unit
ED	Exact Diagonalization
ESD	Empirical Spectral Distribution
FTHFB	Finite Temperature Hartree-Fock-Bogoliubov
GOE	Gaussian Orthogonal Ensemble
GCV	Generalized cross validation
GUE	Gaussian Unitary Ensemble
HF	Hartree-Fock
KL	Kullback-Leibler
LGT	Lattice Gauge Theory
LOOCV	Leave-one-out cross-validation
LSTM	Long Short Term Memory
MAP	Maximum A Posteriori
MLE	Maximum Likelihood Estimation
MP	Marcenko Pastur
NTK	Neural Tangnet Kernel
PAC	Probably Approximately Correct
PQC	Parameterized Quantum Circuit
QAOA	Quantum Approximate Optimization Algorithm
QCD	Quantum Quantum Chromodynamics
QD	Quantum Dot
QNN	Quantum Neural Network
QNTK	Quantum Neural Tangent Kernel
RHKS	Reproducing Hilbert Kernel Space
RMT	Random Matrix Theory
SGD	Stochastic Gradient Descent
SPSA	Simultaneous Perturbation Stochastic Approximation
VQA	Variational Quantum Algorithm
VQE	Variational Quantum Eigensolver
WHRF	Wishart hypertoroidal random fields

Chapter 1: Introduction

> "For the natural philosopher, there are no distinct fields of physics, chemistry, biology or computer science. These are artificial boundaries created by us. What lies in front of us is simply nature, and the joy of discovering and playing with it."
>
> a source who requested anonymity

1.1 Fourth Paradigm

We are living in an extraordinary time in the universe—a sentiment echoed by every generation, yet ours has a unique twist. We stand on the brink of a transformative era: the twilight of carbon-based intelligence and the dawn of its silicon-based successor. Philosophers of science like Jim Gray [5] suggest we are stepping into an unprecedented phase of scientific discovery, known as the fourth paradigm. Long ago, the empirical method laid the foundation for scientific inquiry, marking the first paradigm. It was a time when describing the natural world was a groundbreaking endeavor. Fast forward to the last century, and we find ourselves in the second paradigm, where models became the tools to abstract and generalize those empirical observations. The advent of computational science heralded the third paradigm in recent decades, empowering us to simulate

and understand complex systems in ways previously unimaginable. Now, it appears we are on the cusp of the fourth paradigm. This new era promises to integrate theory, experiment, and simulation with the vast potential of data exploration and intensive science discovery, heralding a future where our understanding of the universe could expand tremendously.

1.2 Classical Machine and Quantum Machine

Leveraging the power of physical systems as computing platforms has become a pivotal development, especially with the recent advancements in quantum computing. Originally, the proposal to use physics in this way aimed to simulate more complex physical phenomena [6]. This leads to an intriguing question: why should the field of physics concern itself with computation or, more broadly, computer science and information theory?

The intricate relationship between physics and computation and information theory is vividly illustrated by Maxwell's demon thought experiment [7], highlighting how classical computation is intrinsically linked to the physical universe, its limitations, or how the entropy of black holes put constraints on many computational and information theories. This concept underscores the foundational principle that information processing and physical laws are deeply interconnected. The Turing machine [8] further exemplifies this connection, serving as a pivotal model that bridges the abstract realm of computation with tangible, physical mechanisms [9].

The evolution of computational paradigms led to the exploration of quantum computing, a field that extends classical computational models to the quantum domain, characterized by significantly lower energy levels. This transition was driven by the promise of quantum computing to leverage the unique properties of quantum mechanics, such as superposition and entanglement,

to achieve computational speedups that are unattainable with classical systems. The allure of quantum computing lies not only in its potential to solve problems deemed intractable for classical computers within a finite timeframe but also in its capacity to challenge and expand our understanding of the fundamental principles of computation itself.

Quantum computing's shiny selling point indeed revolves around its theoretical capability to expedite certain and subset of problems, offering solutions to complex problems much more efficiently than classical approaches. Some examples include factoring large numbers, simulating quantum physical processes, and optimizing large systems, which are tasks where quantum algorithms can outperform their classical counterparts.

However, the significance of quantum computing extends beyond its practical applications. It poses profound questions about the nature of computation, information, and their relationship with the physical laws governing the universe. By pushing the boundaries of what is computationally possible, quantum computing prompts a reevaluation of the limits imposed by classical physics and encourages a deeper inquiry into the principles underlying the physical world and our understanding of it.

1.3 Physics vs. AI

The intriguing question of the relationship between physics and Artificial Intelligence (AI) is one that invites both curiosity and skepticism. Is the frequent juxtaposition of these two fields merely a trend, fueled by hype and buzzwords, or does it reveal a deeper, meaningful connection? At first glance, AI and physics seem to operate within fundamentally different paradigms, almost moving in opposite directions. Physics is dedicated to the discovery and demystification of the

natural world, striving to uncover the underlying principles that govern the universe. In contrast, contemporary AI, particularly in its reliance on neural networks, often treats these networks as 'black boxes.' The intricacies of what occurs inside these networks can be difficult to decipher or may not be the primary focus, provided that the end results are satisfactory. This approach emphasizes the importance of data and computational power over an understanding of the internal mechanisms at play.

This contrast highlights a fundamental difference in approach: physics seeks to understand the world from the bottom up, building a foundation on fundamental principles, while AI adopts a top-down approach, focusing on outcomes and applications without necessarily understanding the underlying processes. This dichotomy is vividly captured in a short essay by Dan Robert, titled 'Why Physics Is Simple and AI Is Hard' [10]. Robert's argument sheds light on the inherent complexity of AI compared to the relative simplicity of physics, at least in terms of conceptual understanding and I would like to review his comment in the following lines.

Let's consider an array of spins in the Ising model, arranged in a $\sqrt{n} \times \sqrt{n}$ grid. Generally, this system can exhibit 2^n distinct configurations. If we assign one of two labels to each configuration it is either trivial or non-trivial—the total number of possible configuration/label pairs escalates to 2^{2^n}, resulting in a phase space of doubly exponential magnitude. Without any underlying rules linking the configuration to its label, no algorithm could surpass the efficiency of a mere lookup table that memorizes all label assignments. This scenario exemplifies the "no-free-lunch" perspective, suggesting that without specific patterns or rules, all algorithms perform equally over all possible problem spaces.

Fortunately, the problems that interest us usually exhibit meaningful relationships between data and labels, placing them within a manageable subset of this vast phase space. This raises the

question: Why are humans capable of effective learning, and why is physics such a powerful tool for deciphering the complexities inherent in nature? The ”no-free-lunch” theorem doesn't seem as daunting in practical scenarios.

One explanation is that humans tend to classify a significant portion of the phase space as meaningless or noise, focusing only on the data with discernible, meaningful patterns. This selective attention might make us overlook hidden patterns within what we dismiss as noise. Indeed, current machine learning techniques, such as neural networks, have demonstrated the ability to identify meaningful relationships in data that humans might not perceive directly. These networks, embodying complex non-linear functions, reveal that human understanding is not equipped to model phenomena of such complexity. However, it prompts a lingering question: Could there be real, non-generated data that follows certain rules, existing only within specific subspaces of the overall phase space?

This refined perspective suggests that while the universe of possible data configurations is vast, the actual, meaningful data likely adheres to certain rules, confining it to a more navigable subspace. This understanding underscores the potential of both human cognition and computational models like neural networks to uncover and learn from the structured patterns that govern the complexity of the world around us.

In other words, humans have an inductive bias and try to see what has been seen before. They look for human-meaningful representations. But human learning may not encompass all that can be learned from the universe. To me, human learning is just part of learning, a subset of the whole phase space that can be explored. One approach is to try to teach machines to learn and find patterns the way humans do, while another approach is to let them go beyond that limit. In that sense, AI can learn patterns that are not recognizable to humans. In this sense, AI is doing

something challenging.

On the other hand, human learning and its approach, physics, seem to have escaped from algorithmic complexity. In this sense, it seems physics builds models that are very simple. But why is that? There can be four properties that lead to this simplicity: 1- Typicality 2- Sparsity 3- Locality 4- Translational Invariance [10].

In a theory with n degrees of freedom, there can be $O(2^n)$ different possible interactions, since each degree of freedom can either participate in the interaction or not. This exponential behavior is daunting, as mentioned before. These "typical" theories are not efficient since the number of experiments needed to find out all interactions increases exponentially and cannot provide good predictive power for us. However, life can be easier with some guidelines. One of them is sparsity. If in our interactions, only k degrees of freedom can participate, then we have only polynomial terms $(n, k) \sim O(n^k/k!)$. Another guideline is locality. It states that only up to k degrees of freedom can interact at the same time: k-locality. We can also observe spatial locality, implied by causality, that two far-off objects cannot participate in one interaction at the same time. By imposing this, we expect the total number to reduce to $O(dn) = O(n)$ if we have a d-dimensional space. Another rule is that we have translational invariance, as a symmetry. This is somehow natural that physics does not depend on where the experiment has been run in the universe. This leads to $O(1)$ number of parameters [10], therefore The sparsity and locality are inductive biases of our learning of the universe via the tools of physics.

In the no-free lunch theorem, if averaged over all possible datasets, there is no distinction between learning algorithms. But in physics, averaging over all experiments gives us a good representation. So, there is a free lunch somehow. One justification is that as local observers, we can only conduct local experiments and therefore we are just living in a tiny subspace of the

general phase space, and that the no-free-lunch theorem doesn't affect us.

1.4 Physics at the Age of AI

During my graduate studies, the scientific community was at the forefront of witnessing the rapid evolution of AI, a field that promised to redefine the boundaries of computation and problem-solving. Meanwhile, the exploration of quantum computing is an active agenda, seeking to harness the quantum nature of the universe to tackle complex problems that remain insurmountable for classical computers operating under traditional logic. The overarching vision of this new computational era is to leverage the principles of physics for routine and critical tasks alike, ranging from encryption to optimization. This ambition extends to all computing paradigms, including innovative approaches like thermal computing, which utilizes the diffusion model to generate novel images or videos, showcasing the versatility and potential of modern computing frameworks [11].

A significant shift in the computational landscape has been the move away from the traditional method of hardcoding algorithms for specific tasks. Instead, the focus has shifted towards enabling machines to learn and deduce solutions independently. In this context, statistical learning emerges as a fundamental component, with the acquisition of knowledge from data becoming a primary and achievable objective. Generative models stand at the forefront of this transition, representing the next frontier in application development.

It is a common belief that studying quantum systems, such as finding the ground state of a quantum many-body system or predicting their evolutions, is challenging with classical machines. This belief stems from the fact that the complexity of representing a quantum system grows

exponentially, $O(2^n)$, with the size n of the system. However, this notion has be challenged under certain conditions.

It turns out that data has significant power. By training machine learning models on data obtained from quantum systems, classical machines, in some certain cases, can achieve efficiencies comparable to those of quantum machines [12]. The power of classical Machine Learning (ML) algorithm over classical algorithms can be demonstrated by one example from work by Huang et al [13]. This research shows that through the efficient classical representation of an unknown quantum system, ML prediction algorithms can capture certain properties (including quantum fidelity, entanglement witness, local observables, two-point correlations, and entanglement entropy) of the quantum system using a method called classical shadow. This leads to the prediction of properties of a quantum system with very few measurements. Furthermore, for tasks like predicting the ground state of the system, it seems that assuming RP $\neq$ NP, there is no randomized classical algorithm that can make an average prediction error with polynomial time in terms of the size of the system. However, there is a classical ML algorithm that, by using polynomial data and computational resources, explores the potential of classical ML algorithms to efficiently predict ground state properties of quantum systems and classify different quantum phases of matter. Under certain conditions, classical ML algorithms can accurately predict the properties of quantum systems after being trained with data derived from measurements of other systems within the same quantum phase. This work not only demonstrates the efficiency of ML in quantum physics but also highlights its capability to outperform traditional computational methods that do not leverage data-driven learning.

In other words, a poly-time classical ML algorithm trained on data can predict better than any poly-time classical algorithm. In fact, it turns out ML algorithms are more useful in this

task since generalization from data can be easier than computing everything, implying that data has computational power. This reveals an intersection between Quantum computation (BQP) and classical algorithms (BPP), and classical ML algorithms with data [13].

To demonstrate another strength of classical ML, Huang et al. showed in another paper [14] that there is an effective classical ML algorithm capable of learning to predict arbitrary quantum processes over embedded classical data into the Hilbert space. This algorithm works not only for polynomial gate sizes of $\mathcal{E}$ but also for arbitrary sizes.

1.5 Quantum Machine and Learning: Quantum Machine Learning

While recognizing that efficient classical machine learning algorithms exist for quantum systems is not trivial, one might still believe that quantum machines should eventually have more advantages since our world is inherently quantum. However, surprisingly, identifying problems where we can achieve quantum advantage is another non-trivial task and the quantum advantage of quantum machine learning (QML) algorithms for classical tasks has not been fully explored.

However, it has been shown that with enough data, classical methods could be as efficient as quantum ones, unless a suitable quantum kernel is found [12]. This kernel must preserve the distance between two quantum states after they transition to feature space.

The trainability of quantum machine learning models, which are proposed based on variational quantum circuits or quantum kernel methods, often suffers from the "Barren Plateau" issue, rendering the algorithms inefficient. For example, determining even the sign of the gradient may require an exponential amount of measurements. On the other hand, it has been shown that with a sufficient amount of data, classical ML algorithms can perform as well as quantum ML for

certain tasks [13]. This narrows down the effectiveness of quantum ML models across all tasks.

While up to this point, the results have favored classical machine learning and highlighted the limitations of quantum approaches for many tasks, there are subsets of problems where quantum learning holds exponential advantages. For example, in Ref. [15], it has been demonstrated that there are exponential separations between learning with and without quantum memory. Additionally, it has been shown that there is a quantum advantage when classical shadow methods are not efficient. The experimental work "Quantum Advantage in Learning States from Experiment" [16] suggests that, in certain tasks, a quantum machine can learn from experiments exponentially faster than classical methods. For an experiment involving n qubits with state ρ, if we aim to learn some property of the system, conventional methods store each measurement in classical memory. In contrast, with quantum enhancement, the quantum states are stored in quantum memory. This quantum advantage applies not only to quantum states but also to quantum processes.

1.6 What AI can do for Physics?

As reviewed in Sec. 1.4, classical machines have recently been used by scientists to leverage intelligence. We have reviewed recent progress in the literature on the application and advantages of classical machine learning (ML) for quantum physics.

In Chapter 5, we discuss another technique from the optimization of ML that inspired us to undertake a project aimed at reducing the cost of simulating the desired Hamiltonian and its intersection with ion traps through the pruning method.

In addition, as we discussed in Section 1.5 , there is a promising quantum advantage in using quantum machine learning for quantum experiments. Once a useful application of quantum

machine learning is identified, it will be time to further study the trainability of quantum neural networks and how their structures can be efficiently optimized. In Chapter 2, we discussed methods of initialization and optimization for navigating the loss function landscape. In Chapter 4, we explored how phase transitions can occur in the trainability of variational quantum circuits, exemplifying quantum neural networks, especially when the model enters the over-parameterization regime.

These are just a few examples of how AI can assist us in automation, tuning, optimization, and state recognition. As discussed earlier, the power of data is key to reducing the difficulty of studying quantum systems with classical machines. Undoubtedly, more profound applications will emerge in the future.

1.7 What Physics can do for AI?

Physical learning, also referred to as human or psychological learning, is often characterized by sparsity and local observation. This concept of sparsity can be applied to a specific case of deep learning to examine the outcomes. In the structure of neural networks, many neurons are interconnected, resulting in interaction patterns that are far from sparse. However, in the limit of large n—also known as the thermodynamic limit—the representation of the system can significantly simplify. The infinite-width limit is one scenario where the system can be described solely by its covariance, rather than by all interactions, thereby reducing complexity from $O(2^n)$ to $O(n^2)$. This is referred to as the overparameterization regime. This concept can also be seen as a $1/n$ expansion in physics, where at the order of $O(1/n^k)$, we allow kth-order neurons to interact with each other. In this context, physical approaches like RG-flow and effective theories can be

applied to understand deep learning models through effective models [10]. We have elaborated on this idea in Chapter 4, followed by previous work in the literature.

In addition, if quantum machines can learn classical data more efficiently, it significantly benefits the intersection of physics and AI. Another promising area is generative models. One application of quantum computers is to produce certain types of distributions exponentially faster. In Chapter 2, we explore how to generate specific distributions using an ion-trap quantum computer as a quantum generative model.

1.8 What Physics can do for Physics?

Quantum computing was initially proposed to leverage physics to enhance our understanding and manipulation of physical systems. In this context, quantum learning models and agents are employed to study complex many-body systems. Additionally, digital and quantum computers are increasingly utilized to simulate quantum systems, albeit currently on a smaller scale.

In Chapter 5 , we discuss the Hamiltonian simulation with ion traps as a form of digital quantum simulation. In Chapter 6, we introduce a novel native fermionic analog quantum simulator to be used for simulating non-perturbative phenomena in quantum field theory and as a tool for lattice gauge theories.

1.9 Structure of the Thesis

In a nutshell, the thesis structure can be described as follows:

In Chapter 2, we examine quantum generative models and propose Bayesian learning strategies to mitigate the barren plateau effect in quantum neural networks.

In Chapter 3, we investigate the effective theories of quantum neural networks in the sparse regime and illustrate how Gaussian processes emerge as a result.

In Chapter 4, we study the generalization capabilities of quantum machine learning models through the lens of random matrix theory. We demonstrate the potential for double descent behavior in quantum models applied to quantum learning tasks, highlighting a phase transition in quantum neural networks.

In Chapter 5, we apply pruning and Hessian-based learning techniques for efficient budget simulation of Hamiltonians with ion trap quantum simulators.

In Chapter. 6, we discuss the development of a simulation proposal of native fermionic analog quantum simulators based on silicon technology.

Chapter 2: Surviving the Barren Plateau in Variational Quantum Circuits with Bayesian Learning Initialization

> "You left your learning rate at home, and now we're wandering this barren wasteland plateau"
>
> Hagar to Adam optimizer

2.1 Abstract

Variational quantum-classical hybrid algorithms are seen as a promising strategy for solving practical problems on quantum computers in the near term. While this approach reduces the number of qubits and operations required from the quantum machine, it places a heavy load on a classical optimizer. While often under-appreciated, the latter is a computationally hard task due to the barren plateau phenomenon in parameterized quantum circuits. The absence of guiding features like gradients renders conventional optimization strategies ineffective as the number of qubits increases. Here, we introduce the fast-and-slow algorithm, which uses Bayesian Learning to identify a promising region in parameter space. This is used to initialize a fast local optimizer to find the global optimum point efficiently. We illustrate the effectiveness of this method on the Bars-and-Stripes (BAS) quantum generative model, which has been studied on

several quantum hardware platforms. Our results move variational quantum algorithms closer to their envisioned applications in quantum chemistry, combinatorial optimization, and quantum simulation problems.

2.2 Introduction

Quantum-classical hybrid algorithms are based on parameterized quantum circuits (PQC) that can prepare different quantum states through variable gate parameters. These algorithms can be adapted to different hardware environments and are, in principle, capable of solving a vast array of problems [17]. This is achieved by outsourcing some of the computational complexity from the quantum device (QPU) to a classical processor (CPU). This keeps the quantum circuits shallow and amenable to noisy devices.

These ideas have been used for developing variational quantum algorithms (VQAs) [18], such as the Variational Quantum Eigensolver (VQE) [19], the Quantum Approximate Optimization Algorithm (QAOA) [20], and Quantum Neural Network (QNN) architectures [21–23]. The original problem is mapped to finding the PQC parameters that minimize a cost function, which is evaluated by performing measurements on the circuit output of the QPU. The results are then provided to the CPU, which employs a classical optimization, or learning, algorithm to find the next set of parameters to feed back to the QPU in an iterative loop. Multiple demonstrations of this quantum-classical hybrid scheme have been realized on small systems [19, 24–29]. The limitations are usually attributed to imperfect quantum hardware, but some of the work points out the importance of the CPU itself [30].

The classical part of the algorithm is challenging for several reasons. The stochastic

nature of QPU readout makes the measured cost function value fluctuate even for a fixed set of parameters. In addition, as the Hilbert space size and the parameter space size increase, the difficulty of finding the global minimum increases exponentially. This indicates that much like non-trivial NP-hard optimization problems, getting trapped in a local minimum is very likely [31, 32].

Additionally, finding the optimal point is made even more difficult by a phenomenon called the "barren plateau" which means that far from any minima, the cost function provides no features to guide the optimization. It can arise for many circuit architectures, including ansatzes with a global cost function [33], highly expressive ansatz circuits [34], highly entangled [35,36] or noisy circuits [37, 38], and the majority of dissipative perceptron-based Quantum Neural Networks (QNN) [39]. It also provides a challenge for parameter initialization, since random initialization of VQAs leads to exponentially small gradients [40].

The existing optimization approaches can generally be divided into gradient-based and gradient-free methods. In the former, the gradient information can be obtained via the parameter shift rule [41–43], or by directly measuring the first- or higher-order partial derivative on the quantum hardware [44,45]. The optimization is then performed using algorithms such as Stochastic Gradient Decent (SGD) [46], Quantum Natural Gradient Decent [47, 48], meta-learning [49], and Simultaneous Perturbation Stochastic Approximation (SPSA) [50]. The latter only uses the value of the cost function and includes methods such as Nelder-Mead, COBYLA, Powell's, and Bayesian-based methods [30, 51–55]. Experiments have revealed the vulnerability of both gradient-based and gradient-free methods to barren plateaus [33, 35–37, 39, 40, 44, 53, 56–58]. While strategies to mitigate or avoid the barren plateau have been proposed [32, 32–34, 58–60], their efficiency in general scenarios remains untested. Others require the circuit to be over-

parameterized [32], which might not be feasible, or demand exponentially scaling resources [56].

In this work, we introduce and evaluate a new technique for finding the global optimum in VQAs, which we call fast-and-slow following Ref. [61]. It employs Bayesian learning, which is gradient-free, as an initialization procedure for subsequent gradient-based optimization, combining global and local information of the parameter landscape. We first describe this method and then test it for different local optimizers on the Bars-and-Stripes (BAS) quantum generative model [30,62]. BAS is a quantum machine learning algorithm, which can be used as a benchmark to study the performance and capabilities of PQCs, and which shows barren plateaus.

2.3 Bayesian Learning For VQAs

Bayesian learning is often viewed as a potent tool in classical optimization, especially when acquiring new data to enhance the model of the cost function is expensive. This approach combines two modes - exploitation and exploration - to strive towards finding the global optimum point. Given its global optimization scheme, this method proves highly beneficial for our problem. The existence of numerous unfavorable local minima and barren plateaus pose a significant challenge to local optimization, which further emphasizes the importance of employing this method. Recent observations suggest that VQC in the overparameterized regime behaves like a Gaussian process [2]. Therefore, employing Bayesian learning could be an effective approach to examining the energy landscape of the VQC in this regime. This concept could also be extended to the more general case, including the underparameterized regime.

In this method, based on the hypothesis, $\mathcal{H}$, for our quantum model, we can assume the prior distribution of the parameters of the quantum circuit $\boldsymbol{\theta} = \{\theta_i\}$. Assuming each parameter

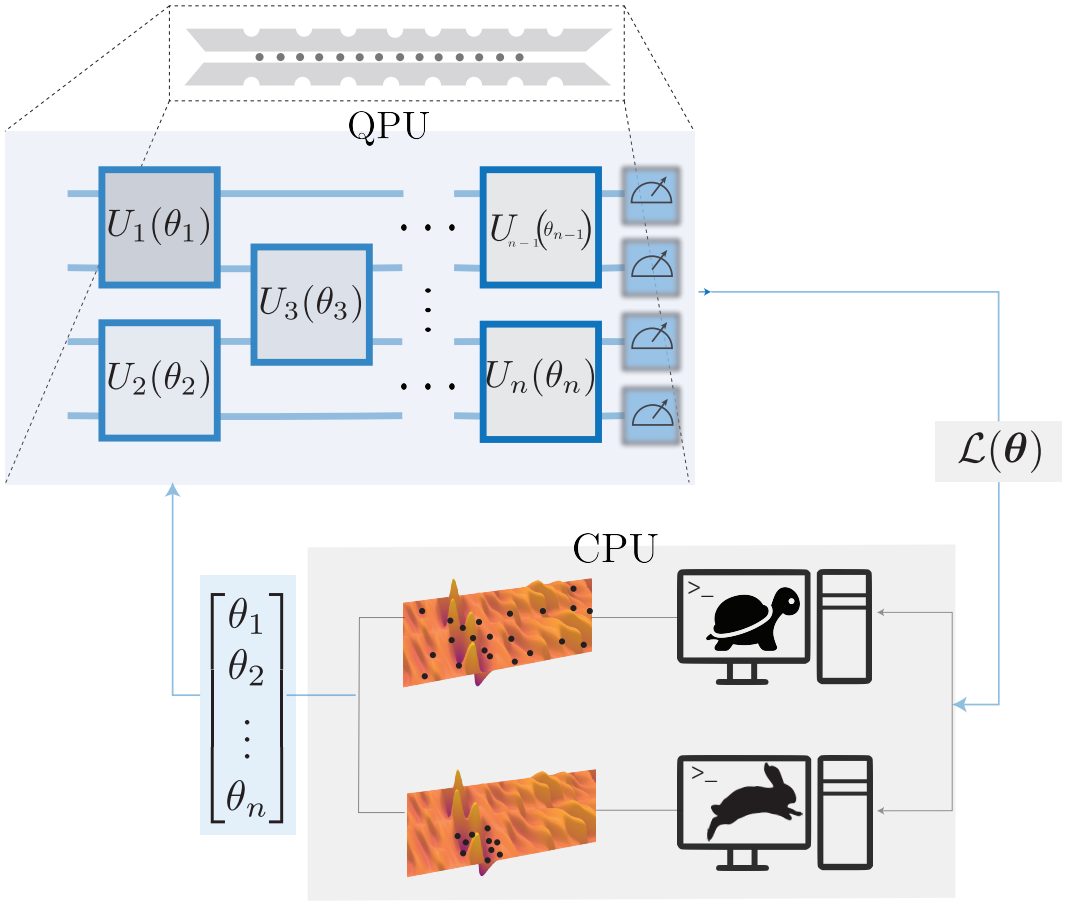

Figure 2.1: The fast-and-slow optimization method for variational quantum algorithms. The QPU executes a quantum circuit consisting of gates $\{U(\theta_i)\}$, parameterized by $\boldsymbol{\theta} = \{\theta_i\}$. The output is used to calculate a cost function value $\mathcal{L}(\boldsymbol{\theta})$, which is passed to an optimizer running on a CPU. The CPU first uses a slow global search method to identify a promising region in parameter space and then a fast local optimizer to find the minimum.

is independent of the others, the prior distribution can be represented as the product of individual posterior distributions $p(\boldsymbol{\theta}) = \prod_{i=1}^{|\boldsymbol{\theta}|} p(\theta_i)$. The task of finding the optimum set of these parameters corresponds to solving the intended optimization problem and updating which can be computed through various approaches such as Maximum A Posteriori (MAP) or Maximum Likelihood Estimation (MLE). In the case of MAP, the optimal parameter values can be determined by maximizing the posterior probability

$$\boldsymbol{\theta}^* = \arg\max_{\theta} p(\theta|\mathbb{O}, \mathcal{H})$$

Upon observing the data points of interest $\mathbb{O}$, we can update our beliefs and make predictions for new data points $\mathbb{P}$ using Bayes' rule:

$$p(\mathbb{P}|\mathbb{O}, \mathcal{H}) = \int \prod_{i}^{|\boldsymbol{\theta}|} d\theta_i \, p(\mathbb{O}|\theta, \mathcal{H}) \, p(\theta|\mathbb{O}, \mathcal{H}) \tag{2.1}$$

One key feature that marks Bayesian inference as an intuitive toolkit for Variational Quantum Algorithms (VQA) is the fact that the distribution of the output of the quantum circuit, y, in the presence of a large number of parameters or qubits, trends towards a Gaussian distribution [2]. This is achieved by defining the output distribution as a series of correlators, up to an order of k, symbolized as $p(y) = e^{-S(y)}/\mathcal{Z}$, whereby:

$$\begin{aligned} S(y) = &\frac{1}{2} \sum_{\mu,\nu=1}^{n} K^{\mu\nu} y_\mu y_\nu \\ &+ \sum_{m=2}^{k} \frac{1}{(2m)!} \sum_{\mu_1,\cdots\mu_{2m}=1} C^{\mu_1\cdots\mu_{2m}} y_{\mu_1} \cdots y_{\mu_{2m}}. \end{aligned} \tag{2.2}$$

In the overparameterization limit, higher-order contributions lessen, thus allowing the output

distribution to be approximated as

$$p(y) \approx \frac{1}{\mathcal{Z}} e^{\frac{1}{2}\sum \mu,\nu=1^n G^{\mu\nu} y_\mu y_\nu} \tag{2.3}$$

Driven by this objective, in the following sections of this paper, we explore this global optimization proposal further, broadening our analysis to encompass more general cases. These cases are particularly interesting as they do not strictly adhere to the overparameterized regime, meaning the number of parameters is not significantly large.

2.4 The Fast-and-Slow Method

Our method has two parts and is shown schematically in Fig. 2.1.

In the first, slow, part we initialize the parameters to zero and perform Bayesian optimization using Gaussian processes. This method is well-suited for this task, since querying the QPU is expensive and results in noisy outputs [63].

The computational complexity of Bayesian optimization increases as the number of samples n gathered from the QPU accumulates, due to the $\mathcal{O}(n^3)$ scaling of the calculation of the covariance matrix inverse [64]. Therefore, this method is not suited for a detailed local search.

In the second, fast, part we use the best parameter set from the slow part to initialize a local optimizer. This is now highly likely to reach the global optimum, since we start in the correct region and there is no longer a barren plateau [65].

There is a trade-off between the number of queries devoted to the global and local optimizers. Too many queries in the slow part waste resources that should be spent on local optimization, while too few queries increase the chance to switch over in a region containing only a local

minimum. The latter might lead to failure since there is no guarantee for a local optimizer to converge to the global optimum after random initialization, regardless of the number of iterations [66]. In practice, the BO shows a distinctive cost function drop after a certain number of iterations for a given circuit. We use this phenomenological criterion as the change-over point in our protocol (see below). Additionally, around this point, the standard deviation of the cost function calculated for multiple batches of the experiment decreases significantly. Note that in general, we expect the switching point to be problem-dependent. The code for the fast-and-slow algorithm used for this work is available on GitHub [1]

2.5 Results

To evaluate our method, we simulate the optimization of BAS circuits on four and six qubits on a classical computer. The BAS [67] maps qubit states in the computational basis to a two-dimensional array of black or white pixels, see appendix A.2 for details. This problem is a good test case since its convergence behavior has been studied on a trapped ion system and it was found to be very well captured by a simple finite-sampling noise model [30].

Specifically, we consider the ensembles BAS$(2, 2)$ and BAS$(2, 3)$ with input $|\psi\rangle = |0\rangle^{\otimes n}$ for $n = 2\times 2$ and $n = 2\times 3$, respectively. The circuit design follows [30] with qubits connectivity given by star-graph, and uses a gate set native to trapped ions. The first layer consists of single-qubit X and Z rotation operators. The following layer applies XX entangling gates to all pairs of qubits. The unitary operator associated with the mentioned circuits, for a total number of layers

[1] `Fast and Slow Algorithm` codebase: `https://github.com/frustea/Quantum-Fast-and-Slow`.

L, can be written as:

$$U(\boldsymbol{\theta}) = \prod_{k=1}^{|\boldsymbol{\theta}|} U_k(\theta_k) = \prod_{\ell=1}^{L} \prod_{\substack{i=1 \\ j=2}}^{n} R_i(\alpha_i^\ell, \beta_i^\ell, \gamma_i^\ell) R_{x_1 x_j}(\phi_j^\ell) \tag{2.4}$$

where we explicitly identify U_k and θ_k corresponding to one and two qubit gates and their parameters in layer ℓ with

$$R_{x_i x_j}(\phi_j^\ell) = e^{-i\phi_j^\ell X_i X_j} \tag{2.5}$$

$$R_i(\alpha_i^\ell, \beta_i^\ell, \gamma_i^\ell) = e^{i\alpha_i^\ell X_i} e^{i\beta_i^\ell Z_i} e^{i\gamma_i^\ell X_i}. \tag{2.6}$$

Expressed in this gate set, the quantum circuits for BAS(2,2) and BAS(2,3) have 26 and 41 variational parameters, respectively.

To ease comparison with [30], the Kullback–Leibler (KL) divergence is used as the cost function, which is a standard metric to compare two distributions [68]:

$$\mathcal{L}_{\mathrm{KL}}(\boldsymbol{\theta}) = \mathbf{KL}\Big(\mathrm{Tr}\big(OU^\dagger(\boldsymbol{\theta})\rho U(\boldsymbol{\theta})\big) || q_{\mathrm{BAS}} \Big). \tag{2.7}$$

where q_{BAS} refers to the desired BAS output distribution.

Since the variance of the cost function gradient, $\mathrm{Var}[\partial_\mu \mathcal{L}] = \langle (\partial_\mu \mathcal{L})^2 - \langle \partial_\mu \mathcal{L} \rangle^2 \rangle$, is exponentially suppressed as a function of qubit number,

$$\mathrm{Var}[\partial_\mu \mathcal{L}] \leq \frac{1}{2^{6n}} f(O, \rho, \rho_{\mathrm{BAS}}) \tag{2.8}$$

there exists a barren plateau in the optimization landscape (see appendix A.1).

To study the performance of the fast-and-slow method, we compare it against strategies with only local or only global optimizers. Specifically, for the pure local schemes, we use the Stochastic Gradient Decent (SGD) [46, 69, 70] and Nelder-Mead (NM) algorithm [71] with random initialization. As a global scheme, we consider BO with parameters initialized to zero. For the fast-and-slow method, we employ the slow BO phase as discussed above, followed by either NM or SGD. Additionally, we consider another hybrid algorithm introduced in Ref. [55], that utilizes a Long Short Term Memory (LSTM) recurrent neural network for initialization followed by NM.

The results are shown for four qubits in Fig. 2.2 and six qubits in Fig. 2.3. The effectiveness of a classical optimizer for VQAs is typically only assessed by the convergence rate of the cost-function without taking into account the quality of the output circuit [55, 59, 72–75]. However, this does not in general make clear when the algorithm gets trapped in a local minimum [76]. For comparison with the target distributions, we show the state populations at different stages of training as figure insets.

The results show that the fast-and-slow algorithm (NM with BO initialization) outperforms the other methods based on the convergence behavior, the final value of the cost function, and its success in generating the desired output distribution. This is even more pronounced when the number of qubits is increased to six, shown in Fig. 2.3.

In our investigations, pure NM was found to perform better than other standard local gradient-free optimizers on their own, such as COBYLA [51] and Powell [52]. Nevertheless, its failure to find the true minimum for six qubits confirms that simplex-based gradient-free optimizers are as susceptible to local minima as gradient-based methods [66].

The fast-and-slow variant involving BO initialization followed by the gradient-based SGD

method is less effective than using NM as the fast stage. The output distributions only partially match the ideal ones, especially when there are more qubits involved. Additionally, pure BO has a low convergence rate and a large classical computational overhead, which means that despite the reliability of discovering the global optimum, our results confirm that it is not practical for VQAs. Finally, LSTM is the weakest strategy for solving our benchmark problems.

2.6 Outlook

Our results show that the fast-and-slow method of initialization and optimization is highly promising since it reduces the number of queries to the QPU substantially and makes training the VQA more practical for a larger number of qubits. The simulated experiment, while well-motivated by being a generic circuit and allowing the comparison with a recent experimental implementation on quantum hardware, only represents a single example problem. Going forward, we will evaluate the method on different kinds of circuits on physical, rather than simulated, quantum hardware.

Furthermore, the fast-and-slow algorithm introduced here represents only the simplest form of a combined scheme with a single switching point and fixed switching criterion. More complex problems might require a dynamic alternation between the fast and slow parts, which has been shown to be beneficial for some problems in classical optimization [61]. Further study is needed to find appropriate methods for determining the switching point and problem-specific adaptations, which will make this method even more powerful.

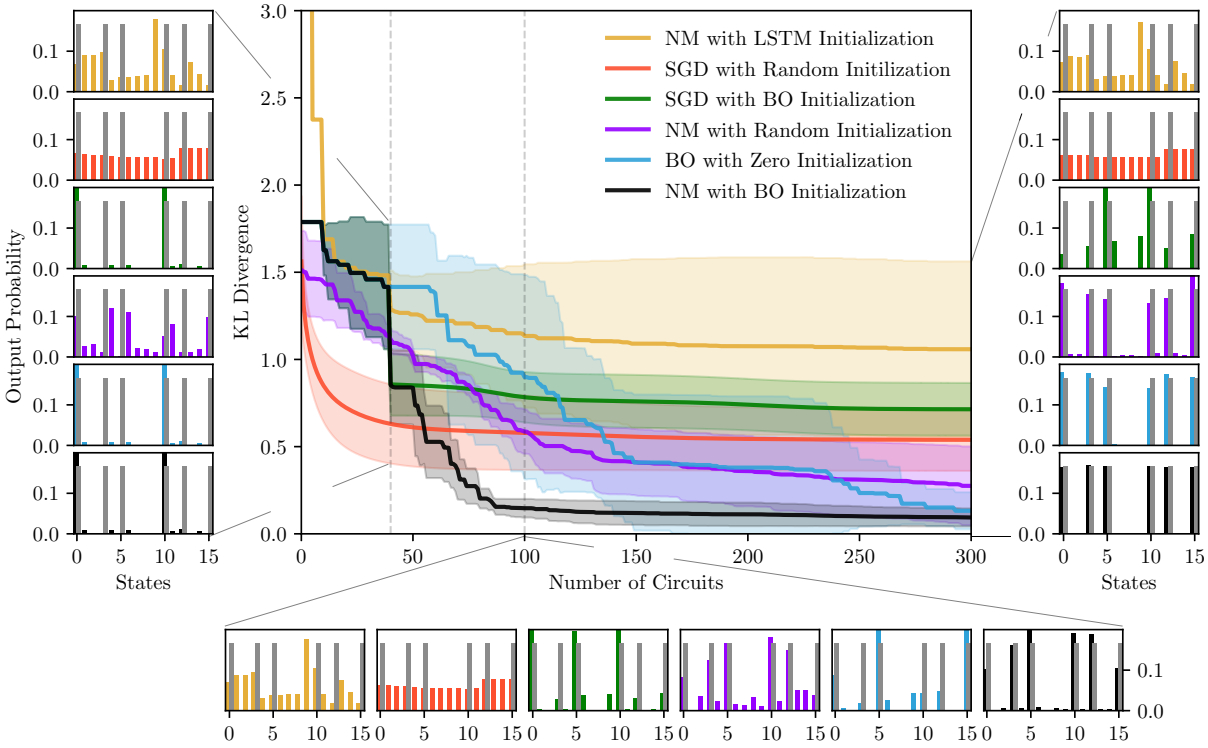

Figure 2.2: Comparison of different optimization methods for the BAS$(2, 2)$ problem with 4 qubits and 26 circuit parameters. The main graph shows the cost function (2.7) against the number of executed circuit instances on the simulated QPU for different combinations of initialization and optimization methods: Nelder-Mead (NM), Stochastic Gradient Descent (SGD), Neural Network (LSTM), and Bayesian Optimization (BO). The fast-and-slow method corresponds to "NM with BO Initialization." For each method, the average value (solid line) and standard deviation based on five repetitions (shaded region) are shown. The output distribution is sampled $N_s = 1024$ times to add statistical errors. The insets show the output distribution at three stages of optimization: 1) after 45 iterations (left), which is the switching point from BO to NM in the fast-and-slow method, 2) after 100 iterations (bottom), when the cost function of fast-and-slow is plateauing, and 3) after 300 iterations (right).

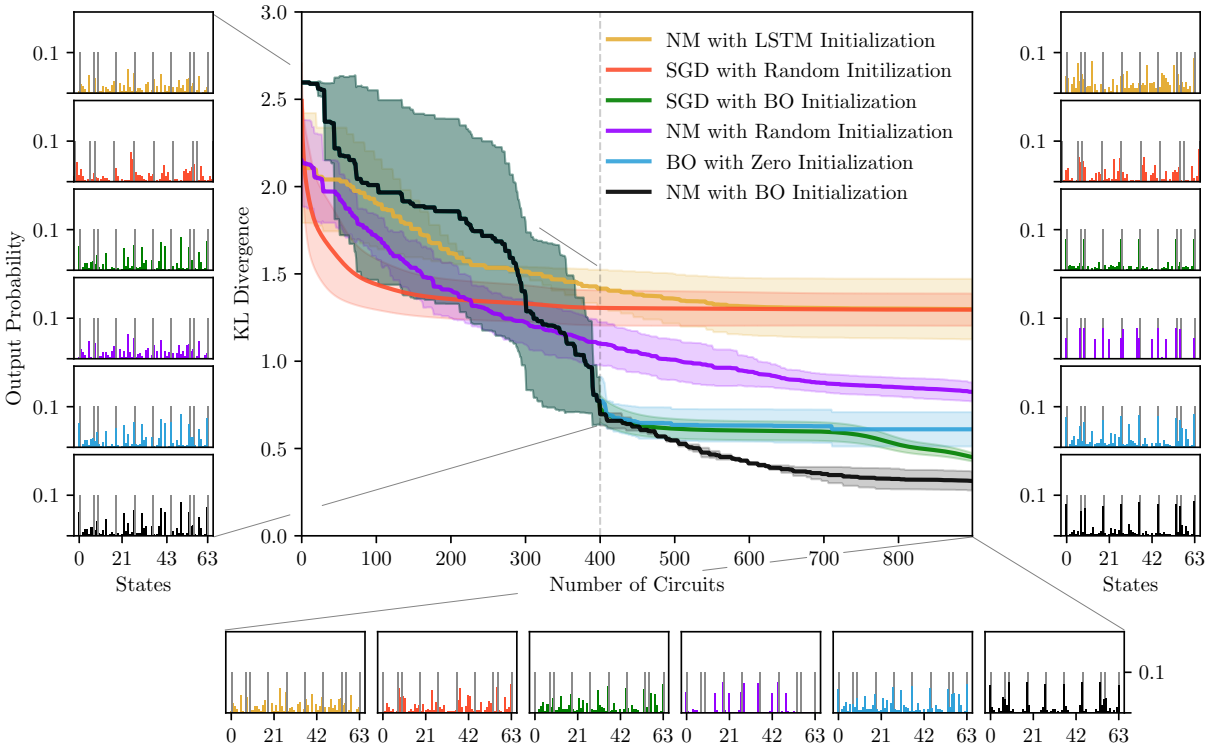

Figure 2.3: Comparison of different optimization methods for the BAS$(2, 3)$ problem with six qubits and 41 circuit parameters (see text): Nelder-Mead (NM), Stochastic Gradient Descent (SGD), Neural Network (LSTM), and Bayesian Optimization (BO). The fast-and-slow method "NM with BO Initialization" is still the best strategy and produces the correct output distribution, but the convergence is slower than for the four-qubit case. The insets show the output distribution at three stages of optimization: 1) after 400 iterations (left), which is the switching point from BO to NM in the fast-and-slow method, 2) after 900 iterations (bottom), and 3) after 1800 iterations (right), which is beyond the range shown in the main plot.

Chapter 3: Deep Quantum Neural Networks are Gaussian Process

"If you gaze long enough into a deep quantum neural network,

Johann Carl Friedrich Gauss also gazes back into you"

Desperate graduate student in his dungeon office

3.1 Abstract

The overparameterization of variational quantum circuits, as a model of Quantum Neural Networks (QNN), not only improves their trainability but also serves as a method for evaluating the property of a given ansatz by investigating their kernel behavior in this regime. In this study, we shift our perspective from the traditional viewpoint of training in parameter space into function space by employing the Bayesian inference in the Reproducing Kernel Hilbert Space (RKHS). We observe the influence of initializing parameters using random Haar distribution results in the QNN behaving similarly to a Gaussian Process (QNN-GP) at wide width or, empirically, at a deep depth. This outcome aligns with the behaviors observed in classical neural networks under similar circumstances with Gaussian initialization. Moreover, we present a framework to examine the impact of finite width in the closed-form relationship using a $1/d$ expansion, where d represents the dimension of the circuit's Hilbert space. The deviation from Gaussian

output can be monitored by introducing new quantum meta-kernels. Furthermore, we elucidate the relationship between GP and its parameter space equivalent, characterized by the Quantum Neural Tangent Kernels (QNTK) . This study offers a systematic way to study QNN behavior in over- and under-parameterized scenarios, based on the perturbation method, and addresses the limitations of tracking the gradient descent methods for higher-order corrections like dQNTK and ddQNTK. Additionally, this probabilistic viewpoint lends itself naturally to accommodating noise within our model.

3.2 Introduction

The capacity for learning and trainability in quantum circuits is an intriguing subject that merits further exploration and discovery. The issue of how trainable variational quantum circuits and quantum neural networks (QNNs) poses a significant challenge that needs to be tackled. The standard approach to training QNN is within the context of *parameter space*. The aim is to find the optimum point in the loss landscape using local gradient-based methods. However, these methods might encounter the Barren Plateau problem [40], where the magnitude of the gradient decreases exponentially as the size of the Hilbert space increases.

Alternatively, we can shift the training process into *functios space*, viewing QNNs as linear combinations of Kernels that exist within the Reproducing Kernel Hilbert Space (RKHS) [21,77]. The learning task in the parametric space of gate's parameters can be transformed into the task of identifying the correct coefficients of kernel regression parameters, which are of the order of the input dataset. This is typically much less than the dimension of the Hilbert space. The process of identifying these coefficients is usually more convex than implementing the original gradient

descent method in the parameter space.

Although the quantum kernel's behavior in different quantum circuit regimes is still a largely uncharted area, recent findings suggest that kernel-based methods can be more successful than gradient methods in mitigating the Barren Plateau problem in under-parameterized regimes [1, 78]. With this evidence, we can now turn our attention in this work to the other part of the spectrum: the over-parameterized regime. We hope that this will enhance our understanding and lay the groundwork for more generic and practical applications in the NISQ era. In this regime, both the functional and parametric methods present more straightforward and comprehensible approaches. Similar to classical Neural Networks (CNNs) [79], the output of the QNN can be determined using the kernel regression method. The kernel employed in this lazy training method is referred to as the Quantum Neural Tangent Kernel (QNTK) [80–84].

An interesting observation has been made regarding CNN when they are over-parameterized through wide layers or deep networks: their output tends to converge towards a Gaussian distribution and Gaussian Process (GP) [85–88]. Given this observation, it's feasible to replace the prior distribution of parameters in classical neural networks with a Gaussian process prior. This process shifts the focus from parameter spaces to the space of functions. A Gaussian process is a probabilistic model that defines a distribution over functions. the idea is to use a prior probability on functions, which is specified as a Gaussian process that determines the shape of the function space, and then update this with the observed data to get a posterior distribution over functions. In contrast to kernel regression, in which one typically needs to make decisions about the kernel hyperparameters, while in Gaussian process regression, these are typically learned from the data. Furthermore, while kernel regression provides a point estimate, Gaussian process regression provides a full probabilistic model, allowing for uncertainty estimation in predictions.

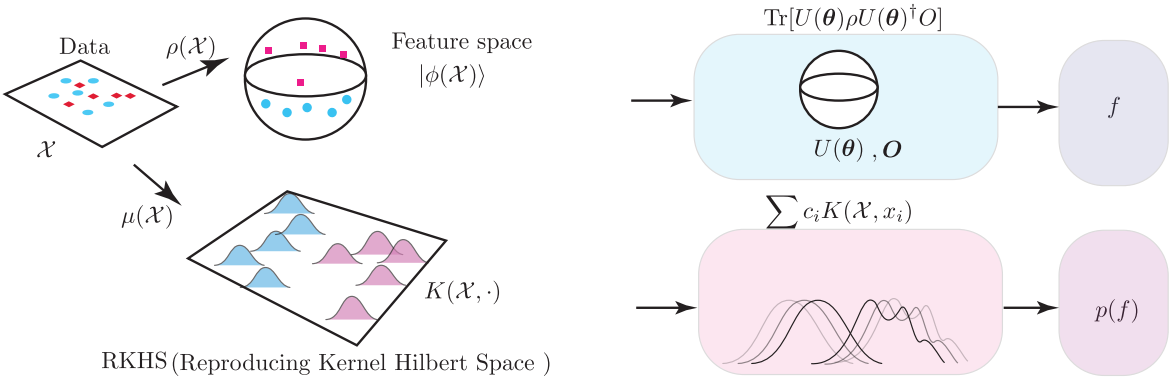

Figure 3.1: Encoding the classical or quantum data can be seen in two way. (top): Encoding in Feature space which is Hilbert space, $|\phi(x)\rangle \in F$. The quantum circuit evolves the feature vector using a parameter θ to predict the label. Training aims to find the optimal θ that achieves the highest criteria, such as minimizing the loss function, for accurate label prediction. (button):Encoding data as a quantum kernel $K(\mathcal{X},\cdot)$. One example of quantum kernel is Fidelity kernel defines as: $K^F(x,x') = |\langle\phi(x),\phi(x')\rangle|^2 = \mathrm{Tr}[\rho(x)\rho(x')]$. The Reproducing Kernel Hilbert Space (RKHS) is the feature space that has canonical feature space if for $K(\cdot,x) \in \mathcal{H}$ for all $x \in \mathcal{X}$ it has a reproducing property $f(x) = \langle f, K(\cdot,x)\rangle_{\mathcal{H}}$. In this method, a training method for quantum circuits that seeks to find the optimal coefficients $\{c_i\}$, which effectively describe the output function $f(x) = \sum_i c_i K(x,x_i)$ based on the observed data points $\{x_i\}$. This technique is commonly referred to as kernel regression. This method can be extended to Bayesian inference which probabilistic kernel regression and predict the $p(f)$ instead of f.

we can think of Gaussian process regression as a probabilistic, kernel-based method, and it's a generalization of kernel regression that also provides uncertainty estimates.

3.2.1 Quantum Meta Kernels

We begin by study the standard structure of variational quantum circuits, integral to quantum neural network models. The structure is given by:

$$U(\boldsymbol{\theta}) = \prod_{\ell=1}^{L} U_i(\theta_i) W_i, \tag{3.1}$$

where, $U_i(\theta_i)$ represents a unitary gate with a variational parameter θ_i. W stands for a fixed and unparameterized section of the circuit. In a common scenario, $U_i(\theta_i)$ can be represented as $U_i(\theta) = e^{i\theta_i X_i}$, where X_i is a Hermitian operator. The layer depth is denoted by L, which is equivalent to the number of parameters $\boldsymbol{\theta} = \{\theta_1, \cdots, \theta_L\}$. By defining $\tilde{U}_i(\theta_i)(\rho) := U_i(\theta_i)\rho U_i^\dagger(\theta_i)$ ans $\tilde{W}_i := W_i \rho W_i^\dagger$. We can express the whole quantum circuit as a quantum model that for a given input ρ_α, it return an output (array or scalar):

$$f_{i,\alpha} = \mathrm{Tr}(\mathcal{U}(\boldsymbol{\theta})(\rho_\alpha)O_i) \tag{3.2}$$

such that

$$\mathcal{U}(\boldsymbol{\theta})(\cdot) = \bigcirc_{\ell=1}^{L}(\tilde{U}_\ell(\theta_\ell) \circ \tilde{W}_\ell)(\cdot) \tag{3.3}$$

In order to analyze the probabilistic behavior of the outputs from our quantum models, it's necessary to examine the k-point correlation function, given by

$$\mathbb{E}_{\boldsymbol{\theta}}[f_{i_1;\alpha_1}(\boldsymbol{\theta}) \cdots f_{i_k;\alpha_k}(\boldsymbol{\theta})] = \mathbb{E}_{\boldsymbol{\theta}}[\mathrm{Tr}\big(\mathcal{U}^{(k)}(\boldsymbol{\theta})(\rho_\alpha^{\otimes k})O^{\otimes k}\big)] \tag{3.4}$$

Where $\mathcal{U}^{(k)}$ represents an extension of Eq.3.3, which is defined as follows:

$$\mathcal{U}^{(k)}(\boldsymbol{\theta})(\rho_\alpha^{\otimes k}) := \bigcirc_{\ell=1}^{L}(\tilde{U}_\ell^{\otimes k}(\theta_\ell) \circ \tilde{W}_\ell^{\otimes k})(\rho_\alpha^{\otimes k}) \tag{3.5}$$

If the gates in a quantum model satisfy the t-design condition

$$\frac{1}{|S|}\sum_{s=1}^{s=|S|} P_{t,t}(U) = \int_{\tilde{U}} d\mu(U) U P_{t,t}(U) \tag{3.6}$$

then, it is possible to analytically evaluate the expectation values. This holds true for overparameterized and deep circuits, where evidence suggests that the t-design condition can be met. In such cases, we can derive analytical and closed-form expressions for these expectations for a random Haar measure ensembles:

$$\begin{aligned}&\int_{\tilde{U}(d)} U_{i_1,j_1}\cdots U_{i_p,j_p} U^{\dagger}_{i',j'}\cdots U^{\dagger}_{i'_p,j'_p} d\mu(U)\\ &= \sum_{\alpha,\beta\in S_p} \delta_{i_1 i'_{\alpha(1)}}\cdots\delta_{i_p i'_{\alpha(p)}}\delta_{j_1 j'_{\beta(1)}}\cdots\delta_{j_p j'_{\beta(p)}} W_{g,d}(\alpha^{-1}\beta),\end{aligned} \tag{3.7}$$

where The $W_{g,d}$ is Weingarten function defined on the symmetric group S_p [89, 90]

To gain a deeper understanding of the non-Gaussian characteristics of the distribution, it is often beneficial to study the connected n-point correlator. This can be achieved by removing the contributions from the *vacuum* state in our observable, according to the Wick's theorem:

$$\begin{aligned}&\mathbb{E}_{\boldsymbol{\theta}}[f_1 f_2\cdots f_n] = \mathbb{E}_{\boldsymbol{\theta}}[f_1 f_2\cdots f_n]|_{\text{connected}}\\ &+ \sum_{\text{all pairing}} \mathbb{E}_{\boldsymbol{\theta}}[f_{\alpha_{1,1}}\cdots f_{\alpha_{m_1,1}}]\cdots\mathbb{E}_{\boldsymbol{\theta}}[f_{\alpha_{m,1}}\cdots f_{\alpha_{m,m}}],\end{aligned} \tag{3.8}$$

where the term "all-pairing" denotes all feasible subgroups with a collective count of m. By adjusting the $f \to f - \mathbb{E}[f]$ we can observe that $\mathbb{E}[f]|\text{connected} = \mathbb{E}[-f]\text{connected}$ This assumption implies that the odd order of correlators will vanish.

Through careful calculation, as described in the appendix, we derive the following result

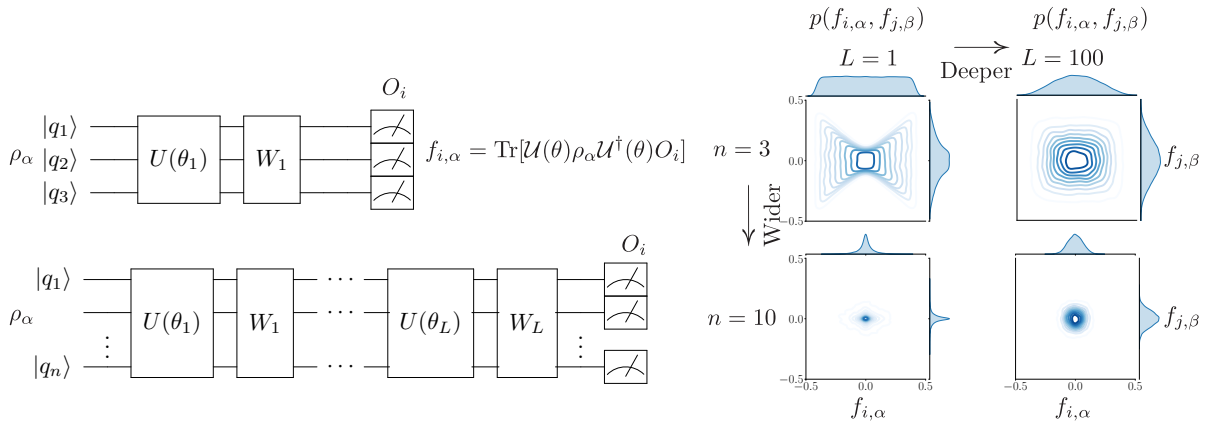

Figure 3.2: In variational quantum circuits, as a model for quantum neural networks (QNNs), the number of qubits, denoted as n and defined as $n = \log(d)$, can be interpreted as the width of the model. To investigate the impact of the width (n) and depth (L) on the output distribution, we conducted simulations of a quantum circuit following the described structure. Each layer of the circuit consists of random two-qubit gates followed by entanglement gates. The observables used in the simulations were constructed from the Pauli Z matrix, forming a complete basis. We generated 10^5 random Haar instances for each circuit with given values of n and L. The joint distribution, $P(f_i, f_j)$, of the output was plotted for two fixed indices i and j. The input of the circuit was constructed from the MNIST dataset, reduced size with the Principal Component Analysis(PAC) , and then mapped to the feature space using the ZZFeaturemap [4]. As observed, as the quantum neural network (QNN) becomes deeper, the output distribution tends to converge more towards a Gaussian distribution.

for two-point correlator :

$$\begin{aligned}
&\mathbb{E}[f_{i_1,\alpha_1} f_{i_2,\alpha_2}]|_{\text{connected}} \\
&= \frac{\text{Tr}\left(O_{i_2} O_{i_1}\right)}{d - d^3} + \frac{\text{Tr}\left(O_{i_2} O_{i_1}\right) \text{Tr}\left(\rho_{\alpha_1} \rho_{\alpha_2}\right)}{d^2 - 1} \\
&+ \frac{\text{Tr}\left(O_{i_1}\right) \text{Tr}\left(O_{i_2}\right)}{d^2 - 1} + \frac{\text{Tr}\left(O_{i_1}\right) \text{Tr}\left(O_{i_2}\right) \text{Tr}\left(\rho_{\alpha_1}\right) \text{Tr}\left(\rho_{\alpha_2}\right)}{d^2}
\end{aligned} \tag{3.9}$$

and similarly, for four-point correlator we obtain:

$$\begin{aligned}
&\mathbb{E}[f_{i_1,\alpha_1} f_{i_2,\alpha_2} f_{i_3,\alpha_3} f_{i_4,\alpha_4}]|_{\text{connected}} \\
&= \frac{d^4 - 8d^2 + 6}{d^2(d^6 - 14d^4 + 49d^2 - 36)} \\
&[\text{Tr}\left(\rho_{\alpha_1} \rho_{\alpha_2} \rho_{\alpha_3} \rho_{\alpha_4}\right) \times \mathcal{V}_4(\{O_i\}) \\
&+ \text{Tr}\left(\{\rho_{\alpha_i} \rho_{\alpha_j} \rho_{\alpha_k}\}\right) \times \mathcal{V}_3(\{O_i\})) \\
&+ \mathcal{O}(\frac{1}{d^5}).
\end{aligned} \tag{3.10}$$

Here, $\mathcal{V}_k$ represents a linear combination of functions that map subsets of $\{O_i\}, \{\rho_i\}, i \in [1, \cdots k]$ to scalar values using the Tr$(\cdot)$ operator.

For large values of d, we can approximate by expansion in terms of Hilbert space dimension :

$$\mathbb{Q} := \mathbb{E}[f_1 f_2] = \frac{Q^{[2]}}{d^2} + \frac{Q^{[3]}}{d^3} + \cdots := \hat{\mathbb{Q}} + \mathbb{Q} + \mathcal{O}(\frac{1}{d^4}) \tag{3.11}$$

and

$$\mathbb{V} := \mathbb{E}[f_1 f_2 f_3 f_4] = \frac{V^{[4]}}{d^4} + \frac{V^{[5]}}{d^5} + \cdots := \hat{\mathbb{V}} + \mathbb{V} + \mathcal{O}(\frac{1}{d^6}) \tag{3.12}$$

such that for example:

$$\mathbb{E}[f_{i_1,\alpha_1} f_{i_2,\alpha_2}]|_{\text{conn.}} = \frac{1}{d^2}[\text{Tr}(\rho_{\alpha_1}\rho_{\alpha_2})\,\text{Tr}(O_{i_1}O_{i_2})] + \mathcal{O}(\frac{1}{d^3}) \tag{3.13}$$

To examine the impact of the number of layers, denoted as L, we can shift our perspective back to the parametric space. In the classical context, it has been observed that $\mathbb{E}[f_1 f_2]$ can be approximated by averaging over $\mathbb{E}[\langle \nabla_{\boldsymbol{\theta}} f, \nabla_{\boldsymbol{\theta}} f \rangle]$, based on Bochner's theorem. This concept has been extended to the quantum scenario in [82, 91]. For the structure like Eq.3.1, if we define:

$$[\mathbb{H}_{ij,\alpha\beta}]_{\mu\nu} := \frac{\partial f_{i,\alpha}}{\partial \theta_\mu}\frac{\partial f_{j,\beta}}{\partial \theta_\nu} \tag{3.14}$$

then the evolution of the output can be described by the following differential equation:

$$df_{i,\alpha} = -\sum_{\mu,\nu} \eta^{\mu\nu}[\mathbb{H}_{ij,\alpha\sigma}]_{\mu\nu}\nabla_{f_{j,\sigma}}\mathcal{L} + \mathcal{O}(\eta^2). \tag{3.15}$$

By defining the left and right operators as $U_{L,\mu} = \prod_{\ell=1}^{\mu-1} W_\ell U_\ell$, $U_{R,\mu} = \prod_{\ell=\mu+1}^{L} W_\ell U_\ell$, $V_{L,\mu} = U_{L,\mu}W_\mu U_\mu$, and $V_{R,\mu} = U_{R,\mu}$, the derivative of the output with respect to a specific parameter (or layer), expressed in a product form, can be represented as follows:

$$\begin{aligned}[\mathbb{H}_{ij,\alpha\beta}]_{\mu\nu} = \text{Tr}\Big(U_{R,\mu}^\dagger [X_\mu, U_\mu^\dagger W_\mu^\dagger U_{L,\mu}^\dagger O_i U_{L,\mu} W_\mu U_\mu] U_{R,\mu}\rho_\alpha\Big) \\ \times \text{Tr}\Big(U_{R,\nu}^\dagger [X_\nu, U_\nu^\dagger W_\nu^\dagger U_{L,\nu}^\dagger O_j U_{L,\nu} W_\nu U_\nu] U_{R,\nu}\rho_\beta\Big)\end{aligned} \tag{3.16}$$

Now, by taking the Haar average over all random unitaries, utilizing Equation 3.7, We

obtain

$$\begin{aligned}\mathbb{E}[\mathbb{H}_{ij,\alpha\beta}]_{\mu\nu} &= \frac{2d}{(d-1)(d+1)(d^2+d)}\times \\ &[\operatorname{Tr}(O_iO_j)\operatorname{Tr}(\rho_\alpha\rho_\beta) - \operatorname{Tr}(O_i)\operatorname{Tr}(O_j)\operatorname{Tr}(\rho_\alpha)\operatorname{Tr}(\rho_\beta)] \\ &\times \operatorname{Tr}(X_\mu X_\nu) = \frac{c}{d^2}\operatorname{Tr}(O_iO_j)\operatorname{Tr}(\rho_\alpha\rho_\beta) + \mathcal{O}(\frac{1}{d^3})\end{aligned} \tag{3.17}$$

where we have defined $c := \frac{\operatorname{Tr}(X_\mu X_\nu)}{d}$, which is typically of order one ($\mathcal{O}(1)$). Based on certain considerations [91], we can assume that the kernel can be approximated by a frozen one and that the variables t are independent in the later stages of training. For simplicity, let's assume $\eta_{\mu\nu} = \delta_{\mu\nu}$. Then the sum over all parameter sizes L arises as follows:

$$\sum_{\mu\nu}\eta^{\mu\nu}[H_{ij,\alpha\beta}]_{\mu\nu} \sim \frac{L}{d^2}\operatorname{Tr}(O_iO_j)\operatorname{Tr}(\rho_\alpha\rho_\beta) + \mathcal{O}(\frac{1}{d^3}) \tag{3.18}$$

This result motivates us to seek a similar property for the quantum neural network as well, akin to what is observed in classical neural networks:

$$\begin{aligned}\mathbb{Q}(\rho_x, \rho_{x'}) &= \mathbb{E}_{\theta\sim p(\theta)}[f_\theta(\rho_x)\cdot f_\theta(\rho_{x'})] \\ &\sim \mathbb{E}_{\theta\sim p(\theta)}[\langle\nabla_\theta f_\theta(\rho_x), \nabla_\theta f_\theta(\rho_{x'})\rangle] = \mathbb{Q}_{\text{NTK}}\end{aligned} \tag{3.19}$$

Thus, as we will explore in the subsequent section, the impact of depth, denoted as L, becomes evident through the faster convergence to a Gaussian distribution:

$$f(t) - f(0) \propto (e^{-L\hat{\mathbb{Q}}})^{t\eta} \tag{3.20}$$

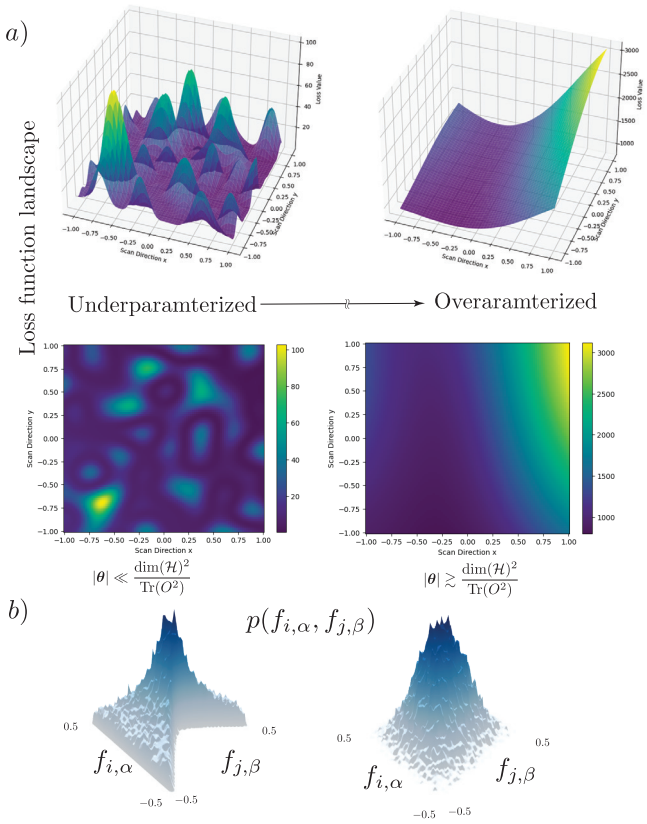

Figure 3.3: The phase transition of the energy landscape of a quantum neural network (QNN) occurs when transitioning from the underparameterized regime to the overparameterized regime. In the underparameterized regime, where the number of parameters in the QNN is low compared to the dimension of the Hilbert space (or the degrees of freedom), the QNN's highly non-convex loss landscape contains unfavorable local minima with eigenvalues of similar magnitudes as the global minimum. However, as the number of parameters increases, the landscape becomes simpler and exhibits numerous favorable local minima. In this scenario, training and converging towards the actual global minimum become much easier. b) The effect of overparameterization in quantum neural networks (QNNs) is the emergence of Gaussian-like output distributions. As the QNN becomes overparameterized, meaning that the number of parameters exceeds the necessary amount to fit the data, the output distribution of the QNN tends to exhibit Gaussian characteristics. This observation suggests that overparameterization promotes a smoother and more concentrated output distribution, resembling a Gaussian distribution.

3.3 Bayesian learning or how to get rid of parameters

For a given quantum model, denoted as $\mathcal{M}$, the circuit architecture associated with it will possess a collection of parameters that may either remain fixed or variable. These variable parameters, referred to as $\boldsymbol{\theta} = \{\theta_i, i \in [1, \cdots, L]\}$ need to be tuned such that the quantum circuit performs the desired output. Since the variational parameters are assumed to be independent of each other, the prior distribution of these parameters is merely the product of the prior distribution of each individual parameter such that $p(\boldsymbol{\theta}|\mathcal{M}) = \prod_{\ell=1}^{L} p(\theta_\ell|\mathcal{M})$.

Recent investigations have delved into how the prior distribution of the $p(\boldsymbol{\theta}|\mathcal{M})$ as a method of initialization strategies of quantum neural networks, such as Gaussian initialization and reduced-domain parameter initialization [92]. These studies suggest that such strategies can enhance convergence speed and alleviate the problem of barren plateaus. However, it should be noted that these assumptions do not guarantee that the global minimum can be reached within a reasonable number of iterations using these initialization methods, and there is a risk of getting trapped in undesirable local minima.

3.3.1 Marginalization of Parameters

When considering a specific model $\mathcal{M}$, our prior hypotheses regarding the behavior of the observables we seek to learn are taken into account. The probability distribution describing our prior belief and prediction of the outcome of a quantum circuit, denoted as $p(\mathbb{P}|\boldsymbol{\theta}, \mathcal{M})$, can be expressed as follows:

$$p(f_{\mathbb{P}}|\mathcal{M}) = \int \prod_{i}^{L} d\theta_i \, p(f_{\mathbb{P}}|\theta_i, \mathcal{M}) \, p(\theta_i|\mathcal{M}) \tag{3.21}$$

Upon observing the data points of interest $\mathbb{O}$, we can update our beliefs and make predictions for new data points $\mathbb{P}$ using the Bayes' rule:

$$p(f_{\mathbb{P}}|f_{\mathbb{O}}, \mathcal{M}) = \int \prod_{i}^{L} d\theta_i \, p(f_{\mathbb{O}}|\theta, \mathcal{M}) \, p(\theta|f_{\mathbb{O}}, \mathcal{M}) \tag{3.22}$$

However, this equation can be simplified by integrating out the parameters, resulting in the following equation [93]:

$$p(f_{\mathbb{P}}|f_{\mathbb{O}}, \mathcal{M}) = \frac{p(f_{\mathbb{P}}, f_{\mathbb{O}}|\mathcal{M})}{p(f_{\mathbb{O}}|\mathcal{M})} \tag{3.23}$$

This formula allows us to update our beliefs and make predictions based on the observed data points without explicitly involving any parameters. In fact, we have bypassed the intermediate step of updating our posterior on the parameters, which can be obtained using different schemes such as Maximum A Posteriori (MAP) or Maximum Likelihood Estimation (MLE). For example, The optimal parameter values with MAP can be found by maximizing the posterior probability $\boldsymbol{\theta}^* = \arg\max_{\theta} p(\theta|\mathbb{O}, \mathcal{M})$.

3.4 Probabilistic model of QNN

In this section, we present a proposition for a probabilistic approach to quantum neural networks. In this novel viewpoint of quantum neural networks, the output of the circuit is represented as a probability distribution, contrasting the traditional approach where the circuit's

output is a delta function across all potential outcomes. The key advantage of this perspective lies in its ability to incorporate uncertainty within the framework, enabling increased flexibility in noise analysis. Furthermore, owing to the inherent probabilistic nature of quantum circuits, the variance from the expectation becomes more pronounced, underscoring its significance.

In general, assuming that the output distribution is symmetric with respect to the origin and neglecting odd-numbered correlation functions, we can describe the output distribution using Equation B.11:

In a general framework, assuming symmetry around the origin in the output distribution and excluding correlations of odd order, we can characterize the output distribution as [93]

$$p(f) = \frac{e^{-S(f)}}{\mathcal{Z}}, \tag{3.24}$$

where the action $S(\cdot)$ is defined as:

$$\begin{aligned} S(f) = &\frac{1}{2} \sum_{\mu,\nu=1}^{n} K^{\mu\nu} f_\mu f_\nu \\ &+ \sum_{m=2}^{\Lambda} \frac{1}{(2m)!} \sum_{\mu_1,\cdots\mu_{2m}=1} C^{\mu_1\cdots\mu_{2m}} f_{\mu_1} \cdots f_{\mu_{2m}}. \end{aligned} \tag{3.25}$$

In this formulation, $C^{\mu_1\cdots\mu_{2m}}$ represents the m-th order couplings, and Λ serves as the truncation threshold for limiting the series expansion up to the Λ-th order. Furthermore, the partition function $\mathcal{Z}$ in the denominator of Equation B.11 is defined as:

$$\mathcal{Z} = \int d^n f e^{-S(f)} \tag{3.26}$$

Here, $C^{\mu_1 \cdots \mu_{2m}}$ represents the m-th order couplings defined as

$$\mathbb{E}[f_1 f_2 \cdots f_m] = \int df^m p(f) f_1 f_2 \cdots f_m, \tag{3.27}$$

and Λ is the limit for truncating the series to the Λ-th order. The partition function, $\mathcal{Z}$ in the denominator of Equation B.11, is given by:

$$\mathcal{Z} = \int d^n f e^{-\mathcal{S}(f)} \tag{3.28}$$

As the number of qubits, denoted by n, increases, the Hilbert space dimension expands exponentially as $d = 2^n$. In the asymptotic regime where d approaches infinity, higher-order corrections within the correlation relation become negligible. Specifically, we observe that $\mathbb{E}[f_1 \cdots f_m] \sim \mathcal{O}(1/d^{m'+2})$ for $m' > 0$. This implies that the action can be perturbed with respect to the dimension of the Hilbert space:

$$S = S^{(0)} + \frac{S^{(2)}}{d^2} + \frac{S^{(4)}}{d^4} + \mathcal{O}\left(\frac{1}{d^6}\right). \tag{3.29}$$

This perturbation approach bears resemblance to the $\frac{1}{d}$ expansion technique employed in the domains of statistical mechanics and quantum field theory [93], where $S^{(0)}$ characterizes the vacuum state of the theory and $S^{(2)}$ represents the first-order interaction and so on.

3.4.1 Infinite Width QNN

In this section, we want to study the extreme over-parameterized case $d \to \infty$ where all higher order terms than quadratic interaction can be neglected: $S \approx S^{(0)} + S^{(2)}/d^2$. In this regime, it becomes possible to express the output distribution of the quantum neural network as a Gaussian distribution.

Our learning task, aimed at determining the cachectic of this distribution, entails observing samples from ensembles of data points and subsequently predicting the output of the quantum neural network for new, unseen data points. We represent the observed datapoints and their corresponding sets as $\mathbb{O} = \{\rho_\beta, f_{i,\beta} := y_{\beta,i}; \beta \in [1, \cdots |\mathbb{O}|], i \in [1, \cdots, n]\}$.Here, $|\mathbb{O}|$ denotes the size of the set of observable operators. In this representation, ρ_β denotes the density matrix of the β-th data point from the observed ensemble, while $y_{i,\beta} := f_{i,\beta}$ represents the true label of this particular data point. Similarly, we define the prediction sets as $\mathbb{P} = \{\rho_\alpha, = f_{j,\alpha}; \alpha \in [1, \cdots |\mathbb{P}|], j \in [1, \cdots, n]\}$. With these two sets, we can represent our updated posterior as follows:

$$p(f_{\mathbb{O}}, f_{\mathbb{P}}) = \frac{1}{Z} \exp\left(-\frac{1}{2} \sum_{i,j=1}^{n} \sum_{\mu_1,\mu_2 \in \mathbb{P}\cup\mathbb{O}} K^{ij,\mu_1\mu_2} f_{i,\mu_1} f_{j,\mu_2} \right) \tag{3.30}$$

where Z is the normalization factor, given by $|2\pi K|^{n^2}$.

Utilizing Bayes' rule, as presented in Equation 3.23, we can gain deeper insights into the QNN's output distribution for a particular data point, denoted as $f_{\mathbb{P}} := f$, based on previously observed data points, $f_{\mathbb{O}}$. Similar computations to those used in classical neural networks, as detailed in [93] and outlined in Appendix B.1, allow us to express this distribution as a Gaussian

distribution, or potentially as a Gaussian process $p(f) = \frac{1}{Z}\exp(S)$ with Gaussian action:

$$\begin{aligned} p(f) &= \frac{1}{Z}\exp(-S), \\ S &= \frac{1}{2}\sum_{\substack{i,j=1 \\ \beta_1,\beta_2\in\mathbb{P}}}^{n} \mathbb{K}^{ij,\beta_1\beta_2}[f_{i,\beta_1} - m^{\infty}_{i,\beta_1}][f_{j,\beta_2} - m^{\infty}_{j,\beta_2}], \end{aligned} \tag{3.31}$$

which is characterized by the following mean and covariance:

$$\begin{aligned} [m]_{i,\mu} &= \sum_{\lambda,\sigma\in\mathbb{O}} K_{ij,\mu\lambda}K^{ij,\lambda\sigma}y_{i,\sigma} := K(\mathbb{P},\mathbb{O})K^{-1}(\mathbb{O},\mathbb{O})\boldsymbol{y}, \\ [\mathbb{K}]_{ij,\mu\nu} &= K_{ij,\mu\nu} - \sum_{\lambda,\sigma\in\mathbb{O}} K_{ij,\mu\lambda}K^{ij,\lambda\sigma}K_{ij,\sigma\nu} \\ &= K(\mathbb{P},\mathbb{O}) - K(\mathbb{P},\mathbb{P})K^{-1}(\mathbb{O},\mathbb{O})K(\mathbb{O},\mathbb{P}). \end{aligned} \tag{3.32}$$

Here, K is a two-point correlation function representing the kernel function. Therefore, we can establish the explicit relationship between the mean and covariance in terms of the inputs, denoted by $\{\rho_\beta\}_{\beta\in\mathbb{O}}$ and observables $\{O\}$:

$$\begin{aligned} [m]_{i,\beta} &= \sum_{\alpha_1,\alpha_2\in\mathbb{O}} \mathbb{E}[f_i f_j]_{\beta,\alpha_1}\mathbb{E}[f_i f_j]^{-1}_{\alpha_1,\alpha_2}y_{i,\alpha_2} \\ &= \sum_{\alpha_1,\alpha_2\in\mathbb{O}} [\mathrm{Tr}(\rho_\beta\rho_{\alpha_1})][\mathrm{Tr}(\rho_{\sharp_1}\rho_{\sharp_2})]^{-1}_{\alpha_1\alpha_2}y_{i,\alpha_2} + \mathcal{O}(\frac{1}{d^2}) \end{aligned} \tag{3.33}$$

Furthermore, the covariance can be calculated using the following expression:

$$\begin{aligned} [\mathbb{K}]_{ij,\beta_1\beta_2} &= \frac{\mathrm{Tr}(O_iO_j)}{d^2}[\mathrm{Tr}(\rho_{\beta_1}\rho_{\beta_2}) \\ &- \sum_{\alpha_1,\alpha_2\in\mathbb{O}} \mathrm{Tr}(\rho_{\beta_1}\rho_{\beta_2})[\mathrm{Tr}(\rho_{\sharp_1}\rho_{\sharp_2})]^{-1}_{\beta_2\alpha_2}\,\mathrm{Tr}(\rho_{\alpha_2}\rho_{\beta_2})] + \mathcal{O}(\frac{1}{d^4}). \end{aligned} \tag{3.34}$$

In literature, the term $\mathrm{Tr}(\rho_x \rho_x)$ is occasionally denoted as the Quantum fidelity kernel $K^{\mathbb{F}}(x, x')$ [12]. Using this notation, we can make the previous equation more understandable:

$$\mathbb{K}_{ij,\mathbb{P}} = \frac{\mathrm{Tr}(O_i O_j)}{d^2}[K^{\mathbb{F}}_{\mathbb{P},\mathbb{O}} - K^{\mathbb{F}}_{\mathbb{P},\mathbb{P}}(K^{\mathbb{F}})^{-1}_{\mathbb{O},\mathbb{O}} K^{\mathbb{F}}_{\mathbb{O},\mathbb{P}}] + \mathcal{O}(\frac{1}{d^4}) \tag{3.35}$$

3.4.2 Parameter space representation

Within the context of parameter space, our learning endeavor can be seen as the creation of a parametric model $f_{\text{QNN}}(\rho; \boldsymbol{\theta})$, accompanied by a distribution $p(\boldsymbol{\theta})$. The aim is to locate the best value of $\boldsymbol{\theta} = \boldsymbol{\theta}^*$, ensuring minimal error considering available computational resources (like the number of qubits, gates, and observed datapoints). The goal is to have our model closely approximate the actual distribution and align accurately with the real datapoints $f_{\text{QNN}}(x; \boldsymbol{\theta}^*) \approx f(x)$. The aspiration is that, with proper initialization near the actual global minimum, we can locate this global minimum using gradient descent methods. As quantum neural networks lean towards overparameterization, this assumption becomes more credible. Given this assumption, the output of the Quantum Neural Network (QNN) can be approximated using a Taylor series:

$$\begin{aligned} f^{i,(t)}_{\alpha} &= f^{i,(0)}_{\alpha} - \eta \sum_{ij,\beta} \mathbb{H}^{ij,\beta\alpha} \epsilon_{j,\beta} \leftrightarrow \mathbb{Q}_{\text{NTK}} \\ &+ \frac{\eta^2}{2} \sum_{ij_1 j_2, \beta_1 \beta_2} d\mathbb{H}^{ij_1 j_2, \alpha \beta_1 \beta_2} \epsilon_{j_1,\beta_1} \epsilon_{j_2,\beta_2} \leftrightarrow \mathrm{d}\mathbb{Q}_{\text{NTK}} \\ &- \frac{\eta^3}{6} \sum_{ij_1 \cdots \alpha_3} dd\mathbb{H}^{ij_1 \cdots \alpha_3} \epsilon_{j_1\beta_1} \epsilon_{j_2\beta_2} \epsilon_{j_3\beta_3} \leftrightarrow \mathrm{dd}\mathbb{Q}_{\text{NTK}} \\ &+ \mathcal{O}(\frac{1}{d^2}) \end{aligned} \tag{3.36}$$

where $\epsilon = \nabla_f \mathcal{L}$ denotes the derivative of the loss function with respect to the output function and $\mathbb{H}$ is defined as:

$$\mathbb{H}_{ij,\alpha\beta} = \sum_{\mu\nu} \eta_{\mu\nu} \frac{\partial f_{i,\alpha}}{\partial \theta_\mu} \frac{\partial f_{j,\beta}}{\partial \theta_\nu}. \tag{3.37}$$

As the width of the Quantum Neural Network (QNN) approaches infinity, $\mathbb{H}$ can be approximated by a frozen kernel, referred to as the Quantum Neural Tangent Kernel (QNTK):

$$\mathbb{H}_{ij,\alpha\beta} = \mathbb{Q}_{ij,\alpha\beta} + \mathcal{O}(\frac{1}{d^2}) \tag{3.38}$$

By comparing the expansion of the parameter space with the functional method outlined in Sec.3.4, we can draw the following analogy:

$$\begin{aligned} \mathbb{Q}_{\text{NTK}} : \mathbb{E}[\frac{\partial f_{i_1,\alpha_1}}{\partial \theta_\mu} \frac{\partial f_{j,\alpha_2}}{\partial \theta_\nu}] &\sim \frac{1}{d^2} \operatorname{Tr}(\rho_{\alpha_1} \rho_{\alpha_2}) \operatorname{Tr}(O_i O_j) \\ &\sim \mathbb{E}[f_{i_1,\alpha_1} f_{j,\alpha_2}] = K_{ij,\alpha_1\alpha_2} \end{aligned} \tag{3.39}$$

Likewise, for the other terms in the Eq.3.36 expansion, these are known as quantum meta kernels, which correspond to the third and fourth-order correlations:

$$\begin{aligned} \mathrm{d}\mathbb{Q}_{\text{NTK}} : \mathbb{E}[\frac{\partial^2 f_{i_1,\alpha_1}}{\partial \theta_\mu \partial \theta_\nu} \frac{\partial f_{i_2,\alpha_2}}{\partial \theta_\lambda} \frac{\partial f_{i_3,\alpha_3}}{\partial \theta_\sigma}] &= 0 \\ \sim \mathbb{E}[f_{i_1,\alpha_1} f_{i_2,\alpha_2} f_{i_3,\alpha_3}], & \end{aligned} \tag{3.40}$$

and

$$\begin{aligned} \mathrm{dd}\mathbb{Q}_{\mathrm{NTK}} : \mathbb{E}[&\frac{\partial^3 f}{\partial\theta_1\partial\theta_2\partial\theta_3}\frac{\partial f}{\partial\theta_4}\frac{\partial f}{\partial\theta_5}\frac{\partial f}{\partial\theta_6}] \\ &+ \mathbb{E}[\frac{\partial^2 f}{\partial\theta_1\partial\theta_2}\frac{\partial^2 f}{\partial\theta_3\partial\theta_4}\frac{\partial f}{\partial\theta_5}\frac{\partial f}{\partial\theta_6}] \\ &\leftrightarrow \mathbb{E}[f_{i_1,\alpha_1} f_{i_2,\alpha_2} f_{i_3,\alpha_3} f_{i_4,\alpha_4}] = \mathbb{V}_{i_1 i_2 i_3 i_4,\alpha_1\alpha_2\alpha_3\alpha_4} \end{aligned} \tag{3.41}$$

Solving Eq.3.36 entails dealing with a complex set of differential equations, which generally do not yield a closed-form solution [93]. However, in the limit of $d \to \infty$, it is acceptable to only retain the linear term. The solution to the differential equation, in terms of steps (represented here by the continuous variable t), can be expressed as:

$$\begin{aligned} f_{i,\alpha}^{(t)} \simeq m_{i,\alpha}^{(t)} + \Sigma_{i,\alpha}^{(t)} = &\sum_{\beta_1,\beta_2\in\mathbb{O}} \mathbb{Q}_{\alpha\beta_1}\mathbb{Q}^{\beta_1\beta_2}(1-e^{-\eta\mathbb{Q}t})y_{i,\beta_2} \\ &+ f_{i,\alpha}^{(0)} - \sum_{\beta_1,\beta_2\in\mathbb{O}} \mathbb{Q}_{\alpha\beta_1}\mathbb{Q}^{\beta_1\beta_2}(1-e^{-\eta\mathbb{Q}t})f_{i,\beta_2}^{(0)}. \end{aligned} \tag{3.42}$$

In the limit of large iteration times, we can determine the output of the circuit (without actually performing any training) as a linear kernel regression:

$$f_{\mathrm{QNN}}(\rho_x) \approx f_{\mathbb{Q}_{\mathrm{NTK}}} = \mathbb{Q}_{\mathrm{NTK}}(\rho_x,\rho_X)^T \cdot \mathbb{Q}_{\mathrm{NTK}}(\rho_X,\rho_X)^{-1} \cdot Y, \tag{3.43}$$

and the optimized parameters at the end of training would be determined as

$$\boldsymbol{\theta}^* = \boldsymbol{\theta}^{(0)} - \eta\nabla_{\boldsymbol{\theta}} f \cdot \mathbb{Q}_{\mathrm{NTK}}^{-1}(\boldsymbol{f}-\boldsymbol{y}) \tag{3.44}$$

To see the connection with the Gaussian process, let's consider the expected output for a particular input ρ_α, which can be given as:

$$\mathbb{E}[f_{i,\alpha}^{(t)}] = \sum_{\beta_1,\beta_2 \in \mathbb{O}} \mathbb{Q}_{\alpha\beta_1} \mathbb{Q}^{\beta_1\beta_2} (1 - e^{-\eta \mathbb{Q} t}) y_{i,\beta_2}, \tag{3.45}$$

which, in the limit of infinite iterations, converges to $m_{i,\alpha}^{(\infty)} := \sum_{\beta_1,\beta_2 \in \mathbb{O}} \mathbb{Q}_{\alpha\beta_1} \mathbb{Q}^{\beta_1\beta_2} y_{i,\beta_2}$.

Likewise, the covariance of the circuit's output will take the following form:

$$\begin{aligned}
&\mathbb{E}[f_{i,\alpha_1}^{(t)} f_{j,\alpha_2}^{(t)}]|_{\text{connected}} = \mathbb{Q}_{\alpha_1\alpha_2} \\
&- \sum_{\beta_1,\beta_2 \in \mathbb{P}} \mathbb{Q}_{\alpha_2\beta_1} \mathbb{Q}^{\beta_1\beta_2} (1 - e^{-\eta \mathbb{Q} t}) \mathbb{Q}_{\alpha_1\beta_2} \\
&- \sum_{\beta_1,\beta_2 \in \mathbb{P}} \mathbb{Q}_{\alpha_1\beta_1} \mathbb{Q}^{\beta_1\beta_2} (1 - e^{-\eta \mathbb{Q} t}) \mathbb{Q}_{\alpha_2\beta_2} \\
&+ \sum_{\beta_1,\cdots,\beta_4 \in \mathbb{P}} \mathbb{Q}_{\alpha_1\beta_1} \mathbb{Q}^{\beta_1\beta_2} [1 - e^{-\eta \mathbb{Q} t}] \mathbb{Q}_{\alpha_2\beta_3} [1 - e^{-\eta \mathbb{Q} t}] \\
&\times \mathbb{Q}^{\beta_3\beta_4} \mathbb{Q}_{\beta_4\beta_2} := \Sigma_{\alpha_1\alpha_2}^{ij,t}.
\end{aligned} \tag{3.46}$$

The higher order moments are of the order $\mathcal{O}(1/d^2)$ and can be disregarded. Based on this observation, we can infer that the most likely distribution to describe the statistics of the output is a Gaussian process. Upon comparing with the functional description of the output distribution, we observe that we obtain the same distribution as predicted by the Gaussian process, particularly as $t \to \infty$, and substituting $\mathbb{Q}$ with $\mathbb{K}$:

$$f^{(t)} \sim \mathcal{GP}(m^{(t)}, \Sigma^{(t)}) \overset{\lim}{\underset{t\to\infty}{\to}} \mathcal{GP}(m^{(\infty)}, \mathbb{K}) \tag{3.47}$$

comparing the linear kernel regression method with the Gaussian process,

$$
\begin{aligned}
f \sim f_{\mathbb{Q}_{\text{NTK}}} &\leftrightarrow \text{Kernel Regression} \\
p(f) \sim \mathcal{N}(\mu, \Sigma) &\leftrightarrow \text{Gaussain Process}
\end{aligned}
\tag{3.48}
$$

3.4.3 Finite Width QNN

When working within the finite width regime of the parameter space, it becomes necessary to consider higher-order terms, such as dQNTK and ddQNTK, which are based on the higher-order derivative terms dH and dHH. Using traditional methods to obtain higher-order corrections in the output distribution, such as for dQNTK, can be unfeasible and not provide a closed-form solution. However, in this section, we demonstrate that by utilizing Bayesian learning, we can obtain higher-order corrections of the output distribution in a closed form, at least for the case of dQNTK.

To enhance the model's ability to capture the finite width regime, it becomes necessary to go beyond the Gaussian distribution and utilize representation learning techniques. By incorporating additional correlation functions into the model, it becomes better equipped to accurately represent the underlying reality.

To obtain a nearly-Gaussian (NG) distribution, comparable to ddQNTK, we need to incorporate the next leading order in finite width, which is of $O(1/d)$. This is because in the nearly-Gaussian distribution, the odd terms are zero or equivalently, dQNTK is zero.

$$
S_{\text{NG}} := \frac{1}{2} \sum_{\mu,\nu}^{n} K^{\mu\nu} f_\mu f_\nu - \frac{\lambda}{4!} \sum_{\nu_1\nu_2\nu_3\nu_4=1}^{n} V^{\nu_1\nu_2\nu_3\nu_4} f_{\nu_1} f_{\nu_2} f_{\nu_3} f_{\nu_4}. \tag{3.49}
$$

such that

$$
\begin{aligned}
K^{\alpha_1\alpha_2} &= \hat{\mathbb{Q}}^{\alpha_1\alpha_2} + \mathcal{O}(\frac{1}{d^3}) \\
V^{\alpha_1\alpha_2\alpha_3\alpha_4} &= \hat{\mathbb{V}}^{(\alpha_1\alpha_2)(\alpha_3\alpha_4)} + \mathcal{O}(\frac{1}{d^5})
\end{aligned}
\tag{3.50}
$$

By employing the same calculations as we did for the infinite width scenario, we can determine the contributions of finite width structures to the mean and covariance:

$$
\begin{aligned}
\mathbb{E}[f_{i,\beta}] &= m^{\infty}_{i,\beta} + \frac{1}{3!} \sum_{j_1,\beta\in\mathbb{P}} K_{ij_1,\beta\beta_1} \\
&\times [\sum_{\substack{j_2j_3j_4 \\ \alpha_2\alpha_3\alpha_4\in\mathbb{O}}} V^{j_1j_2j_3j_4,\beta\alpha_2\alpha_3\alpha_4} y_{j_2,\alpha_2} y_{j_3,\alpha_3} y_{j_4,\alpha_4}] \\
&\sum_{\substack{j_1j_2j_3 \\ \beta_1\beta_2\beta_3\in\mathbb{P}}} [K_{ij_1,\beta\beta_1} K_{j_2j_3,\beta_2\beta_3} + K_{ij_2,\beta\beta_2} K_{j_1j_3,\beta_1\beta_3} \\
&+ K_{ij_3,\beta\beta_3} K_{j_1j_2,\beta_1\beta_2}] \sum_{j_4,\alpha\in\mathbb{O}} V^{j_1j_2j_3j_4,\beta_1\beta_2\beta_3\alpha} y_{j_4,\alpha} \\
&+ \mathcal{O}(\frac{1}{d^4}),
\end{aligned}
\tag{3.51}
$$

and

$$
\begin{aligned}
\Sigma' &= \mathbb{E}[f_{i_1,\mu_1} f_{i_2,\mu_2}]|_{\text{conn.}} = K_{i_1i_2,\mu_1\mu_2} \\
&- \frac{1}{2} \sum_{\substack{j_1j_2j_3j_4=1 \\ \nu_1\nu_2\nu_3\nu_4}} V^{j_1j_2j_3j_4,\nu_1\nu_2\nu_3\nu_4} K_{i_1j_1,\mu_1\nu_1} K_{i_2j_2,\mu_2\nu_2}, \\
&\times K_{j_3j_4,\nu_3\nu_4}
\end{aligned}
\tag{3.52}
$$

where $m^{(\infty)}_{i,\alpha} = \sum_{\beta_1,\beta_2} K_{\alpha_1\beta_1} K^{\beta_1\beta_2} y_{i,\beta_2}$ thus e can refine the kernel regression method by incorporating

finite-size corrections:

$$m' = \bar{f} = m^{(\infty)} + m^{(1/d)} + \mathcal{O}(\frac{1}{d^2}) \tag{3.53}$$

If we aim to maintain the Gaussian approximation, the corrected covariance, which arises from higher orders, and the effects of wiring with others, can be described as

$$f \approx \mathcal{GP}(m', \Sigma'). \tag{3.54}$$

However, and in the large d limit and the output distribution can be approximate better by forth order correlator as :

$$p(f) = p(f|y_\alpha, \hat{\mathbb{Q}}_{\mu\nu}, \hat{\mathbb{V}}_{\mu\nu\delta\sigma}). \tag{3.55}$$

such that $\hat{\mathbb{Q}} = \Sigma'$ and $\hat{\mathbb{V}}$ given by (see appendix for more details)

$$\begin{aligned} \mathbb{V}_{i_1 i_2 i_3 i_4, \mu_1 \mu_2 \mu_3 \mu_4} = & \sum_{j_1 j_2 j_3 j_4} \sum_{\nu_1 \nu_2 \nu_3 \nu_4} V^{j_1 j_2 j_3 j_4, \nu_1 \nu_2 \nu_3 \nu_4} \\ & \times K_{i_1 j_1, \mu_1 \nu_1} K_{i_2 j_2, \mu_2 \nu_2} K_{i_3 j_3, \mu_3 \nu_3} K_{i_4 j_4, \mu_4 \nu_4} + \mathcal{O}(\frac{1}{d^5}) \end{aligned} \tag{3.56}$$

3.5 Conclusion

In this study, we examined variational quantum circuits, which serve as a model for quantum neural networks, from the perspective of function space instead of parameter space. We explored the impact of over-parameterization through the expansion of width and depth. Theoretically and via simulation, we observed that this led to a shift in the output distribution of the quantum models towards a Gaussian process. We also examined how the finite size of the width can skew

the distribution towards non-Gaussianity. We demonstrated how this can be achieved using a $1/d$ expansion.

Chapter 4: Double Descent in Learning with Quantum Machines

"Nobody takes you seriously until you double-descent"

My two-cents

4.1 Abstract

The generalization power of learning and generating with quantum machines is an important subject that has not been fully addressed yet. Quantum machines, due to the exponentially large dimension of their representation space and the curse of dimensionality, are prone to exhibit poor generalization capability. In this work, as a proof of concept, we present a comprehensive study showing that, similar to the classical violation of the bias-variance trade-off wisdom, variational quantum circuits, as an example of quantum neural networks, exhibit double descent behavior and a phase transition when transitioning from underparameterized to overparameterized regimes in terms of test error versus model complexity. To achieve this, we use random matrix theory. Similar to the classical case, we make a connection by modeling the quantum neural network with the theory of spin-glass. We express the quantum circuit unitary evolution in terms of a path integral over the random Haar ensemble and finally use the connection with the random Gaussian distribution and random Wishart distribution.

4.2 Introduction

Can quantum computers transform and enhance learning tasks in the inherently quantum universe? This question drives the exploration of quantum computing's potential to revolutionize data analysis and learning.

To explore this potential, significant research has focused on the trainability of Variational Quantum Circuits (VQC), a subset of Quantum Neural Network (QNN) architecture. These studies aim to understand the potential and limitations of quantum circuits in learning tasks. Quantum learning advantages have been demonstrated in tasks involving unknown physical systems by utilizing quantum-native data stored in quantum memory [16]. This approach exponentially reduces the number of experiments needed to learn system properties compared to classical methods. However, classical data and machine learning models can often achieve capabilities similar to their quantum counterparts, potentially diminishing the quantum advantage in certain tasks [12]. The effectiveness of quantum kernels, which preserve data point distances during feature mapping, is crucial in maintaining this advantage [94].

Another crucial direction of investigation is the generalization capability of quantum machines, which has not been fully addressed in the literature. Generalization is essential in learning tasks as it enables models to apply insights from observed data to predict outcomes for unseen data. Traditional statistical learning suggests a trade-off between bias and variance, resulting in a U-shaped generalization error curve [95]. Low-complexity models suffer from high bias (underfitting), while high-complexity models face high variance (overfitting). An optimal balance point minimizes generalization error. Recent deep learning studies have challenged this belief, showing that highly overparameterized models can achieve near-zero test errors, a phenomenon

known as double descent [96–98].

This study explores how quantum machines can trace generalization and double descent phenomena. We present an analytical example tracking double descent behavior, providing a proof of concept for this phenomenon in quantum computing. We introduce quantum random feature regression to address generalization, scalability, and kernel concentration issues.

4.3 Generalization in Variational Quantum Algorithms

Learning tasks with quantum machines, similar to classical ones, involve identifying a hypothesis, h^*, to reveal the hidden relation between given samples $\{x\}$ from the sample space X and its corresponding labels $\{y\}$ from the target space Y. This relation can be expressed as $y = h^*(x)$. To achieve this goal, one can construct a parametric function, $h_\theta \approx h^* : X \to Y$, to find the best possible parameters that minimize the error between the ground truth and the label predicted by the model.

One approach to build this model is with the Kernel methods [99–101]. Unlike conventional variational quantum algorithms where optimization occurs in the parameter space, the Quantum Kernel method leverages the Reproducing Kernel Hilbert Space (RKHS). The optimal kernel is expressed as a linear combination of individually evaluated kernels for each trained datapoint, $x_i \in D$, with the optimal weight of a_i^* as:

$$f_{a^*}(x) = \sum_{i=1}^{|D|} a_i^* Q(x, x_i) \tag{4.1}$$

and here the quantum kernel, a function over input density matrices, $\rho(x)$, is defined as $Q(x, x') = h(\rho(x), \rho(x'))$, where the input density matrix can either be constructed from classical data

mapped to a feature space or be intrinsically quantum data. One advantage of this method is the convexity of its objective function, which simplifies the training process. However, scalability issues emerge as computations grow with $O(|D|^3)$. There is also an additional challenge: the 'Concentration of the Kernel' phenomenon. This issue is compounded by the need to sample from circuits where shot noise is significant [94]. These issues lead to various forms of kernel concentration caused by the model's expressibility, noise, and global measurement by product. The general forms of these bounds are as follows:

$$\mathrm{P}[Q(x, x') - \mathbb{E}[Q(x, x')] \geq \delta] \leq \mathrm{poly}(1/2^n, N, 1/\delta) \tag{4.2}$$

for n qubits and $|D| = N$. This means that for $N \ll 2^n$, the quantum kernel performs poorly on generalization, such that $f_a(x) \simeq 0$ for all unseen data. This observation motivates us to study the issues of generalization, scalability, and concentration simultaneously in quantum learning tasks.

In the following, we briefly review the mathematical foundations of generalization, a cornerstone concept in both classical and quantum machine learning. The journey begins with the definition of the 'training error' or 'empirical error', represented mathematically as the average loss over all samples in a training dataset:

$$E_S(a) = \frac{1}{N} \sum_{i}^{N=|D|} \mathcal{L}(a, x_i, y_i), \tag{4.3}$$

where $a_s^* = \min_a E_S(a)$ identifies the optimal parameters that minimize this training error. Transitioning from training to prediction, the 'prediction error' or 'population error' emerges

as a critical measure of a model's ability to generalize beyond its training data:

$$E_D(a) = \mathbf{E}_{P_{x,y}\sim D}[\mathcal{L}(a, x_i, y_i)], \tag{4.4}$$

with $a_D^* = \min_a E_D(a)$ marking the parameter set that minimizes the prediction error. The discrepancy between these optimized parameters, or the 'estimation error', is given by $E_D(a_s^*) - E_D(a_D^*)$ highlighting the model's deviation from ideal prediction capabilities. A model's capacity for 'Probably Approximately Correct' (PAC) learning is evaluated by its ability to reduce the estimation error with an increasing volume of data. This adaptability is intricately linked to the Bias-Variance tradeoff, which posits that the generalization error ($E_D(a_s^*)$) can be decomposed into a bias component and a variance component. Classical learning theories have illuminated the phenomenon of 'double descent', where models of excessive complexity paradoxically achieve lower generalization errors, sometimes even approaching zero as they become highly overparameterized.

To evaluate of model performance is crucial for understanding its effectiveness and reliability. Two fundamental concepts in this context are the test error and the generalization error. The test error provides a practical measure of how well a model performs on a specific subset of unseen data, while the generalization error offers a theoretical expectation of the model's performance across the entire data distribution. Although these terms are often used interchangeably, they have distinct definitions and implications. The concept of 'generalization error' can be expressed as:

$$G := E_G(a) = E_D(a_s^*) - E_S(a_s^*) \approx \sup_a E_D(a) - E_S(a),$$

indicating the model's effectiveness in applying learned insights to unseen data. Notably, both

classical and quantum frameworks have established bounds for this error, suggesting it can be polynomially limited by the model's complexity and the inverse of the sample size (poly$(|a|, 1/N)$). The nuanced exploration of quantum models introduces the concept of adjusting the generalization error to account for optimization challenges, such as shot noise, that are unique to quantum computing. This adjustment is vital for accurately assessing a quantum model's performance, particularly in how it manages the delicate balance between theoretical precision and practical implementation.

To pragmatically evaluate test error for the model performance, we can use the metric like Leave-one-out cross-validation (LOOCV) and Generalized cross-validation (GCV), provide a robust framework for examining the double descent phenomenon. Especially in high-dimensional contexts, these validation techniques have proven effective in aligning theoretical predictions with empirical testing errors, offering a comprehensive lens through which to study and understand the intricate dance of bias, variance, and model complexity in the quest for generalizable intelligence.

4.4 Path Integral for QNNs

In this section, we aim to examine the variational quantum circuits from a new perspective, establishing a connection to the emergent phenomena of random feature mapping as the number of parameters increases.

Variational quantum circuits are recognized as a cornerstone in the realm of quantum machine learning. In this paradigm, the input to the circuit is derived from the embedded representation of either a quantum or classical data point, characterized by the $\rho_\alpha = |\psi_\alpha\rangle\langle\psi_\alpha|$ vector were $\alpha \in [1, \cdots, |\mathcal{D}|]$ for data set $\mathcal{D}$. The variational circuit consists of L parameters,

which can be optimized and adjusted to yield the best representation of the input dataset. Without loss of generality, we can express this unitary evolution as

$$U(\theta) = \prod_{\ell=1}^{\ell=L} U_\ell(\theta_\ell) C_\ell, \quad U_\ell(\theta_\ell) = e^{i\theta_\ell P_\ell} \tag{4.5}$$

in terms of vector of parameters $\theta = (\theta_1, \cdots, \theta_L)$. Here P_ℓ represents a Hermitian operator, typically selected from the set of Pauli operators. Meanwhile, C_ℓ signifies fixed operators, predominantly chosen from the Clifford operators. Upon measuring the state evolved by the QNN using the observable operator O, the output label corresponding to the input ρ_α is determined as:

$$f_{\alpha,\theta} = \mathrm{Tr}\big[U(\theta)^\dagger O U(\theta) \rho_\alpha\big]. \tag{4.6}$$

Recent advancements in the literature have introduced various methods to investigate the behavior of the quantum neural network as described in Eq .4.6, particularly in response to changes in the number of parameters or layers. This includes studying the behavior of wide Quantum Neural Networks (QNNs) as the number of qubits approaches infinity, leading to a more tractable method to understand the network's behavior through Quantum Neural Tangent Kernels (QNTK) [83, 102]. Additionally, for networks with finite width, the application of the Gaussian process has been developed, which examines the network in terms of correlation functions and explores the moments of the output distribution [2,103]. Another approach involves the direct use of path integrals through the Taylor expansion of the Pauli operators, as outlined in Ref. [104]. This method is employed to observe the phase transition from the underparameterized regime to the overparameterized regime in a more tractable way. In the following, we review this method.

Beginning with the assumption of the Hermitian property of the generators of parameterized gates, we can express the algebra of the group of generators as $P^{2m} = \mathbb{I}$ and $P^{2m+1} = P$ for $m = 0, 1, 2, \cdots$. This identity enables us to reformulate the unitary operator of each layer using a Taylor expansion, expressed as $U_\ell(\theta_\ell) = \mathbb{I}\cos(\theta_\ell) + iP_\ell \sin(\theta_\ell)$.

Utilizing this representation, the unitary evolution in Eq. (4.6) can be expanded into 2^L terms:

$$U(\theta) = \sum_{\mu \in (0,1)^{\times L}} U_\mu \Omega_\mu, \tag{4.7}$$

where $\mu = (\mu_1, \cdots, \mu_L)$, and each $\mu_i \in \{0, 1\}$. Here, Ω_μ is a multivariate trigonometric polynomial of order L, defined as $\Omega_\mu = \prod_{\ell=1}^{L} \Omega_{\mu_\ell}$, with each term $\Omega_{\mu_\ell} = \cos(\theta)^{1-\mu_\ell} \sin(\theta)^{\mu_\ell}$. The term U_μ represents the unitary operator of the circuit at $\theta = -(\frac{\pi}{2})\mu$, taking the form:

$$U_\mu = (-i)^{||\mu||_*} U(\theta = -\frac{\pi}{2}\mu) = (-i)^{||\mu||_*} \prod_{\ell=1}^{L} P_\ell^{\mu_\ell} C_\ell. \tag{4.8}$$

With these identities, Eq. (4.6) can be rewritten as

$$f_{\alpha,\theta} = \sum_{\mu,\nu \in (0,1)^{\times L}} \Omega_\mu \Omega_\nu \operatorname{Tr}\left[U_\mu^\dagger O U_\nu \rho_\alpha\right]. \tag{4.9}$$

By introducing a weight variable, $\Theta = \otimes_{\mu=1}^{L} \Theta_\mu := \otimes_{\mu=1}^{L} (\cos\theta_\mu, \sin\theta_\mu)^\top$, we can reformulate the path integral expansion of the Quantum Neural Network (QNN) as follows:

$$f_{\alpha,\theta} = \Theta^\top \Lambda_\alpha^\dagger O \Lambda_\alpha \Theta \tag{4.10}$$

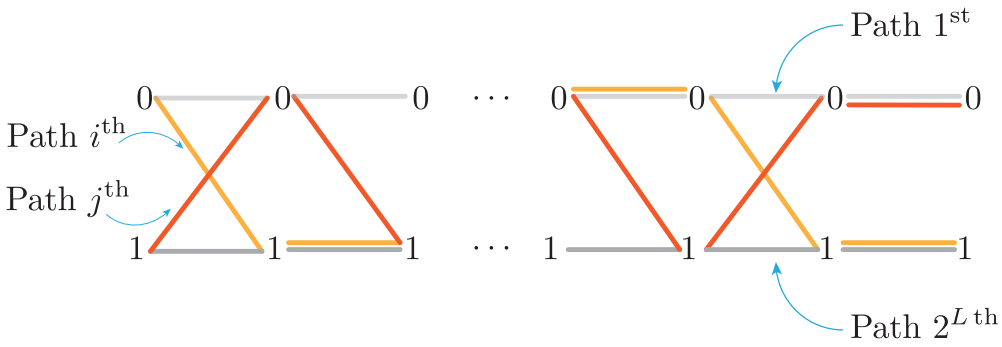

Figure 4.1: The path integral representation of a variational quantum circuit is characterized by the total number of parameters, denoted as L.

where $\Lambda_\alpha = [\Lambda_{\alpha,\mu}] = [U_\mu|\psi_\alpha\rangle]$ is a matrix wherein each row corresponds to one combination of the P operator from all possible configurations of $\mu \in (0,1)^{\times L}$ vector. This matrix representation can be interpreted as a summation over 2^L paths. Each path comprises a string of trigonometric contributions, which are illustrated in Fig.4.1.

4.5 Theory of Spin-Glass and Quantum Neural Network

The Λ_α up to its second moment order aligns closely with the Haar random unitary, leading to nearly identical expectation values. Given this similarity, the operator U_μ can be effectively substituted with the random Haar unitary operator, denoted as $\mathcal{U}_{\text{RH}}$, where 'RH' stands for Random Haar measure unitary. For the first moment, $k = 1$ this difference is exactly zero, and for the general k^{th} moment, According to Theorem. 4 presented in Ref. [104], the deviation can be bounded:

$$\mathbb{E}_{\mathcal{U}}[\text{Tr}\left(U_\mu^\dagger O U_\nu \rho\right)^{\otimes k} - \text{Tr}\left(\mathcal{U}_{\text{RH},\mu}^\dagger O \mathcal{U}_{\text{RH},\nu}\rho\right)^{\otimes k}] \leq 2^{\text{poly}(-n,L,k)} \tag{4.11}$$

By changing the coordinate that In the next section, we will study the behavior of random Haar matrices and their connection to random Gaussian matrices

4.6 On Random Matrix Theory

Random Matrix Theory (RMT) is a branch of linear algebra with surprising applications in many fields. From particle physics, as demonstrated by Wigner, who showed that the energy levels of heavy nuclei can be predicted using RMT predictions [105], to the distribution of zero points of the zeta function in number theory [106, 107]. It also finds applications in finance [108], graph theory [109], and machine learning.

In the realm of machine learning, the loss landscape has been explored from the perspective of the Spin-glass model, both in early works [110–112] and more recent studies [113–116]. This spin-glass method, based on Random Matrix Theory, provides a framework for understanding generalization and the double descent phenomenon in a more tractable way [117–120].

As discussed in the previous section, random matrices can serve as an effective approximation for neural networks in both classical and quantum scenarios. In the context of classical neural networks, the parameters typically follow a Gaussian distribution. These parameters may either be initialized using an independent and identically distributed (i.i.d.) Gaussian distribution ($G \in$ GOE(n) : $G_{ij} \sim \mathcal{N}(1/n), G_{ii} \sim \mathcal{N}(2/n), G_{ij} = G_{ji}$) or may stem from the broader structure of the random Gaussian β-ensemble. The inclusion of the parameter β specifies the underlying assumptions; for instance, the i.i.d. Gaussian case corresponds to $\beta \to 0$, and the Gaussian Orthogonal Ensemble (GOE) is represented with $\beta = 2$. The GOE ensemble possesses two independent properties simultaneously: the entries are both random and independent, and the ensemble is invariant under $U \in O(N)$, meaning if $X \in GOE$, then $UXU^\top \in GOE$. It can be shown that GOE, GUE, and GSE are the only distributions that exhibit these properties, characterized by $\beta = 1, 2,$ and 4. The joint probability distribution of eigenvalues follows the

following form:

$$P_\beta(\lambda) = C_{N\beta} e^{-\frac{\beta N}{2}\sum_{j=1}^{N}\lambda_j^2} \prod_{j<k} |\lambda_j - \lambda_k|^\beta, \tag{4.12}$$

which can be seen as a level repulsion but with an exponential decay weight. By defining the level spacing as $s_i := \lambda_{i+1} - \lambda_i$, in the large matrix limit the spacing distribution function is the Wigner-surmise function: $p(s) = \frac{\pi}{2} s e^{-\frac{\pi s^2}{4}}$. This can also be extended to complex values matrix. Considering the random matrix $n \times n$ with complex variable entries $z_{i,j} = x + iy$ such that $z_{i,i} = \mathcal{N}(0,1)$ and $z_{i,j} = \mathcal{CN}(0,1)$ where $\mathcal{CN}$ denotes the complex Gaussian distribution. Similarly, the Z distribution is invariant under unitary transform $Z \to U^\dagger Z U$.

For a given matrix X of size n, with a set of eigenvalues $\{\lambda_i\}$, the Empirical Spectral Distribution (ESD) can be defined as

$$\mu_{\text{ESD}} = \mu_n := \frac{1}{n}\sum_{i=1}^{n} \delta_{\lambda_i}(X_n)$$

where $\delta(\cdot)$ is the delta function. In many case, we need to calculate the terms like

$$G_n := \frac{1}{n}\sum_{i=1}^{n} \mathbb{E}[g(\lambda_i(X))] = \mathbb{E}\int_{\mathbb{R}} g(\lambda)\hat{\mu_X}(d\lambda) \tag{4.13}$$

to do so, we can take a levarge of the Stieltjes transform. This transform map the probablity measure $\mu \in \mathcal{P}(\mathbb{R})$ into the space of functional $\mathcal{F}(\mathbb{C})$ such that:

$$m_\mu(z) := \int \frac{\mu(dx)}{x - z} = \frac{1}{n}\operatorname{Tr}\big[(A - z\mathbb{I})^{-1}\big], \tag{4.14}$$

such that $m(z) = \lim_{n\to\infty} \mathbb{E}[m_n(z)]$ and the ESD of a matrix can be obtained for the Stieltjet

transform of the matrix with $\lim_{\epsilon\to 0}\frac{1}{\pi}\,\mathrm{Re}[m_\mu(x+i\epsilon)]=\mu$ and and therefore the Eq. 4.13 can be calculated as $G_n=\lim_{\epsilon\to 0}\int g(\lambda)\frac{1}{\pi}\mathrm{Re}(m_{\mu_n})(\lambda+i\epsilon)d\lambda$.

Applying this technique to find the ESD of GOE matrix help us to realized that the By this technique to find that as the matrix size increases, eigenvalues concentrate around the origin with the Wigner-semicircle density function . Comparing the Stilject transform of two matrix with size G_n and G_{n-1} leads us to realize they can be wrttien as the form of $m_n(z)=1/n\sum_{i=1}^{n}1/(-z-m_n(z)+o(n)$ which leads to have recursive relation for the Stiljet transform of G_n matrix:

$$m_n^2+zm_n+1=0 \tag{4.15}$$

therefor in the continuous limit EDS converges to

$$\mu_{\mathrm{SC}}(\lambda)=\frac{1}{2\pi}\sqrt{(4-\lambda^2)}d\lambda. \tag{4.16}$$

On the other hand, in the quantum neural network paradigm, the random matrices of interest are unitary operators measured with the Haar measure. To construct a Haar random matrix, suppose we start with an i.i.d Gaussian matrix, G, and decompose it into $G=QR$. The claim is that Q is Haar random. Furthermore, for any $R\in O(N)$, the matrix RQ has the same distribution. The eigenvalues of a Haar random unitary matrix are uniformly distributed across the unit circle, exhibiting behavior distinct from that observed in classical networks, where $\rho(\lambda)=\frac{1}{2\pi}$. Additionally, the joint probability distribution of these eigenvalues demonstrates a level repulsion property: $p(\lambda)=\prod_{i<j}|e^{i\lambda_i}-e^{i\lambda_j}|^2$. In this context, the spacing distribution follows the Wigner-Dyson form: $p(s)=\frac{32}{\pi^2}s^2e^{-\frac{4s^2}{\pi}}$.

4.6.1 Convergence of Random Haar unitary to Gaussian Distribution

Despite the different behaviour of random matrix with Haar measure and random Gaussion matrix, there is a connection between them. The Haar-distributed orthogonal matrix can be approximated using a random Gaussian matrix. One way to obtain a random unitary matrix, which is drawn from the group of unitary matrices with a uniform distribution, is by constructing the complex Gaussian matrix, G. By decomposing it as $G = UR$ using the Gram-Schmidt orthonormalization procedure, U becomes a random Haar measure matrix. where R is an upper-triangle matrix. This is because U is unitary, and it inherits the uniform distribution from G. It can be shown that selecting m row from the n row of the unitary, denoted by $U_{[m,m]}$, then distance between scaled version of the unitary $\sqrt{n}U_{[m,m]}$ and corresponding gaussian matrix with size m is bounded such that the Euclidean norm of F_i^m generator is less than $\sqrt{(2 - 4/3(1 - (1 - \alpha)^{3/2}/\alpha)m}$ where $\alpha = m/n$. and this distance mererge to zero if $m = O(n/\log n)$ and $m = O(\sqrt{n})$ provides another rate of convergsnce [121]. given

$$\frac{1}{c_{n,m}} \prod_{1 \le j < k \le m} |z_j - z_k|^2 \prod_{j=1}^{m} (1 - |z_j|^2)^{n-m-1} \tag{4.17}$$

for $c_{n,m} = \pi^m m! \prod_{j=0}^{m-1} \binom{n-m+j-1}{j}^{-1} \frac{1}{n-m+j}$ this distribution merges to

$$\frac{m^{\frac{m(m+1)}{2}}}{\pi^m \prod_{k=1}^{m} k!} e^{-m \sum_{i=1}^{m} |z_i|^2} \prod_{i<j} |z_i - z_j|^2. \tag{4.18}$$

which means unitary matrix converges to GUE with $\beta = 2$ in a truncated scenario.

4.6.2 Wishart-Laguerre ensemble

We can extend this study to consider a more general random matrix, G with the size of $d \times n$ and then construct a new matrix by $W = GG^{\dagger}$, we get new ensemble for each β. The distribution of eigenvalues will be given by

$$P(\lambda) = \frac{1}{\mathcal{Z}_{d,n}} e^{-\frac{1}{2}\sum_{i=1}^{N}\lambda_i} \prod_{i=1}^{N} \lambda_i^{\alpha\beta/2} \prod_{j<k} |\lambda_j - \lambda_k|^{\beta} \tag{4.19}$$

where $\alpha = (1 + n - d) - 2/\beta$. The self-consisten equation for Wishard matrix with size n leads to have the realtion as $m_n(z) = (-z + 1/(1 + rm_n(z)))^{-1}$ which in the large limit where $d, n \to \infty$ and $d/n \to \infty$, this density function converges to the Marcenko-Pastur density [122] $\mu(x) \to \frac{1}{\beta d}\mu_{MP}\left(\frac{x}{\beta d}\right)$ such that:

$$\mu_{\text{MP}}(x) = (1 - \frac{1}{r})_+ \delta_0(x) + \frac{\sqrt{(\lambda^+ - x)(x - \lambda^-)}}{2\pi r x} \mathbb{I}_{x\in[\lambda^-,\lambda^+]} dx \tag{4.20}$$

With $\lambda^{\pm} = (1 \pm \sqrt{r})^2$, a key phenomenon of this distribution is the phase transition that occurs. The distribution's behavior is dependent on the value of r relative to one, either concentrating eigenvalues at zero or not. Relevant to our work is the universality of the mentioned distribution. For many random matrices X with properties such as $\mathbb{E}[X_{ij}] = 0$, $\mathbb{E}[X_{ij}^2] = 1$, and $\mathbb{E}[X_{ij}^4] < \infty$, the empirical spectral distribution converges to the Marchenko-Pastur distribution.

Extending this discussion to the complex realm, we examine the distribution of the real part of the Wishart matrix: $2\text{Re}(W) = W + W^{\top}$. We observe that $\text{Re}(W)$ corresponds to the real Wishart distribution with $2n$ parameters. The distribution of eigenvalues can be considered in two

ways: If $\tilde{W} = (W + W^\top)/2$, then the distribution of eigenvalues aligns with the Marchenko-Pastur distribution, but with the ratio r adjusted to $r/2$, where $r = d/n$. If we consider $\tilde{W} = W + W^\top$, then the distribution is modified with r becoming $r/2$, and the eigenvalues are scaled by a factor of half, transforming $(\lambda - \lambda_+)$ to $(\lambda/2 - \lambda_+)$. In both cases, the adjustment of the ratio r and the scaling of eigenvalues reflect the intricate relationship between the Wishart matrix's complex structure and its eigenvalue distribution.

4.7 Double Descent in Generalization

In the preceding section, we explored variational quantum circuits as a quintessential example of Quantum Neural Networks (QNNs), highlighting their function as random feature maps. To train these networks, we utilize input data encapsulated in the input density matrix ρ_α and aim to optimize the objective loss function tailored to the task at hand. For instance, in linear regression, one might opt for the Mean Square Loss (MSE) defined as:

$$\mathcal{L} = \frac{1}{n} \sum_{\alpha=1}^{n} (y_\alpha - \hat{y}_\alpha)^2, \tag{4.21}$$

where $\{y_\alpha\}$ represents the true target values or labels, and $\{\hat{y}_\alpha\}$ denotes the predictions made by the QNN, according to Eq. 4.9:

$$\hat{y}_\alpha = \sum_{\mu,\nu \in (0,1)^{\times L}} \Omega_\mu \Omega_\nu \operatorname{Tr}\left[U_\mu^\dagger O U_\nu X_\alpha\right], \tag{4.22}$$

where $X := [\rho_\alpha]$ with $\rho_\alpha \in \mathbb{C}^{d \times d}$, $U \in \mathbb{C}^{m \times m}$, $\Omega \in \mathbb{R}^{2^L \times 1}$ and $Y := [y_\alpha] \in \mathbb{R}^{1 \times n}$ with $m = d$. According to our notation in Eq. 4.10, we can represent $\hat{y}_\alpha$ in the above equation in vector form

as well:

$$\hat{y}_\alpha := w^\top J_\alpha w, \tag{4.23}$$

with $J_\alpha \in \mathbb{C}^{2^L \times 2^L}$ and $w \in \mathbb{C}^{2^L \times 1}$. Incorporating a regularization term with the hyperparameter λ as $\lambda w^T w$ into the total loss function and subsequently optimizing this function helps identify the optimal parameters where $\nabla_w \mathcal{L}|_{w=w_*} = 0$. This results in $(J + J^T + \lambda I)^{-1} Y (J + J^T) = w_*^T J w_*$. To address the effect of noise, it is crucial to add the noise term to the prediction term like $\hat{Y} := [\hat{y}_\alpha + \epsilon_\alpha]$ such that $\epsilon_\alpha \sim \mathcal{N}(0, \sigma_\epsilon^2)$. To assess the generalization error, one approach is to calculate the generalization errors. Starting with the train error, we have:

$$\begin{aligned} E(\lambda)_{\text{test}} &= \frac{1}{n} ||Y - \hat{Y}|| \\ &= \frac{1}{n} ||Y(I - (J + J^T + \lambda I)^{-1}(J + J^T))||, \end{aligned} \tag{4.24}$$

and defining the resolvent as

$$Q := J + J^T + \lambda I, \tag{4.25}$$

we can express the train error as

$$E(\lambda)_{\text{train}} = \frac{1}{n} \lambda^2 ||YQ||^2. \tag{4.26}$$

In the next step, to calculate the generalization error like the Leave-One-Out Cross-Validation (LOOCV) error, denoted as E_L, and the Generalized Cross-Validation (GCV) error, denoted as E_G, we can find the following relationships:

$$E_L(\lambda) = \frac{1}{n} ||YQ \,\text{diag}(Q)^{-1}||_2^2, \quad E_G(\lambda) = \frac{\frac{1}{n}||YQ||_2^2}{\left(\frac{1}{n}\text{Tr}(Q)\right)^2}. \tag{4.27}$$

The properties of expressions like Eq. 4.26 and Eq. 4.27 have been thoroughly examined in the context of classical neural networks [96, 117–119, 123–126] and It has been observed that in higher dimensions, these terms converge to the same behavior as the test error such that:

$$\lim_{m,n,d\to\infty} E_L(\lambda) = E_G(\lambda) = E_{\text{test}}(\lambda), \tag{4.28}$$

and In line with these foundational works, to find the analytical understanding of the generalization error we can define $\tau_1(\lambda)$ and $\tau_2(\lambda)$ respectively as:

$$\tau_1(\lambda) := \frac{1}{n}\mathbb{E}[\mathrm{Tr}\left[Q(\lambda)^{-1}\right]] \tag{4.29}$$

and

$$\tau_2(\lambda) := \frac{1}{n}\mathbb{E}\,\mathrm{Tr}\left[\frac{1}{n}X^T X Q(\lambda)^{-1}\right] \tag{4.30}$$

and upon this definition, these parameters are integrated into the solution of a set of coupled polynomial equations:

$$\begin{aligned}\frac{\phi}{\psi}[\zeta\tau_2\tau_1 + \phi(\tau_2 - \tau_1)] &= \zeta\tau_2\tau_1(1 - \lambda\tau_1) \\ &= (\tau_1 - \tau_2)\phi[\zeta(\tau_2 - \tau_1) + \eta\tau_1]\end{aligned} \tag{4.31}$$

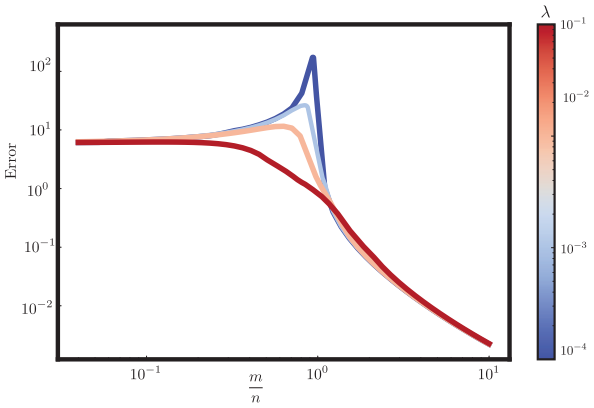

Figure 4.2: Test error as a measure of generalization error in terms of the complexity of the quantum model, represented by the m/n ratio for various regularization hyperparameters, λ. According to the simulation, there is a double descent with a phase transition around $m \sim n$, which leads to an initial increase and then a decrease in the error. In the ideal overparameterized scenario, we expect the generalization error to converge to zero, which contradicts the previous bias-variance trade-off observed in classical cases. Here, for the quantum case, we observe the same behavior.

such that $\phi := d/n$, $\psi := d/m$, $\zeta := (\mathbb{E}_{n\sim\mathcal{N}(0,\sigma_\epsilon^2)}[N\hat{Y}]/\sigma_\epsilon^2)^2$, and $\eta := \mathbb{E}_{n\sim\mathcal{N}(0,\sigma_\epsilon^2)}[n\hat{Y}]$. In the same manner the derivatives of τ_1 and τ_2 respect to the λ have the following form:

$$\begin{aligned}\tau_1' = -\Bigg(&\zeta^2\tau_1^5\tau_2^2\left(\frac{\tau_2\psi\phi}{\tau_1} - \phi(\psi+\phi)\right)\Bigg/ \\ &[(\phi^2(-\zeta^2\tau_1\tau_2^2(\tau_1^2 - (\tau_1-\tau_2)^2\phi) + \\ &\phi\left(\eta\tau_1^2 - \zeta(\tau_1-\tau_2)(\tau_1+2\tau_2)\right))\psi) \\ &\times(\tau_1-\tau_2)^2\left(\zeta^2\tau_1\tau_2^2 + (\zeta(\tau_2-\tau_1)+\eta\tau_1)\right)]\Bigg)\end{aligned} \tag{4.32}$$

and

$$\begin{aligned}\tau_2' = &-\zeta^2\tau_1^3\tau_2^2(\tau_1-\tau_2)\left(\tau_1\psi\phi(\zeta-\eta)+\zeta\phi^2(\tau_1-\tau_2)\right)/\\ &[(\phi^2(-\zeta^2\tau_1\tau_2^2(\tau_1^2-(\tau_1-\tau_2)^2\phi)+\\ &\phi\left(\eta\tau_1^2-\zeta(\tau_1-\tau_2)(\tau_1+2\tau_2)\right)\psi\big)\\ &\times(\tau_1-\tau_2)^2\left(\zeta^2\tau_1\tau_2^2+(\zeta(\tau_2-\tau_1)+\eta\tau_1)\right)\big]\end{aligned} \tag{4.33}$$

such that the expected values for the test and training errors can be computed as:

$$\mathbb{E}_{\text{test}} = \frac{\sigma_\epsilon^2\tau_1' + \tau_2'}{\tau_1^2} \tag{4.34}$$

and

$$\mathbb{E}_{\text{train}} = \lambda^2(\sigma_\epsilon^2\tau_1' + \tau_2') \tag{4.35}$$

Now, since we have a good expression for the test error, we can study the behavior of the learning task in terms of the number of samples, parameters, and the dimension of the random feature quantum map, namely in terms of m/n. To see this, the test error has been plotted in Fig. 4.2 for various regularization terms in terms of m/n. As observed, there is a double descent phenomenon. By increasing m/n, the test error increases for small regularization parameters (ideally zero), and, after the point where $m \sim n$, the test error converges to zero. Therefore, we can achieve zero generalization error in the case of overparameterization, where $m \gg n$.

4.8 Outlook and Conclusion

In this study, we explored the task of generalization with quantum machines. Quantum machines can have poor performance in predicting unseen data due to their intrinsically large exponential representation space, making them prone to poor generalization error. For the first time, we demonstrate a proof of concept that, for a quantum network behaving like a random feature map, similar to classical networks, we can analytically predict the double descent behavior of the prediction error using random matrix theory. This finding challenges the traditional bias-variance trade-off belief. Our results suggest that in the overparameterized regime, quantum circuits, like their classical counterparts, can be useful, at least in theory and concept.

Chapter 5: Efficient Hamiltonian Calibration Through Pruning Control Parameters

"Who knew my fate would collapse into a part-time gardener?"

Brain-damaged quantum scientist

5.1 Abstract

Operating a quantum simulator entails an essential phase: the engineering of the desired Hamiltonian via available experimental controls. In this study, we focus on facilitating arbitrary interaction patterns by fine-tuning the amplitudes of driving lasers in a trapped ion quantum simulator. Construction of sophisticated interaction patterns often requires additional laser tones, subsequently complicating the experimental setup. To address this challenge, we propose adopting an algorithm widely used in machine learning called the optimal brain damage method that uses the Hessian of the cost function to prune unimportant parameters. Employing this strategy, we aim to identify laser amplitudes that reliably produce the desired Hamiltonian while minimizing the need for supplementary laser tones. As a case study, we consider the simulation of interaction patterns inspired by Schwinger and Harper-Hofstader models. The outcomes demonstrate a significant parameter reduction of at least 50% while ensuring a reconstruction error below 1%. Furthermore, we demonstrate that our strategy, utilizing Hessian information to reduce the laser

parameters budget, performs markedly better than a baseline approach where parameters are removed randomly as a no prior knowledge, achieving improvements spanning several orders of magnitude.

5.2 Introduction

Quantum simulators offer a unique platform for in-depth analysis of properties and behavior of quantum systems within a controlled setting [127]. These systems frequently exhibit complexities that surpass the grasp of classical methods, which are confronted with difficulties in handling the rapid expansion of a quantum system's Hilbert space [128]. There are various physical platforms that are being utilized to construct quantum simulators (see e.g., Ref. [128] for a review).

Ion-trap quantum computers are a promising solution for large-scale quantum computing, offering advanced control methods, low error rates, and the capability to create entanglement across numerous qubits while maintaining long coherence times [129–132]. This platform is particularly useful for simulating arbitrary interacting spin-spin models by utilizing long-range phonon mediated interactions between ions [133–135].

Even in a linear trap, the interactions graph of ions can extend beyond their geometric configuration, exhibiting higher-dimensional structures with rich geometries [136]. Within these systems, precise computation and fine-tuning of laser parameters are imperative for accurately designing the effective coupling graph, necessary for desired quantum simulations. While finding the coupling graph of a system for given control parameters is a well-defined forward problem, determining the specific laser parameters to simulate a particular spin-spin interaction graph presents a challenging inverse problem that needs to be addressed [136]. This inverse problem

is a non-linear optimization problem that seeks to minimize the difference of the target and realized Hamiltonians by identifying suitable laser parameters. Existing methods using direct optimization [136] or neural networks [137], typically require the utilization of many laser tones, which can be costly and not always necessary.

In this study, we introduce a new approach for tuning laser parameters that is based on a widely used technique in classical machine learning known as the optimal brain damage pruning algorithm [138]. Originally, pruning was used to optimize neural networks by minimizing their size, thereby reducing computational load while maintaining accuracy by selectively removing less influential parameters, with its criteria often related to the cost function's second derivative [139–142]. Adapting this algorithm to the problem of calibrating a target coupling graph in a trapped-ion quantum simulator thus allows us to simplify the complexity of the experiment while preserving its accuracy.

A fully connected arbitrary interaction graph of N spins entails $N(N-1)/2$ pairwise interactions. To realize this, one can use N^2 tunable laser control parameters corresponding to the Rabi frequencies of N laser beams on N ions [136, 137]. However, in many cases not all N^2 parameters are necessary. We therefore use Hessian information to identify and remove less effective parameters and only keep crucial ones needed for realizing specific spin interactions, while maintaining acceptable reconstruction errors. This reduction is rooted in the physical symmetries and constraints inherent in the physics Hamiltonian.

We investigate the trade-off between pruning percentage, i.e. the percentage of parameters removed, and accurate reconstruction error in interaction graphs, by introducing a quantitative measure of error, calculated as the square norm of the difference between the target coupling matrix and its reconstructed counterpart. Remarkably, our findings demonstrate that acceptable

reconstruction error levels can be maintained even with high pruning percentages.

Through case studies inspired by the Schwinger [143] and the Harper-Hofstadter [144] models, we observed that utilizing at most half of the initial N^2 laser parameters is sufficient to keep the total error below 1%. We emphasize that except in special cases, for a general coupling matrix, it is not a priori clear which of the parameters are more important, and hence we cannot simply start with those reduced set of parameters. To this end, we compare the performance of Hessian-based pruning with a baseline random pruning algorithm in terms of error level and convergence rate, and show that Hessian-based pruning outperforms random pruning in both aspects. Consequently, this efficient optimization method not only reduces the overall optimization time but also enables real-time optimization strategies for dynamic systems. Particularly in scenarios where swift adjustment of parameters is essential and time constraints limit the use of traditional computational resources, our method proves highly advantageous.

5.3 Setup

We consider a trapped ion simulator consisting of N ions, where each of the ions is irradiated with N bi-chromatic laser beams and a global counter-propagating laser beam. The interference between these beams produces Raman beat notes at frequencies of $\omega_0 \pm \mu_n$ for a fixed, but tunable set of μ_n. Here, n can take a value ranging from 1 to the total number of laser beams, N. We have set these frequencies by spacing them from the phonon normal modes, ω_n. Similar to Ref. [145], without loss of generality, we have chosen $\mu_1 = \omega_1 + \epsilon\overline{\delta\omega}$ and $\mu_n = \omega_n + \epsilon(\omega_{n-1} - \omega_n)$, if $n \neq 1$, for small and non-zero constant number ϵ. Here $\overline{\delta\omega}$ denotes the average difference between two adjacent phonon modes. This setup is depicted in Fig. 5.1.

The pairwise interactions between the N laser beams and the N ions can be characterized by N^2 Rabi frequencies $\Omega_{i,n}$, where i and n represent the ion and tone indices, respectively. This setup produces an effective spin-spin coupling Hamiltonian

$$H = \sum_{i,j<i}^{N} J_{i,j}\sigma_i^+\sigma_j^- + \text{h.c}, \tag{5.1}$$

where $\sigma_j^{\pm}$ is the spin raising and lowering operators on ion j, and h.c. indicates hermitian conjugation, see Fig. 5.1. The coupling matrix elements $J_{i,j}$ can be tuned by individual control of the Rabi frequencies $\Omega_{i,n}$ as

$$\begin{aligned} J_{i,j}(\{\Omega_{i,n}\},\{\mu_n\}) &= \sum_{n=1}^{N}\Omega_{i,n}\Omega_{j,n}\sum_{m=1}^{N}\frac{\eta_{i,m}\eta_{j,m}\omega_m}{\mu_n^2-\omega_m^2} \\ &\equiv \sum_{n=1}^{N}\Omega_{i,n}\Omega_{j,n}F_{i,j,n} \end{aligned} \tag{5.2}$$

where ω_m represents the vibrational phonon mode frequencies, $\eta_{i,m} = b_{i,m}\delta k\sqrt{\hbar/(2M\omega_m)}$ is the Lamb-Dicke parameter, $b_{i,m}$ denotes the phonon-mode transformation matrix of the i^{th} ion corresponding with the m^{th} normal mode, and δk represents the wave vector difference of the counter-propagating Raman lasers. Here M is the mass of a single ion, $\hbar$ is the reduced Planck constant, and $F_{i,j,n}$ is the response of the spin-spin coupling J_{ij} to the spectral component n [136].

In general, solving the forward equation (5.2) to compute the values of $J_{i,j}$, given the parameters $\Omega_{i,n}$ and μ_n, is a straightforward task. However, the true challenge lies in solving the inverse problem: determining the Rabi frequencies $\Omega_{i,n}$ that will satisfy Eq. 5.2, given the values of $J_{i,j}$ and μ_n. This problem is highly nonlinear and can potentially lead to unstable solutions [145]. In previous works, a set of N^2 Rabi frequencies $\Omega_{i,n}$ has been used as the control

parameters to successfully engineer a wider range of interaction graphs [136, 137]. However, due to the presence of symmetries and constraints in the desired interaction graph, it is sometimes possible to achieve the same result with fewer control parameters and hence a sparser Rabi frequency matrix.

In order to achieve scalability in simulations with a larger number of ions, it becomes crucial to find an economical solution in terms of laser usage and we suggest pruning can be seen as an effective approach to address this requirement. Given the set of N^2 Rabi frequencies $\Omega_{i,n}$, our aim is to disregard (or prune) as many Rabi frequencies as possible while constructing an approximation $\hat{J}_{i,j}$ of $J_{i,j}$ such that the resulting error defined as

$$E = \frac{||J - \hat{J}||_2^2}{||J||_2^2} = \frac{1}{||J||^2} \sum_{i,j=1}^{N} |J_{i,j} - \hat{J}_{i,j}|^2 \tag{5.3}$$

is minimized. We defined the cost function, E based on the squared error of how different the ion interaction graph rendered by the model, $\hat{J}$, was from the given interaction graph, J.

To evaluate the effect of varying each parameter on the total error, we consider the change in total error δE up to the second order in the change $\Omega_{i,n}$ using the Taylor expansion is given by

$$\begin{aligned} \delta E = &\sum_{i,n} g_{i,n} \delta\Omega_{i,n} + \frac{1}{2} \sum_{i,n} h_{i,n,i,n} \delta\Omega_{i,n}^2 \\ &+ \frac{1}{2} \sum_{i,n \neq j,m} h_{i,n,j,m} \delta\Omega_{i,n} \delta\Omega_{j,m} + O(||\delta\Omega||^3). \end{aligned} \tag{5.4}$$

Here, $\delta\Omega_{i,n}$ denote the change in $\Omega_{i,n}$, $g_{i,n} = \delta E / \delta\Omega_{i,n}$ and $h_{i,n,j,m} = \delta^2 E / \delta\Omega_{i,n} \delta\Omega_{j,m}$ represent

the components of the gradient and Hessian of E with respect to $\Omega_{i,n}$, respectively [1].

Note that the number of parameters $h_{i,n,j,m}$ scale quadratically with the number of variables $\Omega_{i,n}$ and their calculation can quickly become intractable. For example, with 50 ions and 50 tones, there are more than 3×10^6 parameters to calculate. To reduce the computational intensity of this task, we follow Ref. [138] and make a few simplifying assumptions. First, we assume that the effect of pruning multiple Rabi frequencies equals the sum of the effects of pruning each of them individually. This is equivalent to ignoring the cross terms $h_{i,n,j,m}$ with $i \neq j$ and $n \neq m$, leading to the diagonalization of the Hessian. Second, we assume that we are pruning the frequencies after the cost function has converged, i.e. it is at a local minimum, and therefore the gradient $g_{i,n}$ is zero. These assumptions simplify Eq. (5.4) to:

$$\delta E \approx \frac{1}{2} \sum_i h_{i,n,i,n} \delta \Omega_{i,n}^2. \tag{5.5}$$

Note that when removing a parameter we have $\delta\Omega_{i,n} = \Omega_{i,n}$. Therefore, this adds a cost proportional to $\Omega_{i,n}^2$ and its Hessian $h_{i,n,i,n}$. Consequently, a parameter's significance is determined by its magnitude and Hessian. This allows us to rank the parameters based on the on their influence on the error. The parameters than cause the least change in the error when removed are the least significant ones and can be safely removed. While in general $h_{i,n,i,n}$ can be calculated using automatic differentiation efficiently, we calculate them analytically by differentiating Eq. (5.2) to further speed up the pruning procedure.

To accommodate resource constraints, we can selectively remove or prune a certain percentage of less significant parameters, guided by this criteria. This pruning technique is commonly known

[1] The quadratic expansion of the cost function and the subsequent analysis can be straightforwardly extended to complex valued $\Omega_{i,n}$.

as *optimal brain damage pruning* in the neural network literature [138]. In the subsequent section, we delve deeper into the technique of pruning.

5.4 Optimization and Pruning

As previously mentioned, it's not immediately evident which of the $\Omega_{i,n}$ parameters are of primary importance. Consequently, it's often advisable to begin with a larger set of parameters than might seem necessary. In fact, initiating with more parameters can facilitate the optimization process, making it more straightforward and easier to navigate the cost landscape and find a suitable solution [98]. In light of this, we adopt an 'optimize, prune, and fine-tune' strategy [138]. We first find the $\Omega_{i,n}$ parameters, with full capacity of the lasers budgets, that minimize the cost function defined in Eq. (5.3) until achieving a desired threshold for the error. We choose a threshold of 10^{-7} for the value of the cost function as the stopping point.

In the next step, to optimize our resources and stay within the constraints of the laser budget, we initiate pruning. Through this approach, we retain a certain percentage of the control parameters based on specific criteria, while setting the remainder to zero. The parameters that are set to zero are essentially deactivated and will not participate in the next steps.

We execute pruning based on a given criteria using the concept of a mask. The mask, $\mathbb{M}$, serves as an element-wise transformation from the original coupling matrix to its modified counterpart: $\Omega_{i,n} \rightarrow \mathbb{M}_{i,n} * \Omega_{i,n}$. Therefore, when pruning $p\%$ of the parameters, $\mathbb{M}_{i,n} = 0$ corresponds to the discarded parameters, while $\mathbb{M}_{i,n} = 1$ represents the retained ones.

One criteria for constructing the mask is based on the Hessian in Eq. (5.5). The *Hessian mask* utilizes the diagonal elements of the Hessian matrix, as discussed in the previous section. In

this approach, the variables are sorted according to their respective Hessian values $h_{i,n,i,n}\delta\Omega_{i,n}^2$. The top $(100-p)\%$ of the variables, with the highest $h_{i,n,i,n}\delta\Omega_{i,n}^2$ values are selected. Therefore, we have $\mathbb{M}_{i,n}=0$ for the top $(100-p)\%$ and $\mathbb{M}_{i,n}=1$ for the rest.

To further probe the significance of the Hessian-based criteria in potentially enhancing results, as well as to understand if the sheer number of parameters alone is pivotal, we compare our outcomes against those obtained using a *random mask* for benchmarking. In constructing the random mask, we randomly select retained parameters without relying on prior knowledge about the underlying physics of the problem. Specifically, we set $\mathbb{M}_{i,n}=0$ for $p\%$ of the elements chosen at random, and $\mathbb{M}_{i,n}=1$ for the rest. Thus effectively we only keep $(100-p)\%$ of the elements in $\Omega_{i,n}$ at random.

Following the parameter pruning phase, the remaining variables, which have already undergone the pruning stage, are optimized during the fine-tuning stage. The act of pruning inevitably increases the error as predicted by Eq. (5.5). Therefore, as the final fine-tuning step, we optimize the error again using the reduced set of parameters.

To ensure a more refined optimization, we allocate double the iteration budget compared to the initial stage. In our study, the training phase was carried out using gradient descent with the Adam optimizer [146]. We utilized a fixed learning rate of $\eta=10^{-3}$. The iteration budgets were determined based on initial and final epoch numbers, with the final epoch being twice the initial one. These numbers ranged from 10^3 to 10^6, as detailed in the next section.

5.5 Results

We consider the effectiveness of our method in realizing two example coupling matrices. In our first example, drawing inspiration from the Harper-Hofstadter model [144], where for a two-dimensional lattice on the xy plane, under the influence of an external magnetic field in the z direction, the interaction coupling matrix for a two-dimensional lattice incorporates a phase, ϕ, in the y direction:

$$J_{HH} \sim \begin{cases} J_x, \\ \\ J_y e^{i2\pi\phi y}. \end{cases} \tag{5.6}$$

This demonstrates our method's capability to handle coupling matrices with complex values and beyond 1 dimension. The second example is relevant for simulations of the lattice Schwinger model [143]. In this case, the coupling matrix is represented as:

$$J_{Sch} \sim J_x \frac{(N-x)}{N}, \tag{5.7}$$

for a specified one-dimensional lattice of size N in the x direction. This model has also been explored in Ref. [147].

We first illustrate the main idea by considering the Harper-Hofstadter model in Fig. 5.2. Using the full laser capacity we obtain the Rabi matrix $\Omega_{i,n}$ after 3×10^5 iterations, as illustrated in Fig. 5.2(a). This solution is capable of accurately simulating the target J, shown in Fig. 5.2(h) with a cost function value of less than 10^{-14}.

To evaluate the effectiveness of pruning strategies in achieving faithful reconstruction while maintaining a reasonably low laser budget, we compare two levels of pruning: $p = 50\%$ and

$p = 80\%$. The schematic representation of the optimized mask, generated using the Hessian method, is depicted in Fig. 5.2(b,c). The optimized Rabi matrix, corresponding to a pruned laser budget, is depicted in Fig. 5.2(d,e). In order to evaluate the effectiveness of pruning, we have shown the real and imaginary part of the reconstructed $\hat{J}$ matrix, in Fig. 5.2(h). Comparing the reconstructed coupling matrices with pruning levels of $p = 50\%$ and $p = 80\%$ reveals that lower pruning results in fewer imperfections in the reconstruction, as one would expect. However, remarkably, even with a pruning level of $p = 80\%$, the reconstructed matrix remains reasonably close to the ideal one.

In the next part of the study, we focused on analyzing the reconstruction error in terms of the pruning percentage for the two models of interest. As demonstrated in Fig. 5.3, the changes in the cost function relative to the percentage of unpruned parameters highlight the cost-effectiveness of pruning as a technique for maintaining an acceptable level of accuracy in reconstruction. In Fig. 5.3(a), we have examined the dependence of this reconstruction accuracy on the percentage of unpruned parameters for the Schwinger model, while Fig. 5.3(b) represents the same study for the Harper-Hofstadter model. We have also compared the performance of the Hessian pruning strategy with the random pruning technique. Remarkably, in the Schwinger model, the Hessian pruning method achieves an error smaller than 10^{-4} even when activating only 20% of the laser parameters. As expected, reducing the pruning percentage results in a significant increase in accuracy. These pair of case studies indicate that it's feasible to reconstruct the target coupling matrix with reasonable error even when the laser budget is reduced by at least 50%. They further suggest that optimal damage pruning could serve as an effective strategy across a range of physical models.

The third part of our study aimed to investigate the convergence rates of various pruning

strategies. It is essential to examine how different strategies perform in finding the optimum, whether in terms of the number of iterations or their ability to locate the optimum point at all. This analysis is also crucial, given the existing trade-off between optimization time and reconstruction accuracy. Our results indicate that the optimal brain damage algorithm, utilizing the 'optimize, prune and fine-tune' approach, converges faster than the random pruning benchmark, suggesting that our method provides a more efficient and accurate optimization process. As illustrated in Fig. 5.4, the Hessian pruning method yields lower errors as the number of iterations increases, in contrast to the random pruning method, which exhibits either a plateau or a decreased convergence rate with increasing iterations.

The results presented in this study highlight the potential value of the Hessian pruning method as a crucial tool in optimizing quantum systems. This approach not only enhances performance but also reduces both the expenses and complexity associated with the experiments.

5.6 Conclusion and Outlook

This study explored the efficiency of pruning methods in reducing the complexity and cost of quantum simulation. Our investigation probes the impact of various pruning percentages on the accuracy of Hamiltonian reconstruction. We have found that, for some models, a pruning strategy of up to 50% can accomplish minimal error while maintaining a relatively low laser budget. Additionally, we have utilized the Hessian information in our pruning and demonstrated that it surpasses the random benchmark in both quality and convergence rate.

For future study, it will be fruitful to account for decoherence resulting from the first-order spin-dependent coherent displacements. By incorporating time error evolution minimization, we

can achieve higher fidelity in quantum simulation. This can be achieved by augmenting the cost function with a term representing the norm of the spin-phonon coupling operator, which can be added to the main cost function.

Code and Data Availability

The code and sample of data used in this research is available on GitHub: `https://github.com/frustea/Hamiltonian-Simulation-Brain-Damage`

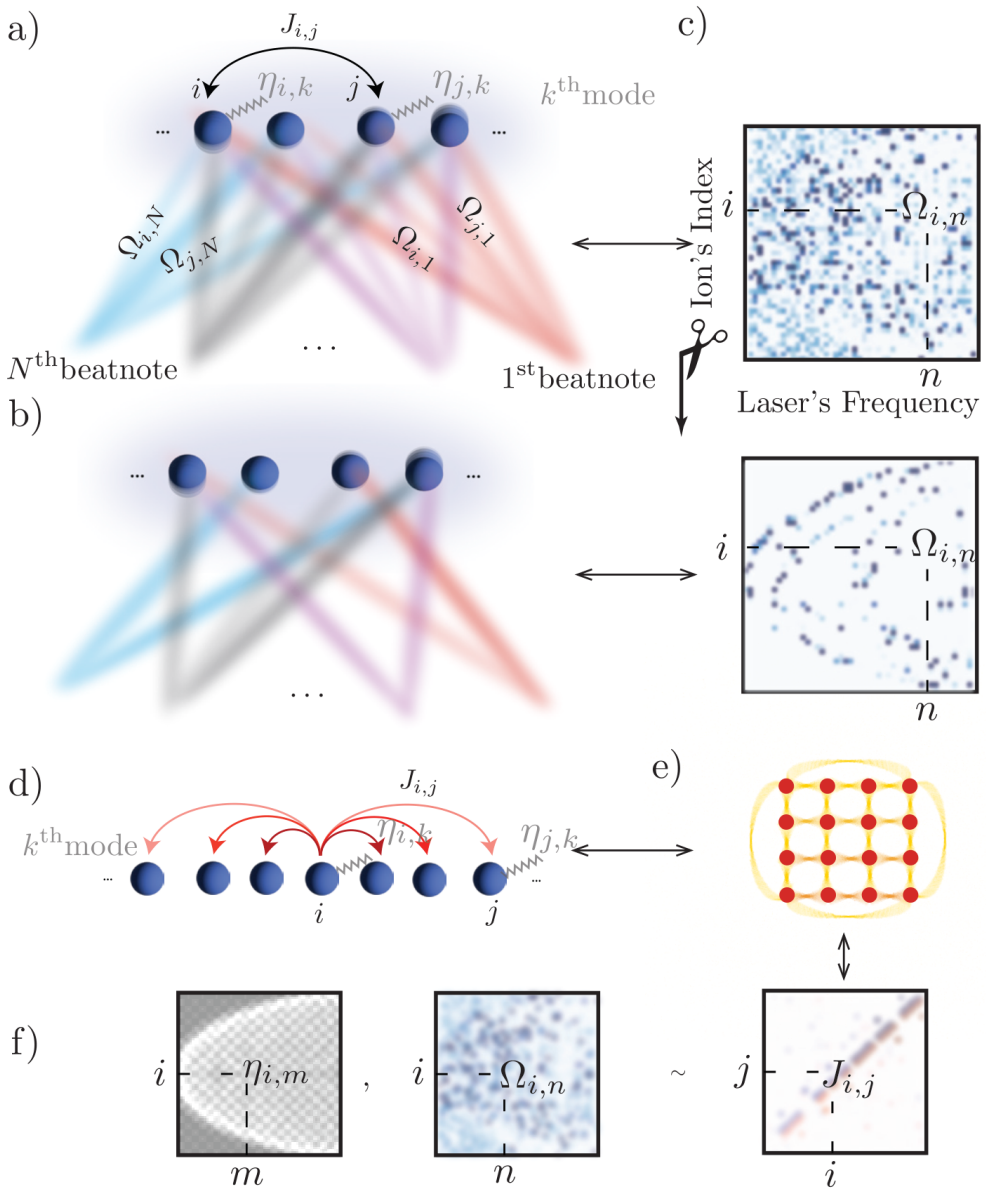

Figure 5.1: **Quantum Simulator with Ion Traps** (a) An array of N trapped ions (illustrated for $N = 4$) are exposed to bichromatic laser beams from the left and a globally counter-propagating beam from the right. The interaction among N ions is shaped by the interference-generated Raman beats and the Rabi frequencies. (b) A specific percentage of laser beams can be deactivated to conserve the laser budget. (c) The ion-laser interaction is determined by a Rabi matrix, $\Omega_{i,n}$. By pruning certain laser-ion interactions, we can create a sparser $\Omega_{i,n}$ matrix and thus reduce the laser budget. (d) The coupling matrix J represents the pairwise interaction between ions. (e) Despite the linear arrangement of the trapped ions, the coupling matrix design enables the generation of a wide range of rich Hamiltonians. (f) By adjusting the Rabi matrix, Ω, and taking into account the ion-phonon interaction Lamb-Dicke matrix, η, we can derive the desired J.

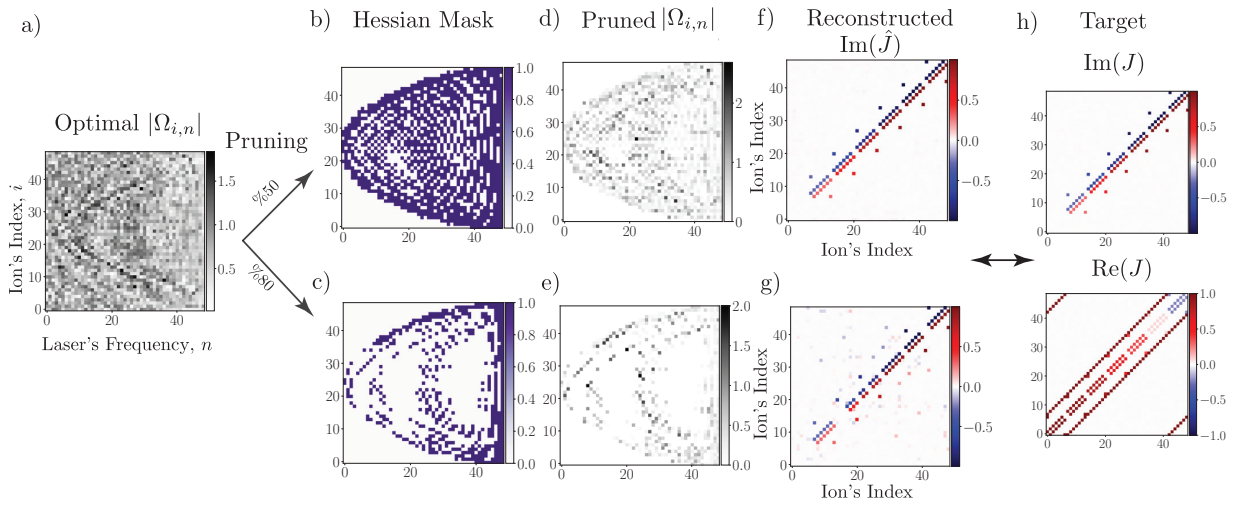

Figure 5.2: **Pruning Method.** (a) The illustration represents the magnitude of optimized Rabi frequencies $|\Omega_{i,n}|$ used to realize the target coupling matrix, which is inspired by the Harper-Hofstadter model with $N = 49$ qubits. The full capacity of lasers is utilized, with no pruning involved. In this model, both $J_{i,j}$ and $\Omega_{i,n}$ are complex-valued. (b,c) The Hessian masks are depicted with varying pruning ratios of 50% and 80%, respectively. In panels (d) and (e), the optimal $|\Omega_{i,n}|$ is obtained using the Hessian method to reconstruct the desired coupling matrix, and the magnitude of the pruned solution is displayed. (f,g) The imaginary part of the realized coupling matrix represented as $\mathrm{Im}(\hat{J})$, is displayed in panels d and e, showcasing the effects of different pruning ratios with the optimal solution. (h) The real and imaginary parts of the target coupling matrix are presented for the Harper-Hofstadter model with a lattice comprising a total of $N = 7 \times 7$ lattice sites.

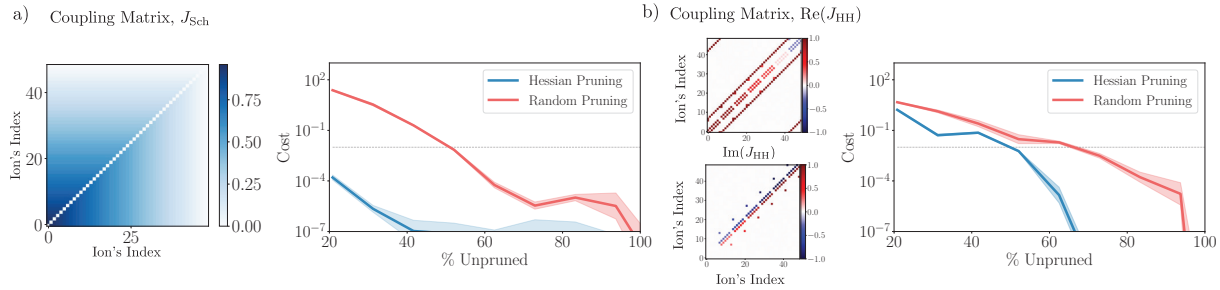

Figure 5.3: **Effectiveness of Pruning for Reconstructing Physical Systems.** (a) On the left, we present Schwinger's $1d$ coupling matrix J_{Sch}, which serves as the target for simulation. On the right, a cost function that measures the reconstruction error (The norm square between the target, J, and the reconstructed one, $\hat{J}$) is plotted as a function of the unpruned percentage. We use this analysis to evaluate the relative performance of the two pruning strategies with Hessian and random masks. The horizontal dashed line shows the one percent error baseline (b) the same evaluation has been repeated using the $2d$ Harper-Hofstadter (HH) model. The cost function is computed by averaging over ten random initializations. For the Schwinger model, this is done after 3×10^6 iterations, while for the HH model, we perform this computation after 3×10^5 iterations. The horizontal dashed line in the graphs represents the baseline for a 1% error rate.

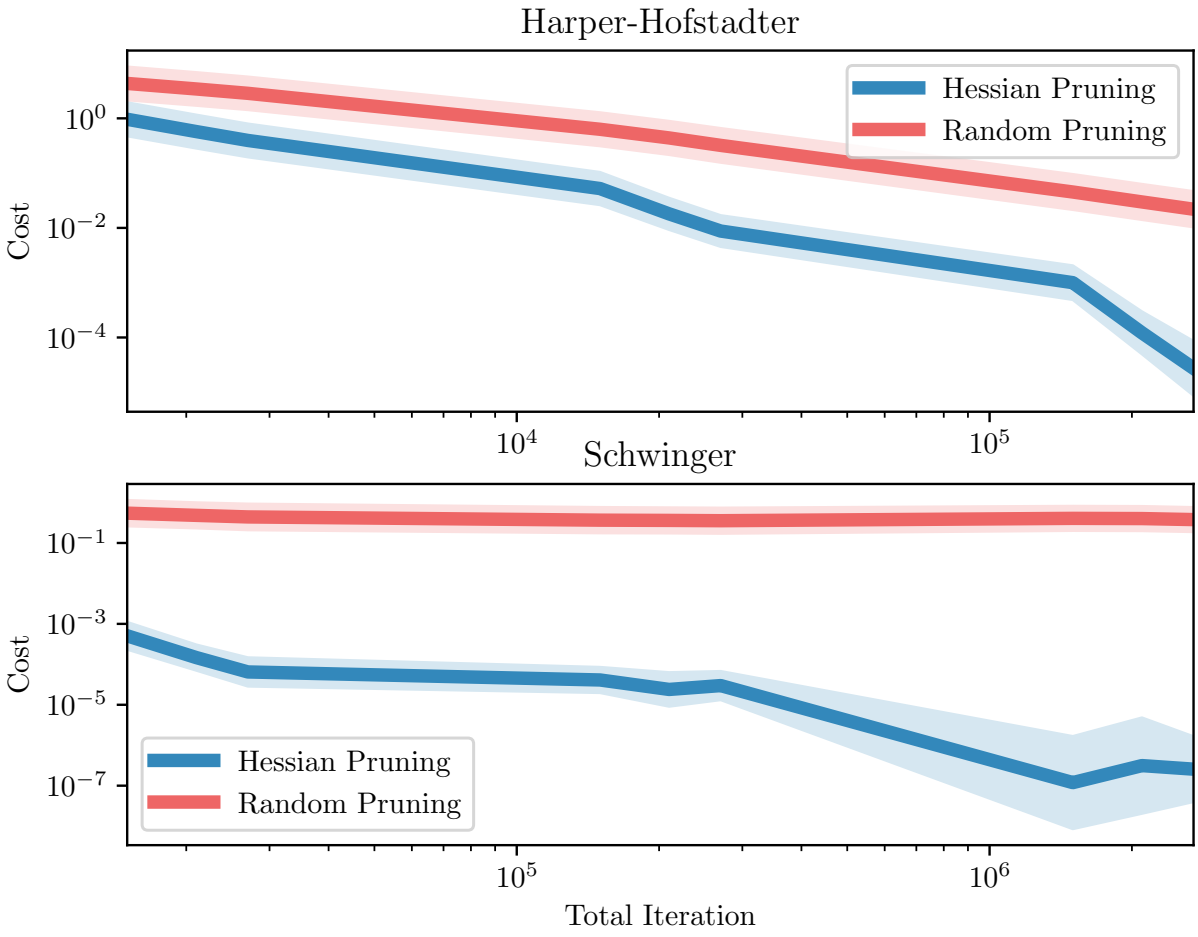

Figure 5.4: **Convergence Rate.** The impact of the total optimization iterations on the reconstruction error for two pruning strategies with Hessian and random masks, each with 50% pruning has been illustrated. This is repeated for a coupling matrices inspired by both the Harper-Hofstadter (top) and Schwinger (bottom) models.

Chapter 6: Analog Quantum Simulator of a Quantum Field Theory with Fermion-Spin Systems in Silicon

"In the age of digital, being analog is a new luxury"

---

iCloude Shannon

6.1 Abstract

Simulating fermions coupled to spin degrees of freedom, relevant for a range of quantum field theories, represents a promising application for quantum simulators. Mapping fermions to qubits is challenging in $2+1$ and higher spacetime dimensions, and mapping bosons demands substantial quantum-computational overhead. These features complicate the realization of mixed fermion-boson quantum systems in digital quantum computers. We propose a native fermion–(large-)spin analog quantum simulator by utilizing dopant arrays in silicon. Specifically, we show how to use a dynamical lattice of coupled nuclear spins and conduction-band electrons to realize a quantum field theory: an extended Jackiw-Rebbi model involving coupled fermions and quantum rotors. We demonstrate the feasibility of observing dynamical mass generation and a confinement-deconfinement quantum phase transition in 1+1 dimensions on this platform, even in the presence of strong long-range Coulomb interactions. Furthermore, we employ finite-

temperature Hartree-Fock-Bogoliubov simulations to investigate the dynamics of mass generation in two-dimensional square and honeycomb arrays, showing that this phenomenon can be simulated with realistic experimental parameters. Our findings reveal two distinct phases, and demonstrate robustness against the addition of Coulomb interactions. Finally, we discuss experimental signatures of the phases through transport and local charge sensing in dopant arrays. This study lays the foundation for quantum simulations of quantum field theories exhibiting fermions coupled to spin degrees of freedom using donors in silicon.

6.2 Introduction

Understanding the origin of the mass of elementary and composite particles has long driven the field of particle and hadronic physics. A spontaneous symmetry breaking of gauge symmetries via the Higgs mechanism gives rise to the mass of elementary particles in the Standard Model [148, 149], while spontaneous breaking of a chiral symmetry greatly influences the spectrum of hadrons in quantum chromodynamics (QCD) [150–152]. Despite this understanding, a complete picture of dynamical mass generation in QCD in, e.g., systems with nonzero fermion density and/or in out-of-equilibrium conditions, and the connection between chiral symmetry breaking and confinement-deconfinement phase transition, are yet to be developed [153–156]. While the method of lattice QCD with the aid of classical computing has opened the door to illuminate part of this picture [157–160], some questions remain intractable classically. Quantum simulation of quantum (gauge) field theories [161–166] provides a unique avenue to explore inherently quantum, nonperturbative, and dynamical phenomena such as quantum phase transitions and mass generation in QCD and other strongly-coupled quantum field theories. We aim to introduce

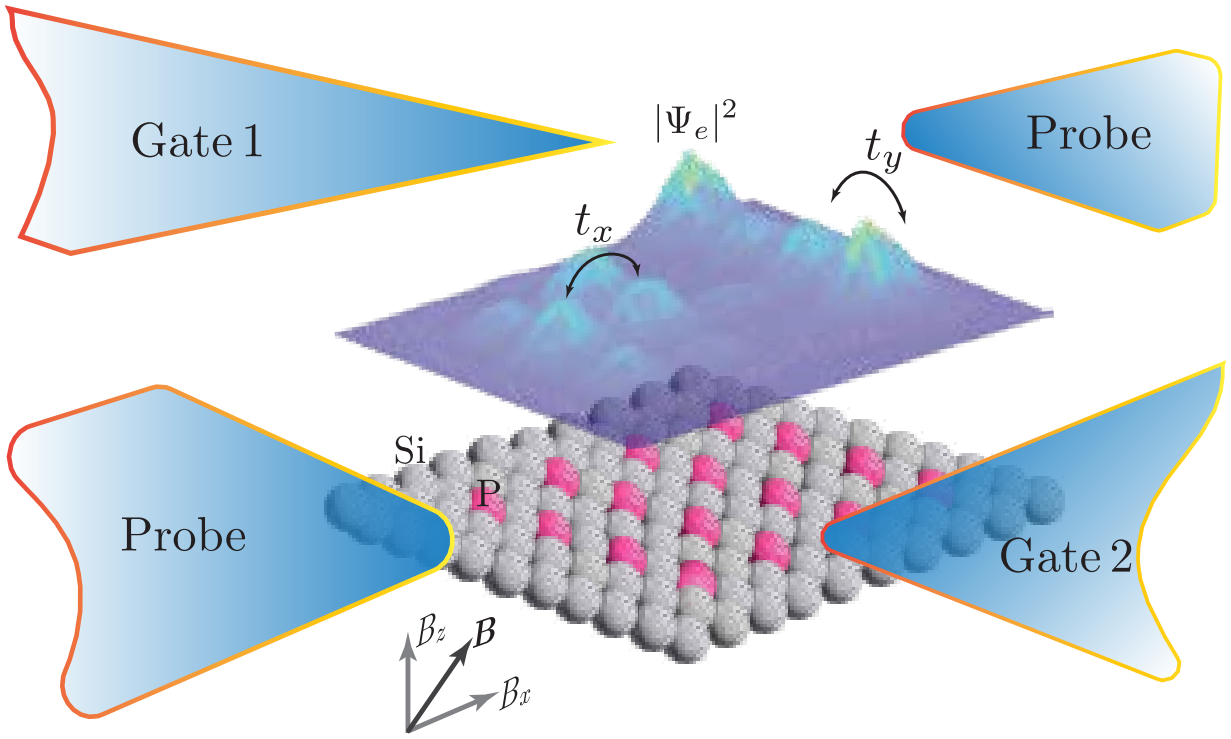

Figure 6.1: **Donor array in silicon.** A schematic illustrating electron localization and tunneling behaviors in a silicon phosphorus-donor array. The lattice model approaches continuity as donor distance tends to zero and lattice size tends to infinity. Electrons can hop in both x and y directions with tunneling rates t_x and t_y. An external magnetic field, $\boldsymbol{B}$, can be applied to polarize electrons in a given direction. The probes (charge or conductance), along with gates, allow indirect inference and control of the internal electron-density configuration, $|\Psi_e|^2$, within the central island, facilitating a comprehensive understanding of electron behavior and phases of the system in the donor lattice structure.

a solid-state analog quantum simulator to explore such questions in a quantum field theory, setting the stage for future experimental implementations.

A range of models for mass generation have been proposed, such as the Nambu model and the Gross-Neveu model [150, 151, 167–171], allowing for qualitative understanding in systems that are simpler to study. An especially important case is *dynamical* mass generation, where mass in the fermion field arises from the spontaneous breakdown of chiral symmetry [167, 170, 172, 173], which may be observed when the confinement-deconfinement phase transition is crossed. One of the simplest models which has been shown to capture the physics of dynamical

mass generation and the confinement-deconfinement quantum phase transition is the Jackiw-Rebbi model [174, 175]. This model consists of matter particles interacting with a dynamical lattice, i.e., a lattice hosting dynamical bosons, see Fig. 6.2. A first analog-quantum-simulation proposal for simulating the Jackiw-Rebbi model in (1+1)D was developed in Ref. [175], but higher dimensional versions were left unexplored. Digital quantum computation could simulate this model using a Jordan-Wigner mapping of fermions [176–179], and e.g., a binary mapping of bosons [180], to qubits, and by digitizing the time-evolution operator in terms of a universal set of gates. These approaches, therefore, demand a large computational overhead and a high level of quantum control. By contrast, analog quantum simulations can produce faithful results, often by a natural mapping of degrees of freedom and by allowing for a continuous evolution. Therefore, finding an analog-simulation method using native fermionic and bosonic matter would greatly improve the scalability of the simulation of the Jackiw-Rebbi model and other quantum field theories in the near term.

We propose a (1+1)D and (2+1)D native fermionic-bosonic platform for quantum simulation of the rotor Jackiw-Rebbi model, based on donors in silicon (see Fig. 6.1). The fermionic degrees of freedom are directly encoded in conduction-band electrons that populate the array, removing the necessity to map fermions to qubits. Dynamical lattices with large local Hilbert-space dimensions are achieved using the local nuclear-spin degree of freedom of the dopants, which range from $\frac{1}{2}$ (P), over $\frac{7}{2}$ (Sb) [181] to $\frac{9}{2}$ (Bi) depending on the choice of dopant atom. This platform has recently been used to simulate small instances of the extended Fermi-Hubbard model in (2+1)D [182–185] and the Su-Schrieffer-Heeger model [186, 187].

These results, in conjunction with similar demonstrations [188, 189], show that scanning tunneling microscopy (STM) lithography can be used to fabricate and probe arrays of dopants

with sub-nanometer precision for applications in quantum simulation [190, 191]. Crucially, the nuclear and electron spins in these systems show extremely long coherence times [192] and, following theoretical proposals [193–198], high-fidelity quantum-information-processing applications have been demonstrated experimentally [199–201]. Dopants in silicon, therefore, exhibit the coherence properties required for high-fidelity quantum simulations. Although current technology is limited to relatively modest lattice sizes on the order of ten sites, progress in fabrication techniques, particularly those demanding atomic precision, have been demonstrated [191, 202, 203]. Moreover, advancements in external gates enable local electrical control of the donor charge states [199, 201].

We show how to map a rotor Jackiw-Rebbi model to a donor platform (see Fig. 6.2), and estimate the parameter regimes in which a faithful simulation can be achieved. We perform exact and approximate (using the Hartee-Fock-Bogoliubov method) numerical simulations to predict phenomena that could be observed in (1+1)D and (2+1)D. In this way, we map out the phase diagram of the model and identify the occurrence of dynamical mass generation, confinement-deconfinement transition, and the effect of thermal fluctuations on chiral-symmetry restoration. Finally, we discuss how these phenomena could be probed in donor-array simulators by local charge sensing and transport measurements. Our experimental and theoretical advances set the stage for future quantum simulations of lattice gauge theories in donors in silicon.

This work is organized as follows. In Sec. 6.3, we introduce the rotor Jackiw-Rebbi model, the donor platform along with its intrinsic Hamiltonian, and the reasoning for why this platform can be thought of as an analog quantum simulator of the rotor Jackiw-Rebbi model. In Sec. 6.4, we investigate the properties of the (1+1)D system and benchmark our results against the findings of Ref. [175]. We further investigate the effect of Coulomb interactions on phases of

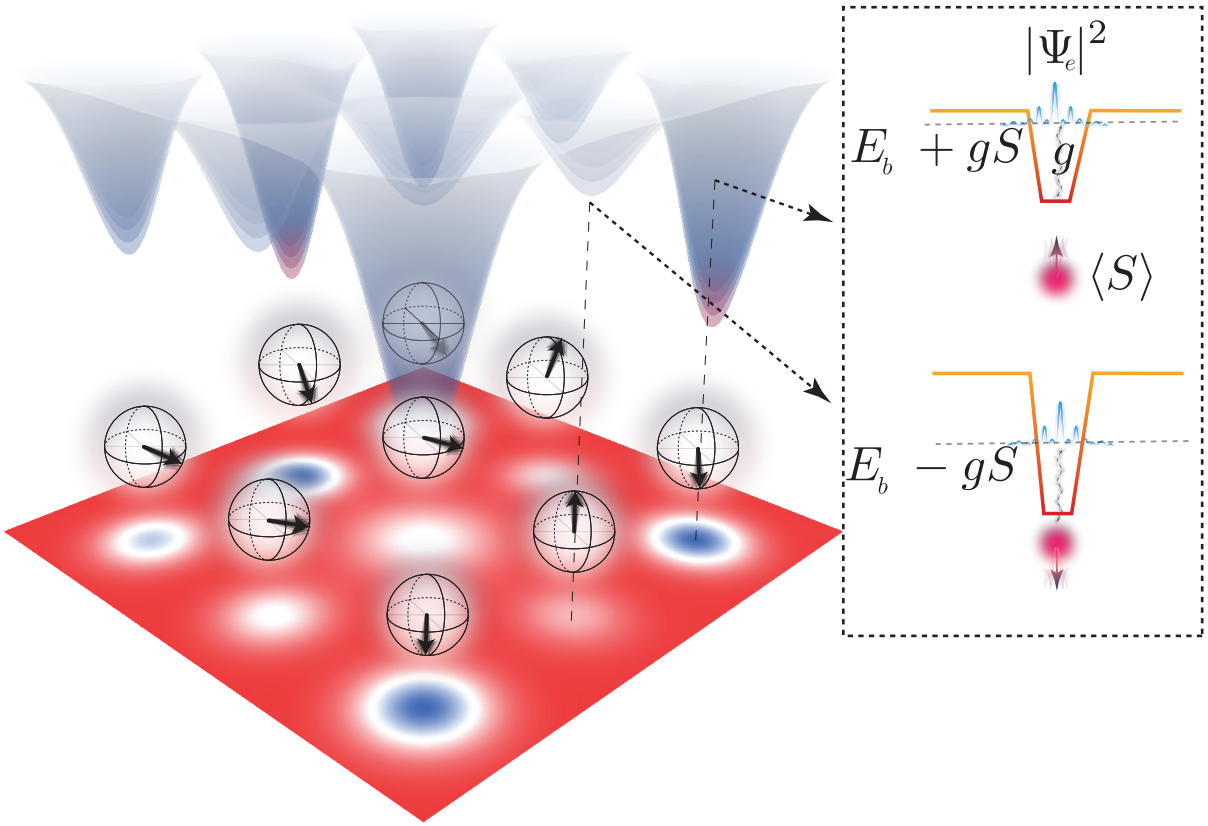

Figure 6.2: **Schematic of a dynamic lattice.** Each individual donor nuclear-spin orientation (illustrated on the Bloch sphere) can dynamically change and locally alter the potential landscape at each fermionic donor-electron site, acting as a dynamical mass term akin to a Jackiw-Rebbi rotor coupled to fermionic matter. Each spin, $\boldsymbol{S}$, which in our platform is represented by the nuclear spin of a donor, interacts with the local density of fermions, $|\Psi_e|^2$, via the hyperfine interaction with strength g. Depending on the orientation of the nuclear spin at each site, the energy level of the system at each site is in the range of $E_b \pm gS$, where E_b represents the binding energy of the electron and nuclear spin.

the model. Next, in Sec. 6.5, we delve into the phase diagram of the (2+1)D array and explore the phenomenon of dynamical mass generation in this extended model. Finally, in Sec. 6.6.2, we discuss the experimental feasibility of detecting the discussed phases in donor arrays by focusing on suitable observables.

6.3 Donors in silicon as an analog quantum simulator of the rotor Jackiw-Rebbi model

In this work, we lay out the reasoning for why donor arrays in silicon provide benefits for the simulation of (lattice) quantum field theories containing fermions and bosons. In particular, we focus on the physics of fermionic systems with a dynamical mass generated from interactions with bosonic degrees of freedom. As a first step, we focus on a proposal for simulating the rotor Jackiw-Rebbi model in (1+1)D and (2+1)D. A proposal for implementing the (1+1)D model using ultra-cold atoms in optical lattices was developed in Ref. [175], which, nonetheless, involved mapping the model to a fully bosonic quantum simulator. In contrary, the fermion-boson simulator of this work provides a more natural path to quantum simulation of the rotor Jackiw-Rebbi model in future implementations.

6.3.1 Model Hamiltonian

Consider a massless Dirac-fermion field Ψ and its adjoint $\overline{\Psi} = \Psi^\dagger\gamma^0$ in $d+1$ spacetime dimensions with $d = 1, 2$. The Dirac gamma matrices satisfy $\{\gamma^\mu, \gamma^\nu\} = 2g^{\mu\nu}$ (under spacetime metric $g^{00} = 1, g^{ii} = -1$ with $i = 1, \cdots, d$). Consider also the vector fields $\boldsymbol{\phi}$ and $\boldsymbol{\ell}$, representing the orientation of a quantum rotor and its angular momentum, respectively. As will be explained in Sec. 6.3.3 and Appendix C.1, in an equivalent lattice formulation, $\boldsymbol{\phi}$ captures the Néel alternation of antiferromagnetic ordering between spins at neighboring lattice sites while the presence of $\boldsymbol{\ell}$ also allows for slow spin fluctuations with respect to uniform ordering. The continuum Hamiltonian

of a corresponding lattice model we aim to study is:

$$H^{(\mathrm{RJR})} = \int d^d x \Big\{ \Big[- ic\overline{\Psi}(\boldsymbol{x})\gamma^i \partial_i \Psi(\boldsymbol{x}) \\ - \overline{\Psi}(\boldsymbol{x}) \big[\boldsymbol{g} \cdot \boldsymbol{\phi}(\boldsymbol{x}) + \gamma^0 \boldsymbol{g} \cdot \boldsymbol{\ell}(\boldsymbol{x}) \big] \Psi(\boldsymbol{x}) \\ - \boldsymbol{h} \cdot \boldsymbol{\ell}(\boldsymbol{x}) \Big] \Big\}. \tag{6.1}$$

The first term in Eq. (6.1) is the free-fermion Hamiltonian, the second term describes the interactions of fermions with bosonic quantum rotors via the coupling vector $\boldsymbol{g}$, and the last term is responsible for rotor's precession in a uniform magnetic field $\boldsymbol{h}$. In (1+1)D, the Hamiltonian is invariant under a discrete chiral transformation, $\Psi \to \gamma^5 \Psi$, with $\gamma^5 = i\gamma^0\gamma^1 = i\sigma^z$, if $\phi = 0$. Such a symmetry gets broken spontaneously if $\langle \phi \rangle \neq 0$, hence generating a dynamical fermion mass in the model. In (2+1)D, no chirality can be defined but the Hamiltonian with $\phi = 0$ is invariant under another discrete transformation, i.e., spatial reflection, that only changes the sign of one of the two components of the position vector, e.g., $x_1 \to -x_1$, transforming the fermion field as $\Psi \to \gamma^1 \Psi$. Again, if $\langle \phi \rangle \neq 0$, such a symmetry gets broken spontaneously, generating a dynamical fermion mass.

The model described by the Hamiltonian in Eq. (6.1) can be identified as a variant of the Jackiw-Rebbi model, as introduced in Ref. [175]. In the original Jackiw-Rebbi model [174], fermions interact with a self-interacting scalar field. In the model considered here, called rotor Jackiw-Rebbi model, fermions interact with rotor fields, and these rotors exhibit no self interactions. This distinction is significant: in the Jackiw-Rebbi model, the contribution from the scalar field to the generation of dynamical mass through symmetry breaking can be explained classically, but this is not the case in the rotor Jackiw-Rebbi model. This model, in fact, bears a stronger

resemblance to the Gross-Neveu models, although without an $O(\mathbb{N})$ symmetry [204].

Due to intrinsically quantum and nonperturbative spontaneous symmetry breaking and dynamical mass generation in the rotor Jackiw-Rebbi model, one needs nonperturbative simulation tools to study model's phases. In this model, spontaneous symmetry breaking turns out to occur within a specific range of external magnetic fields. As is shown in Ref. [175] for the (1+1)D model, the range is notably dependent on a function which cannot be approximated by a Taylor expansion for small but nonzero rotor-fermions coupling. A similar behavior is expected in (2+1)D, as is studied in this work. In the subsequent sections, we will explore in detail how a dopant analog quantum simulator can effectively implement a lattice-discretized version of the rotor Jackiw-Rebbi model in both (1+1)D and (2+1)D.

6.3.2 Simulator Hamiltonian

To investigate how the proposed dopant array, as illustrated in Fig. 6.1, can be used to probe the physics of dynamical mass generation in the rotor Jackiw-Rebbi model, we begin by introducing the platform and its intrinsic Hamiltonian.

To prepare a donor array, first, standard semiconductor processing techniques are used to create a clean surface. The dopant atoms are then incorporated into the surface using scanning-tunneling-microscope hydrogen lithography techniques [205, 206]. Following the incorporation of the dopants, silicon is grown over the array to encapsulate the donors and hold them in place, as well as allow further lithography of metallic top gates. This protected and contollable lattice of dopants then creates a new band structure within the band gap of the underlying silicon crystal. Electrons moving in this dopant lattice can, therefore, be seen as an analog to cold

atoms hopping in an optical lattice, with the silicon lattice only participating as a dielectric, but otherwise being inert. This analogy has opened up the demonstration of this platform as a novel native fermionic quantum simulator with an early application to simulate the Fermi-Hubbard model [1] and beyond [182, 183, 185, 188]. Furthermore, electrons interact with themselves and with the dopant nuclei via Coulomb interactions, and both electron and nuclear spin respond to external magnetic fields. Importantly, the electron spin couples to the nuclear spin via a hyperfine interaction.

Let us discuss these interactions in more detail. The intrinsic Hamiltonian of the dopant analog quantum simulator can be decomposed to

$$H^{(\text{lattice})} = H_\mu + H_\text{k} + H_\text{ff} + H_\text{sf} + H_\text{s}. \tag{6.2}$$

The chemical-potential term, denoted as H_μ, represents the onsite binding energy, E_b, of a single electron to a dopant in the absence of tunneling. By carefully adjusting the energy level of the system to be near the Fermi level, one can control the total electron occupancy in the system. The other contribution to the onsite energy term comes from the local Coulomb potential between the electron and the nuclei of the dopants within the array. Additionally, there is another contribution to the overall electric potential, resulting from the gates and other charges

[1] The effective donor Hubbard model in silicon crystals has parameters significantly smaller than those in the crystal itself. This means modest physical temperatures correspond to extremely low temperatures in Hubbard parameter units. For instance, the on-site Coulomb interaction is less than 400 K. Additionally, the capacity for transport measurements and strong, adjustable long-range Coulomb interactions make this platform a viable alternative to studying the Hubbard model, compared to cold atoms in optical lattices.

surrounding the system, denoted by ϵ [183]. Overall, H_μ can be written as

$$H_\mu = \sum_i \sum_\sigma \left[\big(- E_{b,i} + \epsilon_i \big) c^\dagger_{i,\sigma} c_{i,\sigma} + \sum_{j \neq i} V_{0,ij} c^\dagger_{i,\sigma} c_{i,\sigma} \right]. \tag{6.3}$$

Here, $c^\dagger_{i,\sigma}$ and $c_{i,\sigma}$ represent the electron's creation and annihilation operators, respectively. $\sigma = \uparrow, \downarrow$ is the spin index of the electron, and i denotes the site index within the d-dimensional array with given geometry. For example, this index ranges from 1 to $N = N_s^d$ on a square lattice with side length $L = aN_s$ and lattice spacing, or constant, a. $V_{0,ij}$ represents the strength of electric potential at site i, created by the nucleus at site j. We approximate the interaction potential by $V_{0,ij} = V_0 e^{-\lambda |\boldsymbol{r}_i - \boldsymbol{r}_j|} / |\boldsymbol{r}_i - \boldsymbol{r}_j|$, where the constant term $V_0 = 1/(4\pi\epsilon_0\epsilon_{\text{si}})$ reflects the permittivity of the electric field in silicon, ϵ_{si}, and λ determines how the electric field is reduced due to screening [183, 185, 207]. $\boldsymbol{r}_i$ denotes the position vector of site i.

The kinetic term H_{k} describes the hopping of electrons between neighboring sites in the array. In this study, we assume that the hopping strength can be engineered to be uniform across the system, which demands an atomically precise placement of the donors. In general, the hopping strength decays exponentially with distance, so we restrict this study to nearest-neighbor hopping of strength t:

$$H_{\text{k}} = -t \sum_{\langle i,j \rangle} \sum_\sigma c^\dagger_{i,\sigma} c_{j,\sigma} + \text{h.c.} \tag{6.4}$$

H_{ff} represents the fermion-fermion interaction in the system. This interaction can be modeled as the sum of two components: the Coulomb interaction between fermions across the array and the onsite interaction between two electrons with opposite spins. The strength of the

latter interaction is denoted by U_i:

$$H_{\text{ff}} = \sum_i \left[\sum_{j \neq i} \sum_{\sigma} V_{0,ij} n_{i,\sigma} n_{j,\sigma} + U_i n_{i,\uparrow} n_{i,\downarrow} \right], \tag{6.5}$$

where $n_{i,\sigma} c^\dagger_{i,\sigma} c_{i,\sigma}$ is the number operator for a fermion with spin σ at lattice site i.

H_{sf} represents the most crucial term of relevance to the model we aim to study. It involves the interaction of the dopant nuclear spin $\boldsymbol{I}$ with the electrons,

$$H_{\text{sf}} = g \sum_i s^z_i I^z_i. \tag{6.6}$$

Here, the parameter g represents the hyperfine coupling, and $s^z_i c^\dagger_{i,\uparrow} c_{i,\uparrow} - c^\dagger_{i,\downarrow} c_{i,\downarrow}$ is the electron-spin operator along the z direction. The electrons will be assumed to be spin-polarized in this direction by an external magnetic field, $\boldsymbol{B}$.

We allow for a transverse magnetic field, h_x, arising from time-dependent Nuclear Magnetic Resonance (NMR) control. This leads to an effective Hamiltonian in the rotating frame of the nuclear spins:

$$H_{\text{s}} = -\sum_i \boldsymbol{h} \cdot \boldsymbol{I}_i + \sum_i h_e s^z_i. \tag{6.7}$$

Here, the first term is the rotating-frame Hamiltonian for the nuclear spins in the presence of the NMR drive with the magnetic field in the form of $\boldsymbol{h} = h_z \hat{\boldsymbol{z}} + h_x \hat{\boldsymbol{x}}$. We will work in the limit of a large drive detuning, where $|h_z| \gg |h_x|$. Given this condition, we omit the effect of the transverse magnetic field, h_x, on the electrons. We assume that in this regime, the spin polarization of electrons due to the transverse magnetic field remains constant and is negligible. Finally, h_e is the Zeeman splitting of the electron spin.

In the above Hamiltonian, we work in a configuration where the electrons' spins are polarized in the $|\downarrow\rangle$ direction (see Sec. 6.6.2 for how to create such a polarization). In this case, the spin drops out of the Hamiltonian terms and one gets

$$\begin{aligned} H^{(\text{lattice})} = & -t \sum_{\langle i,j \rangle} \left(c_i^\dagger c_j + \text{h.c.} \right) - \sum_i \mu_i c_i^\dagger c_i \\ & - \sum_i \left(g c_i^\dagger c_i I_i^z + \boldsymbol{h} \cdot \boldsymbol{I}_i \right) \\ & + \sum_i \sum_{j \neq i} V_{0,ij} c_i^\dagger c_i c_j^\dagger c_j . \end{aligned} \tag{6.8}$$

Here, c_i ($c_i^\dagger$) denotes annihilation (creation) operator for the down-spin electron at site i and $\mu_i = E_{b,i} - \epsilon_i - \sum_{j \neq i} V_{0,ij}$. Note that since the total number of electrons in each spin state is conserved, the last term in Eq. (6.7) contributes trivially to the dynamics and is dropped. In the subsequent sections, we explore the connection between this lattice Hamiltonian and the rotor Jackiw-Rebbi model.

6.3.3 The connection between the Rotor Jackiw-Rebbi model and the lattice model

Standard techniques can be employed to map the low-energy limit of a lattice theory of fermions and spins to a continuum quantum field theory, see Ref. [175] and Appendix C.1.

Let us first consider the free-fermion Hamiltonian. Here, we assume a uniform electron chemical potential throughout the lattice such that $\mu_i \mu$ is constant. We further assume a fermionic state with half filling, i.e., $\frac{1}{N} \sum_i \langle c_i^\dagger c_i \rangle = \frac{1}{2}$. There is a quantum field theory describing low-energy excitations around the Fermi points (surface). In (1+1)D, this means linearizing the

dispersion relation $\epsilon(k) = -2t\cos(ka)$ near two (free-fermion) Fermi points at $k_F = \pm\frac{\pi}{2a}$, i.e., $\epsilon(k) \approx (|k| - k_F)v_F$, with the Fermi velocity defined as $v_F 2ta$. By this approximation, the fermionic operators c_i in (1+1)D are reduced to left- and right-moving slowly varying fermion fields, $\psi_+(x)$ and $\psi_-(x)$. These fields map to the staggered lattice fermions of Kogut and Susskind [208] (see Ref. [175]), which is a lattice discretization of the continuum Dirac fermions in Eq. (6.1), upon the identification $\Psi = (\psi_+ \ \psi_-)^T$ and $c = v_f$.

On a (2+1)D square lattice, the (free-fermion) Fermi surface is the boundary of the diamond shape $-\frac{\pi}{\sqrt{2}a} < k_\pm \leq \frac{\pi}{\sqrt{2}a}$ within the Brillouin zone, where $k_\pm = \frac{1}{\sqrt{2}}(k_x \pm k_y)$. Linearizing around this boundary does not give rise to the Dirac fermions of the continuum as is known. Nonetheless, as shown in Appendix C.1 and Sec. 6.5, due to the Fermi Surface admitting a nesting vector at momentum $(\pi/a, \pi/a)$, a Néel-order phase arises in this model too, generating dynamical mass for the fermions. The two-component Ψ field can be understood as pairs of lattice fermions on adjacent sites along the x direction, hence breaking the reflection symmetry [2] discussed in Sec. 6.3.1 in the Néel phase, see Appendix C.1. Alternatively, to recover the continuum Dirac theory in Eq. (6.1), fermions can be placed on a honeycomb lattice. On such a lattice, upon the linearization of the dispersion function, one arrives at $\varepsilon(\boldsymbol{k}) = -v_F \boldsymbol{\kappa} \cdot \boldsymbol{\gamma}$, where $\boldsymbol{\kappa}$ is a small momentum around the Fermi points $\boldsymbol{K}$ and $-\boldsymbol{K}$ with $\boldsymbol{K} = \frac{2\pi}{3a}(1, \frac{1}{\sqrt{3}})$. This recovers the Dirac free-fermion theory upon the identification $c = v_F$ and

$$\Psi = \begin{pmatrix} c_{\pm\boldsymbol{K}+\boldsymbol{\kappa},A} \\ \\ -c_{\pm\boldsymbol{K}+\boldsymbol{\kappa},B} \end{pmatrix} \tag{6.9}$$

around the Fermi points $\pm\boldsymbol{K}$. Here, $c_{\boldsymbol{k},A}$ and $c_{\boldsymbol{k},A}$ are the Fourier transform of the c_i operators

[2] Or in this case, translational symmetry along the x direction.

defined on sublattices A and B of the honeycomb lattice, respectively (see Appendix C.1 for details).

To achieve a low-energy quantum field theory of nuclear spins on the lattice, i.e., a long-wavelength large-spin limit, a continuum field of unit length, $\boldsymbol{\phi}$, can be introduced such that it varies slowly on the scale of a lattice spacing. To allow for a quantum disordered phase with no long-range spin order, it is imperative to also include a component of the spins which is perpendicular to the local orientation of the Néel order, which is denoted by the continuum field $\boldsymbol{\ell}$, as discussed in Appendix C.1. Formally, this can be described as

$$\boldsymbol{I}(\boldsymbol{r}_i) \simeq S\left[\delta_i \boldsymbol{\phi}(\boldsymbol{r}_i)\sqrt{1-a^{2d}\boldsymbol{\ell}^2(\boldsymbol{r}_i)} + a^d \boldsymbol{\ell}(\boldsymbol{r}_i)\right] \tag{6.10}$$

such that $\boldsymbol{\phi}\cdot\boldsymbol{\phi}=1$, $\boldsymbol{\phi}\cdot\boldsymbol{\ell}=0$, and $a^{2d}\boldsymbol{\ell}^2 \ll 1$. Here, δ_i is either 1 or -1 depending on which sublattice, A or B, $\boldsymbol{r}_i$ belongs to, see Ref. [209] for more details.

As shown in Appendix C.1, the low-energy excitations of fermions near the Fermi surface are mediated by the rotors in either the Néel-order phase or the disordered phase. Hence, the hyperfine coupling of nuclear spins to electrons maps to the fermion-rotor interactions in the rotor Jackiw-Rebbi model. Additionally, the nuclear-spin interactions in presence of the NMR drive are naturally reduced to the last term in $H^{(\mathrm{RJR})}$ in Eq. (6.1). Finally, while electron-electron Coulomb interactions do not have an equivalent low-energy description in the rotor Jackiw-Rebbi model, as our numerics show, these interactions do not affect qualitative features of the phases of the model and the dynamical mass generation when experimental parameters are concerned.

With the connection between the (discretized) rotor Jackiw-Rebbi model and the lattice model accessible in the quantum simulator established, we are ready to delve into the study of

the properties and different phases exhibited by the lattice model.

6.4 Phenomenological study of the model in (1+1)D

To investigate the quantum many-body system described by the simulator Hamiltonian in Eq. (6.8), one might consider employing exact diagonalization (ED) techniques. However, the dimensionality of this Hamiltonian grows exponentially with the system size, making the application of ED with available classical computational resources feasible only up to $O(10^1)$. To produce more accurate high-L/a results, studies on system with larger sizes are required. While well-known efficient methods like density-matrix renormalization group (DMRG) [210] and tensor networks [211] are suitable for the (1+1)D cases, extending these methods to (2+1)D has proven challenging. To address this challenge, albeit with a modest sacrifice in accuracy, we have employed the mean-field approach of Hartree-Fock (HF) [212] and finite-temperature Hartree-Fock-Bogoliubov (FTHFB) [213]. These enable the exploration of larger systems with a computational complexity proportional to the system size $O(N)$. Comparing the results obtained from the HF approximation with those from ED for systems up to $O(10)$ lattice sites, we have nonetheless demonstrated that the mean-field approach is a reliable method of approximation, even when considering small values of dopant spin, S. As the system size increases, i.e., in the limit of large L/a and large S, a previous study [175] shows that the mean-field predictions can converge to the exact methods smoothly.

6.4.1 Dynamical mass generation

To study the distinct phases of the lattice model in Eq. (6.8), we can explore the phase space in terms of a set of macroscopic parameters, including hyperfine coupling and the external

longitudinal and transverse magnetic fields, which are denoted respectively as (g, h_z, h_x). We will also investigate the impact of these parameters on the transition between possible phases for given fixed values of dopant spin, tunneling coupling, the temperature of the reservoir surrounding the system, Coulomb-force coupling, chemical potential, and lattice constant, denoted respectively as (S, t, T, V_0, μ, a). The list of parameters has been provided in Appendix. C.6. The boundary condition is another factor that needs to be set in the simulation. We have investigated the effects of open and periodic boundary conditions and found that the periodic one can better mitigate the (undesired) effects of Coulomb interactions. Thus, in this work, we present results concerning the periodic case.

Our numerical simulations reveal that modulating the macroscopic parameters gives rise to two distinct phases within the system, characterized by the phenomenon of dynamical mass generation. Building upon the method described in Ref. [175], we utilize the modified Néel-order parameter, denoted as n_z, as the principal observable to investigate spontaneous symmetry breaking in the phase diagram and to distinguish between different phases. The parameter n_z is defined as

$$n_z \frac{1}{N} \sum_{i=1}^{N} \frac{1}{S} \left(\langle S_1^z S_{2i}^z \rangle - \langle S_1^z S_{2i-1}^z \rangle \right), \tag{6.11}$$

where i denotes the index of the lattice site, N is the total number of lattice sites, and S_i represents the spin of the dopant at location i in the array. Our numerical simulations, conducted using the mean-field HF method, demonstrate the existence of two distinct phases for the (1+1)D lattice model. This phase diagram is presented in Fig. 6.3 (see Appendix C.2 for more details). The phase diagram is derived at zero temperature and one electron above the half-filling state, for a

wide range of gS/t and h_zS/t, and a fixed nonzero transverse magnetic field h_x and given the Coulomb interaction with strength V_0.

The first phase, termed the 'trivial phase', is characterized by all spins being polarized and aligned with the external magnetic field. This alignment results in a zero value for n_z. In this configuration, the fermion density across the system is found to be distributed around half-filling for all lattice sites, indicating the absence of dynamical mass terms in Eq. (6.1). In this phase, the fermions are massless, thereby exhibiting chiral symmetry. This state of the system is analogous to the Luttinger-Liquid (LL) phase for fermions in (1+1)D. In contrast, the 'nontrivial phase' emerges within a specific range of macroscopic parameters, where n_z departs from zero. The corresponding fermion density across the system indicates the presence of dynamical mass generation. As discussed in the preceding section, chiral symmetry is spontaneously broken in this phase, and the system settles into one of the ground states.

6.4.2 Confinement/deconfinement of fractionally charged quasi-particles

To investigate the phenomenon of confinement and deconfinement of fractionally charged fermions coupled to the Néel field, it is essential to introduce a pinning potential as an impurity to break the translational symmetry. By adopting the method detailed in Ref. [175], we add a pinning potential, $H_\epsilon = -\sum_{i=1}^{N} \varepsilon_i(d) S_i^z$, which can lead to fermions localizing at the lattice

positions i_0 and $i_0 + d$ for a certain range of $h_z S/t$ and gS/t. Here,

$$\varepsilon_i(d) = \begin{cases} \varepsilon(-1)^i & 1 \leq i < i_0 \\ \varepsilon(-1)^{i+1} & i_0 \leq i < i_0 + d \\ \varepsilon(-1)^i & i_0 + d \leq i \leq N \end{cases} \tag{6.12}$$

for small pining potential strength $\varepsilon/t = 0.05$ compared to the tunneling coupling. Since the total extra fermionic density is equal to one electron, one can refer to this configuration as fractional charge since at each end, there is half of an electron localized.

To examine the system's dynamics, we calculate the static potential between two fractional charges, $V(d) = E(d) - E_\infty$, where E_∞ denotes the ground-state energy when $d \gg 1$. This analysis unveils two distinct, confined and deconfined, phases. The confined phase features an ascending static potential with respect to d, indicating the binding of fractional charges. In this model, the integer-charged fermion field couples to the rotors field, allowing, under certain conditions, the Néel field's configuration to host localized fractional charge, mirroring quark bags in the phenomenological models of QCD, where the quarks are confined within a finite region of space known as the 'bag' [214, 215] and make up pions, nucleons, and other hadrons. Conversely, the deconfined phase shows a decreasing static potential, signifying no binding between fractional charges. Figure 6.4 illustrates these phases, emphasizing that they can occur even amidst Coulomb repulsion in a silicon platform, highlighting the unique interplay between fractional charges and the Néel-field configuration. In this plot, we choose two coupling strengths: one assuming the Coulomb interaction does not exist, $V_0/(at) = 0$, and the second one with the highest value of $V_0/(at) = 3.6$ for silicon with fixed $a = 4.7$ nm and $t = 7.5$ meV,

which are chosen close to experimentally favorable numbers.

6.5 Phenomenological study of the model in (2+1)D

In the subsequent section, we examine evidence for the occurrence of dynamical mass generation and spontaneous symmetry breaking within the (2+1)D model. As mentioned before, the continuum physics of square and honeycomb lattice models are distinct, and only the latter recovers Dirac fermions of the Jackiw-Rebbi model. Nonetheless, we study both cases in the following.

6.5.1 Dynamical mass generation on a square lattice

We apply both ED for small systems and the HF method for larger systems to investigate phases of the lattice model on a square lattice for a range of macroscopic parameters. Our simulations demonstrate that a phase diagram akin to the one observed in the (1+1)D lattice can also be observed in (2+1)D. Figure 6.5 illustrates the phase diagram for a $N = 10 \times 10$ array obtained using the mean-field HF method.

To extend our study, we further consider the system at a finite temperature, $T1/\beta$, hence consider the thermal expectation value of the total number of fermions, denoted as $\sum_i \langle c_i^\dagger c_i \rangle_\beta$, where expectation value is with respect to the Boltzmann factor $e^{-\beta H^{(\text{lattice})}}$. This expectation value, when considering the grand canonical ensemble at a fixed temperature, becomes a function of the chemical potential, represented as μ.

As shown in Appendix C.3, achieving a half-filling state requires independent tuning of the chemical potential for a given temperature. Within our HF calculation, we have also checked if there is nonzero pairing in the (Bardeen–Cooper–Schrieffer) BCS channel. To start with, we

analyzed the quantity $\tilde{K}\frac{1}{N^2}\sum_{i,j} K_{ij}K_{ij}^*$ where $K_{ij}\langle c_i c_j\rangle_\beta$. The results, as shown in Fig. C.6 in Appendix C.3, demonstrate that the averaged pairing correlator $\langle c_i c_j\rangle_\beta$, remains zero throughout the entire range of chemical potentials and temperatures considered. However, the approximate HF method employed effectively only looks at Coulomb repulsion as a cause for pairing. The possible role of interactions between nuclear-spins and electrons in pairing is not addressed with this approximate method. Other studies [216–218] with a Hamiltonian that shares similar terms as our system indicate that pairing can occur at a certain range of Coulomb coupling and hyperfine coupling $V_0/g \ll 1$. This range is the opposite of the physical condition in the analog quantum simulator of this work, i.e., $V_0/g \gg 1$, and is hence not analyzed further.

Our investigation, according to Fig. 6.6, further reveals that as the temperature deviates from absolute zero, nontrivial phases gradually diminish, ultimately driving the quantum state towards a thermal state, as predicted. Under such circumstances, discrete reflection symmetry in (2+1)D is restored as the temperature rises, causing the fermionic field to revert to a zero-mass state. A similar effect can also be partially induced through the escalation of Coulomb interactions. Nonetheless, for the coupling strength V_0 from zero to the highest value of 123 nm $\cdot$ meV for silicon, the nontrivial Néel-order phase persists, even when considering nonzero temperatures. Finally, the transverse component of the external magnetic field, h_x, introduces fluctuations to the system. As illustrated in Fig. 6.6, increasing h_x has an effect qualitatively analogous to raising the temperature on the restoration of discrete reflection symmetry.

6.5.2 Dynamical mass generation on a honeycomb lattice

In this section, we aim to broaden our study to include another structure in the $(2+1)$D case, specifically focusing on the honeycomb lattice. On one hand, the continuum model of fermions on a honeycomb lattice is more tractable—its tight-binding model admits Dirac fermions like graphene. On the other hand, this structure is of significant interest considering previous research that explored the emergence of superconductivity in the behavior of the system when the ratio of V_0/g couplings falls within a certain regime [216–218]. In these lattice structures, phenomena similar to the confinement-deconfinement transitions observed in (1+1)D may be linked to superconductivity behavior and pairing mechanisms. Recent work in Ref. [219] on a Hamiltonian which incorporates similar interactions has shown signs of unconventional superconductivity, exhibiting staggered d-wave and f-wave pairings, along with topological superconductivity. This phenomenon can be compared to the confinement phenomenon observed in the (1+1)D case.

We apply our numerical procedure to the honeycomb lattice. Employing FTHFB simulations, while incorporating the presence of Coulomb interactions, we have examined the phase diagram for a wide range of $(gS/t, hS/t)$ parameters. We observe a pattern similar to the Néel order within a certain range of an external magnetic field as shown in Fig. 6.7.

Despite the observation of the two phases in this model, realizing the parameter regime relevant to the emergence of superconductivity [216–218] is very challenging because the hyperfine coupling that sets the strength of the sub-lattice potential needs to be comparable to the Coulomb-interaction strength. Instead, a more promising route to explore emergent superconductivity in this platform is to introduce a static sub-lattice potential using external gates or by controlling the number or type of dopant on each site. We leave the investigation of such extensions of our

model as an interesting avenue for future work.

6.6 Experimental Probing

In the following section, we investigate the experimental viability of observing the phase transition described in earlier sections in present doped semiconductor quantum simulators. It is crucial to establish this viability, as the desired phase transitions occur within certain ranges of model parameters that should be matched to the ranges accessible by current laboratory capabilities. Additionally, we discuss methods for preparing the initial state and detecting the system's phase, as well as other relevant observables within our proposed framework for two-dimensional dopant arrays. We remark that all the necessary ingredients for our proposal have been previously demonstrated in experiments with phosphorus donors in silicon [199, 201, 220, 221].

6.6.1 State preparation

The initial phase of an experimental investigation involves setting the system to a preferred initial state. In the magnetic-field range characterized by B, with electron and nuclear gyromagnetic ratios γ_e and γ_n, such that $\gamma_e B \gg g > 2\gamma_n B$, the eigenstates of the fermion–nuclear-spin system at each site, in the absence of hopping and Coulomb interactions, can be segmented into four distinct states. These are ordered from the lowest energy level to the highest as $|\downarrow, \Uparrow\rangle$, $|\downarrow, \Downarrow\rangle$, $|\uparrow, \Downarrow\rangle$, and $|\uparrow, \Uparrow\rangle$, where in this notation, the first spin represents the electron spin, and the second one the nuclear spin. To see the nontrivial phase in the rotor Jackiw-Rebbi model, we prepare the state at each site in the $|\downarrow, \Downarrow\rangle$ state, instead of the ground state, that is $|\downarrow\Uparrow\rangle$ at all sites. The electrons can be polarized to all-$|\Downarrow\rangle$ state using the strong magnetic field. To achieve the desired

spin configuration of nuclear spins, one can use the method that has been widely used for high-fidelity nuclear-spin control [220]. In this method, the nuclear spin can be read via the electron-spin-resonance (ESR) method with high fidelity. Depending on the orientation of the nuclear spin, the external magnetic field experienced by the electron will vary. This variation leads to different resonance frequencies, $\nu_e^{\pm} = \gamma_e B \pm g/2$, for the two distinct nuclear-spin orientations. As a result, it allows for the detection of nuclear-spin states, $|\Uparrow\rangle$ or $|\Downarrow\rangle$. After reading the nuclear spin with this method, if the spin is already polarized as $|\Downarrow\rangle$, no operation is needed, otherwise the nuclear spin on that site can be polarized to $|\Downarrow\rangle$ using NMR fields or using the electric-dipole spin resonance (EDSR) technique of Ref. [221]. This polarization process based on measurement and feedback would need to be repeated individually on each site or parallelized across the array. Alternatively, a more easily scalable approach for large systems is to place a single electron on each dopant site and use dynamical nuclear polarization (DNP) to simultaneously pump the nuclear spins to a polarized state [221, 222].

To engineer the right conditions for the rotor Jackiw-Rebbi model, after polarizing the nuclear spins, we need to change the electron occupation so that there is close to $\frac{1}{2}$ an electron for each dopant site. By choosing the detuning of the nuclear NMR field, one can also ensure that the correct sign of the h_z term is obtained to realize the symmetry-broken phase. Once these conditions are satisfied, we envision that the ground state could be adiabatically prepared by starting from a state with a large chemical-potential difference between each site and then slowly tuning these differences to zero. This can be achieved by controlling the voltages of the gates at each site. Alternatively, it would also be possible to start in a state with zero chemical-potential differences and adiabatically tune the sign of the NMR detuning from positive to negative values.

6.6.2 Accessible parameter regimes

In order to lay the groundwork for analyzing nonperturbative phenomena within (2+1)D systems, selecting simulation parameters that align with the experimental capability is critical. Moreover, the optimal set of parameters needs to be meticulously determined. In Ref. [185], the lattice constant, a, was explored within a range from 10 nm to 4 nm. We have chosen $a = 4.7$ nm for most of our simulations. Due to the oscillatory behavior of the electron's wave function and the exponential dependence of the tunneling rate on the lattice constant, an accurate value of the lattice constant is crucial in obtaining definitive results. Such a high level of control on the value of a has, nonetheless, been recently achieved [185]. With no adverse effects of disorder on resonant tunneling in the two-dimensional arrays, the dopant platform is favorable for studying models in (2+1)D [183].

The hyperfine coupling, which reflects the interaction of electron spin with nuclear spin, is almost a steady parameter (or can be slightly adjusted by applying a strong external electric field). Thus, the main macroscopic variable that allows one to feasibly access the full range of the phase diagram is the ratio of the hyperfine constant to the tunneling rate, g/t, while the external magnetic field can be varied from zero to a higher value. In the following, we discuss the experimental aspects concerning t and g.

Let us denote the tunneling rates between sites i and j as t_{ij}. For an electron at site i with wave function $|\psi_i\rangle$, we characterize the Coulomb potential, incorporating a screening factor λ, by the formula $U_i = -V_0 e^{-\lambda|\boldsymbol{r}-\boldsymbol{r}_i|}/|\boldsymbol{r}-\boldsymbol{r}_i|$. We further define the overlap of wave functions between sites i and j as $S_{ij} = \langle\psi_i|\psi_j\rangle$, and the potential energy due to the interaction at site j on an electron at site i as $V_{ij} = \langle\psi_i|U_j|\psi_i\rangle$. Further define $V'_{ij} = \langle\psi_i|U_j|\psi_j\rangle$. With these definitions,

one can calculate the tunneling rate t_{ij} using the expression $t_{ij} = (S_{ij}V_{ij} - V'_{ij})/(1 - S_{ij}^2)$, as detailed in Refs. [183, 223]. Given the wave function's exponential decay, it is reasonable to consider t_{ij} as approximately zero for sites that are more than two lattice constants apart. For simplicity, we assumed equal spacing along both directions of the lattice, which simplifies t_{ij} to t. In our simulations with spacing $a = 4.7$ nm, we have taken $t = 7.5\ \mathrm{meV}$, consistent with Ref. [183].

The tunneling rate and its profile are strongly influenced by silicon orientation. Silicon wafer orientation refers to the crystallographic directions and planes of the silicon crystal lattice. Each number in these orientations represents a Miller Index, which is a notation system in crystallography used to describe the orientation of planes within a crystal lattice. Among the three main orientations $[100]$, $[111]$, and $[110]$, the last is more favorable for experimental fabrications. To estimate the profile of tunneling as a function of the distance between two adjacent sites, one can use the effective-mass theory, as outlined in Refs. [224–226] and summarized in Appendix C.4.

The hyperfine coupling, g, and the hyperfine splitting energy of phosphorus are contingent upon the specific isotope of phosphorus. For instance, ^{31}P, the most prevalent isotope, has a hyperfine splitting energy approximately in the range of 114.3 MHz to 117 MHz. This coupling can be affected by the Stark shift, which varies as $g(\mathcal{E}) = g(0)(1 + 2.8 \times 10^{-3}\mathcal{E}^2)$ with $g(0) = 0.48\ \mu$eV for external electric field, $\mathcal{E}$ [227]. It can also be affected by other effects such as the engineering of the spin-orbit coupling for a given $\mathcal{E}$.

Having access to the full range of the phase space, we need to make sure h_z/t is of the same order as gS/t. The feasible region for observing the Néel phase in terms of lattice constant is depicted in Fig. 6.8 for the [100] silicon orientation. For the sake of completeness, other orientations are presented in Appendix C.4, Figs. C.8, and C.9. As observed in Fig. 6.8, for any

given lattice constant, there always exists a narrow corridor of external magnetic fields that enable the manifestation of the nontrivial phase in the experimental setup. This corridor is wider in the [111] orientation as shown in Appendix C.4.

Variation of gS/t during the experiment can be challenging. A more feasible approach is to keep gS/t fixed and vary the external magnetic field as a macroscopic parameter, which can still change the system's phase. In this scenario, we are limited to exploring one slice of the 2D phase diagrams studied in Sec. 6.4. Due to the small value of gS/t within the accessible range of parameters, $gS/t \sim 3.2 \times 10^{-5}$, experimental probing occurs at the corner of the phase diagram. Simulating this corner with the HF method is unreliable. However, the ED method for small arrays, as shown in Fig. 6.9, indicates that as long as $|h_x| \ll |h_z|$, in a region where $h_z S/t$ is comparable to gS/t, the Néel phase is expected to be observed. This is indicative of the robustness of nonperturbative phenomena in this system. The numerical simulation in Fig. 6.9(a) shows that for a lattice constant of $a = 4.7$ nm, we expect to observe the Néel phase when the magnetic field is around $1.5 - 2.5$ T. This range is feasible in the current experimental setups.

6.6.3 Probing the system

In this section, we continue our experimental feasibility study by exploring methods to detect the system and identify possible observables. The dopant array is surrounded by electrons from outside of array, which allows electrons to tunnel to the island of the array via source and drain probes. Due to this tunneling capability of the electrons and the system's finite temperature, the total electron count is not fixed.

One method for detecting the phase of a system involves using a global charge sensor.

Such a sensor, which could be a quantum dot situated nearby or a proximal metallic gate, is acutely responsive to changes in the surrounding charge environment. By meticulously tracking variations in the conductance of this sensor, it becomes feasible to discern the addition or subtraction of a single electron from the dopant array. This ability allows for the prompt and precise detection of both the total charge and its transitions. As demonstrated in Fig. 6.10, our numerical simulations for the (2+1)D system on a 2×2 square array reveal that the charge profiles, with respect to variations in g and h_z, are discernible, effectively differentiating between the trivial and nontrivial phases. This method serves as a valuable tool for distinguishing between the phases, thereby enhancing our understanding of the system's phase transition characteristics. A similar study for (1+1)D dimensions has been demonstrated in Appendix C.2, Fig. C.7.

Another method to analyze the state of the system involves investigating the linear conductance, denoted by G, in relation to the chemical potential, denoted by μ. Considering a two-dimensional array where the source and drain interact primarily with the array's leftmost and rightmost columns—and their interaction with the inner parts of the array decreases exponentially—we can illustrate how the dopant array interacts with the leads. This method has been reviewed in Appendix C.5. Our study shows that the pattern of linear conductance can differ depending on which of the two distinct phases the system is in. Nonetheless, the phase-discerning potential of this method is not as prominent as the charge-sensing method.

6.7 Conclusion and outlook

In this study, we proposed utilizing a solid-state framework, specifically a donor array in silicon, as a native fermionic-bosonic analog quantum simulator. The primary objective was to explore

this framework's applicability in studying relativistic phenomena in a quantum field theory, such as dynamical mass generation and confinement-deconfinement phase transitions.

Our study focused on the lattice representation of the rotor Jackiw-Rebbi model. Using numerical mean-field techniques, we explored the model's behavior in both (1+1)D and (2+1)D systems. Notably, for the rotor Jackiw-Rebbi model on a spatial square lattice, we discerned a nontrivial phase akin to its (1+1)D counterpart. In this phase, fermions acquire dynamical mass within the lattice framework, facilitated by an antiferromagnetic order of dopant spin acting as a bosonic field interacting with the fermions. The (1+1)D version of the model showcases the potential to enter a phase wherein charge fractionalization occurs, yielding transitions between confined and deconfined phases involving quark-like quasi-particles. Additionally, thermal effects or an external (transverse) magnetic field could reestablish chiral symmetry by dynamical instabilities akin to those observed in spin models [228]. Extending our (2+1)D model to the honeycomb lattice reveals the presence of a similar nontrivial Néel-order phase. Moreover, phenomena analogous to those observed near the confinement-deconfinement transition can be traced in the creation of a superconductivity phase on a two-dimensional array over a certain range of model parameters, as studied in previous work [219].

Our research further elucidates the experimental feasibility of our proposal, paving the way for potential laboratory realizations and verifications. In relation to existing works, we juxtaposed our framework with proposals in the realm of cold atoms. This comparison emphasized the potential advantage of the solid-state platform of this work, particularly when transitioning to (2+1)D with native fermionic-bosonic simulators. Looking at the broader picture, our approach heralds the potential for empirical observations of confinement-deconfinement phase transitions, as well as the restoration of chiral symmetry at finite temperatures and densities, in a quantum

field theory.

While the model studied in this work presents a streamlined approach to analog quantum simulations, it is essential to recognize its differences compared with lattice gauge theories (LGTs). Unlike LGTs, the rotor Jackiw-Rebbi model does not exhibit gauge invariance, simplifying its implementation within experimental setups. This model, nonetheless, offers a more accessible introduction to analog quantum simulations of quantum field theories, and opens up opportunities to delve into the nonperturbative properties of quantum fields. As we look ahead, our ambition is to develop quantum-control techniques that enforce stringent gauge constraints on the degrees of freedom, making them more suitable for simulating LGTs. This will likely require time-dependent (floquet) engineering and novel approaches to develop a more intricate relationship between nuclear spins and fermions.

In summary, by harnessing engineered artificial lattices using solid-state technologies, we envision significant advancements in quantum simulations of quantum field theories, leading to deeper insights into strongly interacting systems in nuclear and high-energy physics.

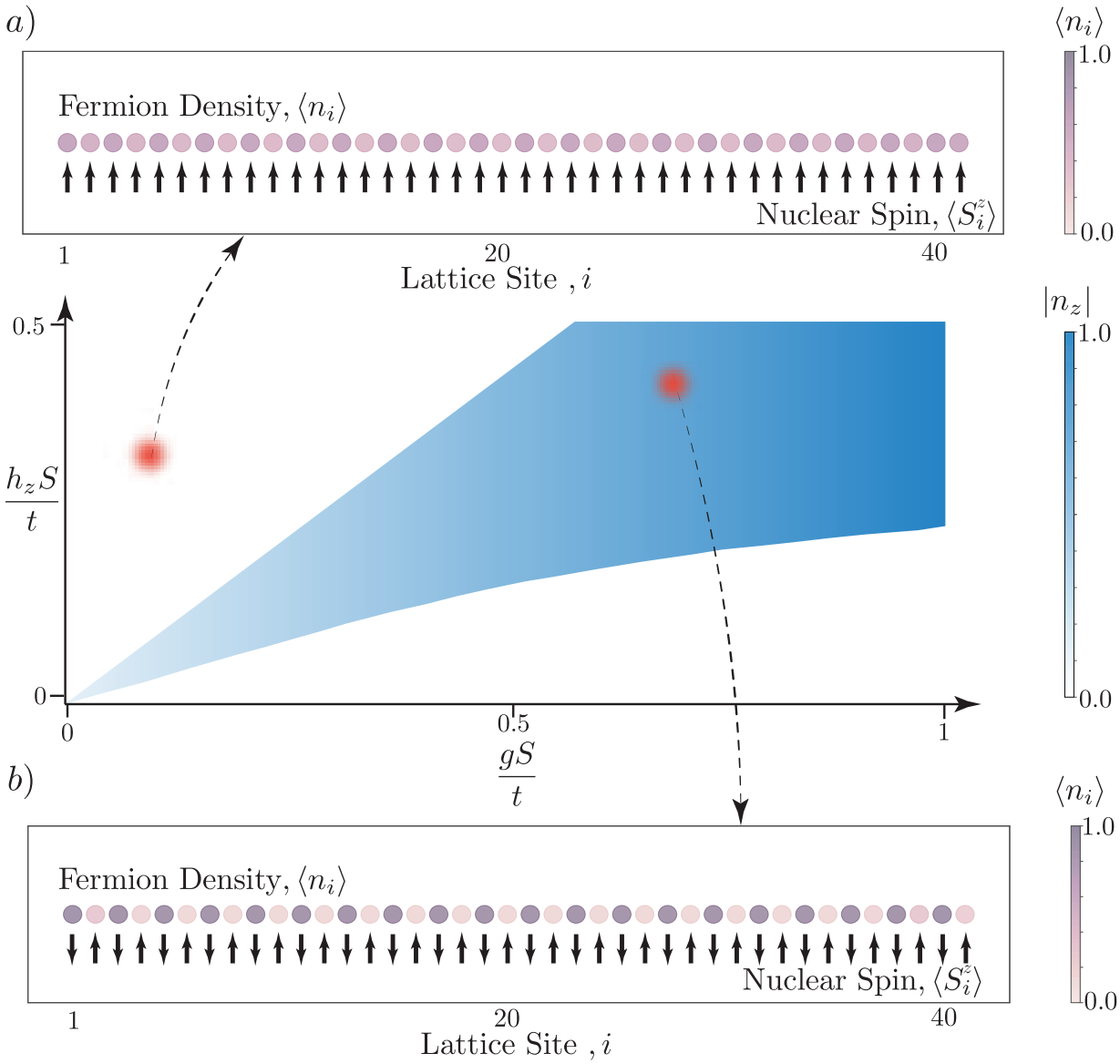

Figure 6.3: **Phase diagram of a (1+1)D system.** The phase diagram obtained from Hartree-Fock simulations, illustrates two distinct phases, trivial (a) and nontrivial (b), influenced by external magnetic fields h_z at fixed h_x. The nontrivial Néel phase, indicated in blue, emerges within a specific range of h_z when $h_x \ll h_z$, while the trivial phase, where all spins are polarized in a single direction, is represented by a white background. The circles represent the density of fermions at each site, where a darker color indicates higher density and the arrows show the orientation of the dopant's spin. The blue color represents the parameter $|n_z|$, where n_z is defined in Eq. (6.11), which is ideally one for the Néel-order phase and zero for the trivial phase. The simulation is done on a one-dimensional array with $N = 43$ sites in a configuration with one fermion above the half-filling state. The arrows represent the spin, $\langle S_i^z \rangle$, of the dopants, while the circles denote the fermion density at each site, indicated as $\langle n_i \rangle$. The parameter $h_x S/t$ is set to 0.01, where h_x denotes the external magnetic field in the x direction and t denotes the hopping parameter. For this plot, we have set $t = 7.5$ meV and $V_0/(at) = 1.1$

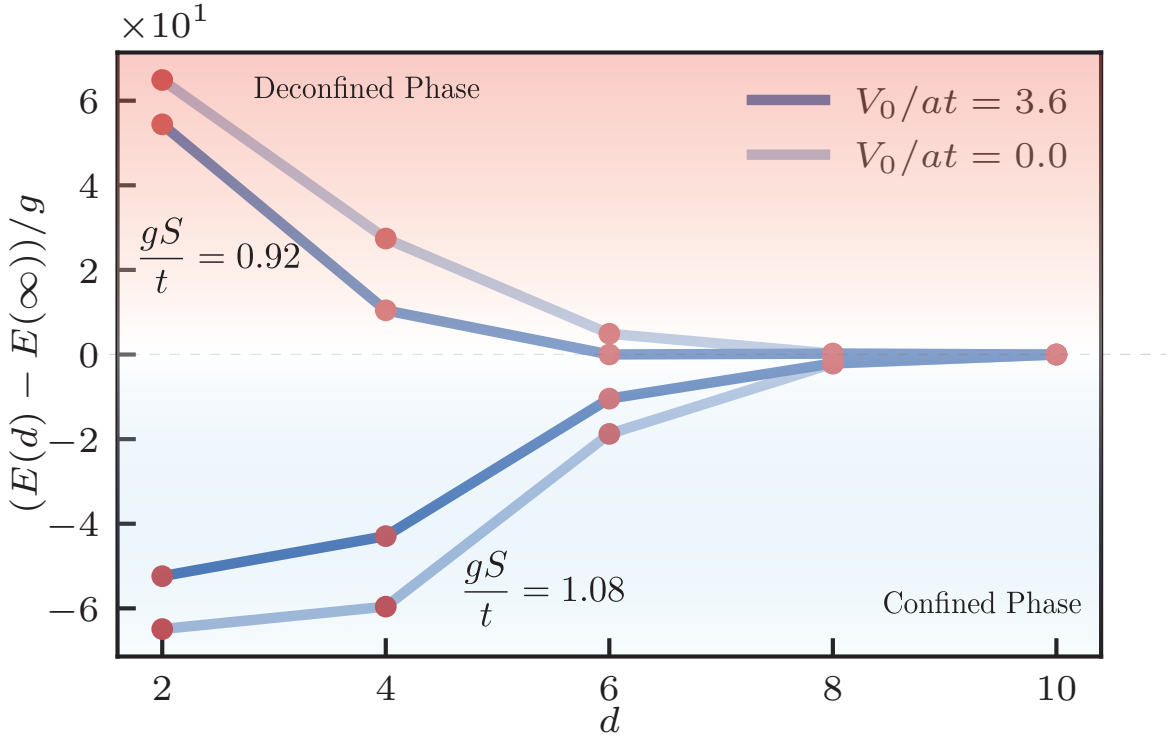

Figure 6.4: **Confinement/deconfinement phase transition.** Plots show the normalized system energy, E, as a function of the pinning-potential range, d, minus the normalized energy in the limit $d \gg 1$. Adjusting gS/t in a certain range with fixed h_z creates quark bags in the Néel phase, increasing energy as d increases (quark confinement). Lowering gS/t below a threshold results in a deconfined phase with reduced energy. Coulomb interaction present in the silicon-based experimental platform does not alter this phenomenon. The numerical simulation is based on the Hartree-Fock method at half-filling with $h_x S/t = 0.01$, $h_z S/t = 0.4$, $a = 4.7$ nm, and $t = 7.5$ meV

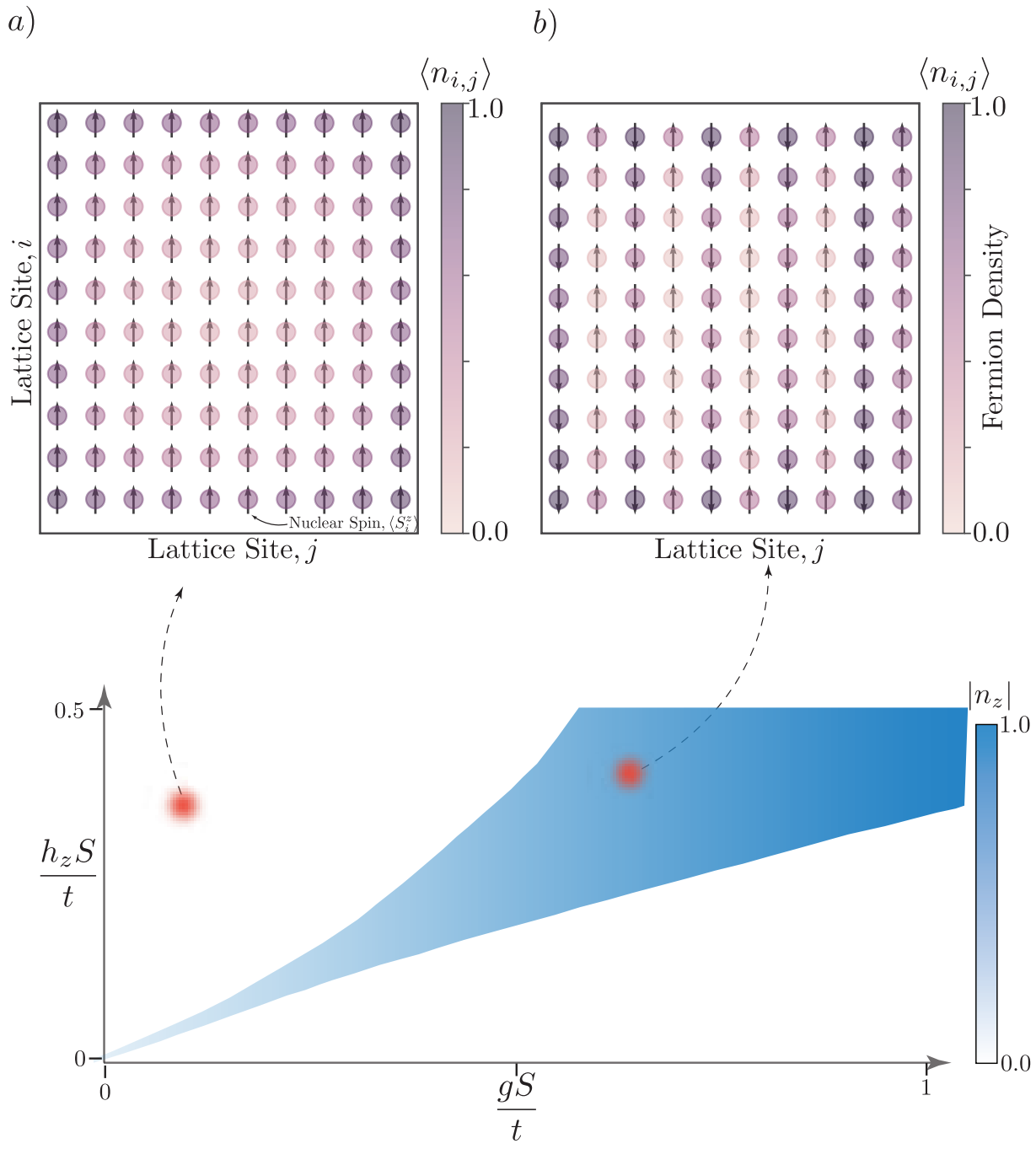

Figure 6.5: **Phase diagram of a (2+1)D system.** Similar to the (1+1)D scenario in Fig. 6.3, the spin configuration and fermion distributions in a two-dimensional square array, $N = 10 \times 10$, are depicted. The arrows represent the spin, $\langle S_z \rangle$, of the dopants, while the circles denote the fermion density at each site, indicated as $\langle n_{i,j} \rangle$. Note that we have now introduced a two-dimensional index (i, j) compared to the linear index i introduced in Sec. 6.3.2. The phase diagram of the system, in terms of macroscopic parameters, comprises two phases: the trivial phase (a) and the Néel-order phase (b). The blue color represents the parameter $|n_z|$ defined in Eq. (6.11), which is ideally one for the Néel-order phase and zero for the trivial phase. For this plot, we have set $t = 7.5$ meV, $h_x S/t = 0.01$, and $V_0/(at) = 1.1$

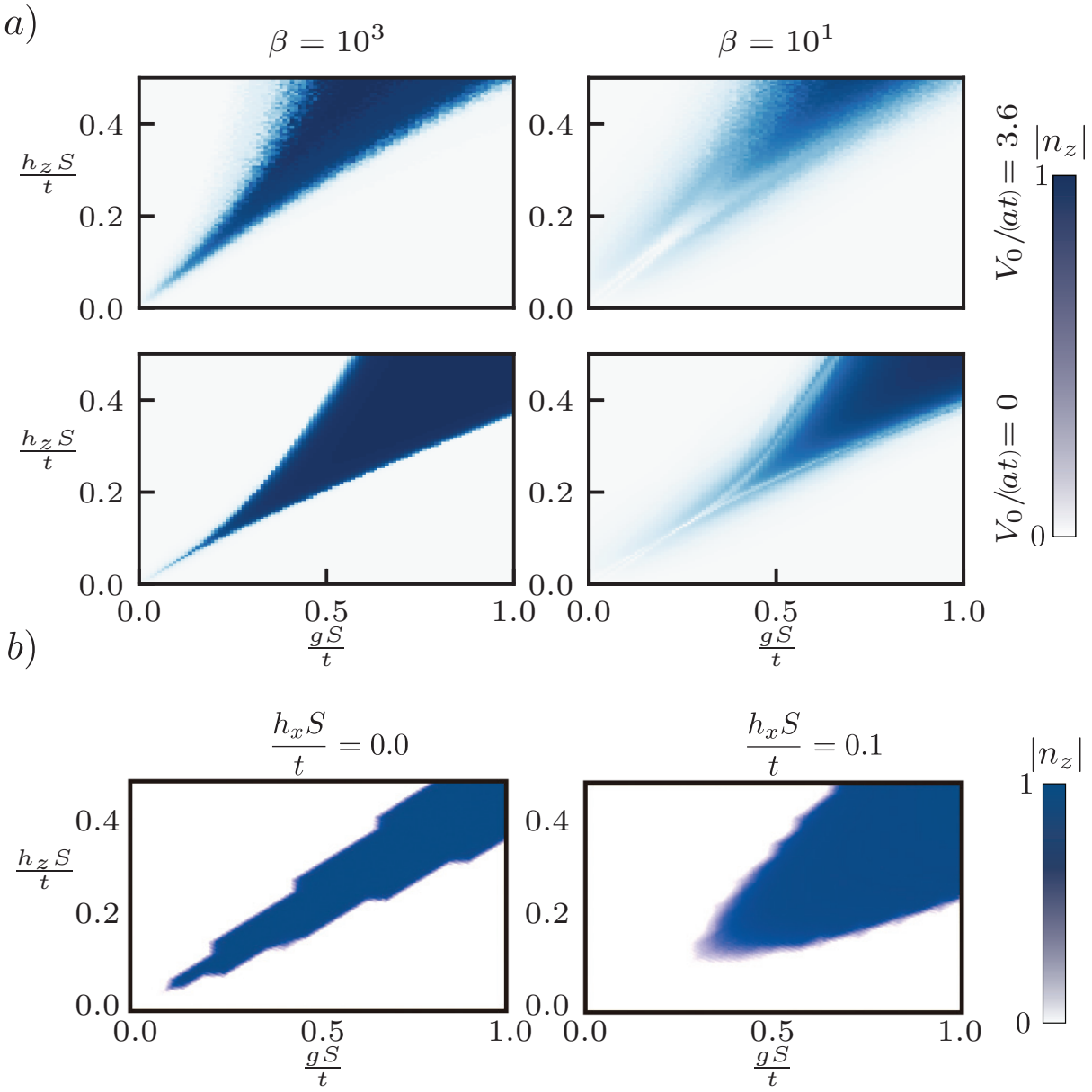

Figure 6.6: **The impact of temperature, Coulomb potential, and transverse magnetic field on the phase diagram of the (2+1)D system.** a) Comparing the subplots in the left and right columns illustrates the influence of increasing temperature on the phase diagram. Additionally, comparing the top and bottom rows sheds light on the effect of Coulomb's repulsion force on the phase diagram. The results are based on the Finite-Temperature Hartree-Fock method for an array of $N = 10 \times 10$, and the chemical potential is tuned such that the system is around half-filling. The blue color represents the parameter $|n_z|$ defined in Eq. (6.11). b) The different phases of the square array are plotted for two different transverse fields, h_x. The simulations for b) are performed using ED for the total number of spin $N = 2 \times 2$ at half-filling. The Coulomb potential is set to $V_0/(at) = 3.6$. The color represents the absolute value of the order parameter, $|n_z|$. In both a) and b), $t = 7.5$ meV, and in part a), $h_x S/t = 0.01$.

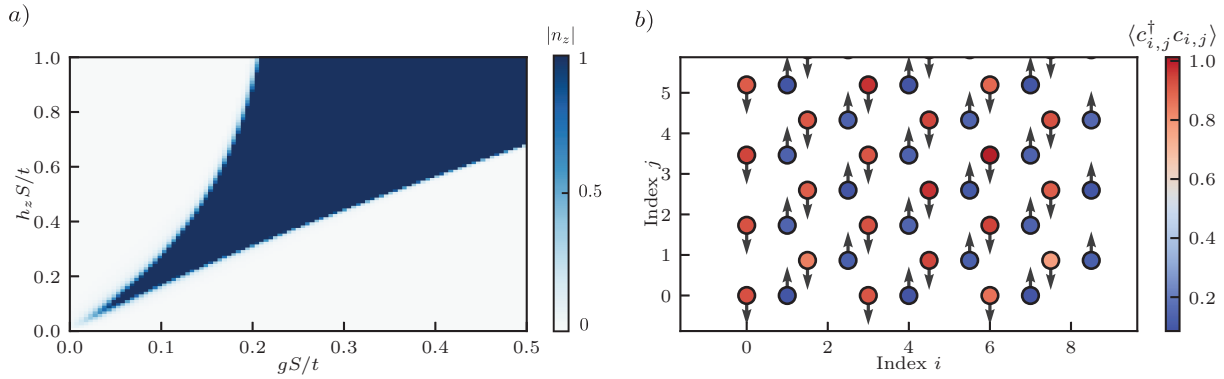

Figure 6.7: **Phase diagram of a (2+1)D honeycomb array for $N = 72$ sites.** a) Similar to the square lattice shown in Fig. 6.5, the phase diagram in terms of macroscopic parameters comprises two phases: the Néel-order phase and the trivial phase, with the presence of Coulomb interaction. The blue color represents the parameter $|n_z|$ defined in Eq. (6.11), which ideally is one for the Néel-order phase and zero for the trivial phase. b) The dopant-spin configuration and fermion-density distributions ($\langle c^\dagger_{i,j} c_{i,j} \rangle$) in the honeycomb lattice are shown for a region where the system exhibits the Néel-order phase. The numerical simulations are based on the finite-temperature Hartree-Fock method with inverse temperature $\beta = 10^3$. The tunneling coupling and horizontal external magnetic field are set similar to those in the square lattice, with $t = 7.5$ meV, $h_x S/t = 0.01$, and $V_0/(at) = 1.1$. The chemical potential is tuned to ensure that the system is around half-filling in the Néel-order phase.

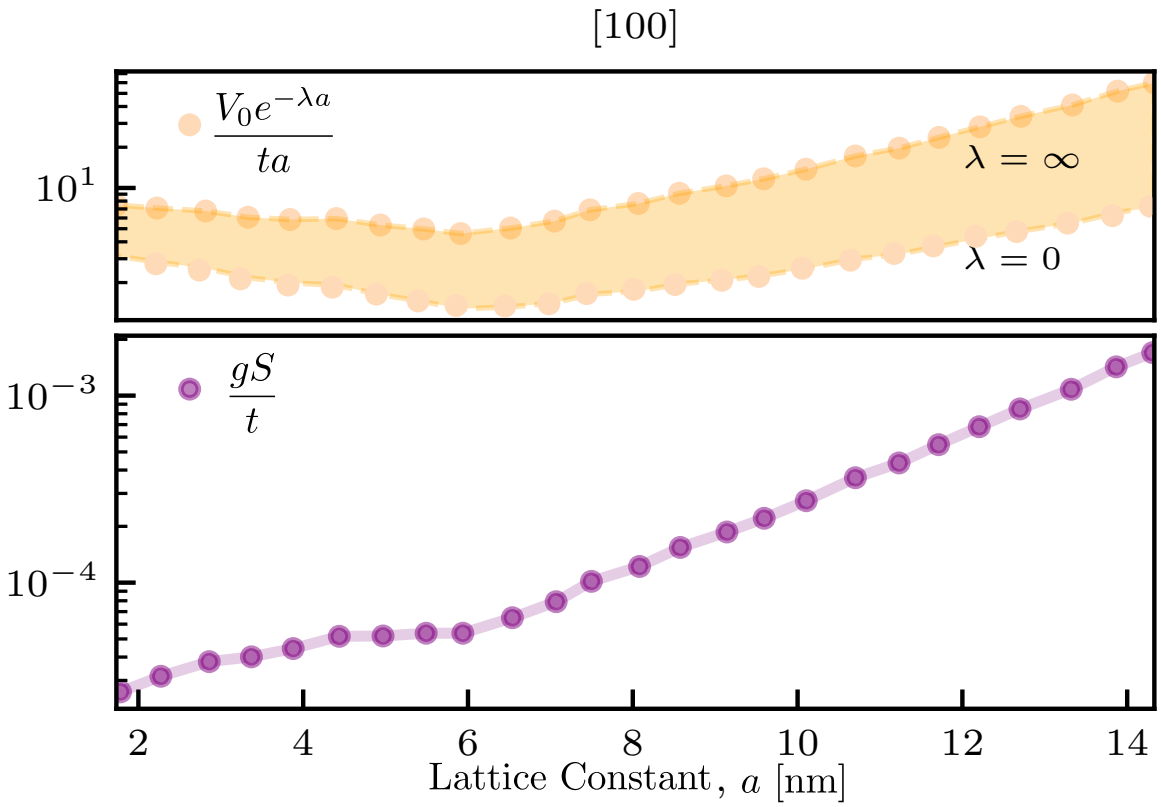

Figure 6.8: **Effect of lattice constant.** The influence of lattice constant, a, on the tunneling coupling, as well as the ratios g/t and h_z/t for fixed values of $g = 0.48$ μeV and $h_z = 2.5$ T, is depicted. The top panel shows the ratio of the Coulomb potential coefficient, V_0, compared to the tunnel coupling across the full range of screening, λ. The bottom panel shows values of gS/t for fixed $g = 0.48$ μeV as a function of the lattice constant.

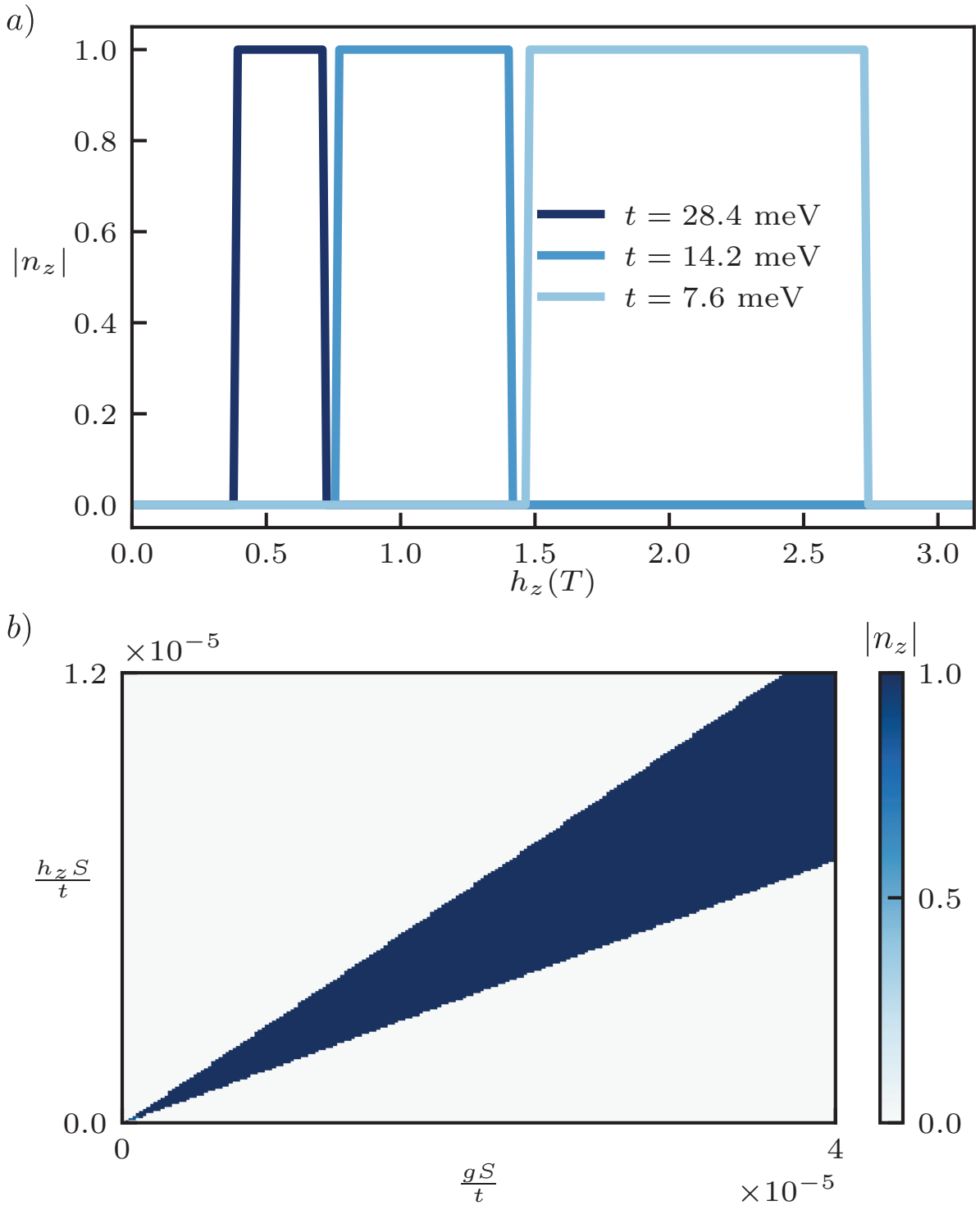

Figure 6.9: **External magnetic field as a macroscopic control.** a) The system is expected to transition through different phases corresponding to varying levels of the (longitudinal) magnetic field for three different values of tunneling coupling. The transition region from the trivial phase ($|n_z| = 0$) to the Néel ordered phase ($|n_z| = 1$) is illustrated for a 2×2 dopant array using the ED method. b) The phase diagram of the 2×2 dopant array, with the region gS/t coupling feasible in an experimental setup, has been simulated using the ED method. For this, the tunneling coupling is set at $t = 7.5$ meV and $h_x S/t = 10^{-7}$.

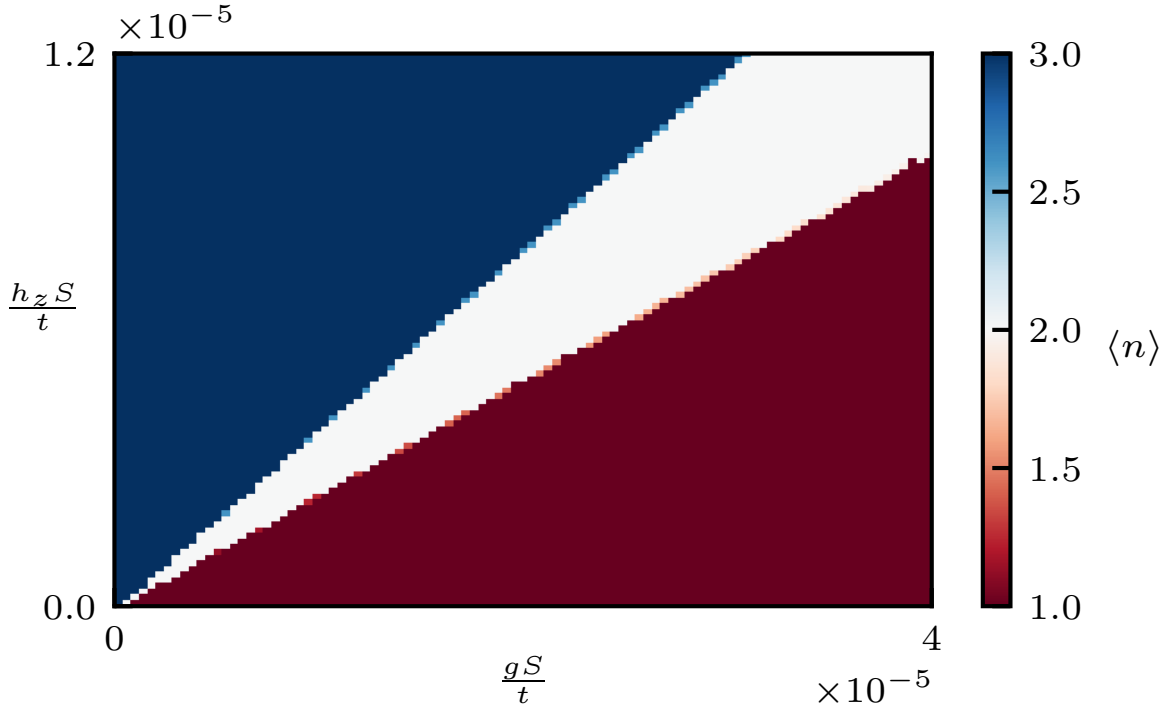

Figure 6.10: **Charge-occupation profile as a probe.** The variations in charge-occupation profiles, detected using a charge sensor, reflect the different phases in the 2×2 square array. The pronounced differences in the charge profiles, particularly in the nontrivial phase, provide evidence for the detection of phase transitions. The charges are calculated by tracing the electrons' density matrix determined at a finite temperature of $T = 10$ mK using the grand canonical ED method. Here, $\langle n \rangle = \sum_i \langle c_i^\dagger c_i \rangle_\beta$. Other parameters used for this simulation are $t = 7.5$ meV, $h_x S/t = 0.01$, and $\mu/t = 0.91$.

Chapter 7: Conclusion

In this thesis, we explored the intricate interplay between quantum computing and machine learning, elucidating how each field can benefit from the other and how quantum systems can be harnessed to simulate other quantum phenomena. This exploration spans the development of hybrid classical-quantum algorithms, the theoretical underpinnings of quantum machine learning, the practical aspects of quantum simulations, and the proposal of innovative frameworks for quantum analog simulations.

7.1 Chapter Summaries and Unified Insights

Chapter 2: Fast-and-Slow Initialization and Optimization

Our investigation into the fast-and-slow method of initialization and optimization revealed its potential to substantially reduce the computational overhead in training variational quantum algorithms (VQAs). This hybrid approach makes VQAs more feasible for larger qubit systems by minimizing the number of queries to the quantum processing unit (QPU). Future work will involve applying this method to diverse circuit types and physical quantum hardware, along with developing dynamic switching schemes for more complex optimization problems.

Chapter 3: Variational Quantum Circuits in Function Space

We analyzed variational quantum circuits as quantum neural networks, focusing on their

behavior in function space. Our study of over-parameterization showed that increasing the width and depth of these circuits leads their output distribution towards a Gaussian process, though finite widths can introduce non-Gaussianity. This insight is crucial for designing robust quantum models and understanding the implications of over-parameterization in practical applications.

Chapter 4: Generalization in Quantum Machines

Addressing the challenge of generalization in quantum machines, we discovered that quantum networks exhibit double descent behavior akin to classical networks. By employing random matrix theory, we demonstrated that over-parameterized quantum circuits could be theoretically beneficial, challenging the traditional bias-variance trade-off. This finding opens new pathways for improving the predictive performance of quantum models on unseen data.

Chapter 5: Pruning Methods for Quantum Simulation

We evaluated the efficiency of pruning methods in quantum simulations, finding that significant complexity and cost reductions could be achieved with minimal error impact. Utilizing Hessian information for pruning outperformed random benchmarks, suggesting a promising direction for optimizing quantum simulations. Future research will incorporate decoherence effects and focus on enhancing fidelity through time error evolution minimization.

Chapter 6: Solid-State Framework for Quantum Simulations

We proposed a solid-state framework using a donor array in silicon as an analog quantum simulator for relativistic phenomena in quantum field theory. Our study of the rotor Jackiw-Rebbi model demonstrated the feasibility of this approach in both (1+1)D and (2+1)D systems, revealing nontrivial phases and potential experimental realizations. This framework offers a compelling alternative to cold atom proposals, particularly for simulating confinement-deconfinement transitions and chiral symmetry restoration in quantum field theories. Future work will develop quantum-

control techniques to enforce gauge constraints, enhancing the simulation of lattice gauge theories.

7.2 Future Directions and Needed Developments

Several key areas require further investigation to build upon the findings of this thesis: Developing adaptive optimization methods that dynamically switch between fast and slow phases, tailored to specific problem characteristics, will enhance the efficiency of VQA training. Exploring the impact of finite sizes and over-parameterization in quantum neural networks will inform the design of more robust quantum models capable of generalizing better to unseen data. Incorporating decoherence and optimizing cost functions to include error evolution will improve the fidelity of pruned quantum simulations, making them more practical for real-world applications. Developing time-dependent (Floquet) engineering and innovative quantum-control techniques to enforce gauge constraints will enable more accurate simulations of lattice gauge theories, bridging the gap between simplified models and complex quantum field theories.

In conclusion, this thesis has been just an early step toward promising directions in quantum computing research. By addressing both theoretical and practical challenges, we have advanced the understanding and applicability of quantum algorithms and simulations, paving the way for future developments in the field.

Appendix A:

A.1 The Barren Plateau in VQAs

Variational circuits can be described as a unitary operation, $U(\boldsymbol{\theta})$, with a set of parameters $\boldsymbol{\theta} = \{\theta_i\}_{i=1}^{m}$ For a given observable $\mathcal{O}_i$, and a fixed initial state ρ, the expectation value can be estimated by executing repetitive measurements on the QPU. In general, these measurements can be used to calculate the cost function defined as

$$\mathcal{L}(\boldsymbol{\theta}) = \sum_i h_i f_i\Big(\text{Tr}\left(\mathcal{O}_i U(\boldsymbol{\theta})\rho U^\dagger(\boldsymbol{\theta})\right)\Big), \tag{A.1}$$

where $\{h_i \in \mathbb{R}, f_i : \mathbb{R} \to \mathbb{R}\}$ encodes the problem.

The goal of VQAs is to find the optimum set of parameters that minimizes the cost function:

$$\boldsymbol{\theta}^\star =_{\boldsymbol{\theta}} \mathcal{L}(\boldsymbol{\theta}). \tag{A.2}$$

In general, the ansatz can be described with a unitary $U(\boldsymbol{\theta})$ as

$$U(\boldsymbol{\theta}) = \prod_{i=1}^{m} U_i(\theta_i), \tag{A.3}$$

where $U(\theta_i) = e^{-i\theta_i\sigma_i}$ and σ_j is a Hermitian 1- or 2-qubit operator and $\sigma_j^2 = \mathbb{I}$. In this

representation, we assume the parameters are independent of each other. To study behaviour of a specific parameter θ_μ, $1 \leq \mu \leq m$, we can split the $U(\boldsymbol{\theta})$ into a left and right part:

$$U(\boldsymbol{\theta}) = U_R(\boldsymbol{\theta}_R)U_L(\boldsymbol{\theta}_L), \tag{A.4}$$

where right and left operators are defined as $U_R(\boldsymbol{\theta}_R) = \prod_{i=1}^{\mu} U_i(\theta_i)$ and $U_L(\boldsymbol{\theta}_L) = \prod_{i=\mu+1}^{m} U_i(\theta_i)$, respectively. The derivative of $U(\boldsymbol{\theta})$ can be written as $\partial_{\theta_\mu} U(\boldsymbol{\theta}) = U_R(-\frac{i}{2}\sigma_\mu)U_L$ and $\partial_{\theta_\mu} U^\dagger(\boldsymbol{\theta}) = U_L^\dagger(\frac{i}{2}\sigma_\mu)U_R^\dagger$

The cost function of our generative model is based on the Kullback–Leibler (KL) divergence function in Eq. (2.7) in the main text. We define $C_i := \text{Tr}(O_i U \rho U^\dagger)$, $q_i := \text{Tr}[O_i \rho_{\text{BAS}}]$, and let $O_i \in \{|i\rangle\langle i|\}_{i=0}^{2^n-1}$. Note that $\partial_{\theta_\mu} \sum_i C_i = 0$. Therefore, the derivative of the cost-function with respect to a single parameter, θ_μ, is given by

$$\partial_\mu \mathcal{L}(\theta) = \sum_{i=0}^{2^n-1} \partial_{\theta_\mu} C_i \log(C_i/q_i), \tag{A.5}$$

where the derivative of C_i respect to the parameter θ_μ can be written as [33]

$$\begin{aligned} \partial_\mu C_i &= -\frac{i}{2}\text{Tr}(U_R^\dagger O_i U_R[\sigma^\mu, U_L \rho U_L^\dagger]) \\ &= \frac{i}{2}\text{Tr}(U_L \rho U_L^\dagger[\sigma^\mu, U_R^\dagger O_i U_R]). \end{aligned} \tag{A.6}$$

In order to calculate the average value of the gradient, $\langle \partial_{\theta_k} \mathcal{L}(\theta) \rangle = \sum_i \langle \partial_\mu C_i \log C_i/q_i \rangle$, we can consider three cases: either U_L, U_R, or both satisfy the 2-design property. This allows us to simplify certain terms in the average by an integral over the Haar measure. A t-design unitary defined as a finite set of unitary operator$\{U_k\}_{k=1}^k \in \mathcal{U}(d)$ with any arbitrary function

$P_{(t,t)}(U)$(which acts at each element of matrix U and $U^\dagger$ with polynomial degree at most t) such that it satisfies the following relation

$$\frac{1}{K}\sum_{k=1}^{K} P_{(t,t)}(U_k) = \int_{\mathcal{U}(d)} d\mu(U) P_{(t,t)}(U), \tag{A.7}$$

where $d\mu(\cdot)$ is a Haar measure over the unitary group $\mathcal{U}(d)$. In general, for a random unitary matrix $U = (U_{ij})_{i\leq i,j\leq d}$, the expectation of the following form with respect to the Haar measure over a unitary group $\mathcal{U}(d)$ is given by

$$\begin{aligned}
&\mathbb{E}[U_{i_1 j_1} U_{i_2 j_2} \cdots U_{i_n j_n} U^*_{i'_1 j'_1} U^*_{i'_2 j'_2} \cdots U^*_{i'_n j'_n}] \\
&= \sum_{\sigma,\tau \in S_n} \delta_{i_1 i'_{\sigma(n)}} \cdots \delta_{i_n i'_{\sigma(n)}} \delta_{j_1 j'_{\sigma}(1)} \cdots \delta_{j_n j'_{\sigma(n)}} \mathrm{Wg}^U(\sigma^{-1}\tau, d) \\
&:= \sum_{\sigma,\tau \in S_n} \delta_\sigma(\mathbf{i}, \mathbf{i}') \delta_\tau(\mathbf{j}, \mathbf{j}') \mathrm{Wg}^U(\sigma^{-1}\tau, d),
\end{aligned} \tag{A.8}$$

where S_n is the symmetric group [90, 229]. The $\mathrm{Wg}(\cdot, d)$ is Weingarten function defined on S_d with the following Fourier expansion:

$$\mathrm{Wg}^U(\sigma, d) = \frac{1}{d!} \sum_{\lambda \vdash n, \ell(\lambda)\leq d} \frac{f^\lambda}{\prod_{i=1}^{\ell(\lambda)} \prod_{j=1}^{\lambda_i} (d+j-1)} \chi^\lambda(\sigma), \tag{A.9}$$

such that for a given λ, χ^λ is the irreducible character of S_d associated with it. f^λ is the degree of χ^λ and $\lambda \vdash n$ is the sum over all partitions of λ defined by Young diagram $\lambda = (\lambda_1, \lambda_2, \cdots \lambda_l)$ of d and $l = \ell(\lambda)$. Applying this theorem for first and second moment of U, over the Haar measure

$d\mu(U)$, provides the following identities based on the calculation over S_1 and S_2 group:

$$\int U_{ij}U^*_{pk}d\mu(U) = \frac{\delta_{ip}\delta_{jk}}{d} \tag{A.10}$$

$$\int U_{i_1j_1}U_{i_2j_2}U^*_{i'_1j'_1}U^*_{i'_2,j'_2}d\mu(U) = \frac{\delta_{i_1i'_1}\delta_{i_2i'_2}\delta_{j_1j'_1}\delta_{j_2j'_2}}{d^2-1}$$

$$- \frac{\delta_{i_1i'_1}\delta_{i_2i'_2}\delta_{j_1j'_2}\delta_{j_2j'_1} + \delta_{i_1i'_2}\delta_{i_1i'_2}\delta_{j_1j'_1}\delta_{j_2j'_2}}{d(d^2-1)}.$$

For $U \in \mathcal{U}(d = 2^n)$ the above identities can be re-written in the form of

$$\int \text{Tr}(UXU^\dagger Y)d\mu(U) = \frac{1}{2^n}\text{Tr}(X)\text{Tr}(Y) \tag{A.11}$$

$$\int \text{Tr}(UXU^\dagger Y)\text{Tr}(UZU^\dagger W)d\mu(U) =$$

$$\frac{\text{Tr}(X)\,\text{Tr}(Y)\,\text{Tr}(Z)\,\text{Tr}(W) + \text{Tr}(XZ)\,\text{Tr}(YW)}{2^{2n}-1}$$

$$- \frac{\text{Tr}(XZ)\,\text{Tr}(Y)\,\text{Tr}(W) + \text{Tr}(X)\,\text{Tr}(Z)\,\text{Tr}(YW)}{2^{3n}-2^n},$$

and

$$\int \text{Tr}\big[UXU^\dagger YUZU^\dagger W\big]d\mu(U) \tag{A.12}$$

$$= \frac{\text{Tr}(X)\,\text{Tr}(Z)\,\text{Tr}(YW) + \text{Tr}(XZ)\,\text{Tr}(Y)\,\text{Tr}(W)}{2^{2n}-1}$$

$$- \frac{\text{Tr}(XZ)\,\text{Tr}(YW) + \text{Tr}(X)\,\text{Tr}(Y)\,\text{Tr}(Z)\,\text{Tr}(W)}{2^n(2^{2n}-1)}. \tag{A.13}$$

For simplicity, we start the calculations with the case that both U_R and U_L are 2-designs. By

applying the above identities to calculate $\mathbb{E}[C_i]$ and $\mathbb{E}[C_iC_j]$, we obtain

$$\begin{aligned}\mathbb{E}[C_i] &= \int \mathrm{Tr}\big(O_iU\rho U^\dagger\big)d\mu(U) \\ &= \frac{\mathrm{Tr}(O_i)\,\mathrm{Tr}(\rho)}{2^n} = \frac{1}{2^n},\end{aligned} \tag{A.14}$$

and

$$\begin{aligned}\mathbb{E}[C_iC_j] &= \int \mathrm{Tr}\big(O_iU\rho U^\dagger\big)\,\mathrm{Tr}\big(O_jU\rho U^\dagger\big)d\mu(U) \\ &= \frac{\mathrm{Tr}(O_i)\,\mathrm{Tr}(O_j)}{2^{2n-1}}[\mathrm{Tr}(\rho)^2 - \frac{\mathrm{Tr}(\rho^2)}{2^n}] \\ &+ \frac{\mathrm{Tr}(O_iO_j)}{2^{2n}-1}[\mathrm{Tr}\big(\rho^2\big) - \frac{\mathrm{Tr}(\rho)^2}{2^n}] \\ &= \frac{1+\delta_{i,j}}{2^{2n}-1}(1-2^{-n}),\end{aligned} \tag{A.15}$$

since for observable in the form of $O_i^{jk} = \delta_{i,j}\delta_{i,k}I^{jk}_{2^n\times 2^n}$, we have $\mathrm{Tr}(O_i) = \mathrm{Tr}(O_i^2) = 1$ and $\sum_{i=0}^{2^{n-1}}\mathrm{Tr}(O_i) = 2^n$. A similar calculation can be repeated for the $\mathbb{E}[\partial_\mu C_i]$:

$$\begin{aligned}\mathbb{E}[\partial_\mu C_i] &= \frac{i}{2}\int \mathrm{Tr}\Big(U_L\rho U_L^\dagger[\sigma^\mu, U_R^\dagger O_iU_R]\Big)d\mu(U_L)d(U_R) \\ &= i\frac{\mathrm{Tr}(\rho)[\mathrm{Tr}(\sigma^\mu),\mathrm{Tr}(O_i)]}{2^{2n+1}} = 0,\end{aligned} \tag{A.16}$$

and therefore $\mathbb{E}[\partial_\mu C_i \log q_i] = 0$. Similarly, the expectation value of the second moment can be calculated as follows:

$$
\begin{aligned}
\mathbb{E}[\partial_\mu C_i \partial_\mu C_j] = -\frac{1}{4}\int \mathrm{Tr}\Big(U_L \rho U_L^\dagger [\sigma^\mu, U_R^\dagger O_i U_R]\Big) \\
&\times \mathrm{Tr}\Big(U_L \rho U_L^\dagger [\sigma^\mu, U_R^\dagger O_j U_R]\Big) d\mu(U_L, U_R) \\
&= \Big(\frac{\mathrm{Tr}(\sigma_\mu)^2 \,\mathrm{Tr}(O_i O_j) + \mathrm{Tr}\big(\sigma_\mu^2\big)\,\mathrm{Tr}(O_i)\,\mathrm{Tr}(O_j)}{2^{2n}-1} \\
&- \frac{\mathrm{Tr}\big(\sigma_\mu^2\big)\,\mathrm{Tr}(O_i O_j) + \mathrm{Tr}(\sigma_\mu)^2\,\mathrm{Tr}(O_i)\,\mathrm{Tr}(O_j)}{2^{3n}-2^n} \\
&- \frac{1}{2^n}\,\mathrm{Tr}\big(\sigma_\mu^2\big)\,\mathrm{Tr}(O_i O_j)\Big) \times \big(\frac{-\,\mathrm{Tr}(\rho^2) + 2^{-n}}{2^{2n}-1}\big).
\end{aligned}
\tag{A.17}
$$

To obtain an upper-bound on $|\langle \partial_\mu \mathcal{L} \rangle|$ we use the Cauchy-Schwarz inequality and the property of logarithmic functions, where for a two random variable x and y, we have $\mathbb{E}[x \log y] \leq \mathbb{E}[xy] - \mathbb{E}[x]$. Applying this identity to calculate $\mathbb{E}[\partial_\mu C_i C_i / q_i]$ leads to the following inequality:

$$
\begin{aligned}
\Big|\mathbb{E}[\partial_\mu C_i \log \frac{C_i}{q_i}]\Big| \leq \Big|\mathbb{E}[\partial_\mu C_i \frac{C_i}{q_i}] - \mathbb{E}[\partial_\mu C_i]\Big| = \Big|\mathbb{E}[\partial_\mu C_i \frac{C_i}{q_i}]\Big| \\
\leq q_i^{-1} \sqrt{\mathbb{E}[(\partial_\mu C_i)^2]}\sqrt{\mathbb{E}[(C_i)^2]}.
\end{aligned}
\tag{A.18}
$$

To avoid the divergence in the numerical calculation of KL divergence we replace the $q_{i,\mathrm{BAS}}$ with the clipper function $\max[\epsilon, q_{i,\mathrm{BAS}}]$ for arbitrary small $\epsilon := \Lambda^{-1}$. By using the result of Eq .(A.17) and Eq. (A.14) and adding all terms from Eq .(A.5), we can derive the following upper bound on the magnitude of expectation value gradient of the cost function:

$$
|\langle \partial_\mu \mathcal{L} \rangle| \leq \sqrt{\frac{2(2^n-1)^2(\Lambda \cdot 2^n + 2\Lambda - 4)^2}{2^{2n}(2^n+1)(2^{2n}-1)^2}} \sim \mathcal{O}(2^{-\frac{3n}{2}}). \tag{A.19}
$$

In the next step, to find the expectation value of the variance of the gradient of the cost function with respect to a parameter θ_μ, $\mathrm{Var}[\partial_\mu \mathcal{L}]$, we start with the its definition and use Cauchy-

Schwarz to get an upper bound on it

$$
\begin{aligned}
\text{Var}[\partial_\mu \mathcal{L}] &= \langle (\partial_\mu \mathcal{L})^2 - \langle \partial_\mu \mathcal{L} \rangle^2 \rangle \\
&= \sum_{i,j} \mathbb{E}[\partial_\mu C_i \log \frac{C_i}{q_i} \partial_\mu C_j \log \frac{C_j}{q_j}] \\
&- \sum_{i} \mathbb{E}[\partial_\mu C_i \log \frac{C_i}{q_i}]^2 \\
&\leq \sum_{i,j} \mathbb{E}[\partial_\mu C_i \frac{C_i}{q_i} \partial_\mu C_j \frac{C_j}{q_j}] \\
&\leq \sum_{i,j} (q_i q_j)^{-1} \Big(\mathbb{E}[(\partial_\mu C_i)^4] \mathbb{E}[(\partial_\mu C_j)^4] \mathbb{E}[C_i^4] \mathbb{E}[C_j^4] \Big)^{\frac{1}{4}}.
\end{aligned}
\tag{A.20}
$$

To calculate the fourth-moment expressions in the right-hand side of the inequality, we assume that both U_R and U_L satisfy the 4-design property. This assumption is motivated by the observation that random local quantum circuits with a depth that grows polynomially in the number of qubits form an approximate unitary t-design, and conjectured to be valid for logarithmic-depth circuits

as well [36, 230, 231]. Based on the 4-design assumption, according to Eq. (A.8):

$$
\begin{aligned}
\mathbb{E}[C_i^4] = & \sum_{\mathbf{i},\mathbf{i}',\mathbf{j},\mathbf{j}'=1}^{4} \mathbb{E}[U_{i_1 j_1} U_{i_2 j_2} U_{i_3 j_3} U_{i_4 j_4} U^*_{i'_1 j'_1} U^*_{i'_2 j'_2} U^*_{i'_3 j'_3} U^*_{i'_4 j'_4}] \\
& \times \prod_{\nu=1}^{4} \rho_{j_\nu i'_\nu} O^i_{j'_\nu i_\nu} = \sum_{\substack{i_1,j_1,\cdots,i_4,j_4 \\ i'_1,j'_1,\cdots,i'_4,j'_4=1}}^{4} \sum_{\sigma,\tau\in S_4} \prod_{\nu=1}^{4} \\
& \times \rho_{j_\nu i'_\nu} O^i_{j'_\nu i_\nu} \delta_\sigma(\mathbf{i},\mathbf{i}') \delta_\tau(\mathbf{j},\mathbf{j}') \mathrm{Wg}^U(\sigma^{-1}\tau, d) \\
& = \sum_{\sigma,\tau\in S_4} \sum_{\substack{i'_1,\cdots i'_4 \\ j'_1,\cdots j'_4=1}}^{4} \prod_{\nu}^{4} O^i_{i'_{\sigma(\nu) j'_\nu}} \rho_{j'_{\tau(\nu)} i'_\nu} \mathrm{Wg}^U(\sigma^{-1}\tau, d) \\
& := \sum_{\sigma,\tau\in S_4} \mathrm{Tr}_{\sigma,\tau}(\rho, O^i) \mathrm{Wg}^U(\sigma^{-1}\tau, d) \\
& \leq \frac{C}{d^4} \sum_{\sigma,\tau\in S_4} \mathrm{Tr}_{\sigma,\tau}(\rho, O^i),
\end{aligned}
\tag{A.21}
$$

where in last inequality is based on the property of Weingarten coefficient [232] and C is a constant number.

Similarly

$$
\begin{aligned}
\mathbb{E}[(\partial_\mu C_i)^4] = & \sum_{\substack{\sigma,\tau\in S_4 \\ \alpha,\beta}} \mathrm{Wg}^U_L(\sigma^{-1}\tau, d) \mathrm{Wg}^U_R(\alpha^{-1}\beta, d) \sum_{\substack{\mathbf{i}',\mathbf{j}',\mathbf{k} \\ \mathbf{k}',\mathbf{l}',\mathbf{l}=1}}^{4} \\
& \sum_{\substack{r_v : r_1 r_2 \\ r_3, r_4 = 0}}^{1} \prod_{\nu=1}^{4} \times \big(\rho_{j'_{\tau(\nu)} i'_\nu} \sigma^\mu_{j'_\nu k_\nu} O^i_{l'_\nu k_\nu} \delta_{k_\nu, \alpha(k'_\nu)} \delta_{i_{\sigma(\nu)}, \beta(l'_\nu)}\big)^{r_\nu} \\
& ((-1) \rho_{j'_{\tau(\nu)} i'_\nu} \sigma^\mu_{l_\nu i_{\sigma(\nu)}} O^i_{l'_\nu k_\nu} \delta_{k_\nu, \alpha(j'_\nu)} \delta_{l_\nu, \beta(l'_\nu)})^{1-r_\nu} \\
:= & \sum_{\substack{\sigma,\tau\in S_4 \\ \alpha,\beta}} \mathrm{Wg}^U_L(\sigma^{-1}\tau, d) \mathrm{Wg}^U_R(\alpha^{-1}\beta, d) \, \mathrm{Tr}^{\alpha,\beta}_{\sigma,\tau}(\sigma^\mu, O^i, \rho) \\
\leq & \frac{C^2}{d^8} \sum_{\substack{\sigma,\tau\in S_4 \\ \alpha,\beta}} \mathrm{Tr}^{\alpha,\beta}_{\sigma,\tau}(\sigma^\mu, O^i, \rho).
\end{aligned}
\tag{A.22}
$$

Consequently, by substituting the Eq. (A.21) and Eq. (A.22) in the Eq. (A.20) we find the variance $\mathrm{Var}[\partial_\mu \mathcal{L}]$, is exponentially suppressed as a function of qubits number since

$$\begin{aligned}\mathrm{Var}[\partial_\mu \mathcal{L}] \leq & \frac{C}{2^{6n}} \sum_{i,j=1}^{2^n} (q_i q_j)^{-1} [\sum_{\substack{\sigma',\tau' \in S_4 \\ \alpha',\beta'}} \sum_{\substack{\sigma,\tau \in S_4 \\ \alpha,\beta}} \mathrm{Tr}_{\sigma,\tau}^{\alpha,\beta}(\sigma^\mu, O^j, \rho) \\ & \mathrm{Tr}_{\sigma,\tau}(\rho, O^i)\, \mathrm{Tr}_{\sigma',\tau'}^{\alpha',\beta'}(\sigma^\mu, O^i, \rho)\, \mathrm{Tr}_{\sigma',\tau'}(\rho, O^i)]^{\frac{1}{4}}\end{aligned} \tag{A.23}$$

A.2 Bars and Strips ensemble

The Bars and Stripes (BAS) [67] ensemble is one of the standard benchmarks used to study the performance of unsupervised generative models. For a given (n, m), this data set, BAS(n, m), can be constructed based on the two-dimensional grid with n rows and m columns where each plaquette can be black (filled) or white (empty) with total number of possible configurations of $2^{n \cdot m}$. Each sample of BAS belongs to a specific subset of these states which the grids are filled to make exclusively i filled columns ($0 \leq i \leq m$) or exclusively j rows ($0 \leq j \leq n$), i.e. bars and stripes, respectively. Therefore, the total number of possible BAS samples is $N_{\mathrm{BAS}(n,m)} \sum_{k=0}^{n} \binom{n}{k} + \sum_{p=0}^{m} \binom{m}{p} - 2 = 2^n + 2^m - 2$. The ratio of total to valid BAS patterns decreases exponentially as $2^{-\min(n,m)}$. To evaluate the performance of a quantum system to generate BAS states, a qBAS score was introuced [62]. It is defined as $\mathrm{qBAS} = \frac{2pr}{p+r}$, where r is the recall number, i.e. the ability to generate all patters of BAS(n, m), and p is the ability to retrieve states belongs to BAS(n, m). In order to observe the whole spectrum of BAS(n, m) patterns, we need to handful of measurements from the circuit. Since each pattern occurs with probability $1/N_{\mathrm{BAS}(n,m)}$, we need to do $N_M = N_{\mathrm{BAS}(n,m)}(1 + \frac{1}{2} + \cdots \frac{1}{N_{\mathrm{BAS}(n,m)}}) \approx$

$2^{\max(m,n)}(\max(m,n)+\gamma)$ measurements where γ is Euler-Macheroni constant.

Appendix B:

B.1 Infinite width QNN

In the context of infinite-width quantum neural networks, the prior distribution takes the form of a simple Gaussian distribution. Consequently, the posterior distribution can be represented as follows:

$$p(f_{\mathbb{O}}, f_{\mathbb{P}}) = \frac{1}{\sqrt{|2\pi K|^{n^2}}} \exp\left(-\frac{1}{2} \sum_{i,j=1}^{n} \sum_{\mu_1,\mu_2 \in \mathbb{P}\cup\mathbb{O}} K^{ij,\mu_1\mu_2} f_{i,\mu_1} f_{j,\mu_2} \right) \tag{B.1}$$

It is possible to divide the series in the exponent into four separate matrices. Starting with

$$K_{ij,\mu_1\mu_2} = \begin{bmatrix} K_{ij,o_1o_2} & K_{ij,o_1p_2} \\ K_{ij,p_1o_2} & K_{ij,p_1p_2} \end{bmatrix} = \begin{bmatrix} \mathbb{E}[f_{i,o_1} f_{j,o_2}] & \mathbb{E}[f_{i,o_1} f_{j,p_2}] \\ \mathbb{E}[f_{i,p_1} f_{j,o_2}] & \mathbb{E}[f_{i,p_1} f_{j,p_2}], \end{bmatrix} \tag{B.2}$$

The inverse of $K_{\mu_1\mu_2}$, for a specific ij index, is expressed as $\sum_{\mu_2} K^{\mu_1\mu_2} K_{\mu_2\mu_3} = \delta_{\mu_1,\mu_3}$. This separation for the first-order correction is valid since $K_{ij,\alpha\beta} \sim \frac{1}{d^2} \operatorname{Tr}(O_i O_j) \operatorname{Tr}(\rho_\alpha \rho_\beta) := M_{ij} G_{\alpha\beta}$ This expression can be broken down into four distinct sectors as follows:

$$K^{\mu_1\mu_2} = \begin{bmatrix} K^{\alpha_1\alpha_2} + \sum_{\alpha_3\alpha_4\in\mathbb{O},\beta_3,\beta_4\in\mathbb{P}} K^{\alpha_1\alpha_3} K_{\alpha_3\beta_3} \mathbb{K}^{\beta_3\beta_4} K_{\beta_4\alpha_4} K^{\alpha_4\alpha_2} & -\sum_{\alpha_3\in\mathbb{O},\beta_3\in\mathbb{P}} K^{\alpha_1\alpha_3} K_{\alpha_3\beta_3} \mathbb{K}^{\beta_3\beta_2} \\ -\sum_{\alpha_3\in\mathbb{O},\beta_3\in\mathbb{P}} \mathbb{K}^{\beta_1\beta_3} K_{\beta_3\alpha_3} K^{\alpha_3\alpha_2} & \mathbb{K}^{\beta_1\beta_2}, \end{bmatrix} \tag{B.3}$$

where in the above notation, $\mathbb{K}^{pp}$ is defined as $(K_{pp} - K_{po}K_{oo}^{-1}K_{op})^{-1}$, and the expression for $\mathbb{K}p_1p_2$ is $Kp_1p_2 - \sum_{o_3,o_4\in\mathbb{O}} K_{p_1o_3}K^{o_3o_4}K_{o_4p_2}$.

Now, We can rewrite the exponent in Eq.B.1 using the $K^{\mu_1\mu_2}$ matrix:

$$
\begin{aligned}
&-\frac{1}{2}\sum_{i,j=1}^{n}\sum_{\mu_1,\mu_2\in\mathbb{P}\cup\mathbb{O}} K^{ij,\mu_1\mu_2}f_{i,\mu_1}f_{j,\mu_2} = -\frac{1}{2}\sum_{ij=1}^{n}\sum_{\beta_1,\beta_2\in\mathbb{P}} \mathbb{K}^{ij,\beta_1\beta_2}f_{i,\beta_1}f_{j,\beta_2} - \frac{1}{2}\sum_{i,j=1}^{n}\sum_{\alpha_1,\alpha_2\in\mathbb{O}} K^{ij,\alpha_1\alpha_2}y_{i,\alpha_1}y_{j,\alpha_2} \\
&-\frac{1}{2}\sum_{i,j=1}^{n}\sum_{\alpha_1,\in\mathbb{O},\beta_1\in\mathbb{P}} K^{ij,\alpha_1\beta_1}f_{i,\beta_1}y_{j,\alpha_1} - \frac{1}{2}\sum_{i,j=1}^{n}\sum_{\alpha_1,\in\mathbb{O},\beta_1\in\mathbb{P}} K^{ij,\beta_1\alpha_1}f_{j,\beta_1}y_{i,\alpha_1} \\
&= -\frac{1}{2}\sum_{i,j=1}^{n}\sum_{\beta_1,\beta_2\in\mathbb{P}} \mathbb{K}^{ij,\beta_1\beta_2}[f_{i,\beta_1} - \sum_{\alpha_3,\alpha_4\in\mathbb{O}} K_{ij,\beta_1\alpha_3}K^{ij,\alpha_3\alpha_4}y_{j,\alpha_4}][f_{i,\beta_2} - \sum_{\alpha_3',\alpha_4'\in\mathbb{O}} K_{ij,\beta_2\alpha_3'}K^{ij,\alpha_3'\alpha_4'}y_{j,\alpha_4'}] \\
&-\frac{1}{2}\sum_{ij=1}^{n}\sum_{\alpha_1,\alpha_2\in\mathbb{O}} K^{ij,\alpha_1\alpha_2}y_{i,\alpha_1}y_{j,\alpha_2} - \frac{1}{2}\sum_{i,j=1}^{n}\sum_{\beta_1,\beta_2\in\mathbb{O}} \mathbb{K}^{ij,\beta_1\beta_2}(\sum_{\alpha_3,\alpha_4\in\mathbb{O}} K_{ij,\beta_1\alpha_3}K^{ij,\alpha_3\alpha_4}y_{i,\alpha_4}) \\
&\times(\sum_{\alpha_3',\alpha_4'\in\mathbb{O}} K_{ij,\beta_2\alpha_3'}K^{ij,\alpha_3'\alpha_4'}y_{j,\alpha_4'}).
\end{aligned}
\tag{B.4}
$$

By defining $m_{i,\beta}^{\infty} = \sum_{\alpha_1\alpha_2} K_{ij,\beta\alpha_1}K^{ij,\alpha_1\alpha_2}y_{j,\alpha_2}$, we can ultimately express the posterior distribution Eq.B.1 as:

$$
\begin{aligned}
p(f) := p(f_{\mathbb{O}}, f_{\mathbb{P}}) = \frac{1}{\sqrt{|2\pi K|^n}}\exp\Bigg(&-\frac{1}{2}\sum_{ij=1}^{n}\sum_{\alpha_1,\alpha_2\in\mathbb{O}} K^{ij,\alpha_1\alpha_2}y_{i,\alpha_1}y_{j,\alpha_2} - \frac{1}{2}\sum_{ij=1}^{n}\sum_{\beta_1,\beta_2\in\mathbb{O}} \mathbb{K}^{ij,\beta_1\beta_2}m_{i,\beta_1}^{\infty}m_{j,\beta_2}^{\infty}\Bigg) \\
&\times -\frac{1}{2}\sum_{ij=1}^{n}\sum_{\beta_1,\beta_2\in\mathbb{P}} \mathbb{K}^{ij,\beta_1\beta_2}[f_{i,\beta_1} - m_{i,\beta_1}^{\infty}][f_{j,\beta_2} - m_{j,\beta_2}^{\infty}]
\end{aligned}
\tag{B.5}
$$

The aforementioned joint posterior distribution lets us ascertain our desired posterior distribution

for unobserved data $f \in \mathbb{O}$, as outlined in Eq.3.23:

$$p(f|f_{\mathbb{O}}) = C_{(2)}(f_{\mathbb{O}}) \times \exp\left[-\frac{1}{2}\sum_{ij=1}^{n}\sum_{\beta_1,\beta_2\in\mathbb{P}} \mathbb{K}^{ij,\beta_1\beta_2}[f_{i,\beta_1} - m^{\infty}_{i,\beta_1}][f_{j,\beta_2} - m^{\infty}_{j,\beta_2}]\right], \tag{B.6}$$

where $C(f_{\mathbb{O}})$ is solely a function of the previously observed data, $f_{\mathbb{O}}$, and can be considered as a constant.

Therefore, we can deduce that in the case of an infinitely deep scenario, the output of the QNN follows a Gaussian process with the respective mean and variance:

$$\begin{aligned} p(f) &\sim \mathcal{GP}(m, \mathbb{K}), \\ [m]_{i,\mu} &= \sum_{\lambda,\sigma\in\mathbb{O}} K_{ij,\mu\lambda}K^{ij,\lambda\sigma}y_{i,\sigma}, \\ [\mathbb{K}]_{ij,\mu\nu} &= K_{ij,\mu\nu} - \sum_{ij,\lambda,\sigma\in\mathbb{O}} K_{ij,\mu\lambda}K^{ij,\lambda\sigma}K_{ij,\sigma\nu}. \end{aligned} \tag{B.7}$$

or equivalently

$$
\begin{aligned}
[m]_{i,\beta} &= \sum_{\alpha_1,\alpha_2\in\mathbb{O}} K_{ij,\beta\alpha_1}K^{ij,\alpha_1\alpha_2}y_{i,\alpha_2} = \sum_{\alpha_1,\alpha_2\in\mathbb{O}} \mathbb{E}[f_i f_j]_{\beta,\alpha_1}\mathbb{E}[f_i f_j]^{-1}_{\alpha_1,\alpha_2}y_{i,\alpha_2} \\
&= \sum_{\alpha_1,\alpha_2\in\mathbb{O}} [\frac{1}{d^2}\operatorname{Tr}(O_iO_j)\operatorname{Tr}(\rho_\beta\rho_{\alpha_1})][\frac{1}{d^2}\operatorname{Tr}(O_iO_j)\operatorname{Tr}(\rho_{\sharp_1}\rho_{\sharp_2})]^{-1}_{\alpha_1\alpha_2}y_{i,\alpha_2} + \mathcal{O}(\frac{1}{d^2}) \\
[\mathbb{K}]_{ij,\beta_1\beta_2} &= K_{ij,\beta_1\beta_2} - \sum_{\alpha_1,\alpha_2\in\mathbb{O}} K_{ij,\beta_1\beta_2}K^{ij,\beta_2\alpha_2}K_{ij,\alpha_2\beta_2} \\
&= \mathbb{E}[f_i f_j]_{\beta_1\beta_2} - \sum_{\alpha_1,\alpha_2\in\mathbb{O}} \mathbb{E}[f_i f_j]_{\beta_1\beta_2}\mathbb{E}[f_i f_j]^{-1}_{\beta_2\alpha_2}\mathbb{E}[f_i f_j]_{\alpha_2\beta_2} \\
&= \frac{\operatorname{Tr}(O_iO_j)}{d^2}[\operatorname{Tr}(\rho_{\beta_1}\rho_{\beta_2}) - \sum_{\alpha_1,\alpha_2\in\mathbb{O}} \operatorname{Tr}(\rho_{\beta_1}\rho_{\beta_2})\operatorname{Tr}(\rho_{\sharp_1}\rho_{\sharp_2})]^{-1}_{\beta_2\alpha_2}\operatorname{Tr}(\rho_{\alpha_2}\rho_{\beta_2})] + \mathcal{O}(\frac{1}{d^4}) \\
&:= \frac{\operatorname{Tr}(O_iO_j)}{d^2}[K^{\mathbb{Q}}_{\beta_1\beta_2} - \sum_{\alpha_1,\alpha_2\in\mathbb{O}} K^{\mathbb{Q}}_{\beta_1\beta_2}(K^{\mathbb{Q}})^{-1}_{\beta_1 2\alpha_2}K^{\mathbb{Q}}_{\alpha_2\beta_2}] + \mathcal{O}(\frac{1}{d^4})
\end{aligned}
\tag{B.8}
$$

B.2 Beyond Gaussian Distribution and $\frac{1}{d}$ Expansion

Here, we utilize the notation as prescribed by [93] and reproduce the calculation performed in that textbook for our quantum scenario, where the k-point functions may not exhibit perfect symmetry.

This is due to the fact that despite the orthonormal random matrix which can be written as sum over pairings, this theorem doesn't hold to the random unitary in general

This comes from the observation that

$$
\mathbb{E}[f_1\cdots f_k] = \mathbb{E}[\operatorname{Tr}\big(U_1\rho_1U^\dagger O_1\big)\cdots\operatorname{Tr}\big(U_k\rho_kU^\dagger O_k\big)] \tag{B.9}
$$

By assuming the parity symmetry of the output , f, with respect to zero, we can describe the output distribution by series of the even moments(correlation function) denominated as $p(f)$. These moments are defined as:

$$\mathbb{E}[f_1 f_2 \cdots f_k] = \int df^k p(f) f_1 f_2 \cdots f_k \tag{B.10}$$

which is zero for while is$k$ is an odd number. Based on these $k-$point correlators, the distributions can be defined as follows:

$$p(f) = \frac{e^{-S(f)}}{\mathcal{Z}} \tag{B.11}$$

such that the action, $S(\cdot)$ is given by:

$$S(f) = \frac{1}{2} \sum_{\mu,\nu=1}^{n} K^{\mu\nu} f_\mu f_\nu + \sum_{m=2}^{\Lambda} \frac{1}{(2m)!} \sum_{\mu_1,\cdots\mu_{2m}=1} C^{\mu_1\cdots\mu_{2m}} f_{\mu_1} \cdots f_{\mu_{2m}}, \tag{B.12}$$

Here, $C^{\mu_1\cdots\mu_{2m}}$ is the m-th order couplings, and Λ is the practical limit for cutting the series and limiting it to some Λ-th order. The partition function, $\mathcal{Z}$ in the denominator in Eq.B.11is defined as:

$$\mathcal{Z} = \int d^n f e^{-S(f)} \tag{B.13}$$

.

An action with a small fourth-order interaction can provide the first leading order of deviation from Gaussian distribution. This nearly Gaussian action can be defined as follows:

$$S_{\text{NG}} := \frac{1}{2} \sum_{\mu,\nu=1}^{n} K^{\mu\nu} f_\mu f_\nu - \frac{\lambda}{4!} \sum_{\nu_1\nu_2\nu_3\nu_4=1}^{n} V^{\nu_1\nu_2\nu_3\nu_4} f_{\nu_1} f_{\nu_2} f_{\nu_3} f_{\nu_4} + \mathcal{O}(\lambda^2). \tag{B.14}$$

We can take this one step further and construct actions beyond nearly Gaussian, and so forth:

$$\begin{aligned} S_{\text{NNG}} :=& \frac{1}{2}\sum_{\mu,\nu=1}^{n} K^{\mu\nu} f_\mu f_\nu - \frac{\lambda}{4!}\sum_{\nu_1\nu_2\nu_3\nu_4=1}^{n} V^{\nu_1\nu_2\nu_3\nu_4} f_{\nu_1} f_{\nu_2} f_{\nu_3} f_{\nu_4} \\ &+ \frac{\lambda^2}{4!}\sum_{\nu_1\nu_2\nu_3\nu_4,\nu_5,\nu_6=1}^{n} U^{\nu_1\nu_2\nu_3\nu_4\nu_5\nu_6} f_{\nu_1} f_{\nu_2} f_{\nu_3} f_{\nu_4} f_{\nu_5} f_{\nu_6} + \mathcal{O}(\lambda^3) \end{aligned} \tag{B.15}$$

The partition function of the nearly Gaussian action can be calculated by:

$$\begin{aligned} \mathcal{Z}_{\text{NG}} &= \int \prod_\mu df_\mu e^{-S(f)} = \sqrt{|2\pi K|}\mathbb{E}_K[e^{-\frac{\lambda}{4!}\sum_{\nu_1\nu_2\nu_3\nu_4=1}^{n} V^{\nu_1\nu_2\nu_3\nu_4} f_{\nu_1} f_{\nu_2} f_{\nu_3} f_{\nu_4}}] \\ &= \sqrt{|2\pi K|}\mathbb{E}_K[1 - \frac{\lambda}{4!}\sum_{\nu_1\nu_2\nu_3\nu_4=1}^{n} V^{\nu_1\nu_2\nu_3\nu_4} f_{\nu_1} f_{\nu_2} f_{\nu_3} f_{\nu_4} + \mathcal{O}(\lambda^2)] \\ &= \sqrt{|2\pi K|}[1 - \frac{3\lambda}{4!}\sum_{\nu_1\nu_2\nu_3\nu_4} V^{\nu_1\nu_2\nu_3\nu_4} K_{\nu_1\nu_2} K_{\nu_3\nu_4} + \mathcal{O}(\lambda^2)] \end{aligned} \tag{B.16}$$

In the third line, we used the Wicks theorem which holds for Gaussian distribution:

$$\mathbb{E}_K[f_1 \cdots f_{2k}] = \sum_{\text{all pairs}} \mathbb{E}_K[f_{i_1} f_{j_1}] \cdots \mathbb{E}_K[f_{i_k} f_{j_k}] \tag{B.17}$$

the second term in the nearly-Gaussian action can be re-written in terms of Δ:

$$
\begin{aligned}
S_2 &= \frac{1}{4!}[\sum_{\substack{j_1j_2j_3j_4\\ \mu_1\mu_2\mu_3\mu_4\mathbb{O}\cup\mathbb{P}}} V^{j_1j_2j_3j_4,\mu_1\mu_2\mu_3\mu_4} f_{j_1,\mu_1} f_{j_2,\mu_2} f_{j_3,\mu_3} f_{j_4,\mu_4}] \\
&= \frac{1}{4!}[\sum_{\substack{j_1j_2j_3j_4\\ \mu_1\mu_2\mu_3\mu_4\mathbb{O}}} V^{j_1j_2j_3j_4,\mu_1\mu_2\mu_3\mu_4} y_{j_1,\mu_1} y_{j_2,\mu_2} y_{j_3,\mu_3} y_{j_4,\mu_4}] \\
&+ \sum_{j_1j_2j_3j_4} \sum_{\beta_1\beta_2\beta_3\beta_4\in\mathbb{P}} V^{j_1j_2j_3j_4,\beta_1\beta_2\beta_3\beta_4} f_{j_1,\beta_1} f_{j_2,\beta_2} f_{j_3,\beta_3} f_{j_4,\beta_4} \\
&+ 4 \sum_{\substack{j_1,j_2\\ \beta_1\beta_2\in\mathbb{P}}} f_{j_1,\beta_1} f_{j_2,\beta_2} \sum_{\substack{j_3j_4\\ \alpha_3\alpha_4\in\mathbb{O}}} V^{j_1j_2j_3j_4,\beta_1\beta_2\alpha_3\alpha_4} y_{j_3,\alpha_3} y_{j_4,\alpha_4} \\
&4 \sum_{\substack{j_1j_2j_3\\ \beta_1\beta_2\beta_3\in\mathbb{P}}} f_{j_1,\beta_1} f_{j_2,\beta_2} f_{j_3,\beta_3} \sum_{j_4,\alpha\in\mathbb{O}} V^{j_1j_2j_3j_4,\beta_1\beta_2\beta_3\alpha} y_{j_4,\alpha} \\
&4 \sum_{j_1,\beta\in\mathbb{P}} f_{j_1,\beta} \sum_{\substack{j_2j_3j_4\\ \alpha_2\alpha_3\alpha_4\in\mathbb{O}}} V^{j_1j_2j_3j_4,\beta\alpha_2\alpha_3\alpha_4} y_{j_2,\alpha_2} y_{j_3,\alpha_3} y_{j_4,\alpha_4}
\end{aligned}
\tag{B.18}
$$

Now, with the explicit relations for S_1 and S_2, we can derive the correlation functions in terms of K, V, and the y variables. similar to the classical one, by adhering to the notation and methodology in [93], we can write the first-order correlation function, the mean, as:

$$
\begin{aligned}
\mathbb{E}[f_{i,\beta}] &= \int df p(f|y) f_{i,\beta} = \int df \frac{e^{-S_1}}{Z}[e^{-S_2} f_{i,\beta}] = \int df \frac{e^{-S_1}}{Z'}[e^{-S_2(f-m^\infty)}((f_{i,\beta}-m^\infty_{i,\beta})+m^\infty_{i,\beta})] \\
&= m^\infty_{i,\beta} + \mathbb{E}_{S_1}[(f_{i,\beta}-m^\infty_{i,\beta}) e^{S_2(f-m^\infty)}] \\
&= m^\infty_{i,\beta} + \frac{1}{3!}\sum_{j_1,\beta\in\mathbb{P}} K_{ij_1,\beta\beta_1}[\sum_{\substack{j_2j_3j_4\\ \alpha_2\alpha_3\alpha_4\in\mathbb{O}}} V^{j_1j_2j_3j_4,\beta\alpha_2\alpha_3\alpha_4} y_{j_2,\alpha_2} y_{j_3,\alpha_3} y_{j_4,\alpha_4}] \\
&\frac{1}{3!}\sum_{\substack{j_1j_2j_3\\ \beta_1\beta_2\beta_3\in\mathbb{P}}} [K_{ij_1,\beta\beta_1} K_{j_2j_3,\beta_2\beta_3} + K_{ij_2,\beta\beta_2} K_{j_1j_3,\beta_1\beta_3} + K_{ij_3,\beta\beta_3} K_{j_1j_2,\beta_1\beta_2}] \sum_{j_4,\alpha\in\mathbb{O}} V^{j_1j_2j_3j_4,\beta_1\beta_2\beta_3\alpha} y_{j_4,\alpha}
\end{aligned}
\tag{B.19}
$$

we can evaluate the second moment using the following equation:

$$\begin{aligned}\mathbb{E}[f_{\mu_1} f_{\mu_2}] &= \frac{1}{\mathcal{Z}} \int \prod_{\mu} df_{\mu} e^{-S(f)} f_{\mu_1} f_{\mu_2} = \frac{\sqrt{|2\pi K|}}{\mathcal{Z}} \mathbb{E}_K[f_{\mu_1} f_{\mu_2} e^{-\frac{\lambda}{4!}\sum_{\nu_1\nu_2\nu_3\nu_4} V^{\nu_1\nu_2\nu_3\nu_4} f_{\nu_1} f_{\nu_2} f_{\nu_3} f_{\nu_4}}] \\ &= \frac{1}{\mathcal{Z}} [\mathbb{E}_K[f_{\mu_1} f_{\mu_2}] - \frac{\lambda}{4!} \sum_{\nu_1\nu_2\nu_3\nu_4} V^{\nu_1\nu_2\nu_3\nu_4} \mathbb{E}_K[f_{\mu_1} f_{\mu_2} f_{\nu_1} f_{\nu_2} f_{\nu_3} f_{\nu_4}] + \mathcal{O}(\lambda^2)] \\ &= K_{\mu_1\mu_2} - \frac{\lambda}{2} \sum_{\nu_1\nu_2\nu_3\nu_4} V^{\nu_1\nu_2\nu_3\nu_4} K_{\mu_1\nu_1} K_{\mu_2\nu_2} K_{\nu_3\nu_4} + \mathcal{O}(\lambda^2),\end{aligned} \tag{B.20}$$

and we obtain a similar outcome for the connected two-point correlator because:

$$\mathbb{E}[f_{\mu_1} f_{\mu_2}]|_{\text{connected}} = \mathbb{E}[f_{\mu_1} f_{\mu_2}] - \mathbb{E}[f_{\mu_1}]\mathbb{E}[f_{\mu_2}] = \mathbb{E}[f_{\mu_1} f_{\mu_2}]. \tag{B.21}$$

Now, by incorporating the measurement indices, we get:

$$\mathbb{E}[f_{i_1,\mu_1} f_{i_2,\mu_2}]|_{\text{conn.}} = K_{i_1 i_2, \mu_1\mu_2} - \frac{\lambda}{2} \sum_{\substack{j_1 j_2 j_3 j_4 = 1 \\ \nu_1\nu_2\nu_3\nu_4}} V^{j_1 j_2 j_3 j_4, \nu_1\nu_2\nu_3\nu_4} K_{i_1 j_1, \mu_1\nu_1} K_{i_2 j_2, \mu_2\nu_2} K_{j_3 j_4, \nu_3\nu_4} + \mathcal{O}(\lambda^2) \tag{B.22}$$

Our subsequent action entails computing the fourth moment:

$$
\begin{aligned}
\mathbb{E}[f_{\mu_1} f_{\mu_2} f_{\mu_3} f_{\mu_4}] &= \int \prod_{\mu} df_{\mu} e^{-\mathcal{S}(f)} f_{\mu_1} f_{\mu_2} f_{\mu_3} f_{\mu_4} \\
&= \frac{\sqrt{|2\pi K|}}{\mathcal{Z}} [\langle f_{\mu_1} f_{\mu_2} f_{\mu_3} f_{\mu_4} \rangle_K - \frac{\lambda}{4!} \sum_{\nu_1 \nu_2 \nu_3 \nu_4} V^{\nu_1 \nu_2 \nu_3 \nu_4} \langle f_{\mu_1} f_{\mu_2} f_{\nu_1} f_{\nu_2} f_{\nu_3} f_{\nu_4} \rangle_K + \mathcal{O}(\lambda^2)] \\
&= \frac{\sqrt{|2\pi K|}}{\mathcal{Z}} [(\sum_{\text{all 3 pairing}} K_{\mu_{\ell_1} \mu_{\ell_2}} K_{\mu_{\ell_3} \mu_{\ell_4}}) - \frac{\lambda}{4!} \sum_{\text{all 15 pairing}} K_{\mu_{\ell_1} \mu_{\ell_2}} \cdots K_{\mu_{\ell_5} \mu_{\ell_6}} + \mathcal{O}(\lambda^2)] \\
&= [1 - \frac{3\lambda}{4!} \sum_{\nu_1 \nu_2 \nu_3 \nu_4} V^{\nu_1 \nu_2 \nu_3 \nu_4} K_{\nu_1 \nu_2} K_{\nu_3 \nu_4} + \mathcal{O}(\lambda^2)] \times [(\sum_{\text{all 3 pairing}} K_{\mu_{\ell_1} \mu_{\ell_2}} K_{\mu_{\ell_3} \mu_{\ell_4}}) \\
&- \frac{\lambda}{4!} \sum_{\text{all 15 pairing}} K_{\mu_{\ell_1} \mu_{\ell_2}} \cdots K_{\mu_{\ell_5} \mu_{\ell_6}} + \mathcal{O}(\lambda^2)] \\
&= K_{\mu_1 \mu_2} K_{\mu_3 \mu_4} \\
&- \frac{\lambda}{4!} \sum_{\nu_1 \nu_2 \nu_3 \nu_4} V^{\nu_1 \nu_2 \nu_3 \nu_4} [12 K_{\mu_1 \nu_1} K_{\mu_2 \nu_2} K_{\mu_3 \mu_4} K_{\nu_3 \nu_4} + 12 K_{\mu_3 \nu_1} K_{\mu_4 \mu_2} K_{\mu_1 \mu_2} K_{\nu_3 \nu_4}] \\
&+ K_{\mu_1 \mu_3} K_{\mu_2 \mu_4} \\
&- \frac{\lambda}{4!} \sum_{\nu_1 \nu_2 \nu_3 \nu_4} V^{\nu_1 \nu_2 \nu_3 \nu_4} [12 K_{\mu_1 \nu_1} K_{\mu_3 \nu_3} K_{\mu_2 \mu_4} K_{\nu_3 \nu_4} + 12 K_{\mu_2 \nu_1} K_{\mu_4 \mu_3} K_{\mu_1 \mu_3} K_{\nu_3 \nu_4}] \\
&+ K_{\mu_1 \mu_4} K_{\mu_2 \mu_3} \\
&- \frac{\lambda}{4!} \sum_{\nu_1 \nu_2 \nu_3 \nu_4} V^{\nu_1 \nu_2 \nu_3 \nu_4} [12 K_{\mu_1 \nu_1} K_{\mu_4 \nu_3} K_{\mu_2 \mu_3} K_{\nu_3 \nu_4} + 12 K_{\mu_2 \nu_1} K_{\mu_3 \mu_4} K_{\mu_1 \mu_4} K_{\nu_3 \nu_4}] \\
&- \lambda \sum_{\nu_1 \nu_2 \nu_3 \nu_4} V^{\nu_1 \nu_2 \nu_3 \nu_4} K_{\mu_1 \nu_1} K_{\mu_2 \nu_2} K_{\mu_3 \nu_3} K_{\mu_4 \nu_4} + \mathcal{O}(\lambda^2) \\
&= \mathbb{E}[f_{\mu_1} f_{\mu_2}] \mathbb{E}[f_{\mu_3} f_{\mu_4}] + \mathbb{E}[f_{\mu_1} f_{\mu_3}] \mathbb{E}[f_{\mu_2} f_{\mu_4}] + \mathbb{E}[f_{\mu_1} f_{\mu_4}] \mathbb{E}[f_{\mu_2} f_{\mu_3}] \\
&- \lambda \sum_{\nu_1 \nu_2 \nu_3 \nu_4} V^{\nu_1 \nu_2 \nu_3 \nu_4} K_{\mu_1 \nu_1} K_{\mu_2 \nu_2} K_{\mu_3 \nu_3} K_{\mu_4 \nu_4} + \mathcal{O}(\lambda^2),
\end{aligned}
\tag{B.23}
$$

Then, after incorporating the measurement indices, we obtain:

$$\mathbb{E}[f_{i_1,\mu_1} f_{i_2,\mu_2} f_{i_3,\mu_3} f_{i_4,\mu_4}]|_{\text{connected}} = \tag{B.24}$$

$$-\lambda \sum_{\substack{j_1 j_2 j_3 j_4 = 1 \\ \nu_1 \nu_2 \nu_3 \nu_4}} V^{j_1 j_2 j_3 j_4, \nu_1 \nu_2 \nu_3 \nu_4} K_{i_1 j_1, \mu_1 \nu_1} K_{i_2 j_2, \mu_2 \nu_2} K_{j_3 j_4, \mu_3 \nu_3} K_{\mu_4 \nu_4} + \mathcal{O}(\lambda^2) \tag{B.25}$$

With the relation in Eq.B.20 and Eq.B.24 we can Find explicit form of K and V:

$$\mathbb{Q}^{i_1 i_2}_{\mu_1 \mu_2} = K^{i_1 i_2}_{\mu_1 \mu_2} - \frac{\lambda}{2} \sum_{j_1 j_2 j_3 j_4} \sum_{\nu_1 \nu_2 \nu_3 \nu_4} V^{\nu_1 \nu_2 \nu_3 \nu_4}_{j_1 j_2 j_3 j_4} K^{j_1 i_1}_{\mu_1 \nu_1} K^{j_2 i_2}_{\mu_2 \nu_1} K^{j_3 i_3}_{\nu_3 \nu_4} + \mathcal{O}(\lambda^2) \tag{B.26}$$

and

$$\mathbb{V}_{\mu_1 \mu_2 \mu_3 \mu_4} = -\lambda \sum_{\nu_1 \nu_2 \nu_3 \nu_4} V^{\nu_1 \nu_2 \nu_3 \nu_4} K_{\mu_1 \nu_1} K_{\mu_2 \nu_2} K_{\mu_3 \nu_3} K_{\mu_4 \nu_4} + \mathcal{O}(\lambda^2) \tag{B.27}$$

$$\mathbb{V}_{i_1 i_2 i_3 i_4, \mu_1 \mu_2 \mu_3 \mu_4} = -\lambda \sum_{j_1 j_2 j_3 j_4} \sum_{\nu_1 \nu_2 \nu_3 \nu_4} V^{j_1 j_2 j_3 j_4, \nu_1 \nu_2 \nu_3 \nu_4} K_{i_1 j_1, \mu_1 \nu_1} K_{i_2 j_2, \mu_2 \nu_2} K_{i_3 j_3, \mu_3 \nu_3} K_{i_4 j_4, \mu_4 \nu_4} + \mathcal{O}(\lambda^2) \tag{B.28}$$

B.3 Haar average

In this section, we will demonstrate how to compute the two-point correlation functions as a quantum kernel.

$$\mathbb{Q} := \mathbb{E}_{p \sim \text{Haar}(U(\boldsymbol{\theta}))}[f_{i_1,\alpha_1}(U(\boldsymbol{\theta})) f_{i_2,\alpha_2}(U(\boldsymbol{\theta}))] \tag{B.29}$$

and four point correlation function as quantum kernel Quantum meta Kernel

$$\mathbb{V} := \mathbb{E}_{p\sim \text{Haar}(U(\boldsymbol{\theta}))}[f_{i_1,\alpha_1}(U(\boldsymbol{\theta}))f_{i_2,\alpha_2}(U(\boldsymbol{\theta}))f_{i_3,\alpha_3}(U(\boldsymbol{\theta}))f_{i_4,\alpha_4}(U(\boldsymbol{\theta}))] \tag{B.30}$$

and how get express them as series of Hilbert space's dimension, d:

$$\mathbb{Q}_{i_1 i_2,\mu_1\mu_2} = \mathbb{E}[f_{i_1,\mu_1} f_{i_2,\mu_2}] = \frac{Q^{[2]}_{i_1 i_2,\mu_1\mu_2}}{d^2} + \frac{Q^{[3]}_{i_1 i_2,\mu_1\mu_2}}{d^3} + \cdots := \hat{\mathbb{Q}}_{i_1 i_2,\mu_1\mu_2} + \mathbb{Q}_{i_1 i_2,\mu_1\mu_2} + \mathcal{O}(\frac{1}{d^4}) \tag{B.31}$$

and Similarly

$$\mathbb{V}_{i_1 i_2 i_3 i_4,\mu_1\mu_2\mu_3\mu_4} = \mathbb{E}[f_{i_1,\mu_1} f_{i_2,\mu_2} f_{i_3,\mu_3} f_{i_4,\mu_4}] = \frac{V^{[4]}_{\sharp}}{d^4} + \frac{V^{[5]}_{\sharp}}{d^5} + \cdots := \hat{\mathbb{V}}_{\sharp} + \mathbb{V}_{\sharp} + \mathcal{O}(\frac{1}{d^6}) \tag{B.32}$$

B.3.1 Two point correlation

In order to calculate the two-point correlation, for $t-$design circuit, as discusse the main text, it is necessary to perform Haar averaging over terms such as $\text{Tr}(\cdot)\,\text{Tr}(\cdot)$. To transform this form into the identity described in Equation 3.7, we can define projection operators $P_{r_1 r_2}$ in the following manner:

$$\begin{aligned}\operatorname{Tr}\big(\rho_1 U O_1 U^\dagger\big)\operatorname{Tr}\big(\rho_2 U O_2 U^\dagger\big) &= \sum_{i_1}\sum_{i_2}\langle i_1|\rho_1 U O_1 U^\dagger|i_1\rangle\langle i_2|\rho_2 U O_2 U^\dagger|i_2\rangle \\ &= \sum_{i_1,i_2}\operatorname{Tr}\big(P_{21}\rho_1 U O_1 U^\dagger P_{12}\rho_2 U O_2 U^\dagger\big) \\ &:= \sum_{i_1,i_2}\operatorname{Tr}\big(\tilde{\rho}_1 U O_1 U^\dagger \tilde{\rho}_2 U O_2 U^\dagger\big),\end{aligned} \tag{B.33}$$

where we have defined $P_{12} := |i_1\rangle\langle i_2|$, $P_{21} := |i_2\rangle\langle i_1|$ and $P\rho := \tilde{\rho}$. Then according to Eq.3.7

$$\begin{aligned}\mathbb{E}[\operatorname{Tr}\big(\tilde{\rho}_1 U O_1 U^\dagger \tilde{\rho}_2 U O_2 U^\dagger\big)] = \frac{1}{d^2-1}[\operatorname{Tr}(O_1)\operatorname{Tr}(O_2)\operatorname{Tr}(\tilde{\rho}_1\tilde{\rho}_2) + \operatorname{Tr}(O_1O_2)\operatorname{Tr}(\tilde{\rho}_1)\operatorname{Tr}(\tilde{\rho}_2)] \\ - \frac{1}{d^3-d}[\operatorname{Tr}(O_1O_2)\operatorname{Tr}(\tilde{\rho}_1\tilde{\rho}_2) + \operatorname{Tr}(O_1)\operatorname{Tr}(O_2)\operatorname{Tr}(\tilde{\rho}_1)\operatorname{Tr}(\tilde{\rho}_2))]\end{aligned} \tag{B.34}$$

Now, based on the given definition, we can rephrase $\tilde{\rho}$ as ρ as a following:

$$\operatorname{Tr}(\tilde{\rho}_1\tilde{\rho}_2) = \operatorname{Tr}(P_{21}\rho_1 P_{12}\rho_2) = \langle i_1|\rho_1|i_1\rangle\langle i_2|\rho_2|i_2\rangle \to \sum_{i_1,i_2}\operatorname{Tr}(\tilde{\rho}_1\tilde{\rho}_2) = \operatorname{Tr}(\rho_1)\operatorname{Tr}(\rho_2). \tag{B.35}$$

Similarly, we can apply the same rephrasing to other term:

$$\operatorname{Tr}(\tilde{\rho}_1)\operatorname{Tr}(\tilde{\rho}_2) = \operatorname{Tr}(P_{21}\rho_1)\operatorname{Tr}(P_{12}\rho_2) = \langle i_1|\rho_1|i_2\rangle\langle i_2|\rho_2|i_1\rangle \to \sum_{i_1 i_2}\operatorname{Tr}(\tilde{\rho}_1)\operatorname{Tr}(\tilde{\rho}_2) = \operatorname{Tr}(\rho_1\rho_2) \tag{B.36}$$

Therefore, Equation B.34 can be expressed using the actual density matrix as follows:

$$\begin{aligned}\mathbb{E}[\mathrm{Tr}\big(\rho_1 U O_1 U^\dagger\big)\,\mathrm{Tr}\big(\rho_2 U O_2 U^\dagger\big)] &= \sum_{i_1,i_2}\mathbb{E}[\mathrm{Tr}\big(\tilde{\rho}_1 U O_1 U^\dagger \tilde{\rho}_2 U O_2 U^\dagger\big)] \\ &= \frac{1}{d^2-1}[\mathrm{Tr}(O_1)\,\mathrm{Tr}(O_2)\,\mathrm{Tr}(\rho_1)\,\mathrm{Tr}(\rho_2) + \mathrm{Tr}(O_1O_2)\,\mathrm{Tr}(\rho_1\rho_2)] \\ &- \frac{1}{d^3-d}[\mathrm{Tr}(O_1O_2)\,\mathrm{Tr}(\rho_1)\,\mathrm{Tr}(\rho_2) + \mathrm{Tr}(O_1)\,\mathrm{Tr}(O_2)\,\mathrm{Tr}(\rho_1\rho_2))].\end{aligned} \tag{B.37}$$

To calculate the connected form of the two-point correlator, we can utilize the fact that the expectation value of odd correlations is zero. Similar to the previous identity, we obtain the following expression:

$$\begin{aligned}\mathbb{E}[f_{i_1,\alpha_1} f_{i_2,\alpha_2}]|_{\text{connected}} &= \mathbb{E}[f_{i_1,\alpha_1} f_{i_2,\alpha_2}] - \mathbb{E}[f_{i_1,\alpha_1}]\mathbb{E}[f_{i_2,\alpha_2}] \\ &= \frac{\mathrm{Tr}\,(O_{i_2}O_{i_1})}{d-d^3} + \frac{\mathrm{Tr}\,(O_{i_2}O_{i_1})\,\mathrm{Tr}\,(\rho_{\alpha_1}\rho_{\alpha_2})}{d^2-1} + \frac{\mathrm{Tr}\,(O_{i_1})\,\mathrm{Tr}\,(O_{i_2})}{d^2-1} \\ &+ \frac{\mathrm{Tr}\,(O_{i_1})\,\mathrm{Tr}\,(O_{i_2})\,\mathrm{Tr}\,(\rho_{\alpha_1})\,\mathrm{Tr}\,(\rho_{\alpha_2})}{d^2}.\end{aligned} \tag{B.38}$$

At large d, the two point correlator exhibits the following behavior:

$$\mathbb{E}[f_{i_1,\alpha_1} f_{i_2,\alpha_2}]|_{\text{connected}} = \frac{1}{d^2}[\mathrm{Tr}(\rho_{\alpha_1}\rho_{\alpha_2})\,\mathrm{Tr}(O_{i_1}O_{i_2})] + \mathcal{O}(\frac{1}{d^3}) \tag{B.39}$$

B.3.2 Four-point correlator

We can employ the same method discussed in Section B.3.1 to derive closed-form expressions for the four-point correlation function. We begin by considering the four-point interaction term:

$$\begin{aligned}
&\mathrm{Tr}\big(\rho_1 U O_1 U^\dagger\big)\,\mathrm{Tr}\big(\rho_2 U O_2 U^\dagger\big)\,\mathrm{Tr}\big(\rho_3 U O_3 U^\dagger\big)\,\mathrm{Tr}\big(\rho_4 U O_4 U^\dagger\big) \\
&= \sum_{i_1,i_2,i_3,i_4} \mathrm{Tr}\big(P_{41}\rho_1 U O_1 U^\dagger P_{12}\rho_2 U O_2 U^\dagger P_{23}\rho_3 U O_3 U^\dagger P_{34}\rho_3 U O_4 U^\dagger\big) \\
&= \sum_{i_1,i_2,i_3,i_4} \mathrm{Tr}\big(\tilde{\rho}_1 U O_1 U^\dagger \tilde{\rho}_2 U O_2 U^\dagger \tilde{\rho}_3 U O_3 U^\dagger \tilde{\rho}_4 U O_4 U^\dagger\big).
\end{aligned} \tag{B.40}$$

such that the projection operators map the density matrix to

$$\tilde{\rho}_1 = P_{41}\rho_1 = |i_4\rangle\langle i_1|\rho_1 \quad \tilde{\rho}_2 \tag{B.41}$$

$$= P_{12}\rho_2 = |i_1\rangle\langle i_2|\rho_2, \quad , \tilde{\rho}_3 = P_{23}\rho_3 = |i_2\rangle\langle i_3|\rho_3 \quad , \tilde{\rho}_4 \tag{B.42}$$

$$= P_{34}\rho_4 = |i_3\rangle\langle i_4|\rho_4. \tag{B.43}$$

By this definition, we can observe that, for example, $\mathrm{Tr}(\tilde{\rho}_1\tilde{\rho}_2\tilde{\rho}_3\tilde{\rho}_4) = \mathrm{Tr}(\rho_1)\,\mathrm{Tr}(\rho_2)\,\mathrm{Tr}(\rho_3)\,\mathrm{Tr}(\rho_4) = 1$. Similarly, $\mathrm{Tr}(\tilde{\rho}_1\tilde{\rho}_4\tilde{\rho}_3\tilde{\rho}_2) = \mathrm{Tr}(\rho_1\rho_3)\,\mathrm{Tr}(\rho_2\rho_4)$, and so on. Now by employing Eq.3.7 we get the bare four point correlator as follows with the help of [89] package:

$$\int_{\mathcal{N}(d)} \mathrm{Tr}\big(U^\dagger O U X U^\dagger O U Y U^\dagger O U Z U^\dagger O U W\big) d\mu(U) = \frac{d^4 - 8d^2 + 6}{d^2(d^6 - 14d^4 + 49d^2 - 36)} \times [$$

$$\mathrm{Tr}\,(O_1)\,\mathrm{Tr}\,(O_2)\,\mathrm{Tr}\,(O_3)\,\mathrm{Tr}\,(O_4)\,\mathrm{Tr}(XYZW) + \mathrm{Tr}\,(O_2O_1)\,\mathrm{Tr}\,(O_3)\,\mathrm{Tr}\,(O_4)\,\mathrm{Tr}(Y)\mathrm{Tr}(XZW)$$

$$\mathrm{Tr}\,(O_3O_2)\,\mathrm{Tr}\,(O_1)\,\mathrm{Tr}\,(O_4)\,\mathrm{Tr}(Z)\mathrm{Tr}(XYW) + \mathrm{Tr}\,(O_3O_1)\,\mathrm{Tr}\,(O_2)\,\mathrm{Tr}\,(O_4)\,\mathrm{Tr}(XW)\mathrm{Tr}(ZY)$$

$$\mathrm{Tr}\,(O_2O_3O_1)\,\mathrm{Tr}\,(O_4)\,\mathrm{Tr}(Y)\mathrm{Tr}(Z)\mathrm{Tr}(XW) + \mathrm{Tr}\,(O_3O_2O_1)\,\mathrm{Tr}\,(O_4)\,\mathrm{Tr}(XZYW)$$

$$\mathrm{Tr}\,(O_4O_2)\,\mathrm{Tr}\,(O_1)\,\mathrm{Tr}\,(O_3)\,\mathrm{Tr}(WZ)\mathrm{Tr}(XY) + \mathrm{Tr}\,(O_4O_1)\,\mathrm{Tr}\,(O_2)\,\mathrm{Tr}\,(O_3)\,\mathrm{Tr}(X)\mathrm{Tr}(ZWY)$$

$$\mathrm{Tr}\,(O_2O_4O_1)\,\mathrm{Tr}\,(O_3)\,\mathrm{Tr}(X)\mathrm{Tr}(Y)\mathrm{Tr}(WZ) + \mathrm{Tr}\,(O_4O_2O_1)\,\mathrm{Tr}\,(O_3)\,\mathrm{Tr}(XZWY)$$

$$\mathrm{Tr}\,(O_4O_3O_1)\,\mathrm{Tr}\,(O_2)\,\mathrm{Tr}(XWYZ) + \mathrm{Tr}\,(O_4O_3)\,\mathrm{Tr}\,(O_1)\,\mathrm{Tr}\,(O_2)\,\mathrm{Tr}(W)\mathrm{Tr}(XYZ)$$

$$\mathrm{Tr}\,(O_4O_3O_2)\,\mathrm{Tr}\,(O_1)\,\mathrm{Tr}(XYWZ) + \mathrm{Tr}\,(O_3O_4O_1)\,\mathrm{Tr}\,(O_2)\,\mathrm{Tr}(W)\mathrm{Tr}(X)\mathrm{Tr}(ZY)$$

$$\mathrm{Tr}\,(O_4O_3O_2O_1)\,\mathrm{Tr}(WY)\mathrm{Tr}(XZ) + \mathrm{Tr}\,(O_3O_4O_2)\,\mathrm{Tr}\,(O_1)\,\mathrm{Tr}(W)\mathrm{Tr}(Z)\mathrm{Tr}(XY)$$

$$\mathrm{Tr}\,(O_3O_4O_2O_1)\,\mathrm{Tr}(W)\mathrm{Tr}(XZY) + \mathrm{Tr}\,(O_4O_2O_3O_1)\,\mathrm{Tr}(Z)\mathrm{Tr}(XWY)$$

$$\mathrm{Tr}\,(O_2O_4O_3O_1)\,\mathrm{Tr}(Y)\mathrm{Tr}(XWZ) + \mathrm{Tr}\,(O_3O_2O_4O_1)\,\mathrm{Tr}(X)\mathrm{Tr}(WZY)$$

$$\mathrm{Tr}\,(O_3O_1)\,\mathrm{Tr}\,(O_4O_2)\,\mathrm{Tr}(XWZY) + \mathrm{Tr}\,(O_2O_3O_4O_1)\,\mathrm{Tr}(W)\mathrm{Tr}(X)\mathrm{Tr}(Y)\mathrm{Tr}(Z)$$

$$\mathrm{Tr}\,(O_3O_2)\,\mathrm{Tr}\,(O_4O_1)\,\mathrm{Tr}(X)\mathrm{Tr}(Z)\mathrm{Tr}(WY) + \mathrm{Tr}\,(O_2O_1)\,\mathrm{Tr}\,(O_4O_3)\,\mathrm{Tr}(W)\mathrm{Tr}(Y)\mathrm{Tr}(XZ)]$$

$$+ \frac{1}{d^5 - 10d^3 + 9d} \times [\cdots \text{ 49 terms } \cdots]$$

$$+ \frac{3\,(2d^2 - 3)}{d^2\,(d^6 - 14d^4 + 49d^2 - 36)} \times [\cdots \text{ 52 terms } \cdots]$$

$$+ \frac{1}{d^7 - 14d^5 + 49d^3 - 36d} \times [\cdots \text{ 53 terms } \cdots].$$

(B.44)

Then, according to the Wick theorem:

$$\mathbb{E}[f_1 f_2 f_3 f_4]|_{\text{connected}} = \mathbb{E}[f_1 f_2 f_3 f_4] - \mathbb{E}[f_1 f_2]\mathbb{E}[f_3 f_4] - \mathbb{E}[f_1 f_3]\mathbb{E}[f_2 f_4] - \mathbb{E}[f_1 f_4]\mathbb{E}[f_2 f_3] \quad \text{(B.45)}$$

Hence, the connected four-point correlator can be expressed as:

$$\begin{aligned}
&\mathbb{E}[\mathrm{Tr}\big(\rho_{\alpha_1} U O_i U^\dagger\big)\,\mathrm{Tr}\big(\rho_{\alpha_2} U O_j U^\dagger\big)\,\mathrm{Tr}\big(\rho_{\alpha_3} U O_k U^\dagger\big)\,\mathrm{Tr}\big(\rho_{\alpha_4} U O_\ell U^\dagger\big)]|_{\text{connected}} \\
&= \mathbb{E}[\mathrm{Tr}\big(\rho_{\alpha_1} U O_i U^\dagger\big)\,\mathrm{Tr}\big(\rho_{\alpha_2} U O_j U^\dagger\big)\,\mathrm{Tr}\big(\rho_{\alpha_3} U O_k U^\dagger\big)\,\mathrm{Tr}\big(\rho_{\alpha_4} U O_\ell U^\dagger\big)] \\
&- \mathbb{E}[\mathrm{Tr}\big(\rho_{\alpha_1} U O_i U^\dagger\big)\,\mathrm{Tr}\big(\rho_{\alpha_2} U O_j U^\dagger\big)]\mathbb{E}[\mathrm{Tr}\big(\rho_{\alpha_3} U O_k U^\dagger\big)\,\mathrm{Tr}\big(\rho_{\alpha_4} U O_\ell U^\dagger\big)] \\
&- \mathbb{E}[\mathrm{Tr}\big(\rho_{\alpha_1} U O_i U^\dagger\big)\,\mathrm{Tr}\big(\rho_{\alpha_3} U O_k U^\dagger\big)]\mathbb{E}[\mathrm{Tr}\big(\rho_{\alpha_2} U O_j U^\dagger\big)\,\mathrm{Tr}\big(\rho_{\alpha_4} U O_\ell U^\dagger\big)] \\
&- \mathbb{E}[\mathrm{Tr}\big(\rho_{\alpha_1} U O_i U^\dagger\big)\,\mathrm{Tr}\big(\rho_{\alpha_4} U O_\ell U^\dagger\big)]\mathbb{E}[\mathrm{Tr}\big(\rho_{\alpha_2} U O_j U^\dagger\big)\,\mathrm{Tr}\big(\rho_{\alpha_3} U O_k U^\dagger\big)].
\end{aligned} \quad \text{(B.46)}$$

This leads to a closed-form relation for the connected four-point correlator:

$$\begin{aligned}
\mathbb{E}[f_{i_1,\alpha_1} f_{i_2,\alpha_2} f_{i_3,\alpha_3} f_{i_4,\alpha_4}]|_{\text{connected}} = \frac{d^4 - 8d^2 + 6}{d^2(d^6 - 14d^4 + 49d^2 - 36)} \times [\\
&\mathrm{Tr}\left(\rho_{\alpha_1}\rho_{\alpha_2}\rho_{\alpha_3}\rho_{\alpha_4}\right) \times [\mathrm{Tr}\left(O_{i_1}O_{i_2}O_{i_3}O_{i_4}\right) + \mathrm{Tr}\left(O_{i_1}O_{i_2}O_{i_4}O_{i_3}\right) \\
&\mathrm{Tr}\left(O_{i_1}O_{i_3}O_{i_2}O_{i_4}\right) + \mathrm{Tr}\left(O_{i_1}O_{i_3}O_{i_4}O_{i_2}\right) + \mathrm{Tr}\left(O_{i_1}O_{i_4}O_{i_2}O_{i_3}\right) + \mathrm{Tr}\left(O_{i_1}O_{i_4}O_{i_3}O\right. \\
&\mathrm{Tr}\left(\rho_{\alpha_1}\rho_{\alpha_2}\rho_{\alpha_3}\right)\left(\mathrm{Tr}\left[O_{i_2}O_{i_3}O_{i_1}\right] + \mathrm{Tr}\left(O_{i_3}O_{i_2}O_{i_1}\right)\right)\mathrm{Tr}\left(O_{i_4}\right) \\
&\mathrm{Tr}\left(\rho_{\alpha_1}\rho_{\alpha_2}\rho_{\alpha_4}\right)\left(\mathrm{Tr}\left(O_{i_2}O_{i_4}O_{i_1}\right) + \mathrm{Tr}\left(O_{i_4}O_{i_2}O_{i_1}\right)\right)\mathrm{Tr}\left(O_{i_3}\right) \\
&\mathrm{Tr}\left(\rho_{\alpha_1}\rho_{\alpha_3}\rho_{\alpha_4}\right)\left(\mathrm{Tr}\left(O_{i_3}O_{i_4}O_{i_1}\right) + \mathrm{Tr}\left(O_{i_4}O_{i_3}O_{i_1}\right)\right)\mathrm{Tr}\left(O_{i_2}\right) \\
&\mathrm{Tr}\left(\rho_{\alpha_2}\rho_{\alpha_3}\rho_{\alpha_4}\right)\mathrm{Tr}\left(O_{i_1}\right)\left(\mathrm{Tr}\left(O_{i_3}O_{i_4}O_{i_2}\right) + \mathrm{Tr}\left(O_{i_4}O_{i_3}O_{i_2}\right) - 2\mathrm{Tr}\left(O_{i_2}\right)\mathrm{Tr}\left(O_{i_3}\right)\mathrm{T}\right. \\
&+ \mathcal{O}(\frac{1}{d^5})
\end{aligned} \quad \text{(B.47)}$$

Appendix C:

C.1 Continuum Limit and Effect of Boson-Fermion Interactions

The connection between lattice Hamiltonians to relativistic quantum field theories is established in a standard way by resorting to the low-energy limit of the former. In this appendix, we examine the low-energy limit of the Hamiltonian in Eq. (6.8), first on the square lattice and then on the honeycomb lattice. The connection to Dirac fermions of the continuum theory is made clear in the latter case. The case of the (1+1)D lattice is analyzed in detail in prior work, including in Ref. [175].

C.1.1 Square lattice: Fermi surface coupled to nuclear spins

First, we consider the free (kinetic) part of Eq. (6.8) on a square lattice, which represents a tight-binding fermion model,

$$H_{\mathrm{k}} = -\sum_{\langle i,j\rangle} t\left(c_i^\dagger c_j + \text{h.c.}\right) - \mu\sum_i n_i. \tag{C.1}$$

We assume the electron chemical potential is uniform throughout the lattice and further restrict it to $\mu = 0$, i.e., the half-filling limit. Let us define the momentum-space fermionic operator,

$$c_{\boldsymbol{k}} = \frac{1}{\sqrt{N}} \sum_i e^{-i\boldsymbol{k}\cdot\boldsymbol{r}_i} c_i, \tag{C.2}$$

where N is the number of lattice sites, $\boldsymbol{r}_i$ is the position vector associated with site i, and $\boldsymbol{k}$ is the momentum. In this basis,

$$H_{\text{k}} = -2t \sum_{\boldsymbol{k}} \big[\cos(k_x a) + \cos(k_y a) \big] c^\dagger_{\boldsymbol{k}} c_{\boldsymbol{k}}. \tag{C.3}$$

The ground state of H_{free} is depicted in Fig. C.1. All states within the diamond-shaped Fermi surface (shaded grey) are occupied.

Now consider the interaction of electrons with the nuclear spins in Eq. (6.8), which in momentum space reads: $-g \sum_{\boldsymbol{q},\boldsymbol{k}} c^\dagger_{\boldsymbol{k}+\boldsymbol{q}} c_{\boldsymbol{k}} I^z_{\boldsymbol{q}}$. Notice in Fig. C.1 that the Fermi surface has a nesting vector of $\boldsymbol{Q} = (\pi/a, \pi/a)$: for any point $\boldsymbol{k}$ that lies on the Fermi surface, $\boldsymbol{k} + \boldsymbol{Q}$ also lies on the Fermi surface. Thus, any bosonic mode of momentum $\boldsymbol{Q}$ that couples to the fermions, scatters an electron on the Fermi surface to a different point also on the Fermi surface, leaving its energy unchanged. Since we are interested in low-energy excitations of fermions around the Fermi surface, it is useful to focus on the bosonic modes centered around $\boldsymbol{q} = \boldsymbol{0}$ and $\boldsymbol{q} = \boldsymbol{Q}$. For us, the bosons in question are the nuclear spins. Then, $\boldsymbol{q} = 0$ corresponds to uniform spin order and $\boldsymbol{q} = \boldsymbol{Q} = (\pi/a, \pi/a)$ corresponds to Néel order. This provides further motivation for our choice of decomposition of the nuclear spins into the Néel and uniform components in Eq. (6.10).

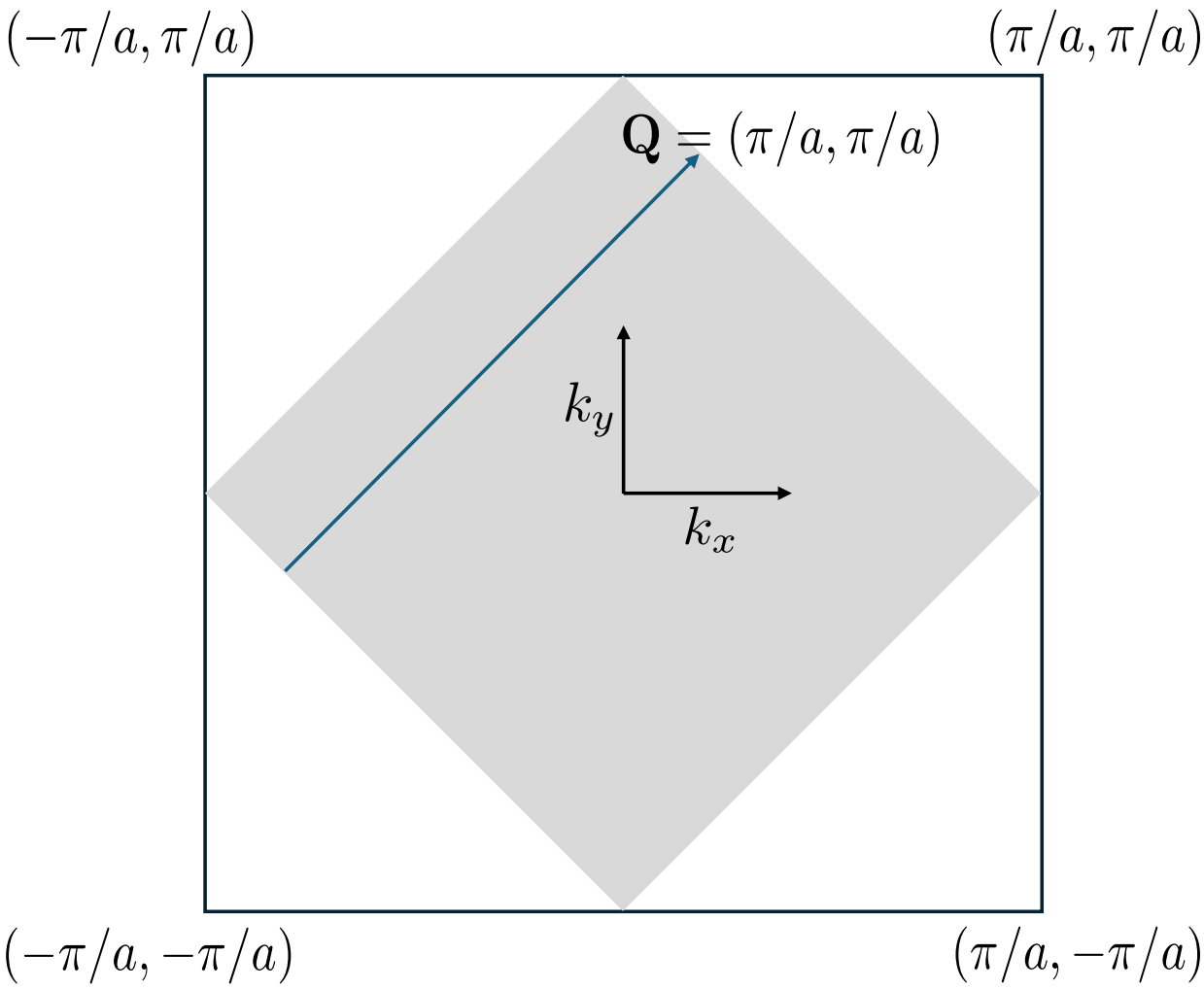

Figure C.1: **Tight-binding model at half-filling on a square lattice.** The Brillouin zone (square) and the Fermi surface of the square-lattice tight-binding model at half-filling (grey diamond) are depicted. The nesting vector $\boldsymbol{Q} = (\pi/a, \pi/a)$ is also shown, see the text for details.

Let us assume $a^{2d}\boldsymbol{\ell}^2 \ll 1$ and decompose the unit Néel vector $\boldsymbol{\phi}$ as

$$\boldsymbol{\phi}(x, y) = \phi_0 \hat{\boldsymbol{z}} + \delta\boldsymbol{\phi}(x, y), \tag{C.4}$$

where $\phi_0 \hat{\boldsymbol{z}} \equiv \langle \boldsymbol{\phi} \rangle$ is constant over each lattice site, and $\delta\boldsymbol{\phi} \equiv \boldsymbol{\phi} - \langle \boldsymbol{\phi} \rangle$ is the fluctuating part of

the Néel field. Here, $\hat{\boldsymbol{z}}$ is a unit vector in the internal (nuclear-spin) z-direction. So,

$$\boldsymbol{I}(x,y) = S\left[(-1)^{\frac{x}{a}+\frac{y}{a}}\left(\phi_0\hat{\boldsymbol{z}} + \delta\boldsymbol{\phi}(x,y)\right) + a^2\boldsymbol{\ell}(x,y)\right]. \tag{C.5}$$

With this ansatz, consider the interaction between the fermions and nuclear spins. We see that when the average Néel field ϕ_0 is nonzero, there is a term that couples every fermion at the Fermi surface to a different Fermion $\boldsymbol{Q}$ away in momentum space (Fig. C.1). As a consequence, the degeneracy between two points on the Fermi surface that are separated by $\boldsymbol{Q}$ is split. Hence, a gap opens up along the Fermi surface, which means at half-filling, the occupied free-fermion state is gapped. This also results in the halving of the Brillouin zone down to the shaded region in Fig. C.1. When $\phi_0 \neq 0$, the new unit cell has a two-site A-B basis shown in Fig. C.2. Another symmetry that is broken is the reflection symmetry around lines parallel to the x or y axes that pass through points $\boldsymbol{R} + (\frac{a}{2}, \frac{a}{2})$ for a site $\boldsymbol{R}$ belonging to the original square lattice.

Let us now define

$$c_{\boldsymbol{k},A} = \sqrt{\frac{2}{N}}\sum_{i\in A} c_i e^{-i\boldsymbol{k}\cdot\boldsymbol{r}_i}, \tag{C.6}$$

$$c_{\boldsymbol{k},B} = \sqrt{\frac{2}{N}}\sum_{i\in B} c_i e^{-i\boldsymbol{k}\cdot\boldsymbol{r}_i}, \tag{C.7}$$

$$\Psi_{\boldsymbol{k}} \equiv \begin{pmatrix} c_{\boldsymbol{k},A} & c_{\boldsymbol{k},B} \end{pmatrix}^T, \tag{C.8}$$

and further do a change of variables from (k_x, k_y) to (k_+, k_-) where $k_\pm = \frac{1}{\sqrt{2}}(k_x \pm k_y)$. The new

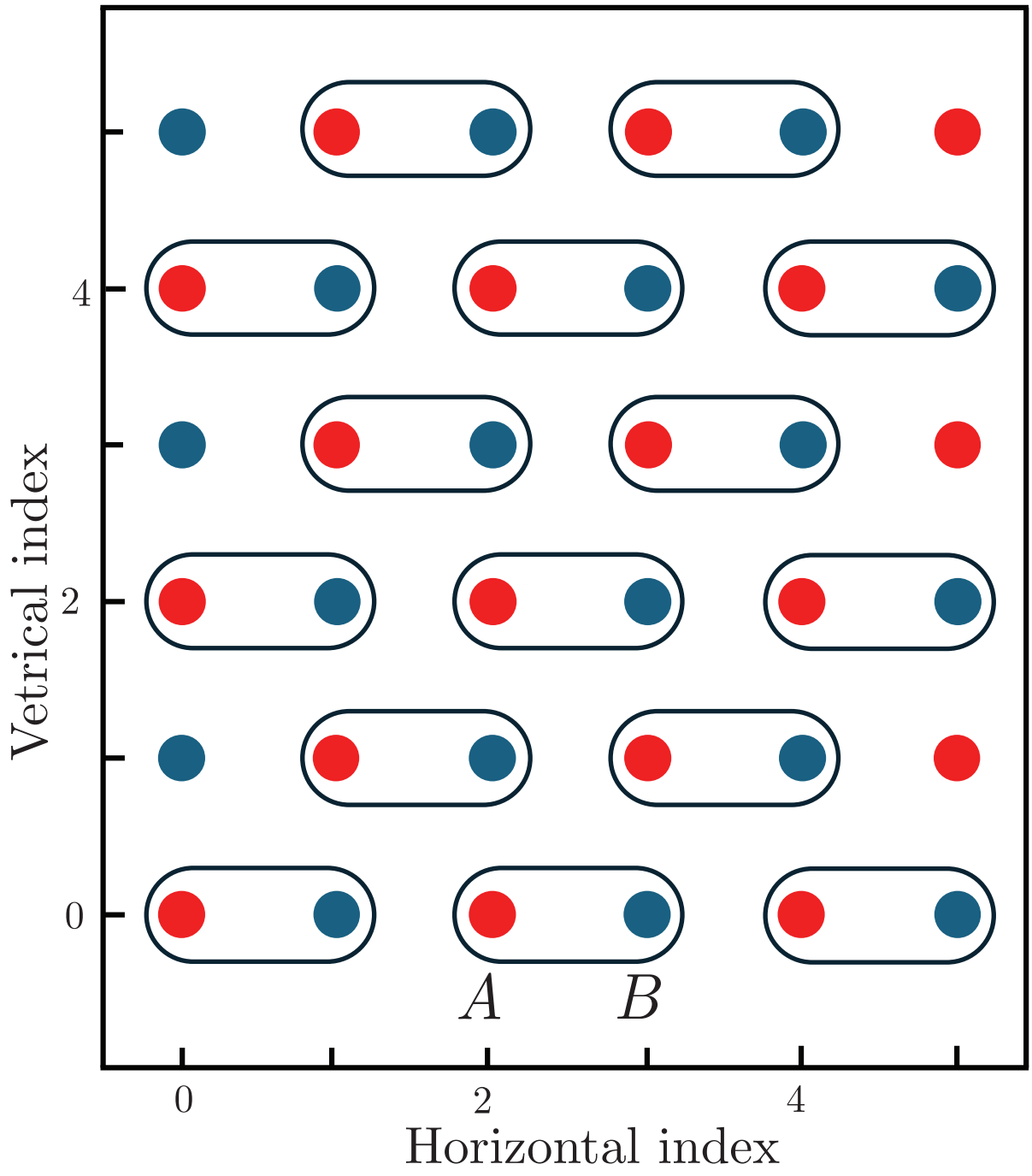

Figure C.2: **Square lattice and Néel order.** Schematic of the putative lattice structure in the lattice fermionic-bosonic model when $\phi_0 \neq 0$, i.e., when there is a nonzero Néel order. The two-site unit cell is marked. The sites labeled red (A sites) have nuclear spins pointing up (in the σ^z basis) and those labeled blue (B sites) have nuclear spins pointing down.

Brillouin zone, i.e., the shaded region in Fig. C.1, is given by

$$-\frac{\pi}{\sqrt{2}a} < k_{\pm} \leq \frac{\pi}{\sqrt{2}a}. \tag{C.9}$$

In this notation, the fermionic Hamiltonian H_f obtained by retaining only the terms involving the fermions in Eq. (6.8) is given by

$$\begin{aligned} H_f = \sum_{\boldsymbol{k}\in\overline{\mathrm{BZ}}} \Psi^{\dagger}_{\boldsymbol{k}} \Bigg\{ & -4t \cos\left(\frac{k_+ a}{\sqrt{2}}\right) \cos\left(\frac{k_- a}{\sqrt{2}}\right) \tau^x \\ & - gS\phi_0 \tau^z \Bigg\} \Psi_{\boldsymbol{k}} \\ & - gS \sum_{\boldsymbol{k},\boldsymbol{q}} \Psi^{\dagger}_{\boldsymbol{k}+\boldsymbol{q}} \left[\delta\phi^z_{\boldsymbol{q}}\, \tau^z + \ell^z_{\boldsymbol{q}}\right] \Psi_{\boldsymbol{k}}. \end{aligned} \tag{C.10}$$

Here, $\overline{\mathrm{BZ}}$ denotes the reduced Brillouin zone defined in Eq. (C.9) and τ^i denote Pauli matrices in the A-B-site indices. The spectrum of the part of H_f without the fluctuation terms of the last line is thus given by

$$\begin{aligned} & \varepsilon_f(\boldsymbol{k}) \\ & \quad = \pm \left\{ (gS\phi_0)^2 + 16t^2 \cos^2\left(\frac{k_+ a}{\sqrt{2}}\right) \cos^2\left(\frac{k_- a}{\sqrt{2}}\right) \right\}^{1/2}. \end{aligned} \tag{C.11}$$

We see that the higher-energy band has minimum energy along the boundary of the shaded Brillouin zone in Fig. C.1, i.e. along $k_+ = \pm\frac{\pi}{\sqrt{2}a}$, and separately along $k_- = \pm\frac{\pi}{\sqrt{2}a}$. Here, the minimum energy fermionic excitations occur along an entire locus of points in momentum space, as opposed to a single momentum, say $\boldsymbol{k} = \boldsymbol{0}$. Hence, this theory does not map to a (discretized) Dirac theory. Nonetheless, it exhibits the dynamical mass generation explored in

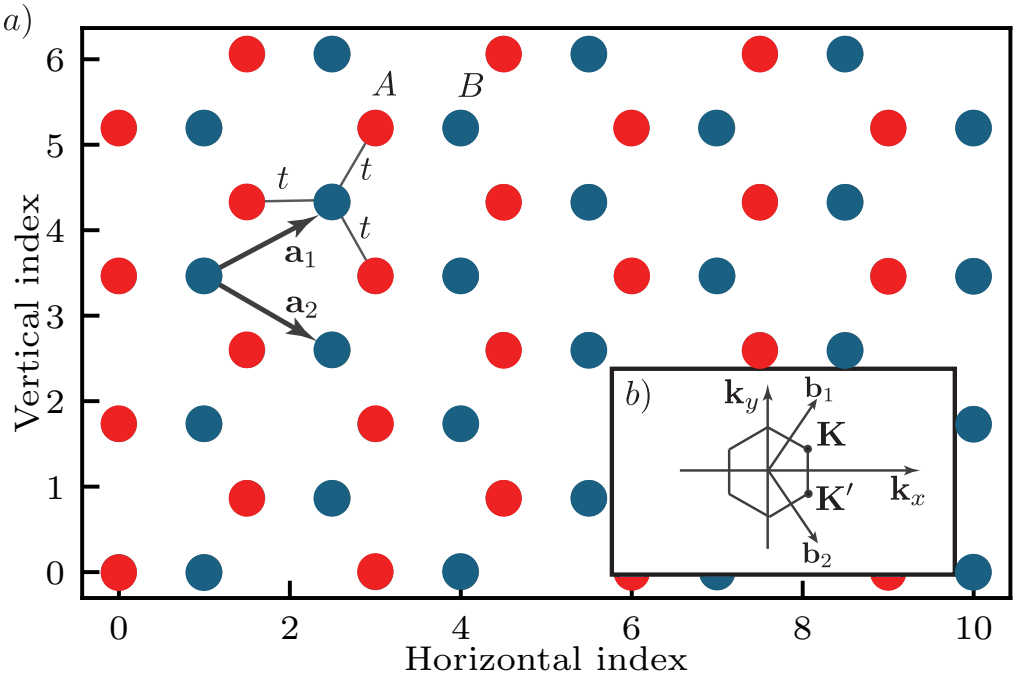

Figure C.3: **Tight-binding model at half-filling on a honeycomb lattice.** a) The interactions in a honeycomb lattice can be described as the interaction of each sublattice point, A and B, with its three nearest neighbors, characterized by strength t. Basis vectors $\boldsymbol{a}_{1,2}$ are also shown. b) The Brillouin zone and the nodes, $\boldsymbol{K}$ and $\boldsymbol{K}'$, as discussed in the main text, along with the basic vectors on the reciprocal lattice.

this work.

C.1.2 Honeycomb lattice: Dirac Fermions coupled to nuclear spins

Let us revisit the interactions between fermions and nuclear spins on the honeycomb lattice, which readily reveal a Dirac-fermion property. To see how, we briefly review the tight-binding model of fermions on a honeycomb lattice. For this lattice array, one may choose basis vectors $\boldsymbol{a}_1 = \frac{a}{2}(3, \sqrt{3})$ and $\boldsymbol{a}_2 = \frac{a}{2}(3, -\sqrt{3})$, and the basis vector in the reciprocal lattice $\boldsymbol{b}_1 = \frac{2\pi}{3a}(1, \sqrt{3}), \boldsymbol{b}_2 = \frac{2\pi}{3a}(1, -\sqrt{3})$ such that $\boldsymbol{b}_j \cdot \boldsymbol{a}_i = 2\pi\delta_{i,j}$. Depending on the site, a fermion may hop forward along the x axis, or hop along the $\boldsymbol{a}_1$ and $\boldsymbol{a}_2$ vectors. Therefore, it is useful to define two sublattices A

and B, as shown in Fig. C.3, each containing one type of the sites. Now upon defining $c_{\boldsymbol{k},A}$, $c_{\boldsymbol{k},B}$, and $\Psi_{\boldsymbol{k}}$ as in Eqs. (C.6)-(C.8), the fermion kinetic Hamiltonian can be written as:

$$H_{\rm k} = \sum_{\boldsymbol{k}} \Psi^{\dagger}_{\boldsymbol{k}} h(\boldsymbol{k}) \Psi_{\boldsymbol{k}} \tag{C.12}$$

with

$$h(\boldsymbol{k}) = -\,t\, e^{ik_x a} \times \begin{pmatrix} 0 & e^{-i\boldsymbol{k}\cdot\boldsymbol{a}_1} + e^{-i\boldsymbol{k}\cdot\boldsymbol{a}_2} + 1 \\ e^{i\boldsymbol{k}\cdot\boldsymbol{a}_1} + e^{i\boldsymbol{k}\cdot\boldsymbol{a}_2} + 1 & 0 \end{pmatrix}. \tag{C.13}$$

Let us now expand this Hamiltonian around the points of the Brillouin zone, $\boldsymbol{K} = \frac{2\pi}{3a}(1, \frac{1}{\sqrt{3}})$ and $\boldsymbol{K}' = \frac{2\pi}{3a}(1, -\frac{1}{\sqrt{3}})$ (which is equivalent to $-\boldsymbol{K}$ up to a reciprocal lattice vector). For values $\boldsymbol{k} = \pm\boldsymbol{K} + \boldsymbol{\kappa}$ with small $|\boldsymbol{\kappa}|$, this leads to

$$\begin{aligned} h(\pm\boldsymbol{K} + \boldsymbol{\kappa}) &= -v_F(\kappa_x \sigma_y \mp \kappa_y \sigma_x) \\ &= -v_F(\mp\kappa_x i\gamma^2 \pm \kappa_y i\gamma^1), \end{aligned} \tag{C.14}$$

at linear order in $\boldsymbol{\kappa}$ and upon a rescaling of the fermion fields with a phase. Here, we have defined the γ matrices as $\gamma^0 = \sigma^z$, $\gamma^1 = i\sigma^x$, and $\gamma^2 = \pm i\sigma^y$. Now note that $\gamma^0 h(\pm\boldsymbol{K} + \boldsymbol{\kappa})\gamma^0 = -v_f(\kappa_x \gamma^0\gamma^1 + \kappa_y \gamma^0\gamma^2)$. For this reason, we can define Ψ as done in Eq. (6.9), which is the transformed version of the original $\Psi_{\boldsymbol{k}}$, i.e., $\Psi_{\boldsymbol{k}} \to \gamma^0 \Psi_{\boldsymbol{k}}$. Comparing this behavior with that of Dirac fermions, i.e., the kinetic term in the Hamiltonian in Eq. (6.1), we observe that the behavior of electrons in the honeycomb lattice near the nodes identified can be approximated by massless

Dirac fermions in (2+1)D with an effective speed of light $c = v_F = \frac{3ta}{2}$. Note that in odd spacetime dimensions, there are two irreducible representations for the Clifford algebra which are not related by a similarity transformation [233], hence the two sets of γ matrices introduced above. Alternatively, one may work with one set of γ matrices and still recover the Dirac equation of motion by expanding around both Dirac points $\pm\boldsymbol{K}$. This requires different redefinitions of $\Psi_{\boldsymbol{k}}$ at each Dirac point, which can be obtained straightforwardly.

Finally, upon coupling these fermions to bosons, and considering a phase with a nonzero ϕ_0 (Néel order in the rotor picture), the reflection symmetry along e.g., lines parallel to the y direction passing through hexagon centers gets broken, corresponding to spontaneous breaking of the $\Psi(x, y) \to \gamma^1\Psi(-x, y)$ symmetry in the original Dirac Hamiltonian, hence a fermion mass gets generated dynamically.

C.2 Supplementary Plots

A number of supplemental results were left out from the main text and will be presented here, along with accompanying discussions. These include the effect of the chemical potential on the phase diagram (of a square array), a discussion of correlations in both the trivial and nontrivial phases, and the charge-occupation profile for a one-dimensional array.

C.2.1 Effect of chemical potential

To examine the influence of the chemical potential on the system's phase, we showcase the phase diagram for three different chemical potentials in Fig. C.4. The chemical potential can be adjusted to regulate the electron transport from the Fermi sea (i.e., the surrounding probes) to the

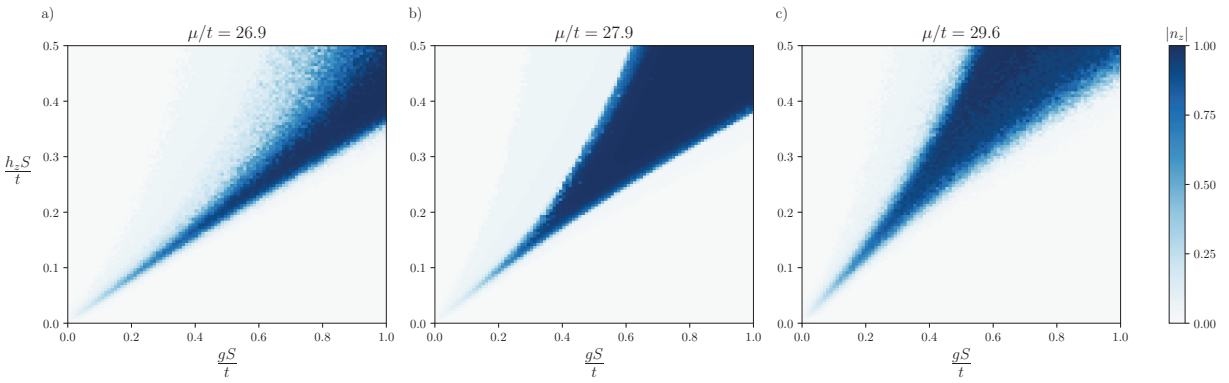

Figure C.4: **Effect of chemical potential on the phase diagram.** This figure displays the phase diagram of a (2+1)D system with size of $N = 10 \times 10$ at half filling. n_z denotes the order parameter defined in Eq. (6.11). The diagram is rendered for three different chemical potentials, μ, each normalized with the tunneling coupling $t = 7.5$ meV. The inverse temperature for all subplots is uniformly fixed at $\beta = 100$ and $h_x S/t = 0.01$.

dopant array. Thus, to achieve a half-filling state, it is feasible to adjust the appropriate exterior chemical potential. This is particularly important in the finite-temperature scenario, where our control is limited to the expected value of the total number of electrons on the array.

C.2.2 Trivial phase

In the main text, our focus was on the nontrivial phase in which both the dynamical mass and Néel order are evident. For a comprehensive understanding, we briefly discuss the contrasting phase named 'trivial'. In the (1+1)D context, this phase corresponds to the Luttinger-Liquid (LL) phase. When plotting the correlation function, $\langle c_i^\dagger c_{i+d} \rangle$, against d (the separation between two sites), an oscillatory pattern emerges. As illustrated in Fig. C.5, this contrasts with an exponential trend and is consistent with the characteristic charge-density wave (CDW) observed in (1+1)D systems. The precise form of the correlation depends on the specific model and boundary conditions. For finite-temperature scenarios, this correlation can be approximated as: $\langle c_i^\dagger c_{i+d} \rangle \sim \rho_0 + A\cos(Bd)/d^{1+\delta} + \cdots$ where ρ_0, A, B, and δ are functions of the model's

parameters, such as temperature and Fermi momentum [234]. In the (2+1)D context, the theory of Luttinger Liquid cannot be extended straightforwardly. However, an oscillatory pattern remains evident, as shown in Fig. C.5(b) and (d).

(Thermal) correlation functions, as well as total fermion occupations, are also plotted for the two-dimensional array for the nontrivial phase in Fig. C.6. As explained in Sec. 6.5.1, these results indicate that the pairing mechanism due to only Coulomb potential is unlikely to explain the nontrivial phase observed in this model. However, due to the limitations of the HF method, it cannot address other contributions to pairing, such as those caused by a combination of the Coulomb potential and electron-spin interactions. We leave these aspects to future studies.

C.2.3 Charge-occupation profile in (1+1)D

In alignment with Fig. 6.10 and the discussion in the experimental section 6.6, we exhibit the outcomes of the simulations for the charge-occupation profile of the (1+1)D system with $N = 43$ at a finite temperature in Fig. C.7. As shown, while the nontrivial phase exhibits a wide range of stable charge occupations across the phase diagram, the trivial phase is more layered, exhibiting different charges as the macroscopic parameters are changed. This feature can be used to probe the two phases in the one-dimensional array.

C.3 Finite-Temperature Hartee-Fock-Bogoluivov Method

The Hartree-Fock method [235] constricts the wave function $|\psi\rangle$ to a specific form known as a Slater determinant, which aims to find the minimum energy that best approximates the system, thus finding a state as close as possible to the ground state. The Hartree-Fock-Bogoliubov (HFB)

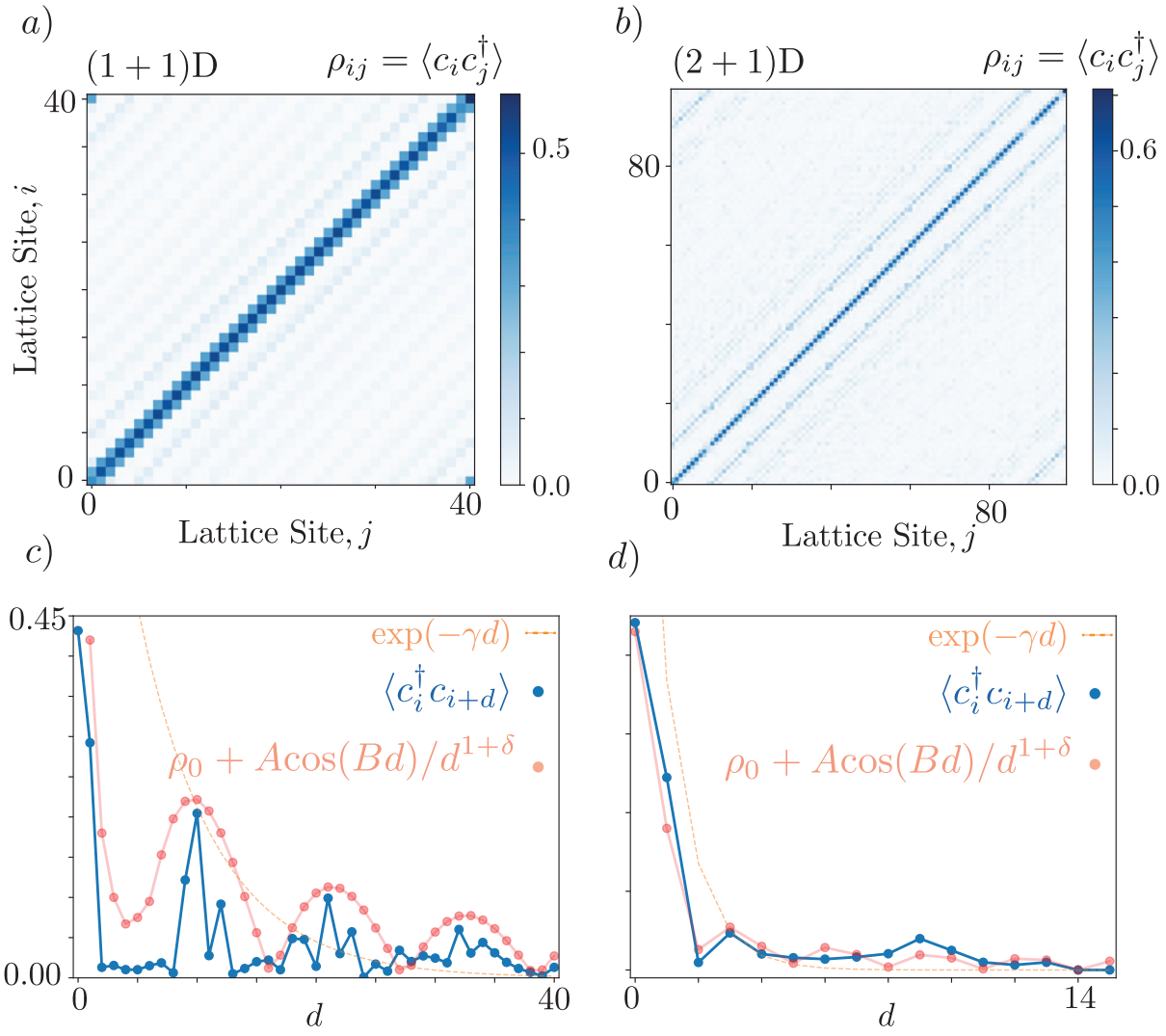

Figure C.5: **Correlation function and fermion behavior in the trivial phase.** a) and b) The single-particle density matrix of the fermions in their trivial phase illustrates behavior akin to a Luttinger Liquid in (1+1)D. c) The correlation function $\langle c_i^\dagger c_{i+d} \rangle$ is plotted as a function of d for a fixed position $i = N/2$. The correlation function has been tested against two analytical functions suggested by theoretical predictions, see Sec. C.2.2 for more details. One behavior is exponential decay characterized by the parameter γ, while the other is oscillatory decay characterized by the parameters ρ_0, A, B, and δ. These parameters are obtained by minimizing the distance (mean square error) between the data and the analytical function. d) Analogous calculation for the (2+1)D scenario with size $N = 10 \times 10$. The lattice indices in the (2+1)D case are defined by row-major order.

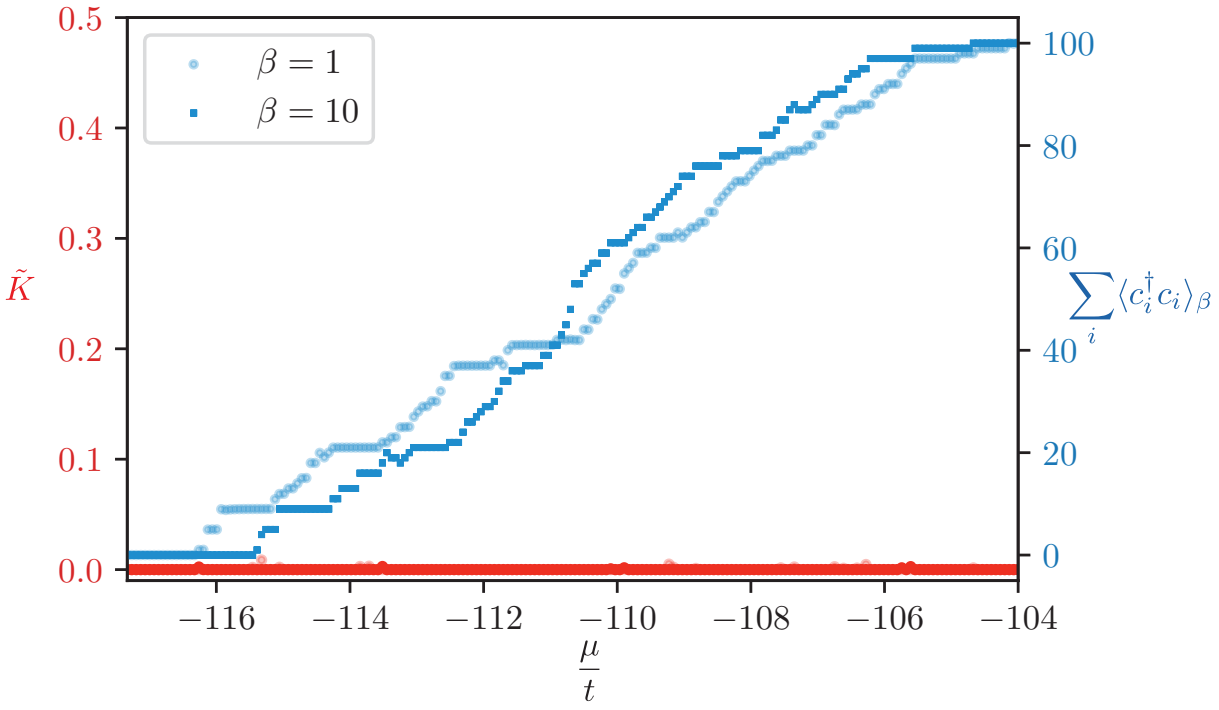

Figure C.6: **Correlation functions for a** 10×10 **array at two inverse temperatures** β**.** We show the total occupation number $\sum_i \langle c_i^\dagger c_i \rangle_\beta$ (right axis) and the average pairing matrix $\tilde{K} \sum_{i,j} K_{ij} K_{ij}^* / N^2$ with $K_{ij} = \langle c_j c_i \rangle_\beta$. Here, the lattice constant is $a = 4.7\,\mathrm{nm}$, the tunneling coupling is $t = 7.5\,\mathrm{meV}$, the Coulomb potential strength is $V_0 S/(td) = 3.6$, and the transverse component of the external magnetic field is set to $h_x S/t = 0.01$. As we can observe, $\tilde{K}$ is almost zero for the entire range of chemical potential, suggesting that $\langle c_i c_j \rangle$ is zero using the Hartree-Fock method.

method [213] serves as a more generalized single-particle theory that builds upon the Hartree-Fock method. In this method, one considers the actual Hamiltonian, H, defined in terms of fermionic operators $c_i^\dagger, c_i$, and approximates this using quasi-particle operators $a_i^\dagger, a_i$, yielding an approximate Hamiltonian $\tilde{H} = \sum_{i=1}^{N} \tilde{E}_i a_i^\dagger a_i$ with the approximate ground state $|\Phi\rangle$. In order to effectively apply the HFB method, one needs to expand the energy expectation value $\frac{\langle\Phi|H|\Phi\rangle}{\langle\Phi|\Phi\rangle}$ up to the second order in terms of the largest energy scale in the Hamiltonian. In the Fermi-Hubbard model, this is normally the hopping terms, associated with the coupling t.

The HFB method at finite temperature can be established by minimizing the grand canonical ensemble's free energy

$$\Omega = E - T\mathcal{S} - \mu n. \tag{C.15}$$

with $\mathcal{S}$ standing for the van-Neumann entropy and n standing for electron occupation. We start with the transition from the fermionic operator basis, represented as $\{c\}$, to the quasi-particle basis, denoted as $\{a\}$:

$$\begin{aligned} a_i^\dagger &= \sum_j \left(U_{ij} c_j^\dagger + V_{ij} c_j \right), \\ a_i &= \sum_j \left(V_{ij}^* c_j^\dagger + U_{ij}^* c_j \right), \end{aligned} \tag{C.16}$$

such that the matrices U and V satisfy the following set of identities

$$UU^\dagger + VV^\dagger = 1, \quad UV^T + VU^T = 0. \tag{C.17}$$

The single-particle density matrix, represented as $\rho_{ij} = \langle a_j^\dagger a_i \rangle$, can be rewritten in the following

manner:

$$\rho = U^T f U^* + V^\dagger (1 - f) V, \tag{C.18}$$

where $f(E) = (1 + e^{E/(k_B T)})^{-1}$ is the Fermi-Dirac distribution. Likewise, the pairing matrix, denoted as $K_{ij} = \langle a_j a_i \rangle$, can be described as:

$$K = U^T f V^* + V^\dagger (1 - f) U, \tag{C.19}$$

In finite-temperature conditions, the vacuum state of quasi-particles no longer serves as a reference for the product state, causing Wick's theorem to be inapplicable. Despite this, ensemble averaging remains a valid technique for statistical analysis [213, 236]. In the case of a Hamiltonian featuring quartic interaction, the interaction component can be approximated as follows:

$$\langle c_i^\dagger c_j^\dagger c_\ell c_k \rangle = \langle c_i^\dagger c_k \rangle \langle c_j^\dagger c_\ell \rangle - \langle c_i^\dagger c_\ell \rangle \langle c_j^\dagger c_k \rangle + \langle c_i^\dagger c_j^\dagger \rangle \langle c_\ell c_k \rangle. \tag{C.20}$$

Leveraging the aforementioned relationship, we can express a general Hamiltonian, which has up to quadratic interaction, with general tunneling matrix t, as:

$$\begin{aligned} H_{ij} &= t_{ij} + \Gamma_{ij} - \mu, \\ \Gamma_{ij} &= \sum_{i,j,k,\ell} \bar{V}_{ijk\ell} \rho_{k\ell}, \\ \Delta_{ij} &= \frac{1}{2} \sum_{k,\ell} \bar{V}_{ijk\ell} K_{k\ell}, \end{aligned} \tag{C.21}$$

and the energy can be described through the following expression

$$E = \mathrm{Tr}\left[t\rho + \frac{1}{2}\Gamma\rho\right] - \mathrm{Tr}\left[\frac{1}{2}\Delta K^*\right]. \tag{C.22}$$

Similarly, the grand-canonical free energy can be expressed as

$$\begin{aligned}\Omega = &\sum_{i,j}(\Gamma - \mu)_{ij}\rho_{ji} + \frac{1}{2}\sum_{i,j,k,\ell}\bar{V}_{ijk\ell}\rho_{\ell j}\rho_{ki} \\ &+ \frac{1}{4}\sum_{i,j,k,\ell}\bar{V}_{ijk\ell}K^*_{ij}K_{k\ell} \\ &+ k_BT\sum_i\left[f_i\ln f_i + (1-f_i)\ln(1-f_i)\right].\end{aligned} \tag{C.23}$$

By setting the variation of the grand canonical potential, denoted as $\delta\Omega$, equal to zero at a given value of β, one can determine the ground state of the system

$$\begin{pmatrix} H & \Delta \\ -\Delta^* & -H^* \end{pmatrix}\begin{pmatrix} U_i \\ V_i \end{pmatrix} = E_i\begin{pmatrix} U_i \\ V_i \end{pmatrix}. \tag{C.24}$$

This set of equations is markedly nonconvex. Nonetheless, it is expected that with a suitable initial setup, one can achieve convergence to the global minimum with iterative methods. We have used this method in the main text and Appendices for the majority of our calculations of fermion densities and correlations.

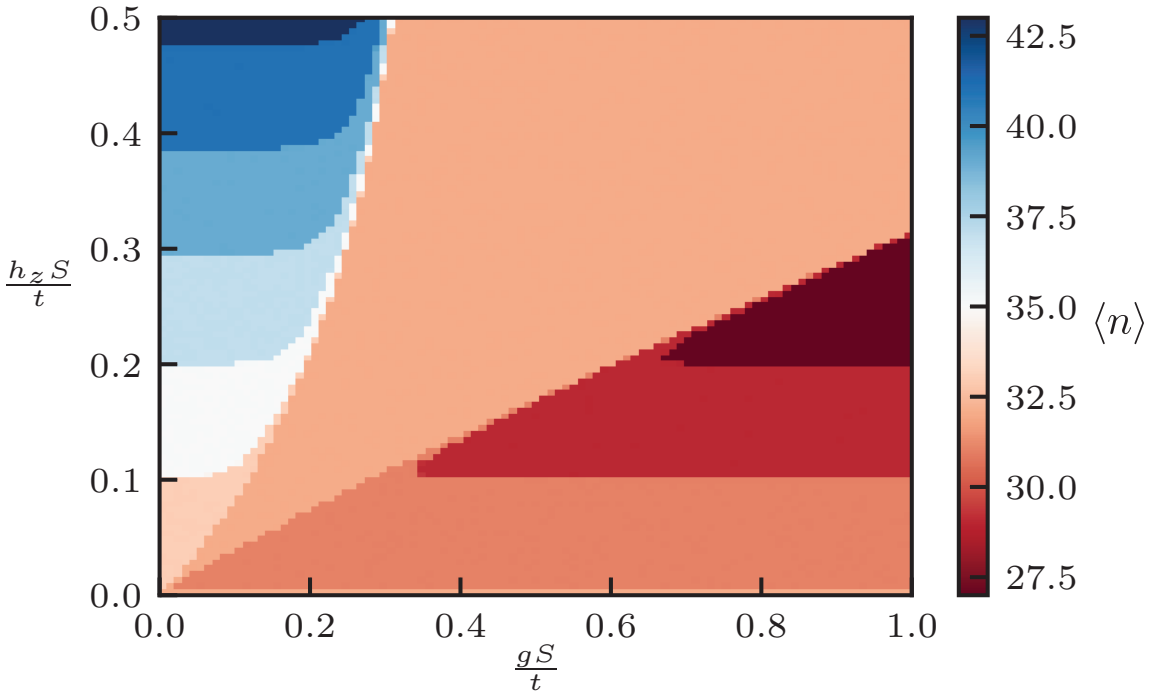

Figure C.7: **Charge-occupation profile for a (1+1)D system.** Similar to Fig. 6.10, the variations in charge-occupation profiles have been simulated for the $N = 64$ one-dimensional array. The charges are simulated by tracing the single-particle density matrix determined at a finite temperature of $T = 10$ mK. Here, $\langle n \rangle = \sum_i \langle c_i^\dagger c_i \rangle_\beta$. The tunneling coupling is set at $t = 7.5$meV, $\mu/t = 11.9$, $h_x S/t = 0.01$, and periodic boundary condition are used. The calculations are performed using the FTHFB method.

C.4 Dopants in Silicon

In this section, we briefly outline the general description of an electron's wave function bound to a dopant in silicon and its connection to calculating the tunneling coupling of an electron from one dopant site to another. Each donor has the ability to be host of one electron in its neutral state, referred to as $D0$, or two electrons when in its negatively charged state, termed $D-$. The binding energy for an isolated neutral $D0$ center is approximately 45 meV. In this study, our main focus is on the ground state of the donor in silicon, denoted as $1sA_1$ in the literature.

The wave function of an electron can be written as an expansion of Bloch functions around

the lower part of the conduction band. The conduction band of silicon can be characterized by six valleys located at

$$\boldsymbol{K} = 0.85 \times \frac{2\pi}{a_{\text{Si}}}\{[\pm 1, 0, 0], [0, \pm 1, 0], [0, 0, \pm 1]\}$$

from the Γ point of the Brillouin zone. The Γ point represents the center of the Brillouin zone, where the wave vector $\boldsymbol{k}$ is zero. It serves as a reference point for defining other points in the reciprocal space. The lattice constant of silicon, denoted as a_{Si}, is approximately 0.54 nm [237]. The 6-fold expansion of the wave function around the sub-valley conduction [238] can be written as:

$$\psi_{A_1}(\boldsymbol{r}) = \frac{1}{\sqrt{6}} \sum_{i \in \pm\{x,y,z\}} F_i(\boldsymbol{r})\phi_i(\boldsymbol{r}). \tag{C.25}$$

Here, $F(\boldsymbol{r})$ represents the slowly varying envelope function, while $\phi(\boldsymbol{r})$ denotes the Bloch function for each valley [226]. These Bloch functions can be characterized by [224]:

$$\phi_i(\boldsymbol{r}) = u_i(\boldsymbol{r})e^{i\boldsymbol{K_i}\cdot\boldsymbol{r}}. \tag{C.26}$$

When multiple dopants are present, the interaction of electrons from different valleys, known as valley-orbital coupling, leads to the breaking of the 6-fold degeneracy. Typically, only two states, $\pm z$, have lower energy. The wave function can be expressed as a superposition of these

two components:

$$\psi_{A_1} = \frac{1}{\sqrt{2}}(\psi_{+z} + \psi_{-z}) \tag{C.27}$$

$$= \frac{1}{\sqrt{2}}F(\boldsymbol{r})[\phi_{+z}(\boldsymbol{r}) \pm \phi_{-z}(\boldsymbol{r})]. \tag{C.28}$$

The envelope function can be determined via the variational method. Following Ref. [224], one can expand it over a finite set of orbital basis states:

$$F_i(\boldsymbol{r}) = \sum_{\nu=1}^{N} A_{i,\nu} F_{i,\nu}(\boldsymbol{r}) \tag{C.29}$$

such that for example:

$$F_{z,\nu} \sim x^{n_x} y^{n_y} z^{n_z} e^{-\alpha_\perp (x^2+y^2)} e^{-\alpha_\parallel z^2} \tag{C.30}$$

The parameters $\{n_x, n_y, n_z, \alpha_\perp, \alpha_\parallel\}$ need to be obtained numerically using the variational method.

To write the full Hamiltonian for the variational method, one can use the Shindo-Nara multi-valley effective-mass theory [239] to express the kinematic term as a combination of two terms with two masses. For example, in the $+z$ direction:

$$T_z = -\frac{\hbar^2}{2m_\perp}\left[\frac{\partial^2}{\partial x^2} + \frac{\partial^2}{\partial y^2} + \gamma\frac{\partial^2}{\partial z^2}\right], \tag{C.31}$$

where $\gamma m_\perp/m_\parallel$ with $m_\perp = 0.19\,m$ and $m_\parallel = 0.91m$. The full Hamiltonian can then be written as:

$$EF_i(\boldsymbol{r}) = [\boldsymbol{T}_i + U(\boldsymbol{r})]F_i(\boldsymbol{r}) + \sum_{\lambda \in \pm\{x,y,z\}} C_{\lambda i}(\boldsymbol{r}) F_i(\boldsymbol{r}). \tag{C.32}$$

Here, F_i was introduced after Eq. (C.25), $\boldsymbol{T}_i$ denotes the kinetic term that encompasses two effective masses, symbolized as $m_\perp$ and $m_\parallel$. The attractive binding potential $U(\boldsymbol{r})$ due to a donor in silicon is well approximated as a screened Coulomb potential at long distances, up to corrections that are discussed in Ref. [224]. $C_{\lambda i}(\boldsymbol{r})\phi^*_\lambda(\boldsymbol{r})\phi_i(\boldsymbol{r})U(\boldsymbol{r})$ represents the coupling between different valleys. Leveraging these mathematical constructs enables a method to find the envelope function, $F(\boldsymbol{r})$, and Bloch functions, $u_i(\boldsymbol{r})$, by minimizing the ground-state energy using the variational method. This procedure leads to a full description of the wave function in Eq. (C.25). The tunneling coupling between dopant sites can then be calculated, as outlined in Section 6.6.2.

In line with Fig. 6.8, Figs. C.9 and C.8 present the calculated tunneling coupling, t, for two of the three orientations of the silicon array, provided for completeness. To plot these figures, we directly use the numerical representation of the wave function and the tunneling coupling as a function of distance from the center of the dopant, provided in Ref. [224]. For more detailed numerical information, please refer to the supplementary material of Ref. [224]. It is worth highlighting, as demonstrated in Fig. C.9, that the $[111]$ silicon orientation provides the most expansive viable region for the emergence of the Néel phase. This trait might render the $[111]$ orientation especially intriguing. Nonetheless, a primary concern associated with this orientation is the oscillatory nature of the wave function in the $[111]$ direction, which results in variations in the tunneling coupling.

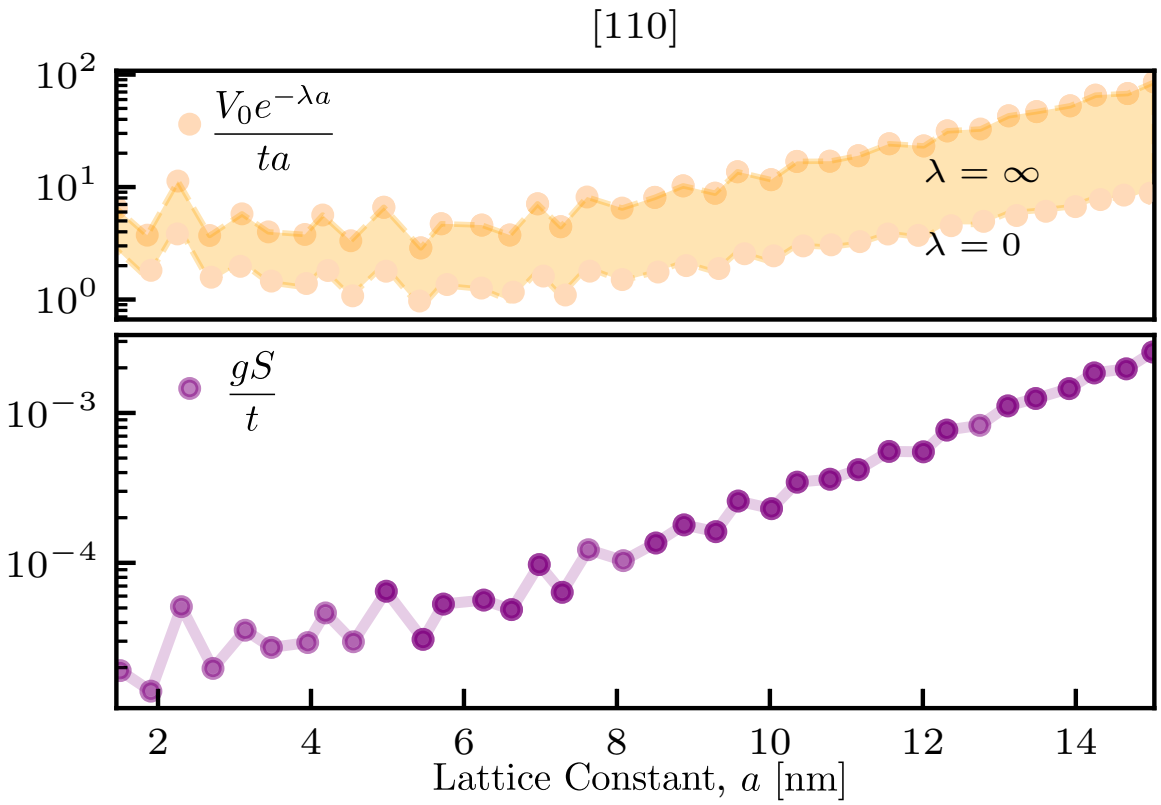

Figure C.8: **Effect of lattice constant for [110] orientation.** The effect of the lattice constant, a, on the tunneling coupling, t, is plotted for a $[110]$ silicon crystal orientation for fixed values of $g = 0.48$ μeV and $h_z = 2.5$ T. The top panel shows the ratio of the Coulomb potential coefficient, V_0, compared to the tunneling coupling across the full range of screening, λ. The bottom panel shows values of gS/t for fixed $g = 0.48$ μeV as a function of the lattice constant.

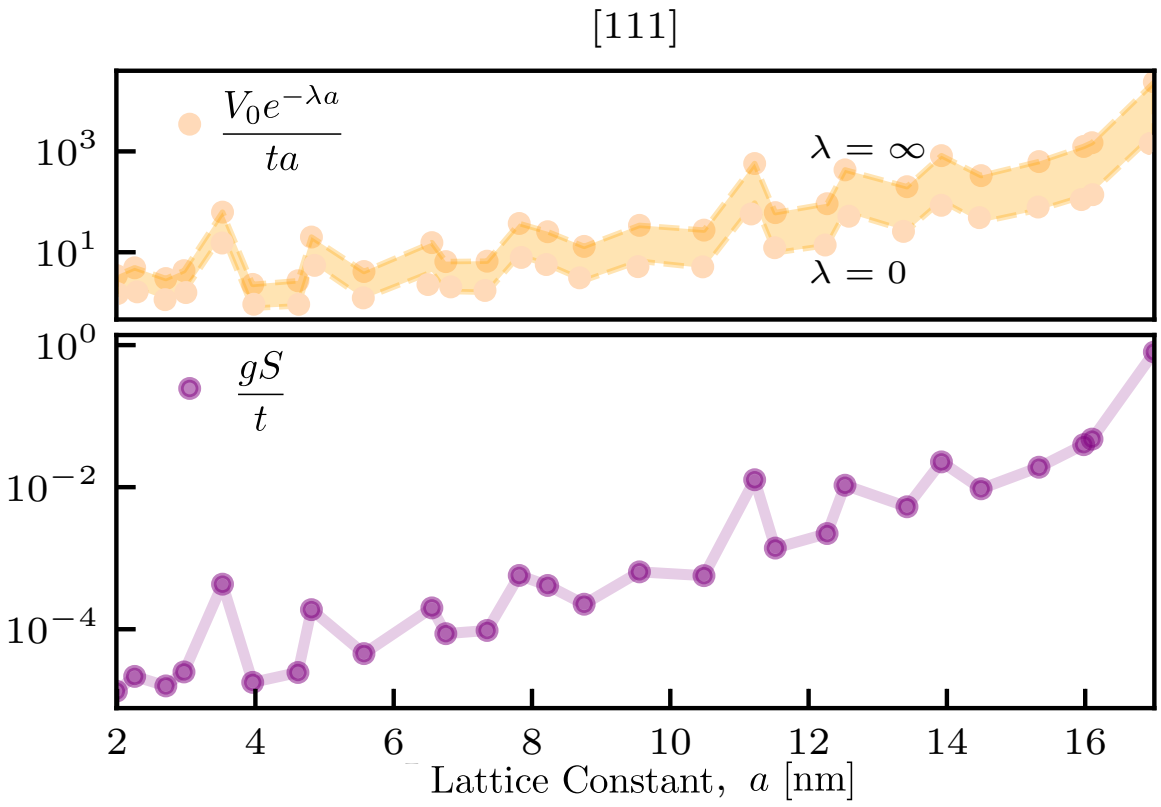

Figure C.9: **Effect of lattice constant for [111] orientation.** The effect of the lattice constant, a, on the tunneling coupling, t, is plotted for a $[111]$ silicon crystal orientation for fixed values of $g = 0.48$ μeV and $h_z = 2.5$ T. The top panel shows the ratio of the Coulomb-potential coefficient, V_0, compared to the tunneling coupling across the full range of screening, λ. The bottom panel shows values of gS/t for fixed $g = 0.48$ μeV as a function of the lattice constant.

C.5 Linear Response Conductance as a Probe

In this section, we review the method for probing the donor systems, as discussed in Sec. 6.6, through linear conductance. We begin by modeling the system as an island of electrons hosted by donors interacting with the Fermi sea, using the following Hamiltonian [183]:

$$H = H^{(\text{lattice})} + H^{(\text{probes})} + H^{(\text{interaction})}, \tag{C.33}$$

with $H^{(\text{lattice})}$ already defined in Eq. (6.8) of the main text and

$$\begin{aligned} H^{(\text{probes})} &= \sum_{k \in B^L} \epsilon_k^L c_k^\dagger c_k + \sum_{k \in B^R} \epsilon_k^R c_k^\dagger c_k, \\ H^{(\text{interaction})} &= \mathcal{C} \sum_{i \in cL,\ j \in L} c_i^\dagger c_j + \text{h.c.} \\ &\quad + \mathcal{C} \sum_{i \in cR,\ j \in R} c_i^\dagger c_j + \text{h.c.} \end{aligned} \tag{C.34}$$

Here, L and B^L (R and B^R) refer to the left (right) probe (in position and momentum space, respectively) with associated momentum modes ϵ_k^L (ϵ_k^R). cL (cR) refers to the sites on a column in the two-dimensional dopant array adjacent to the left (right) probe. The coupling to the left and right probes, $\mathcal{C}$, is assumed equal. This coupling depends on the potential barrier at the probe-dopant interface, and decreases exponentially with the separation between the dopants and the probes [183].

Using the approach outlined in Beenakker's theory of resonant tunneling and linear-response theory for quantum dots [240], one can investigate the linear response conductance of electrons between reservoirs at a specified temperature, T_r, and a chemical potential, μ, applied to a dopant

array with a temperature T perceived as a quantum-dot island.

We denote by E_α^n with $\alpha = 0, 1, 2, \cdots$ the electron energy in level α given n total electrons in the array, and let $\{n\}$ be all electron configurations with total electron number n corresponding to the same energy. The linear conductance, G, can be derived from the stationary current from the left barrier to the right barrier in the regime linear in the potential difference applied between the two probes, divided by the potential difference. It can be shown to have the form [183, 240]:

$$G = G_{0,T} \sum_{\alpha,\alpha'} \sum_{\{n\}} Q_{\alpha,\alpha'}^{\{n\}} P_\alpha^{\{n\}} [1 - f_{\text{FD}}(E_\alpha^n - E_{\alpha'}^{n-1}\mu)]. \tag{C.35}$$

Here, $G_{0,T} = e^2/(k_B T_r)$ and

$$Q_{\alpha,\alpha'}^{\{n\}} = \frac{\Gamma_{\alpha,\alpha'}^{L,\{n\}} \Gamma_{\alpha,\alpha'}^{R,\{n\}}}{\Gamma_{\alpha,\alpha'}^{L,\{n\}} + \Gamma_{\alpha,\alpha'}^{R,\{n\}}} \tag{C.36}$$

represents the contribution from the quantum tunneling rates. Note that in accordance with Fermi's golden rule, the tunneling rate can be ascertained by observing that the transition of an electron is feasible when its energy matches the energy difference between the state of the array with an additional electron, $E_\alpha^n - E_{\alpha'}^{n-1}$. This involves the matrix element of the electrons' creation operator at the edges between the state of the array with n electrons, $\left|\Psi_\alpha^{\{n\}}\right\rangle$, and $n-1$ electrons, $\left|\Psi_{\alpha'}^{\{n-1\}}\right\rangle$:

$$\Gamma_{\alpha,\alpha'}^{L,\{n\}} = \Gamma \sum_{i \in cL} |\langle \Psi_\alpha^{\{n\}} | c_i^\dagger | \Psi_{\alpha'}^{\{n-1\}} \rangle|^2, \tag{C.37}$$

with $\Gamma = 2\pi \mathcal{C}^2$ and cL denoting sites belonging to the leftmost column of the two-dimensional array. A similar expression applies to the right probe. Furthermore, $f_{\text{FD}}(\cdot)$ in Eq. (C.35) is the Fermi-Dirac distribution, $f_{\text{FD}}(E-\mu) = (1+e^{\frac{E-\mu}{k_B T}})^{-1}$. Finally, the stationary probability function

$P_\alpha^{\{n\}}$ in Eq. (C.35) is given by:

$$P_\alpha^{\{n\}} = \frac{e^{-(1/k_BT)(E_\alpha^n - n\mu)}}{\sum_{\alpha'} \sum_{\{n\}} e^{-(1/k_BT)(E_{\alpha'}^n - n\mu)}}. \tag{C.38}$$

This expression is valid under the assumption that the system and probe possess their thermal state as distinct temperatures. This assumption holds as long as probing occurs at fast time scales compared with the equilibration time of the system-probe composite.

To explore the concept of linear conductance as a tool for detecting the different phases of the dopant array, we employed the ED method to simulate the actual wave function of the system, albeit for a limited size. In Fig. C.10, we plot the linear conductance as a function of the chemical potential for a 2×2 square array over a range of temperatures. We adjust the macroscopic parameters to place the system phase in a nontrivial state. As can be observed in finite-temperature scenarios, with parameters that realistically align with experimental setups around $T_r = 10$ mK [185] and $T \ll 1$ mK, the resonance features are both detectable and pronounced.

Moving forward, to investigate the potential for observing phase-transition signatures through conductance behavior, we plot the conductance over a range of external magnetic fields as a macroscopic parameter, for a 2×2 square array. As illustrated in Fig. C.11, the conductance resonance profile varies between nontrivial and trivial phases. Consequently, this suggests that conductance measurement may serve as a probe for exploring and discerning the phases of the system.

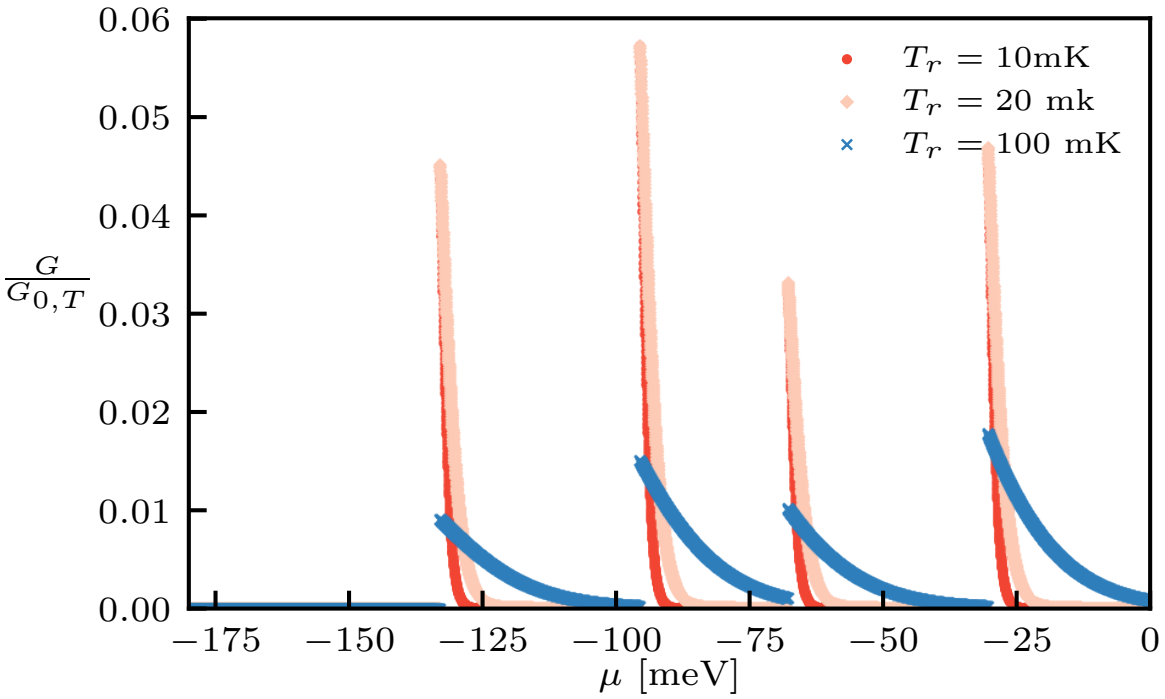

Figure C.10: **Effect of temperature on linear conductance of a 2×2 array.** The variation in the (normalized) linear-conductance response, G, with respect to chemical potential, μ, has been simulated for an experimental setup consisting of a 2×2 square dopant array at three distinct reservoir temperatures, T_r, obtained from ED. For the simulation, the following system parameters are used, $gS/t = 4 \times 10^{-5}$, $h_z S/t = 10^{-5}$, and $h_x/h_z = 0.01$.

C.6 Numerical Simulation Parameters

In the numerical simulations conducted for this study, specific values of parameters within experimentally feasible ranges have been used. Here, we provide a list of these parameters to ensure completeness and reproducibility.

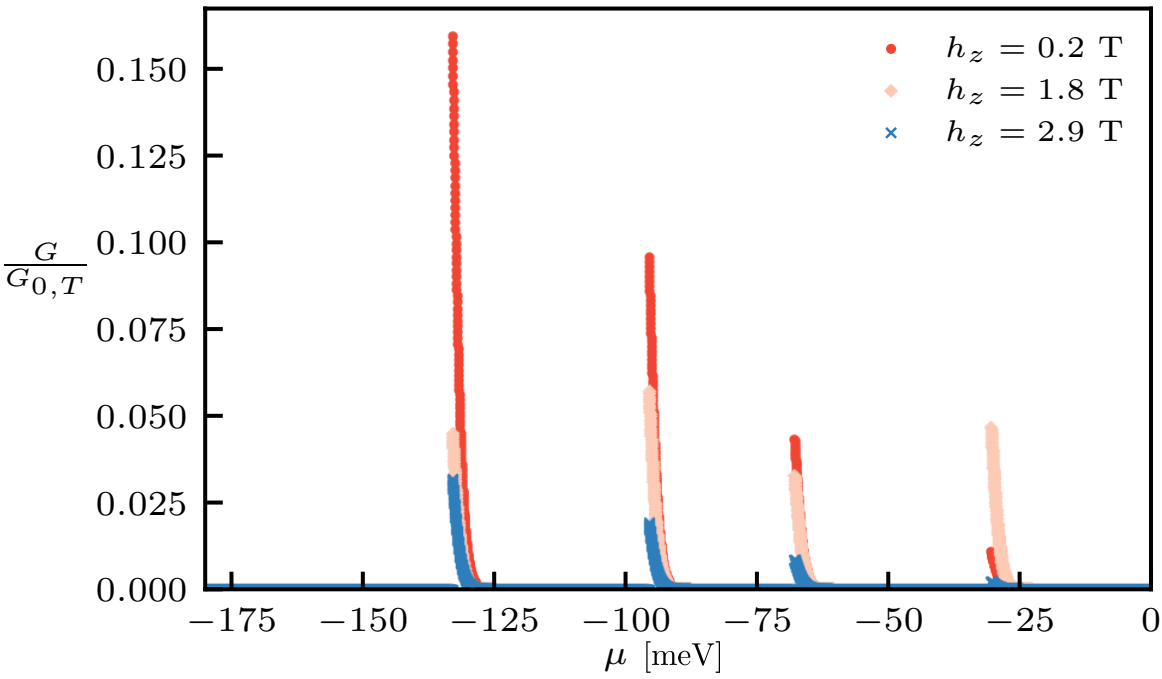

Figure C.11: **Effect of external magnetic field on linear conductance of a 2×2 array.** The variation in the (normalized) linear-conductance response, G, with respect to chemical potential, μ, has been simulated for an experimental setup consisting of a 2×2 square dopant array. To investigate the dependency of the system's linear response on its phase, the conductance is simulated using the ED method for three distinct external magnetic fields, h_z, at $gS/t = 4 \times 10^{-5}$. These magnetic fields correspond to different phases of the system, as elaborated in the main text. As we can observe, the conductance profile at $h_z = 1.8$ T is different from the other two, indicating a nontrivial phase. The variations in these fields lead to noticeable changes in the response profile. The temperature of the array is set to $T = 0.01$ mK, and the temperature of the reservoir is set to $T_r = 10$ mK.

Parameter	Description	Type	Value
S	Nuclear spin	Constant	$1/2$
t	Tunneling coupling	Constant	7.5 meV
g	Hyperfine coupling	Constant	0.48 μeV
h_z	External (longitudinal) magnetic field	Variable	$[0 - O(1)]$ Tesla
h_x	External (transverse) magnetic field	Variable	$[0 - O(10^{-2})]$ Tesla
β	Inverse of temperature	Variable	$[0 - O(10^{3})]$
V_0	Coulomb coupling	Constant	123 nm $\cdot$ meV
λ	Coulomb screening	Variable	$[0 - \infty]$ nm^{-1}
μ	Chemical potential	Variable	$[\pm O(10^{2}))]$ meV
a	Lattice constant	Constant	4.7 nm
d	Distance between pinned spins	Variable	$[0 - O(N)]$
N	Total sites number	Variable	$[1 - O(10^{2})]$
BC	Boundary condition	Constant	Periodic

Table C.1: Summary of numerical values of parameters and other features adopted in the simulations of this work.

Bibliography

[1] Ali Rad, Alireza Seif, and Norbert M Linke. Surviving the barren plateau in variational quantum circuits with bayesian learning initialization. *arXiv preprint arXiv:2203.02464*, 2022.

[2] Ali Rad. Deep quantum neural networks are gaussian process. *arXiv preprint arXiv:2305.12664*, 2023.

[3] Ali Rad, Alexander Schuckert, Eleanor Crane, Gautam Nambiar, Fan Fei, Jonathan Wyrick, Richard M Silver, Mohammad Hafezi, Zohreh Davoudi, and Michael J Gullans. Analog quantum simulator of a quantum field theory with fermion-spin systems in silicon. *arXiv preprint arXiv:2407.03419*, 2024.

[4] Vojtěch Havlíček, Antonio D Córcoles, Kristan Temme, Aram W Harrow, Abhinav Kandala, Jerry M Chow, and Jay M Gambetta. Supervised learning with quantum-enhanced feature spaces. *Nature*, 567(7747):209–212, 2019.

[5] Kristin M Tolle, D Stewart W Tansley, and Anthony JG Hey. The fourth paradigm: Data-intensive scientific discovery [point of view]. *Proceedings of the IEEE*, 99(8):1334–1337, 2011.

[6] Richard P Feynman et al. Simulating physics with computers. *Int. j. Theor. phys*, 21(6/7), 2018.

[7] Harvey Leff and Andrew F Rex. *Maxwell's Demon 2 Entropy, Classical and Quantum Information, Computing*. CRC Press, 2002.

[8] Andrew Hodges and Alan Turing. The enigma (centenary edition), 2012.

[9] Seth Lloyd. Ultimate physical limits to computation. *Nature*, 406(6799):1047–1054, 2000.

[10] Daniel A Roberts. Why is ai hard and physics simple? *arXiv preprint arXiv:2104.00008*, 2021.

[11] Denis Melanson, Mohammad Abu Khater, Maxwell Aifer, Kaelan Donatella, Max Hunter Gordon, Thomas Ahle, Gavin Crooks, Antonio J Martinez, Faris Sbahi, and Patrick J Coles. Thermodynamic computing system for ai applications. *arXiv preprint arXiv:2312.04836*, 2023.

[12] Hsin-Yuan Huang, Michael Broughton, Masoud Mohseni, Ryan Babbush, Sergio Boixo, Hartmut Neven, and Jarrod R McClean. Power of data in quantum machine learning. *Nature communications*, 12(1):2631, 2021.

[13] Hsin-Yuan Huang, Richard Kueng, Giacomo Torlai, Victor V Albert, and John Preskill. Provably efficient machine learning for quantum many-body problems. *Science*, 377(6613):eabk3333, 2022.

[14] Hsin-Yuan Huang, Sitan Chen, and John Preskill. Learning to predict arbitrary quantum processes. *PRX Quantum*, 4(4):040337, 2023.

[15] Sitan Chen, Jordan Cotler, Hsin-Yuan Huang, and Jerry Li. Exponential separations between learning with and without quantum memory. In *2021 IEEE 62nd Annual Symposium on Foundations of Computer Science (FOCS)*, pages 574–585. IEEE, 2022.

[16] Hsin-Yuan Huang, Michael Broughton, Jordan Cotler, Sitan Chen, Jerry Li, Masoud Mohseni, Hartmut Neven, Ryan Babbush, Richard Kueng, John Preskill, et al. Quantum advantage in learning from experiments. *Science*, 376(6598):1182–1186, 2022.

[17] Marco Cerezo, Andrew Arrasmith, Ryan Babbush, Simon C Benjamin, Suguru Endo, Keisuke Fujii, Jarrod R McClean, Kosuke Mitarai, Xiao Yuan, Lukasz Cincio, et al. Variational quantum algorithms. *Nature Reviews Physics*, 3(9):625–644, 2021.

[18] Jarrod R McClean, Jonathan Romero, Ryan Babbush, and Alán Aspuru-Guzik. The theory of variational hybrid quantum-classical algorithms. *New Journal of Physics*, 18(2):023023, 2016.

[19] Alberto Peruzzo, Jarrod McClean, Peter Shadbolt, Man-Hong Yung, Xiao-Qi Zhou, Peter J Love, Alán Aspuru-Guzik, and Jeremy L O'brien. A variational eigenvalue solver on a photonic quantum processor. *Nature communications*, 5(1):1–7, 2014.

[20] Edward Farhi, Jeffrey Goldstone, and Sam Gutmann. A quantum approximate optimization algorithm. *arXiv preprint arXiv:1411.4028*, 2014.

[21] Maria Schuld and Nathan Killoran. Quantum machine learning in feature hilbert spaces. *Physical review letters*, 122(4):040504, 2019.

[22] Maria Schuld, Ilya Sinayskiy, and Francesco Petruccione. The quest for a quantum neural network. *Quantum Information Processing*, 13(11):2567–2586, 2014.

[23] Nathan Wiebe, Ashish Kapoor, and Krysta M Svore. Quantum nearest-neighbor algorithms for machine learning. *Quantum information and computation*, 15(3-4):318–358, 2015.

[24] Abhinav Kandala, Antonio Mezzacapo, Kristan Temme, Maika Takita, Markus Brink, Jerry M Chow, and Jay M Gambetta. Hardware-efficient variational quantum eigensolver for small molecules and quantum magnets. *Nature*, 549(7671):242–246, 2017.

[25] Eugene F Dumitrescu, Alex J McCaskey, Gaute Hagen, Gustav R Jansen, Titus D Morris, T Papenbrock, Raphael C Pooser, David Jarvis Dean, and Pavel Lougovski. Cloud quantum computing of an atomic nucleus. *Physical review letters*, 120(21):210501, 2018.

[26] Cornelius Hempel, Christine Maier, Jonathan Romero, Jarrod McClean, Thomas Monz, Heng Shen, Petar Jurcevic, Ben P Lanyon, Peter Love, Ryan Babbush, et al. Quantum chemistry calculations on a trapped-ion quantum simulator. *Physical Review X*, 8(3):031022, 2018.

[27] Peter JJ O'Malley, Ryan Babbush, Ian D Kivlichan, Jonathan Romero, Jarrod R McClean, Rami Barends, Julian Kelly, Pedram Roushan, Andrew Tranter, Nan Ding, et al. Scalable quantum simulation of molecular energies. *Physical Review X*, 6(3):031007, 2016.

[28] Christian Kokail, Christine Maier, Rick van Bijnen, Tiff Brydges, Manoj K Joshi, Petar Jurcevic, Christine A Muschik, Pietro Silvi, Rainer Blatt, Christian F Roos, et al. Self-verifying variational quantum simulation of lattice models. *Nature*, 569(7756):355–360, 2019.

[29] JS Otterbach, R Manenti, N Alidoust, A Bestwick, M Block, B Bloom, S Caldwell, N Didier, E Schuyler Fried, S Hong, et al. Unsupervised machine learning on a hybrid quantum computer. *arXiv preprint arXiv:1712.05771*, 2017.

[30] Daiwei Zhu, Norbert M Linke, Marcello Benedetti, Kevin A Landsman, Nhung H Nguyen, C Huerta Alderete, Alejandro Perdomo-Ortiz, Nathan Korda, A Garfoot, Charles Brecque, et al. Training of quantum circuits on a hybrid quantum computer. *Science advances*, 5(10):eaaw9918, 2019.

[31] Lennart Bittel and Martin Kliesch. Training variational quantum algorithms is np-hard–even for logarithmically many qubits and free fermionic systems. *arXiv preprint arXiv:2101.07267*, 2021.

[32] Martin Larocca, Nathan Ju, Diego García-Martín, Patrick J Coles, and M Cerezo. Theory of overparametrization in quantum neural networks. *arXiv preprint arXiv:2109.11676*, 2021.

[33] Marco Cerezo, Akira Sone, Tyler Volkoff, Lukasz Cincio, and Patrick J Coles. Cost function dependent barren plateaus in shallow parametrized quantum circuits. *Nature communications*, 12(1):1–12, 2021.

[34] Zoë Holmes, Kunal Sharma, M Cerezo, and Patrick J Coles. Connecting ansatz expressibility to gradient magnitudes and barren plateaus. *arXiv preprint arXiv:2101.02138*, 2021.

[35] Taylor L Patti, Khadijeh Najafi, Xun Gao, and Susanne F Yelin. Entanglement devised barren plateau mitigation. *Physical Review Research*, 3(3):033090, 2021.

[36] Carlos Ortiz Marrero, Mária Kieferová, and Nathan Wiebe. Entanglement-induced barren plateaus. *PRX Quantum*, 2(4):040316, 2021.

[37] Samson Wang, Enrico Fontana, Marco Cerezo, Kunal Sharma, Akira Sone, Lukasz Cincio, and Patrick J Coles. Noise-induced barren plateaus in variational quantum algorithms. *Nature Communications*, 12(1):1–11, 2021.

[38] Yuxuan Du, Min-Hsiu Hsieh, Tongliang Liu, Shan You, and Dacheng Tao. Learnability of quantum neural networks. *PRX Quantum*, 2(4):040337, 2021.

[39] Kunal Sharma, Marco Cerezo, Lukasz Cincio, and Patrick J Coles. Trainability of dissipative perceptron-based quantum neural networks. *arXiv preprint arXiv:2005.12458*, 2020.

[40] Jarrod R McClean, Sergio Boixo, Vadim N Smelyanskiy, Ryan Babbush, and Hartmut Neven. Barren plateaus in quantum neural network training landscapes. *Nature communications*, 9(1):1–6, 2018.

[41] Gian Giacomo Guerreschi and Mikhail Smelyanskiy. Practical optimization for hybrid quantum-classical algorithms. *arXiv preprint arXiv:1701.01450*, 2017.

[42] Maria Schuld, Ville Bergholm, Christian Gogolin, Josh Izaac, and Nathan Killoran. Evaluating analytic gradients on quantum hardware. *Physical Review A*, 99(3):032331, 2019.

[43] Andrea Mari, Thomas R Bromley, and Nathan Killoran. Estimating the gradient and higher-order derivatives on quantum hardware. *Physical Review A*, 103(1):012405, 2021.

[44] Marco Cerezo and Patrick J Coles. Higher order derivatives of quantum neural networks with barren plateaus. *Quantum Science and Technology*, 6(3):035006, 2021.

[45] Marco Cerezo and Patrick J Coles. Impact of barren plateaus on the hessian and higher order derivatives. *arXiv preprint arXiv:2008.07454*, 2020.

[46] Ryan Sweke, Frederik Wilde, Johannes Meyer, Maria Schuld, Paul K Fährmann, Barthélémy Meynard-Piganeau, and Jens Eisert. Stochastic gradient descent for hybrid quantum-classical optimization. *Quantum*, 4:314, 2020.

[47] James Stokes, Josh Izaac, Nathan Killoran, and Giuseppe Carleo. Quantum natural gradient. *Quantum*, 4:269, 2020.

[48] Jonas M Kübler, Andrew Arrasmith, Lukasz Cincio, and Patrick J Coles. An adaptive optimizer for measurement-frugal variational algorithms. *Quantum*, 4:263, 2020.

[49] Max Wilson, Rachel Stromswold, Filip Wudarski, Stuart Hadfield, Norm M Tubman, and Eleanor G Rieffel. Optimizing quantum heuristics with meta-learning. *Quantum Machine Intelligence*, 3(1):1–14, 2021.

[50] James C Spall et al. Multivariate stochastic approximation using a simultaneous perturbation gradient approximation. *IEEE transactions on automatic control*, 37(3):332–341, 1992.

[51] Michael JD Powell. A direct search optimization method that models the objective and constraint functions by linear interpolation. In *Advances in optimization and numerical analysis*, pages 51–67. Springer, 1994.

[52] Michael JD Powell. An efficient method for finding the minimum of a function of several variables without calculating derivatives. *The computer journal*, 7(2):155–162, 1964.

[53] Andrew Arrasmith, M Cerezo, Piotr Czarnik, Lukasz Cincio, and Patrick J Coles. Effect of barren plateaus on gradient-free optimization. *Quantum*, 5:558, 2021.

[54] Xavier Bonet-Monroig, Hao Wang, Diederick Vermetten, Bruno Senjean, Charles Moussa, Thomas Bäck, Vedran Dunjko, and Thomas E O'Brien. Performance comparison of optimization methods on variational quantum algorithms. *arXiv preprint arXiv:2111.13454*, 2021.

[55] Guillaume Verdon, Michael Broughton, Jarrod R McClean, Kevin J Sung, Ryan Babbush, Zhang Jiang, Hartmut Neven, and Masoud Mohseni. Learning to learn with quantum neural networks via classical neural networks. *arXiv preprint arXiv:1907.05415*, 2019.

[56] Zoë Holmes, Andrew Arrasmith, Bin Yan, Patrick J Coles, Andreas Albrecht, and Andrew T Sornborger. Barren plateaus preclude learning scramblers. *Physical Review Letters*, 126(19):190501, 2021.

[57] Kaining Zhang, Min-Hsiu Hsieh, Liu Liu, and Dacheng Tao. Toward trainability of quantum neural networks. *arXiv preprint arXiv:2011.06258*, 2020.

[58] AV Uvarov and Jacob D Biamonte. On barren plateaus and cost function locality in variational quantum algorithms. *Journal of Physics A: Mathematical and Theoretical*, 54(24):245301, 2021.

[59] Edward Grant, Leonard Wossnig, Mateusz Ostaszewski, and Marcello Benedetti. An initialization strategy for addressing barren plateaus in parametrized quantum circuits. *Quantum*, 3:214, 2019.

[60] Tyler Volkoff and Patrick J Coles. Large gradients via correlation in random parameterized quantum circuits. *Quantum Science and Technology*, 6(2):025008, 2021.

[61] Mark McLeod, Stephen Roberts, and Michael A Osborne. Optimization, fast and slow: optimally switching between local and bayesian optimization. In *International Conference on Machine Learning*, pages 3443–3452. PMLR, 2018.

[62] Marcello Benedetti, Delfina Garcia-Pintos, Oscar Perdomo, Vicente Leyton-Ortega, Yunseong Nam, and Alejandro Perdomo-Ortiz. A generative modeling approach for benchmarking and training shallow quantum circuits. *npj Quantum Information*, 5(1):1–9, 2019.

[63] Peter I Frazier. A tutorial on bayesian optimization. *arXiv preprint arXiv:1807.02811*, 2018.

[64] Bobak Shahriari, Kevin Swersky, Ziyu Wang, Ryan P Adams, and Nando De Freitas. Taking the human out of the loop: A review of bayesian optimization. *Proceedings of the IEEE*, 104(1):148–175, 2015.

[65] Junyu Liu, Francesco Tacchino, Jennifer R Glick, Liang Jiang, and Antonio Mezzacapo. Representation learning via quantum neural tangent kernels. *arXiv preprint arXiv:2111.04225*, 2021.

[66] Russell R Barton and John S Ivey Jr. Modifications of the nelder-mead simplex method for stochastic simulation response optimization. Technical report, Institute of Electrical and Electronics Engineers (IEEE), 1991.

[67] David JC MacKay and David JC Mac Kay. *Information theory, inference and learning algorithms*. Cambridge university press, 2003.

[68] Solomon Kullback and Richard A Leibler. On information and sufficiency. *The annals of mathematical statistics*, 22(1):79–86, 1951.

[69] Shai Shalev-Shwartz and Shai Ben-David. *Understanding machine learning: From theory to algorithms*. Cambridge university press, 2014.

[70] Aram W Harrow and John C Napp. Low-depth gradient measurements can improve convergence in variational hybrid quantum-classical algorithms. *Physical Review Letters*, 126(14):140502, 2021.

[71] John A Nelder and Roger Mead. A simplex method for function minimization. *The computer journal*, 7(4):308–313, 1965.

[72] Leo Zhou, Sheng-Tao Wang, Soonwon Choi, Hannes Pichler, and Mikhail D Lukin. Quantum approximate optimization algorithm: Performance, mechanism, and implementation on near-term devices. *Physical Review X*, 10(2):021067, 2020.

[73] Roeland Wiersema, Cunlu Zhou, Yvette de Sereville, Juan Felipe Carrasquilla, Yong Baek Kim, and Henry Yuen. Exploring entanglement and optimization within the hamiltonian variational ansatz. *PRX Quantum*, 1(2):020319, 2020.

[74] Andrea Skolik, Jarrod R McClean, Masoud Mohseni, Patrick van der Smagt, and Martin Leib. Layerwise learning for quantum neural networks. *Quantum Machine Intelligence*, 3(1):1–11, 2021.

[75] Ernesto Campos, Aly Nasrallah, and Jacob Biamonte. Abrupt transitions in variational quantum circuit training. *Physical Review A*, 103(3):032607, 2021.

[76] Kathleen E Hamilton, Eugene F Dumitrescu, and Raphael C Pooser. Generative model benchmarks for superconducting qubits. *Physical Review A*, 99(6):062323, 2019.

[77] Maria Schuld. Supervised quantum machine learning models are kernel methods. *arXiv preprint arXiv:2101.11020*, 2021.

[78] Samuel Duffield, Marcello Benedetti, and Matthias Rosenkranz. Bayesian learning of parameterised quantum circuits. *Machine Learning: Science and Technology*, 4(2):025007, 2023.

[79] Arthur Jacot, Franck Gabriel, and Clément Hongler. Neural tangent kernel: Convergence and generalization in neural networks. *Advances in neural information processing systems*, 31, 2018.

[80] Junyu Liu, Khadijeh Najafi, Kunal Sharma, Francesco Tacchino, Liang Jiang, and Antonio Mezzacapo. Analytic theory for the dynamics of wide quantum neural networks. *Physical Review Letters*, 130(15):150601, 2023.

[81] Norihito Shirai, Kenji Kubo, Kosuke Mitarai, and Keisuke Fujii. Quantum tangent kernel. *arXiv preprint arXiv:2111.02951*, 2021.

[82] Junyu Liu, Francesco Tacchino, Jennifer R Glick, Liang Jiang, and Antonio Mezzacapo. Representation learning via quantum neural tangent kernels. *PRX Quantum*, 3(3):030323, 2022.

[83] Junyu Liu, Zexi Lin, and Liang Jiang. Laziness, barren plateau, and noise in machine learning. *arXiv preprint arXiv:2206.09313*, 2022.

[84] Erfan Abedi, Salman Beigi, and Leila Taghavi. Quantum lazy training. *Quantum*, 7:989, 2023.

[85] Radford M. Neal. Priors for infinite networks. 1996.

[86] Jaehoon Lee, Yasaman Bahri, Roman Novak, Samuel S Schoenholz, Jeffrey Pennington, and Jascha Sohl-Dickstein. Deep neural networks as gaussian processes. *arXiv preprint arXiv:1711.00165*, 2017.

[87] Roman Novak, Lechao Xiao, Jaehoon Lee, Yasaman Bahri, Greg Yang, Jiri Hron, Daniel A Abolafia, Jeffrey Pennington, and Jascha Sohl-Dickstein. Bayesian deep convolutional networks with many channels are gaussian processes. *arXiv preprint arXiv:1810.05148*, 2018.

[88] Jaehoon Lee, Lechao Xiao, Samuel Schoenholz, Yasaman Bahri, Roman Novak, Jascha Sohl-Dickstein, and Jeffrey Pennington. Wide neural networks of any depth evolve as linear models under gradient descent. *Advances in neural information processing systems*, 32, 2019.

[89] Motohisa Fukuda, Robert König, and Ion Nechita. Rtni—a symbolic integrator for haar-random tensor networks. *Journal of Physics A: Mathematical and Theoretical*, 52(42):425303, 2019.

[90] Zbigniew Puchała and Jarosław Adam Miszczak. Symbolic integration with respect to the haar measure on the unitary group. *arXiv preprint arXiv:1109.4244*, 2011.

[91] Junyu Liu, Khadijeh Najafi, Kunal Sharma, Francesco Tacchino, Liang Jiang, and Antonio Mezzacapo. An analytic theory for the dynamics of wide quantum neural networks. *arXiv preprint arXiv:2203.16711*, 2022.

[92] Kaining Zhang, Liu Liu, Min-Hsiu Hsieh, and Dacheng Tao. Escaping from the barren plateau via gaussian initializations in deep variational quantum circuits. *Advances in Neural Information Processing Systems*, 35:18612–18627, 2022.

[93] Daniel A Roberts, Sho Yaida, and Boris Hanin. *The principles of deep learning theory*. Cambridge University Press Cambridge, MA, USA, 2022.

[94] Supanut Thanasilp, Samson Wang, Marco Cerezo, and Zoë Holmes. Exponential concentration and untrainability in quantum kernel methods. *arXiv preprint arXiv:2208.11060*, 2022.

[95] Trevor Hastie, Robert Tibshirani, Jerome H Friedman, and Jerome H Friedman. *The elements of statistical learning: data mining, inference, and prediction*, volume 2. Springer, 2009.

[96] Chiyuan Zhang, Samy Bengio, Moritz Hardt, Benjamin Recht, and Oriol Vinyals. Understanding deep learning (still) requires rethinking generalization. *Communications of the ACM*, 64(3):107–115, 2021.

[97] Mikhail Belkin, Siyuan Ma, and Soumik Mandal. To understand deep learning we need to understand kernel learning. In *International Conference on Machine Learning*, pages 541–549. PMLR, 2018.

[98] Mikhail Belkin, Daniel Hsu, Siyuan Ma, and Soumik Mandal. Reconciling modern machine-learning practice and the classical bias–variance trade-off. *Proceedings of the National Academy of Sciences*, 116(32):15849–15854, 2019.

[99] Thomas Hofmann, Bernhard Schölkopf, and Alexander J Smola. Kernel methods in machine learning. 2008.

[100] Vern I Paulsen and Mrinal Raghupathi. *An introduction to the theory of reproducing kernel Hilbert spaces*, volume 152. Cambridge university press, 2016.

[101] Bernhard Schölkopf and Alexander J Smola. *Learning with kernels: support vector machines, regularization, optimization, and beyond*. MIT press, 2002.

[102] Junyu Liu, Khadijeh Najafi, Kunal Sharma, Francesco Tacchino, Liang Jiang, and Antonio Mezzacapo. Analytic theory for the dynamics of wide quantum neural networks. *Phys. Rev. Lett.*, 130:150601, Apr 2023.

[103] Diego García-Martín, Martin Larocca, and M Cerezo. Deep quantum neural networks form gaussian processes. *arXiv preprint arXiv:2305.09957*, 2023.

[104] Eric R Anschuetz. Critical points in hamiltonian agnostic variational quantum algorithms. *arXiv preprint arXiv:2109.06957*, 2021.

[105] Norbert Rosenzweig and Charles E. Porter. "repulsion of energy levels" in complex atomic spectra. *Phys. Rev.*, 120:1698–1714, Dec 1960.

[106] Hugh L Montgomery. The pair correlation of zeros of the zeta function. In *Proc. Symp. Pure Math*, volume 24, pages 181–193, 1973.

[107] Andrew M Odlyzko. On the distribution of spacings between zeros of the zeta function. *Mathematics of Computation*, 48(177):273–308, 1987.

[108] Jean-Philippe Bouchaud and Marc Potters. Financial applications of random matrix theory: a short review. *arXiv preprint arXiv:0910.1205*, 2009.

[109] Paul Erd6s and Alfréd Rényi. On the evolution of random graphs. *Publ. Math. Inst. Hungar. Acad. Sci*, 5:17–61, 1960.

[110] Daniel J. Amit, Hanoch Gutfreund, and H. Sompolinsky. Spin-glass models of neural networks. *Phys. Rev. A*, 32:1007–1018, Aug 1985.

[111] Elizabeth Gardner and Bernard Derrida. Optimal storage properties of neural network models. *Journal of Physics A: Mathematical and general*, 21(1):271, 1988.

[112] Viktor Dotsenko. *An introduction to the theory of spin glasses and neural networks*, volume 55. World Scientific, 1994.

[113] Yann N Dauphin, Razvan Pascanu, Caglar Gulcehre, Kyunghyun Cho, Surya Ganguli, and Yoshua Bengio. Identifying and attacking the saddle point problem in high-dimensional non-convex optimization. *Advances in neural information processing systems*, 27, 2014.

[114] Levent Sagun, V Ugur Guney, Gerard Ben Arous, and Yann LeCun. Explorations on high dimensional landscapes. *arXiv preprint arXiv:1412.6615*, 2014.

[115] Anna Choromanska, MIkael Henaff, Michael Mathieu, Gerard Ben Arous, and Yann LeCun. The Loss Surfaces of Multilayer Networks. In Guy Lebanon and S. V. N. Vishwanathan, editors, *Proceedings of the Eighteenth International Conference on Artificial Intelligence and Statistics*, volume 38 of *Proceedings of Machine Learning Research*, pages 192–204, San Diego, California, USA, 09–12 May 2015. PMLR.

[116] Marco Baity-Jesi, Levent Sagun, Mario Geiger, Stefano Spigler, Gérard Ben Arous, Chiara Cammarota, Yann LeCun, Matthieu Wyart, and Giulio Biroli. Comparing dynamics: Deep neural networks versus glassy systems. In *International Conference on Machine Learning*, pages 314–323. PMLR, 2018.

[117] Trevor Hastie, Andrea Montanari, Saharon Rosset, and Ryan J Tibshirani. Surprises in high-dimensional ridgeless least squares interpolation. *Annals of statistics*, 50(2):949, 2022.

[118] Song Mei and Andrea Montanari. The generalization error of random features regression: Precise asymptotics and the double descent curve. *Communications on Pure and Applied Mathematics*, 75(4):667–766, 2022.

[119] Ben Adlam and Jeffrey Pennington. The neural tangent kernel in high dimensions: Triple descent and a multi-scale theory of generalization. In *International Conference on Machine Learning*, pages 74–84. PMLR, 2020.

[120] Song Mei and Andrea Montanari. The generalization error of random features regression: Precise asymptotics and double descent curve. arxiv e-prints, page. *arXiv preprint arXiv:1908.05355*, 2019.

[121] Carlos E González-Guillén, Carlos Palazuelos, and Ignacio Villanueva. Euclidean distance between haar orthogonal and gaussian matrices. *Journal of Theoretical Probability*, 31:93–118, 2018.

[122] LA Pastur and VA Martchenko. The distribution of eigenvalues in certain sets of random matrices. *Math. USSR-Sbornik*, 1(4):457–483, 1967.

[123] Ben Adlam, Jake Levinson, and Jeffrey Pennington. A random matrix perspective on mixtures of nonlinearities for deep learning. *arXiv preprint arXiv:1912.00827*, 2019.

[124] Jeffrey Pennington and Pratik Worah. Nonlinear random matrix theory for deep learning. *Advances in neural information processing systems*, 30, 2017.

[125] Arthur Jacot, Berfin Simsek, Francesco Spadaro, Clément Hongler, and Franck Gabriel. Kernel alignment risk estimator: Risk prediction from training data. *Advances in neural information processing systems*, 33:15568–15578, 2020.

[126] Preetum Nakkiran, Gal Kaplun, Yamini Bansal, Tristan Yang, Boaz Barak, and Ilya Sutskever. Deep double descent: Where bigger models and more data hurt. *Journal of Statistical Mechanics: Theory and Experiment*, 2021(12):124003, 2021.

[127] Christopher Monroe, Michael G Raymer, and Jacob Taylor. The US National Quantum Initiative: From act to action. *Science*, 364(6439):440–442, 2019.

[128] Ehud Altman, Kenneth R. Brown, Giuseppe Carleo, Lincoln D. Carr, Eugene Demler, Cheng Chin, Brian DeMarco, Sophia E. Economou, Mark A. Eriksson, Kai-Mei C. Fu, Markus Greiner, Kaden R.A. Hazzard, Randall G. Hulet, Alicia J. Kollár, Benjamin L. Lev, Mikhail D. Lukin, Ruichao Ma, Xiao Mi, Shashank Misra, Christopher Monroe, Kater Murch, Zaira Nazario, Kang-Kuen Ni, Andrew C. Potter, Pedram Roushan, Mark Saffman, Monika Schleier-Smith, Irfan Siddiqi, Raymond Simmonds, Meenakshi Singh, I.B. Spielman, Kristan Temme, David S. Weiss, Jelena Vučković, Vladan Vuletić, Jun Ye, and Martin Zwierlein. Quantum simulators: Architectures and opportunities. *PRX Quantum*, 2:017003, Feb 2021.

[129] C Huerta Alderete, Shivani Singh, Nhung H Nguyen, Daiwei Zhu, Radhakrishnan Balu, Christopher Monroe, CM Chandrashekar, and Norbert M Linke. Quantum walks and

dirac cellular automata on a programmable trapped-ion quantum computer. *Nature Communications*, 11(1), 2020.

[130] Wen Lin Tan, Harvey Kaplan, Arinjoy De, Guido Pagano, Christopher Monroe, Lingzhen Guo, and Florian Marquardt. Many-body dephasing in a trapped-ion quantum simulator. *Bulletin of the American Physical Society*, 2020.

[131] SA Moses, CH Baldwin, MS Allman, R Ancona, L Ascarrunz, C Barnes, J Bartolotta, B Bjork, P Blanchard, M Bohn, et al. A race track trapped-ion quantum processor. *arXiv preprint arXiv:2305.03828*, 2023.

[132] Thomas Monz, Philipp Schindler, Julio T Barreiro, Michael Chwalla, Daniel Nigg, William A Coish, Maximilian Harlander, Wolfgang Hänsel, Markus Hennrich, and Rainer Blatt. 14-qubit entanglement: Creation and coherence. *Physical Review Letters*, 106(13):130506, 2011.

[133] David Hayes, Steven T Flammia, and Michael J Biercuk. Programmable quantum simulation by dynamic hamiltonian engineering. *New Journal of Physics*, 16(8):083027, 2014.

[134] Michael Biercuk. The advantages of trapped-ion quantum computation. In *APS March Meeting Abstracts*, volume 2018 of *APS Meeting Abstracts*, page B05.002, January 2018.

[135] Christopher Monroe, Wes C Campbell, L-M Duan, Z-X Gong, Alexey V Gorshkov, Paul W Hess, Rajibul Islam, Kihwan Kim, Norbert M Linke, Guido Pagano, et al. Programmable quantum simulations of spin systems with trapped ions. *Reviews of Modern Physics*, 93(2):025001, 2021.

[136] Simcha Korenblit, Dvir Kafri, Wess C Campbell, Rajibul Islam, Emily E Edwards, Zhe-Xuan Gong, Guin-Dar Lin, Lu-Ming Duan, Jungsang Kim, Kihwan Kim, et al. Quantum simulation of spin models on an arbitrary lattice with trapped ions. *New Journal of Physics*, 14(9):095024, 2012.

[137] Yi Hong Teoh, Marina Drygala, Roger G Melko, and Rajibul Islam. Machine learning design of a trapped-ion quantum spin simulator. *Quantum Science and Technology*, 5(2):024001, 2020.

[138] Yann LeCun, John Denker, and Sara Solla. Optimal brain damage. *Advances in neural information processing systems*, 2, 1989.

[139] Yann LeCun, John Denker, and Sara Solla. Optimal brain damage. *Advances in neural information processing systems*, 2:598–605, 1989.

[140] Babak Hassibi and David Stork. Second order derivatives for network pruning: Optimal brain surgeon. *Advances in neural information processing systems*, 5:164–171, 1992.

[141] Babak Hassibi, David G Stork, and Gregory J Wolff. Optimal brain surgeon and general network pruning. In *IEEE international conference on neural networks*, pages 293–299. IEEE, 1993.

[142] Jan Gorodkin, Lars Kai Hansen, Anders Krogh, Claus Svarer, and Ole Winther. A quantitative study of pruning by optimal brain damage. *International journal of neural systems*, 4(02):159–169, 1993.

[143] Julian Schwinger. Gauge invariance and mass. ii. *Physical Review*, 128(5):2425, 1962.

[144] Philip George Harper. Single band motion of conduction electrons in a uniform magnetic field. *Proceedings of the Physical Society. Section A*, 68(10):874, 1955.

[145] Yi Hong Teoh, Marina Drygala, Roger G Melko, and Rajibul Islam. Machine learning design of a trapped-ion quantum spin simulator. *Quantum Science and Technology*, 5(2):024001, 2020.

[146] Diederik P Kingma and Jimmy Ba. Adam: A method for stochastic optimization. *arXiv preprint arXiv:1412.6980*, 2014.

[147] Zohreh Davoudi, Mohammad Hafezi, Christopher Monroe, Guido Pagano, Alireza Seif, and Andrew Shaw. Towards analog quantum simulations of lattice gauge theories with trapped ions. *Physical Review Research*, 2(2):023015, 2020.

[148] F. Englert and R. Brout. Broken Symmetry and the Mass of Gauge Vector Mesons. *Phys. Rev. Lett.*, 13:321–323, 1964.

[149] Peter W. Higgs. Broken Symmetries and the Masses of Gauge Bosons. *Phys. Rev. Lett.*, 13:508–509, 1964.

[150] Y. Nambu and G. Jona-Lasinio. Dynamical model of elementary particles based on an analogy with superconductivity. i. *Phys. Rev.*, 122:345–358, Apr 1961.

[151] Y. Nambu and G. Jona-Lasinio. Dynamical model of elementary particles based on an analogy with superconductivity. ii. *Phys. Rev.*, 124:246–254, Oct 1961.

[152] Antonio Pich. Chiral perturbation theory. *Reports on Progress in Physics*, 58(6):563, 1995.

[153] J. B. Kogut and M. A. Stephanov. *The phases of quantum chromodynamics: From confinement to extreme environments*, volume 21. Cambridge University Press, 12 2004.

[154] John B. Kogut, M. Stone, H. W. Wyld, W. R. Gibbs, J. Shigemitsu, Stephen H. Shenker, and D. K. Sinclair. Deconfinement and Chiral Symmetry Restoration at Finite Temperatures in SU(2) and SU(3) Gauge Theories. *Phys. Rev. Lett.*, 50:393, 1983.

[155] Edward Shuryak. Recent progress in understanding deconfinement and chiral restoration phase transitions. *EPJ Web Conf.*, 137:01018, 2017.

[156] N. Brambilla et al. QCD and Strongly Coupled Gauge Theories: Challenges and Perspectives. *Eur. Phys. J. C*, 74(10):2981, 2014.

[157] Christof Gattringer and Christian B. Lang. *Quantum chromodynamics on the lattice*, volume 788. Springer, Berlin, 2010.

[158] Y. Aoki et al. FLAG Review 2021. *Eur. Phys. J. C*, 82(10):869, 2022.

[159] Andreas S Kronfeld. Lattice qcd and particle physics. Technical report, Brookhaven National Lab.(BNL), Upton, NY (United States); Argonne National . . . , 2022.

[160] Zohreh Davoudi et al. Report of the Snowmass 2021 Topical Group on Lattice Gauge Theory. In *Snowmass 2021*, 9 2022.

[161] Mari Carmen Banuls, Rainer Blatt, Jacopo Catani, Alessio Celi, Juan Ignacio Cirac, Marcello Dalmonte, Leonardo Fallani, Karl Jansen, Maciej Lewenstein, Simone Montangero, et al. Simulating lattice gauge theories within quantum technologies. *The European physical journal D*, 74(8):1–42, 2020.

[162] Natalie Klco, Alessandro Roggero, and Martin J. Savage. Standard model physics and the digital quantum revolution: thoughts about the interface. *Rept. Prog. Phys.*, 85(6):064301, 2022.

[163] Christian W Bauer, Zohreh Davoudi, A Baha Balantekin, Tanmoy Bhattacharya, Marcela Carena, Wibe A de Jong, Patrick Draper, Aida El-Khadra, Nate Gemelke, Masanori Hanada, et al. Quantum simulation for high-energy physics. *PRX Quantum*, 4(2):027001, 2023.

[164] Christian W. Bauer, Zohreh Davoudi, Natalie Klco, and Martin J. Savage. Quantum simulation of fundamental particles and forces. *Nature Rev. Phys.*, 5(7):420–432, 2023.

[165] Alberto Di Meglio, Karl Jansen, Ivano Tavernelli, Constantia Alexandrou, Srinivasan Arunachalam, Christian W Bauer, Kerstin Borras, Stefano Carrazza, Arianna Crippa, Vincent Croft, et al. Quantum computing for high-energy physics: State of the art and challenges. summary of the qc4hep working group. *arXiv preprint arXiv:2307.03236*, 2023.

[166] Jad C Halimeh, Monika Aidelsburger, Fabian Grusdt, Philipp Hauke, and Bing Yang. Cold-atom quantum simulators of gauge theories. *arXiv preprint arXiv:2310.12201*, 2023.

[167] Tetsuo Hatsuda and Teiji Kunihiro. Qcd phenomenology based on a chiral effective lagrangian. *Physics Reports*, 247(5-6):221–367, 1994.

[168] David J. Gross and André Neveu. Dynamical symmetry breaking in asymptotically free field theories. *Phys. Rev. D*, 10:3235–3253, Nov 1974.

[169] D. J. Gross. Applications of the Renormalization Group to High-Energy Physics. *Conf. Proc. C*, 7507281:141–250, 1975.

[170] Alexandre B Zamolodchikov and Alexey B Zamolodchikov. Exact s matrix of gross-neveu "elementary" fermions. *Physics Letters B*, 72(4):481–483, 1978.

[171] S. P. Klevansky. The nambu—jona-lasinio model of quantum chromodynamics. *Rev. Mod. Phys.*, 64:649–708, Jul 1992.

[172] Edward Witten. Chiral symmetry, the 1/n expansion and the su (n) thirring model. *Nuclear Physics B*, 145(1):110–118, 1978.

[173] B Berg and P Weisz. Exact s-matrix of the chiral invariant su (n) thirring model. *Nuclear Physics B*, 146(1):205–214, 1978.

[174] Roman Jackiw and Cláudio Rebbi. Solitons with fermion number $1/2$. *Physical Review D*, 13(12):3398, 1976.

[175] Daniel Gonzalez-Cuadra, Alexandre Dauphin, Monika Aidelsburger, Maciej Lewenstein, and Alejandro Bermudez. Rotor jackiw-rebbi model: a cold-atom approach to chiral symmetry restoration and charge confinement. *Prx Quantum*, 1(2):020321, 2020.

[176] P. Jordan and E. Wigner. Über das paulische Äquivalenzverbot. *Zeitschrift für Physik*, 47(9–10):631–651, September 1928.

[177] Ian D. Kivlichan, Jarrod McClean, Nathan Wiebe, Craig Gidney, Alán Aspuru-Guzik, Garnet Kin-Lic Chan, and Ryan Babbush. Quantum simulation of electronic structure with linear depth and connectivity. *Phys. Rev. Lett.*, 120:110501, Mar 2018.

[178] Stasja Stanisic, Jan Lukas Bosse, Filippo Maria Gambetta, Raul A. Santos, Wojciech Mruczkiewicz, Thomas E. O'Brien, Eric Ostby, and Ashley Montanaro. Observing ground-state properties of the fermi-hubbard model using a scalable algorithm on a quantum computer. *Nat. Comm.*, 13(1), October 2022.

[179] Kevin Hemery, Khaldoon Ghanem, Eleanor Crane, Sara L. Campbell, Joan M. Dreiling, Caroline Figgatt, Cameron Foltz, John P. Gaebler, Jacob Johansen, Michael Mills, Steven A. Moses, Juan M. Pino, Anthony Ransford, Mary Rowe, Peter Siegfried, Russell P. Stutz, Henrik Dreyer, Alexander Schuckert, and Ramil Nigmatullin. Measuring the loschmidt amplitude for finite-energy properties of the fermi-hubbard model on an ion-trap quantum computer, 2023.

[180] Yuan Liu, Shraddha Singh, Kevin C. Smith, Eleanor Crane, John M. Martyn, Alec Eickbusch, Alexander Schuckert, Richard D. Li, Jasmine Sinanan-Singh, Micheline B. Soley, Takahiro Tsunoda, Isaac L. Chuang, Nathan Wiebe, and Steven M. Girvin. Hybrid oscillator-qubit quantum processors: Instruction set architectures, abstract machine models, and applications. *in preparation*, 2024.

[181] Xi Yu, Benjamin Wilhelm, Danielle Holmes, Arjen Vaartjes, Daniel Schwienbacher, Martin Nurizzo, Anders Kringhøj, Mark R. van Blankenstein, Alexander M. Jakob, Pragati Gupta, Fay E. Hudson, Kohei M. Itoh, Riley J. Murray, Robin Blume-Kohout, Thaddeus D. Ladd, Andrew S. Dzurak, Barry C. Sanders, David N. Jamieson, and Andrea Morello. Creation and manipulation of schrödinger cat states of a nuclear spin qudit in silicon, 2024.

[182] J. Salfi, J. A. Mol, R. Rahman, G. Klimeck, M. Y. Simmons, L. C. L. Hollenberg, and S. Rogge. Quantum simulation of the hubbard model with dopant atoms in silicon. *Nature Communications*, 7(1), April 2016.

[183] Nguyen H Le, Andrew J Fisher, and Eran Ginossar. Extended hubbard model for mesoscopic transport in donor arrays in silicon. *Physical Review B*, 96(24):245406, 2017.

[184] Eleanor Crane. Quantum computation and simulation in silicon donors: From optically-controlled entangling gates to the hubbard model. *UCL Discovery - UCL Discovery*, Dec 2021.

[185] Xiqiao Wang, Ehsan Khatami, Fan Fei, Jonathan Wyrick, Pradeep Namboodiri, Ranjit Kashid, Albert F Rigosi, Garnett Bryant, and Richard Silver. Experimental realization of an extended fermi-hubbard model using a 2d lattice of dopant-based quantum dots. *Nature Communications*, 13(1):6824, 2022.

[186] Nguyen H. Le, Andrew J. Fisher, Neil J. Curson, and Eran Ginossar. Topological phases of a dimerized fermi–hubbard model for semiconductor nano-lattices. *npj Quantum Information*, 6(1), February 2020.

[187] M. Kiczynski, S. K. Gorman, H. Geng, M. B. Donnelly, Y. Chung, Y. He, J. G. Keizer, and M. Y. Simmons. Engineering topological states in atom-based semiconductor quantum dots. *Nature*, 606(7915):694–699, June 2022.

[188] Mitchell Kiczynski, SK Gorman, Helen Geng, MB Donnelly, Yousun Chung, Yu He, JG Keizer, and MY Simmons. Engineering topological states in atom-based semiconductor quantum dots. *Nature*, 606(7915):694–699, 2022.

[189] Yu-Ling Hsueh, Ludwik Kranz, Daniel Keith, Serajum Monir, Yousun Chung, Samuel K Gorman, Rajib Rahman, and Michelle Y Simmons. Hyperfine-mediated spin relaxation in donor-atom qubits in silicon. *Physical Review Research*, 5(2):023043, 2023.

[190] E. Crane, A. Kölker, T. Z. Stock, N. Stavrias, K. Saeedi, M. A. W. van Loon, B. N. Murdin, and N. J. Curson. Hydrogen resist lithography and electron beam lithography for fabricating silicon targets for studying donor orbital states. *Journal of Physics: Conference Series*, 1079:012010, August 2018.

[191] Taylor J. Z. Stock, Oliver Warschkow, Procopios C. Constantinou, Juerong Li, Sarah Fearn, Eleanor Crane, Emily V. S. Hofmann, Alexander Kölker, David R. McKenzie, Steven R. Schofield, and Neil J. Curson. Atomic-scale patterning of arsenic in silicon by scanning tunneling microscopy. *ACS Nano*, 14(3):3316–3327, March 2020.

[192] Thomas F. Watson, Bent Weber, Yu-Ling Hsueh, Lloyd C. L. Hollenberg, Rajib Rahman, and Michelle Y. Simmons. Atomically engineered electron spin lifetimes of 30 s in silicon. *Science Advances*, 3(3), March 2017.

[193] B. E. Kane. A silicon-based nuclear spin quantum computer. *Nature*, 393(6681):133–137, May 1998.

[194] C. D. Hill, L. C. L. Hollenberg, A. G. Fowler, C. J. Wellard, A. D. Greentree, and H.-S. Goan. Global control and fast solid-state donor electron spin quantum computing. *Phys. Rev. B*, 72:045350, Jul 2005.

[195] Joe O'Gorman, Naomi H Nickerson, Philipp Ross, John JL Morton, and Simon C Benjamin. A silicon-based surface code quantum computer. *npj Quantum Information*, 2(1), February 2016.

[196] M. Veldhorst, H. G. J. Eenink, C. H. Yang, and A. S. Dzurak. Silicon cmos architecture for a spin-based quantum computer. *Nature Communications*, 8(1), December 2017.

[197] Eleanor Crane, Thomas Crane, Alexander Schuckert, Nguyen H. Le, Kristian Stockbridge, Steven Chick, and Andrew J. Fisher. Optically controlled entangling gates in randomly doped silicon. *Phys. Rev. B*, 100:064201, Aug 2019.

[198] E. Crane, A. Schuckert, N. H. Le, and A. J. Fisher. Rydberg entangling gates in silicon. *Phys. Rev. Res.*, 3:033086, Jul 2021.

[199] Y. He, S. K. Gorman, D. Keith, L. Kranz, J. G. Keizer, and M. Y. Simmons. A two-qubit gate between phosphorus donor electrons in silicon. *Nature*, 571(7765):371–375, July 2019.

[200] Ludwik Kranz, Stephen Roche, Samuel K. Gorman, Joris. G. Keizer, and Michelle Y. Simmons. High-fidelity cnot gate for donor electron spin qubits in silicon. *Phys. Rev. Appl.*, 19:024068, Feb 2023.

[201] Ian Thorvaldson, Dean Poulos, Christian M Moehle, Saiful H Misha, Hermann Edlbauer, Jonathan Reiner, Helen Geng, Benoit Voisin, Michael T Jones, Matthew B Donnelly, Luis F Pena, Charles D Hill, Casey R Myers, Joris G Keizer, Yousun Chung, Samuel K Gorman, Ludwik Kranz, and Michelle Y Simmons. Grover's algorithm in a four-qubit silicon processor above the fault-tolerant threshold. *arXiv*, 2024.

[202] SR Schofield, NJ Curson, MY Simmons, FJ Rueß, Toby Hallam, Lars Oberbeck, and RG Clark. Atomically precise placement of single dopants in si. *Physical review letters*, 91(13):136104, 2003.

[203] Jonathan Wyrick, Xiqiao Wang, Ranjit V Kashid, Pradeep Namboodiri, Scott W Schmucker, Joseph A Hagmann, Keyi Liu, Michael D Stewart Jr, Curt A Richter, Garnett W Bryant, et al. Atom-by-atom fabrication of single and few dopant quantum devices. *Advanced Functional Materials*, 29(52):1903475, 2019.

[204] David J Gross and Andre Neveu. Dynamical symmetry breaking in asymptotically free field theories. *Physical Review D*, 10(10):3235, 1974.

[205] Muhammad Usman, Juanita Bocquel, Joe Salfi, Benoit Voisin, Archana Tankasala, Rajib Rahman, Michelle Y Simmons, Sven Rogge, and LCL Hollenberg. Spatial metrology of dopants in silicon with exact lattice site precision. *Nature nanotechnology*, 11(9):763–768, 2016.

[206] Xiqiao Wang, Jonathan Wyrick, Ranjit V Kashid, Pradeep Namboodiri, Scott W Schmucker, Andrew Murphy, MD Stewart Jr, and Richard M Silver. Atomic-scale control of tunneling in donor-based devices. *Communications Physics*, 3(1):82, 2020.

[207] Minsoo Kim, SG Xu, AI Berdyugin, Alessandro Principi, Sergey Slizovskiy, Na Xin, Piranavan Kumaravadivel, Wenjun Kuang, Matthew Hamer, Roshan Krishna Kumar, et al. Control of electron-electron interaction in graphene by proximity screening. *Nature communications*, 11(1):2339, 2020.

[208] John Kogut and Leonard Susskind. Hamiltonian formulation of wilson's lattice gauge theories. *Physical Review D*, 11(2):395, 1975.

[209] Subir Sachdev. Quantum antiferromagnets in two dimensions. *arXiv preprint cond-mat/9303014*, 1993.

[210] Steven R White. Density matrix formulation for quantum renormalization groups. *Physical review letters*, 69(19):2863, 1992.

[211] Johannes Hauschild and Frank Pollmann. Efficient numerical simulations with tensor networks: Tensor network python (tenpy). *SciPost Physics Lecture Notes*, page 005, 2018.

[212] Gabriele Giuliani and Giovanni Vignale. *Quantum theory of the electron liquid*. Cambridge university press, 2005.

[213] Alan L Goodman. Finite-temperature hfb theory. *Nuclear Physics A*, 352(1):30–44, 1981.

[214] A Chodos, RL Jaffe, K Johnson, and Charles B Thorn. Baryon structure in the bag theory. *Physical Review D*, 10(8):2599, 1974.

[215] Kenneth Johnson et al. The mit bag model. *Acta Phys. Pol. B*, 6(12):8, 1975.

[216] Yuchi He, Kang Yang, Jonas B Hauck, Emil J Bergholtz, and Dante M Kennes. Superconductivity of repulsive spinless fermions with sublattice potentials. *Physical Review Research*, 5(1):L012009, 2023.

[217] Valentin Crépel and Liang Fu. New mechanism and exact theory of superconductivity from strong repulsive interaction. *Science Advances*, 7(30):eabh2233, 2021.

[218] Valentin Crépel, Tommaso Cea, Liang Fu, and Francisco Guinea. Unconventional superconductivity due to interband polarization. *Physical Review B*, 105(9):094506, 2022.

[219] Yuchi He, Kang Yang, Jonas B. Hauck, Emil J. Bergholtz, and Dante M. Kennes. Superconductivity of repulsive spinless fermions with sublattice potentials. *Phys. Rev. Res.*, 5:L012009, Jan 2023.

[220] Jarryd J Pla, Kuan Y Tan, Juan P Dehollain, Wee H Lim, John JL Morton, Floris A Zwanenburg, David N Jamieson, Andrew S Dzurak, and Andrea Morello. High-fidelity readout and control of a nuclear spin qubit in silicon. *Nature*, 496(7445):334–338, 2013.

[221] Rostyslav Savytskyy, Tim Botzem, Irene Fernandez de Fuentes, Benjamin Joecker, Jarryd J. Pla, Fay E. Hudson, Kohei M. Itoh, Alexander M. Jakob, Brett C. Johnson, David N. Jamieson, Andrew S. Dzurak, and Andrea Morello. An electrically driven single-atom flip-flop qubit. *Science Advances*, 9(6):eadd9408, 2023.

[222] J. Järvinen, J. Ahokas, S. Sheludyakov, O. Vainio, L. Lehtonen, S. Vasiliev, D. Zvezdov, Y. Fujii, S. Mitsudo, T. Mizusaki, M. Gwak, SangGap Lee, Soonchil Lee, and L. Vlasenko. Efficient dynamic nuclear polarization of phosphorus in silicon in strong magnetic fields and at low temperatures. *Phys. Rev. B*, 90:214401, Dec 2014.

[223] Xuedong Hu, Belita Koiller, and S Das Sarma. Charge qubits in semiconductor quantum computer architecture: Tunnel coupling and decoherence. *Physical Review B*, 71(23):235332, 2005.

[224] John King Gamble, N Tobias Jacobson, Erik Nielsen, Andrew D Baczewski, Jonathan E Moussa, Inès Montaño, and Richard P Muller. Multivalley effective mass theory simulation of donors in silicon. *Physical Review B*, 91(23):235318, 2015.

[225] Amintor Dusko, AL Saraiva, and Belita Koiller. Splitting valleys in si/sio 2: Identification and control of interface states. *Physical Review B*, 89(20):205307, 2014.

[226] W Kohn and JM Luttinger. Theory of donor states in silicon. *Physical Review*, 98(4):915, 1955.

[227] G Feher. Electron spin resonance experiments on donors in silicon. i. electronic structure of donors by the electron nuclear double resonance technique. *Physical Review*, 114(5):1219, 1959.

[228] Joaquin F. Rodriguez-Nieva, Alexander Schuckert, Dries Sels, Michael Knap, and Eugene Demler. Transverse instability and universal decay of spin spiral order in the heisenberg model. *Phys. Rev. B*, 105:L060302, Feb 2022.

[229] Benoît Collins. Moments and cumulants of polynomial random variables on unitarygroups, the itzykson-zuber integral, and free probability. *International Mathematics Research Notices*, 2003(17):953–982, 2003.

[230] Fernando GSL Brandao, Aram W Harrow, and Michał Horodecki. Local random quantum circuits are approximate polynomial-designs. *Communications in Mathematical Physics*, 346(2):397–434, 2016.

[231] Aram Harrow and Saeed Mehraban. Approximate unitary t-designs by short random quantum circuits using nearest-neighbor and long-range gates. *arXiv preprint arXiv:1809.06957*, 2018.

[232] Ingo Roth, Richard Kueng, Shelby Kimmel, Y-K Liu, David Gross, Jens Eisert, and Martin Kliesch. Recovering quantum gates from few average gate fidelities. *Physical review letters*, 121(17):170502, 2018.

[233] Jeong-Hyuck Park. Lecture note on clifford algebra. *Journal of the Korean Physical Society*, 81(1):1–17, 2022.

[234] Eduardo Fradkin. *Field theories of condensed matter physics*. Cambridge University Press, 2013.

[235] Douglas Rayne Hartree. The wave mechanics of an atom with a non-coulomb central field. part ii. some results and discussion. In *Mathematical Proceedings of the Cambridge Philosophical Society*, volume 24, pages 111–132. Cambridge University Press, 1928.

[236] Alekse Alekseevich Abrikosov, Lev Petrovich Gorkov, and Igor Ekhielevich Dzyaloshinski. *Methods of quantum field theory in statistical physics*. Courier Corporation, 2012.

[237] Marıa José Calderón, André Saraiva, Belita Koiller, and S Das Sarma. Quantum control and manipulation of donor electrons in si-based quantum computing. *Journal of Applied Physics*, 105(12), 2009.

[238] Frederick Seitz and David Turnbull. *Solid state physics*, volume 5. Academic Press, 1957.

[239] Koichi Shindo and Hisashi Nara. The effective mass equation for the multi-valley semiconductors. *Journal of the Physical Society of Japan*, 40(6):1640–1644, 1976.

[240] Carlo WJ Beenakker. Theory of coulomb-blockade oscillations in the conductance of a quantum dot. *Physical Review B*, 44(4):1646, 1991.